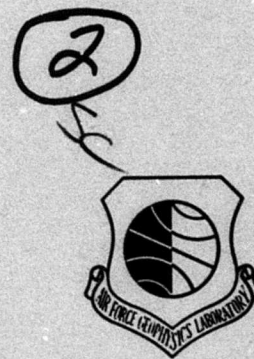


AD No. AD A 051192
DDC FILE COPY

AFGL-TR-77-0149
ENVIRONMENTAL RESEARCH PAPERS, NO. 603



**Hydrometeor Data and Analytical-Theoretical
Investigations Pertaining to the SAMS Rain
Erosion Program of the 1972-73 Season at
Wallops Island, Virginia
AFGL/SAMS Report No. 5**

VERNON G. PLANK

5 July 1977



Approved for public release; distribution unlimited.

METEOROLOGY DIVISION PROJECT 627A
AIR FORCE GEOPHYSICS LABORATORY
HANSCOM AFB, MASSACHUSETTS 01731

AIR FORCE SYSTEMS COMMAND, USAF

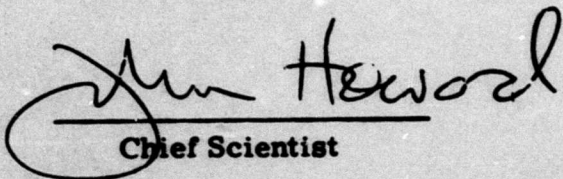


ORIGINAL CONTAINS COLOR PLATES: ALL DDC
REPRODUCTIONS WILL BE IN BLACK AND WHITE

This report has been reviewed by the ESD Information Office (OI) and is releasable to the National Technical Information Service (NTIS).

This technical report has been reviewed and is approved for publication.

FOR THE COMMANDER


Chief Scientist

Qualified requestors may obtain additional copies from the Defense Documentation Center. All others should apply to the National Technical Information Service.

Unclassified

SECURITY CLASSIFICATION OF THIS PAGE (When Data Entered)

Environmental research papers

REPORT DOCUMENTATION PAGE		READ INSTRUCTIONS BEFORE COMPLETING FORM	
1. REPORT NUMBER AFGL-TR-77-0149	2. GOVT ACCESSION NO. AFGL-ERP-603	3. REPORT'S CATALOG NUMBER	
4. TITLE (and Subtitle) HYDROMETEOR DATA AND ANALYTICAL-THEORETICAL INVESTIGATIONS PERTAINING TO THE SAMS RAIN EROSION PROGRAM OF THE 1972-73 SEASON AT WALLOPS ISLAND, VIRGINIA - AFGL/SAMS REPORT No. 5.		5. TYPE OF REPORT & PERIOD COVERED Interim 1972-1973	
7. AUTHOR(s) Vernon G./Plank		6. PERFORMING ORG. REPORT NUMBER ERP No. 603	
9. PERFORMING ORGANIZATION NAME AND ADDRESS Air Force Geophysics Laboratory (LY) Hanscom AFB, Massachusetts 01731		10. PROGRAM ELEMENT, PROJECT, TASK AREA & WORK UNIT NUMBERS 63311F 627A0001	
11. CONTROLLING OFFICE NAME AND ADDRESS Air Force Geophysics Laboratory (LY) Hanscom AFB, Massachusetts 01731		12. REPORT DATE 5 Jul 77	
14. MONITORING AGENCY NAME & ADDRESS (if different from Controlling Office)		13. NUMBER OF PAGES 239	
		15. SECURITY CLASS. (if applicable) Unclassified	
16. DISTRIBUTION STATEMENT (of this Report) Approved for public release; distribution unlimited.		15a. DECLASSIFICATION/DOWNGRADING SCHEDULE	
17. DISTRIBUTION STATEMENT (of the abstract entered in Block 20, if different from Report)		DDC REPRODUCED MAR 14 1978 REGULATORY B	
18. SUPPLEMENTARY NOTES ORIGINAL CONTAINS COLOR PLATES: ALL DDC REPRODUCTIONS WILL BE IN BLACK AND WHITE			
19. KEY WORDS (Continue on reverse side if necessary and identify by block number) SAMS--ABRES Liquid-water-content Rain erosion Radar reflectivity factor East coast winter storms Radar meteorology Wallops Island, Virginia Cloud physics Precipitation Aircraft storm measurements			
20. ABSTRACT (Continue on reverse side if necessary and identify by block number) Radar, aircraft, and surface measurement information is presented concerning the liquid-water-content values and size distribution properties of the hydrometeors that existed along the trajectory paths of the four SAMS missiles that were fired into Wallops storms during the 1972-73 season. The storm situations are described by references to weather maps, satellite photographs, radar photographs, and time-altitude cross sections. The hydrometeor conditions at the launch times of the missiles, along the path trajectories, are assessed from surface rainfall information, radar data, and			

1 409 578 All

19. (Cont)

Hydrometeors
 Hydrometeor spectra
 Hydrometeor-spectra models
 M-Z correlations
 Accuracy enhancement of
 M-Z correlations
 New technique in cloud physics
 Rain spectra
 Snow spectra
 Ice-crystal spectra

Radar-aircraft-satellite
 observations of storms
 NASA Flight Center
 NASA Wallops
 Disdrometer measurements
 Rain-size distributions
 Comparative rain-spectra

20. (Cont)

aircraft measurements made during storm flights that immediately followed the missile firings. The procedures are explained whereby the values of liquid-water-content and estimates of hydrometeor size-distribution were determined for the trajectories.

The results of several analytical and theoretical investigations are reported which led to the discovery of a new spectral parameter that can be computed from aircraft size-distribution data (for hydrometeors) with considerably better accuracy than either M (liquid-water-content) or Z (aircraft-determined radar-reflectivity-factor) can be computed. This parameter is discussed extensively and conclusions are drawn regarding the accuracy enhancement to the overall SAMS analyses that would be achievable by its use.

The mathematics and assumptions of the double-truncated, SAMS "precipitation model" are presented and the descriptivity of the model is demonstrated relative to particular data results.

ACCESSION for		
NTIS	White Section	<input checked="" type="checkbox"/>
DOC	Buff Section	<input checked="" type="checkbox"/>
UNANNOUNCED		<input type="checkbox"/>
JUSTIFICATION _____		
BY _____		
DISTRIBUTION/AVAILABILITY CODES		
Dist.	AVAIL.	and/or SPECIAL
A		

Preface

The AFCRL program of measurements supporting the SAMS rain erosion project at Wallops Island, Virginia during the 1972-73 season was conducted as a joint team effort by various members of the Weather Radar and Convective Cloud Physics Branches of the Meteorology Laboratory, AFCRL. * Contractual support was provided by the Applied Physics Laboratory of Johns Hopkins University and by Meteorology Research Inc., Altadena, California. The program was directed by Dr. Robert M. Cunningham, of the Convective Cloud Physics Branch, and supervised by Dr. Kenneth R. Hardy, of the Weather Radar Branch.

The AFCRL and contract contributors to the measurement program are identified in the following list, and their efforts toward the accomplishment of the SAMS objectives are acknowledged. Special thanks are extended to Mr. Alfred A. Spatola and Mr. Robert O. Berthel for their considerable help in performing analyses and computations, and reviewing, and criticizing the manuscript.

<u>Name</u>	<u>Organization</u>	<u>Role</u>
Dr. Morton L. Barad	LY*	Director, Meteorology Laboratory
Mr. Chankey N. Touart	LY	AFCRL Program Manager for Weather Erosion Programs June 1973 to present
Dr. Robert M. Cunningham	LYC**	Director of AFCRL Measurement Program at Wallops Island, Virginia
Dr. Kenneth R. Hardy	LYW [†]	Supervisor of AFCRL Radar Measurements Program at Wallops Island, Virginia

* Air Force Cambridge Research Laboratories (AFCRL) was redesignated Air Force Geophysics Laboratory (AFGL) 1 February 1976.

Preface

<u>Name</u>	<u>Organization</u>	<u>Role</u>
Mr. Kenneth M. Glover	LYW	
Dr. Arnold A. Barnes, Jr.	LYW	
Mr. Albert C. Chmela	LYW	
Mr. Graham M. Armstrong	LYW	
Mr. Edward F. Duquette	LYW	
Mr. Alexander W. Bishop	LYW	
1/Lt James Metcalf	LYW	
Mr. Vernon G. Plank	LYC	
Lt. Col. James F. Church	LYC	
Mr. Alfred A. Spatola	LYC	
Mr. Robert O. Berthel	LYC	
Ms. Barbara A. Main	LYC	
Mr. Donald W. McLeod	LYC	
Mr. Morton Glass	LYC	
Mr. George Ritscher	LYC	
Mr. Russell M. Peirce, Jr.	LYC	
Mr. Konstantins Pocs	LYC	
Mrs. Elizabeth Kintigh	LYC	
CMSgt Thomas W.K. Hobbs	LYC	
TSgt James E. Bush	LYC	
MSgt Thomas W. Moraski	LYC	
Ms. JoAnne E. Waters	LYC	
SSgt Dennis E. Karoleski	LYC	
Sgt David L. Bakke	LYC	
Sgt Curtis H. Waechtler	LYC	
Mr. Jack Howard	APL ^{††}	Radar Station Mgr. at Wallops Island, Virginia
Mr. Norris Beasley	APL	
Mr. Norm Gebo	APL	
Mr. Charles Ponder	APL	
Mr. Herbert Seeman	APL	
Mr. Norman Parker	APL	
Mr. Harold Lord	APL	
Mr. Richard Gagnon	APL	
Mr. Larry Greer	APL	
Dr. Isadore Katz	APL	
Dr. Thomas Konrad	APL	
Mr. James Meyer	APL	
Mrs. Ella Dobson	APL	

Preface

<u>Name</u>	<u>Organization</u>	<u>Role</u>
Mr. Donald Takeuchi	MRI ^{†††}	
Mr. Alfonso Ollivares	MRI	
Mr. Ralph Martin	MRI	
Mr. Larry Boardman	MRI	

* LY - Meteorology Laboratory, Air Force Cambridge Research Laboratories.

** LYC - Convective Cloud Physics Branch, Meteorology Laboratory.

† LYW - Weather Radar Branch, Meteorology Laboratory.

†† APL - Applied Physics Laboratory, Johns Hopkins University,
Silver Springs, Maryland.

††† MRI - Meteorology Research Inc., Altadena, California

Contents

1. INTRODUCTION	17
2. FLIGHT CIRCUMSTANCES AND WEATHER CONDITIONS	19
3. PROFILES OF LIQUID-WATER-CONTENT AND INTEGRAL OF LIQUID-WATER-CONTENT FOR THE MISSILE TRAJECTORIES AS DETERMINED FROM RADAR DATA	19
4. CLOUD LIQUID-WATER-CONTENT VALUES FOR THE MISSILE TRAJECTORIES	22
5. COMMENTS	25
REFERENCES	27
APPENDIX A: Synoptic Weather Maps, Satellite Photographs and Storm Cross Sections	29
APPENDIX B: Radar Structure of Storms at the Missile Launch Times	39
APPENDIX C: Computation of Hydrometeor Parameters from the Radar Data	49
APPENDIX D: Precipitation Measurements at the Surface Level	79
APPENDIX E: AFCRL Flights, Summary Notes and Particular Analyses, for the 1972-73 Season	91
APPENDIX F: Liquid-Water-Content and Size Distribution Information Acquired from the MRI, Navajo Aircraft	173
APPENDIX G: Summary and "Best Estimate" Information about the Spectral Distribution and Total Values of the Number Concentration and Liquid-Water-Content of the Hydrometeors along the Missile Trajectories	183
APPENDIX H: Special Background Studies	221

Illustrations

1.	Profiles of Liquid-Water-Content and Integral of Liquid-Water-Content for the Missile Trajectory of Flight Q2-6360 (Unit No. R487101) of 2 February 1973, Launched at 1408:00 GMT	20
2.	Profiles of Liquid-Water-Content and Integral of Liquid-Water-Content for the Missile Trajectory of Flight Q2-6361 (Unit No. R487102) of 2 February 1973, Launched at 1408:30 GMT	21
3.	Profiles of Liquid-Water-Content and Integral of Liquid-Water-Content for the Missile Trajectory of Flight Q2-6362 (Unit No. R487103) of 27 February 1973, Launched at 1040:00 GMT	22
4.	Profiles of Liquid-Water-Content and Integral of Liquid-Water-Content for the Missile Trajectory of Flight Q2-6363 (Unit No. R487104) of 27 February 1973, Launched at 1040:30 GMT	23
5.	Percent Frequency of Occurrence Isolines of Cloud Liquid-Water-Content, as Determined From the Johnson-Williams (JW) Instrument of the AFGL C-130A Aircraft	25
A1.	Surface Weather Maps for the Eastern United States for 1200, 1500, and 1800 GMT, 2 February 1973	30
A2.	Surface Weather Maps for the Eastern United States for 0900, 1200, and 1500 GMT, 27 February 1973	30
A3.	Photograph Obtained From the Synchronous Satellite, ATS-3, Showing the Cloud System Associated With the Storm of 2 February 1973, 1400Z.	31
A4.	Photograph Obtained From the Polar-Orbiting Satellite, DAPP, Showing the Cloud System Associated With the Storm of 2 February 1973, Approximately 1730Z.	31
A5.	Photograph Obtained From the Synchronous Satellite, ATS-3, Showing the Cloud System Associated With the Storm of 27 February 1973, 1356Z.	32
A6.	Photograph Obtained From the Polar-Orbiting Satellite, DAPP, Showing the Cloud System Associated With the Storm of 27 February 1973, Approximately 1630Z.	32
A7.	Time-Altitude Cross-Section for the Wallops Storm of 2 February 1973, for the Time Period 00 GMT to 2400 GMT	34
A8.	Time-Altitude Cross-Section for the Wallops Storm of 27 February 1973, for the Time Period 00 GMT to 2400 GMT	35
B1.	RHI Diagram With Colored, Contoured Regions of 5 dB Signal Differential Which Illustrate the Radar Structure of the Storm of 2 February 1973 in the 146° Azimuth Direction About 30 sec Prior to the Launch Time of the First Missile Fired on This Day	40
B2.	RHI Diagram With Colored, Contoured Regions of 5 dB Signal Differential Which Illustrate the Radar Structure of the Storm of 2 February 1973 in the 146° Azimuth Direction at About the Launch Time of the Second Missile Fired on This Day	41
B3.	RHI Diagram With Colored, Contoured Regions of 5 dB Signal Differential Which Illustrate the Radar Structure of the Storm of 27 February 1973 in the 146° Azimuth Direction at About the Launch Time of the First Missile Fired on This Day	42

Illustrations

B4.	RHI Diagram With Colored, Contoured Regions of 5 dB Signal Differential Which Illustrate the Radar Structure of the Storm of 27 February 1973 in the 146° Azimuth Direction About 1 min and 30 sec After the Launch Time of the Second Missile Fired on This Day	43
B5.	RHI Photographs Obtained With the FPS-18 Radar on 27 February 1973 at the Launch Times of the Two Missiles Fired on This Day	45
B6.	RHI Photographs Obtained With the FPS-18 Radar on 27 February 1973 Which Were Taken in the Launch Direction Approximately 6 min Before Launch and 5 min After Launch	45
B7.	RHI Photographs Obtained With the FPS-18 Radar on 27 February 1973 Which Were Taken in the Launch Direction at the Approximate Mid-Time Point of the Aircraft Measurement Period and Near the End of the Aircraft Measurement Period	46
C1.	Portions of the RHI Diagrams for the Two Missile Launches of 2 February 1973 Which Show the Detailed \perp Signal-Structure of the Storm in the Immediate Vicinity of the Trajectory Paths	50
C2.	Portions of the RHI Diagrams for the Two Missile Launches of 27 February 1973 Which Show the Detailed \perp Signal-Structure of the Storm in the Immediate Vicinity of the Trajectory Paths	51
C3.	Profiles of the Radar Integration Signal and the Radar Volume Reflectivity for the Missile Trajectory of Flight No. Q2-6360 (Unit No. R487 101) of 2 February 1973, Launched at 1408:00 GMT	53
C4.	Profiles of the Radar Integration Signal and the Radar Volume Reflectivity for the Missile Trajectory of Flight No. Q2-6361 (Unit No. R487 102) of 2 February 1973, Launched at 1408:30 GMT	53
C5.	Profiles of the Radar Integration Signal and the Radar Volume Reflectivity for the Missile Trajectory of Flight No. Q2-6362 (Unit No. R487 103) of 27 February 1973, Launched at 1040:00 GMT	54
C6.	Profiles of the Radar Integration Signal and the Radar Volume Reflectivity for the Missile Trajectory of Flight No. Q2-6363 (Unit No. R487 104) of 27 February 1973, Launched at 1040:30 GMT	55
C7.	Profiles of the Radar Reflectivity Factors for Water and Ice Hydrometeors for the Missile Trajectory of Flight No. Q2-6360 (Unit No. R487 101) of 2 February 1973, Launched at 1408:00 GMT	56
C8.	Profiles of the Radar Reflectivity Factor for Water and Ice Hydrometeors for the Missile Trajectory of Flight No. Q2-6361 (Unit No. R487 102) of 2 February 1973, Launched at 1408:30 GMT	56
C9.	Profiles of the Radar Reflectivity Factor for Water and Ice Hydrometeors for the Missile Trajectory of Flight No. Q2-6262 (Unit No. R487 103) of 27 February 1973, Launched at 1040:00 GMT	57

Illustrations

C10.	Profiles of the Radar Reflectivity Factor for Water and Ice Hydrometeors for the Missile Trajectory of Flight No. Q2-6363 (Unit No. R487104) of 27 February 1973, Launched at 1040:30 GMT	57
C11.	The Hydrometeor Regions and Zones Within the Storm of 2 February 1973 and the Profile of Precipitation Rate for the Missile Trajectory of Flight No. Q2-6360 (Unit No. R478101) Launched at 1408:00 GMT	58
C12.	The Hydrometeor Regions and Zones Within the Storm of 2 February 1973 and the Profile of Precipitation Rate for the Missile Trajectory of Flight No. Q2-6361 (Unit No. R487102) Launched at 1408:30 GMT	58
C13.	The Hydrometeor Regions and Zones Within the Storm of 27 February 1973 and the Profile of Precipitation Rate for the Missile Trajectory of Flight No. Q2-6362 (Unit No. 487103) Launched at 1040:00 GMT	59
C14.	The Hydrometeor Regions and Zones Within the Storm of 27 February 1973 and the Profile of Precipitation Rates for the Missile Trajectory of Flight No. Q2-6363 (Unit No. R487104) Launched at 1040:30 GMT	59
D1.	Map Showing Siting Locations of Rain Gauges and Disdrometers Relative to the Missile Launch Pads	80
D2.	Time-Plots of Precipitation Rate and Liquid-Water-Content at the Surface Level for the 3-hr Period Centered About the Launch Times of the Missiles, From Disdrometer Data Acquired at the Launch Site on 2 February 1973	81
D3.	Time-Plots of Precipitation Rate and Liquid-Water-Content at the Surface Level for the 3-hr Period Centered About the Launch Times of the Missiles, From Tipping-Bucket Data Acquired at the Launch Site and South Site on 2 February 1973	82
D4.	Time-Plots of Precipitation Rate and Liquid-Water-Content at the Surface Level for the Period 1/2-hr Prior to Launch Time to 1-1/2-hr Subsequent to Launch Time, From Disdrometer Data Acquired at the Launch Site on 27 February 1973	84
D5.	Time-Plots of Precipitation Rate and Liquid-Water-Content at the Surface Level for the 3-hr Period Centered About the Launch Times of the Missiles, From Tipping-Bucket Data Acquired at the Launch Site and South Site on 27 February 1973	85
E1.	The Relationship for Different Crystal Types, Between the Length Measures Defined by Heymsfield and Knollenberg (1972) and Kajikawa (1972) and the Equivalent-Melted-Diameters	107
F2.	Plots of M vs Z for the Different Sizing Methods, Different Samples and Different Assumptions About Ice Crystal Type and Analytical Procedures	113
F3.	An Illustration of How the M vs Z Data of Tables F7 and F8 Fit the Heymsfield-Cunningham Regression Equation for Bullet-Rosette Ice Crystals	115
F4.	Illustration of the Form Factor Values Associated With Representative Hydrometeor Distributions of Exponential, Lower-Diameter-Truncated Exponential and Other Modified-Exponential Types	126

Illustrations

E5.	Illustrations of the Form Factor Values Associated With Representative Hydrometeor Distributions of Bi-Modal and Truncated Bi-Modal Types	127
E6.	Particular Isolines of k , for Single Hydrometeor Samples, as Plotted From Eq. (E49)	130
E7.	Isolines of k Corresponding to the Basic Foil Data of Tables E4 and E5 and to the Data of Table E9, Which Have Been Converted Into Terms of Equivalent-Melted-Diameter by the Various Text-Discussed Methods and Assumptions	132
E8.	Illustrations of Class-by-Class Proportionality Which Yield Identical Values of the Form Factor, F	139
E9.	Plots of F , N_T and k , vs Z_g , for Rain Data From Disdrometer A Obtained on 22 March 1972	140
E10.	Plots of F , N_T and k , vs Z_g , for Rain Data From Disdrometer B Obtained on 22 March 1972	141
E11.	Plots of F , N_T and k , vs Z_g , for the Data of Ohtake and Henmi for Large-Snow of Dendritic-Stellar Type	142
E12.	Plots of F , N_T , and k , vs Z_g , for the Ice-Crystal Data of PVM-5	143
E13.	Illustrations of the Spectral Characteristics and Trends of the Form Factor Data of Ohtake and Henmi	150
E14.	An Illustration of How the k , Z Data of Tables E8 and E9 Fit the k vs Z Equation of Heymsfield and Cunningham, Which Pertains to C_1 Ice-Crystals of Bullet-Rosette Type	154
E15.	Equation Plots of the Decimal Uncertainties of Radar Reflectivity Factor, Liquid-Water-Content and the Spectral Parameter k , for Large Snow of Type LS_3	160
E16.	Equation Plots of the Decimal Uncertainties of Radar Reflectivity Factor, Liquid-Water-Content and the Spectral Parameter k , for Small Snow of Type SS_g	160
E17.	Equation Plots of the Decimal Uncertainties of Radar Reflectivity Factor, Liquid-Water-Content and the Spectral Parameter k , for Ice Crystals of Type C_1	161
E18.	Example of Nomogram of k vs Z With Isolines of M	162
E19.	Nomographic Illustration of the Uncertainties and "Uncertainty Areas" of M and Z for the Case in Which These Parameters are Both Computed From Spectral Data	164
E20.	Nomographic Illustration of the Uncertainties and "Uncertainty Areas" of M and Z for the Case in Which M is Computed From Spectral Data and Z is Measured by Radar	164
E21.	Nomographic Illustration of the Uncertainties and "Uncertainty Areas" of k and Z for the Case in Which k is Computed From Spectral Data and Z is Measured by Radar	165
E22.	Cross-Plot of the Aircraft Spectral Values of M Plotted vs the Radar-Measured Values of Z , for the Data of PVM-5, Pass 8	166
E23.	Cross-Plot of the Aircraft Spectral Values of k Plotted vs the Radar-Measured Values of Z , for the Data of PVM-5, Pass 8	167

Illustrations

E24.	Examples of Trajectory Profiles of Radar-Measured Z, of Aircraft-Radar Determined k and the Resultant M Profile Computed From $M = k\sqrt{Z}$	172
F1.	Frequency Distribution of Cloud Liquid-Water-Content for Five Different Flight Altitudes in Storm of 2 February 1973	181
F2.	Spatial Variations of Raindrop Size-Distributions in Descent From 5000 to 3000 ft During Storm of 27 February 1973	182
G1.	Values of the Truncation Ratio for Particle Number Concentration as a Function of d^Λ and D_m^Λ	197
G2.	Values of the Truncation Ratio for Distributed Liquid-Water-Content as a Function of d^Λ and D_m^Λ	198
G3.	Values of the Truncation Ratio for Distributed Radar-Reflectivity-Factor as a Function of d^Λ and D_m^Λ	200
G4.	Values of the Truncation Parameter, ψ , as a Function of d^Λ and D_m^Λ	202
G5.	Values of the Truncation Parameter, ϕ , as a Function of d^Λ and D_m^Λ	203
G6.	Values of D_o/D' as a Function of d^Λ and D_m^Λ	204
G7.	Values of D_o/D' as a Function of d/D_o and D_m/D_o	206
G8.	Comparisons of Model Predicted Maximum Particle Sizes With the Maximum Sizes Determined From Aircraft, Foil-Impactor Data for Large Sampling Volumes	215
G9.	Value Trends With Z of the Form Factor, of the Total Number Concentration of the Drops or Particles and of the Spectral Parameter, k, as Prescribed by the SAMS Precipitation Model for Four Hydrometeor Types	217
H1.	Values of the Form Factor as a Function of ΛD_n and n, for ΛD_n Values Ranging From -20 to 140, No Lower Diameter Truncation	225
H2.	Values of the Form Factor as a Function of ΛD_n and n, for ΛD_n Values in the Typical Atmospheric Range of -5 to 20, No Lower Diameter Truncation	226
H3.	Values of the Form Factor as a Function of ΛD_n and n, Atmospheric Range, With Lower Diameter Truncation of $d = \Delta D$	227
H4.	Values of the Form Factor as a Function of ΛD_n and n, Atmospheric Range, With Lower Diameter Truncation of $d = 2\Delta D$	228
H5.	Values of the Form Factor as a Function of ΛD_n and n, Atmospheric Range, With Lower Diameter Truncation of $d = 3\Delta D$	228

Tables

1.	Hydrometeor Regions, Types and Equations Used in the 1972-73 Season	24
B1.	Color code of Signal Intensity Used With the Computer RHI Diagrams of Figures B1 and B2	44
B2.	Shading Code Used With the Video-Integrated RHI Photographs of Figures B5 through B7	46
C1.	Tabulation of the Numerical Values of the Radar and Hydrometeor Parameters for Missile Flight No. Q2-6360 (Unit No. R487101) of 2 February 1973, Launched at 1408:00 GMT	62
C2.	Tabulation of the Numerical Values of the Radar and Hydrometeor Parameters for Missile Flight No. Q2-6361 (Unit No. R487102) of 2 February 1973, Launched at 1408:30 GMT	66
C3.	Tabulation of the Numerical Values of the Radar and Hydrometeor Parameters for Missile Flight No. Q2-6362 (Unit No. R487103) of 27 February 1973, Launched at 1040:00 GMT	70
C4.	Tabulation of the Numerical Values of the Radar and Hydrometeor Parameters for Missile Flight No. Q2-6363 (Unit No. R487104) of 27 February 1973, Launched at 1040:30 GMT	74
D1.	Comparison Rainrates Determined for Two Sites and Time Intervals During the Storm of 26 February 1973	87
D2.	Comparison Spectra of Raindrop Number Concentration, Liquid-Water-Content and Radar Reflectivity Factor, Determined by Disdrometers and Filter Paper Samples, for Two Sites and Time Intervals During the Storm of 26 February 1973	88
E1.	Dates and Times of the AFGL C-130A Flights in Support of SAMS-ABRES During the 1972-73 Season, With Comments About Mission Results	92
E2.	Flight Director's Notes Concerning the General Hydrometeor Conditions at the Different Flight Levels in the Storm of 2 February 1973	93
E3.	The Sizes, by Altitude Layer, of the Ten Largest Snow or Ice Particles Measured, by Two Analysts, A ₁ and A ₂ , From the Foil Record of the "Ascent Portion" of the C-130A Sortie of 2 February 1973	100
E4.	Number Concentrations of Ice Particles as Counted in Classes of Maximum Particle Dimension, for Three Foil Samples Obtained on 2 February 1973	102
E5.	Number Concentration of Ice Particles as Counted in Classes of Average Particle Dimension, for Two Foil Samples Obtained on 2 February 1973	103
E6.	Distributions of Ice-Particle Number-Concentration for Different Sizing Methods, Different Samples and Different Assumptions About Ice-Crystal Type and Analytical Procedures	109
E7.	Distributions of Ice-Particle Liquid-Water-Content for Different Sizing Methods, Different Samples and Different Assumptions About Ice-Crystal Type and Analytical Procedures	111

Tables

E8.	Distributions of Ice-Particle Radar-Reflectivity-Factors for Different Sizing Methods, Different Samples and Different Assumptions About Ice Crystal Type and Analytical Procedures	111
E9.	Values of the α Coefficients and of $\sqrt{N_T}$, F and k for the Number Concentration Data for Ice Particles of Table E6	123
E10.	Ranges of the Values of $\sqrt{N_T}$, F and k for the Rain Samples of Table D2 and for the Ice Particle Samples of Tables E4, E5, and E9	124
E11.	Values of the Regression Parameters for the Rain, Large-Snow and Ice-Crystal Data of Figures E9, E10, E11 and E12	148
E12.	Approximate Average Values of the Terms of Eq. (E89) and Average Values of the Terms of Eq. (91) for the Comparative Cases Involving the Foil Samples Described in the Text	158
F1.	Quick-Look Summary of Cloud Particles in Storm of 2 February 1973, Wallops Island, Virginia	175
F2.	Foil Data for Flight of 2 February 1973	176
F3.	Raindrop Size Distribution for Storm of 2 February 1973	176
F4.	Notes of Hydrometeor Conditions During Flight of 27 February 1973	177
F5.	Summary of Continuous Cloud Particle Replicator Data Observations for Storm of 27 February 1973	177
F6.	Foil Data Summary for Storm of 27 February 1973	178
F7.	Foil Data Size-Distribution Summary for Storm on 27 February 1973, Wallops Island	179
F8.	Additional Foil Data for Storm on 27 February 1973	180
G1.	Diameter Classes Specified for SAMS	185
G2.	Summary and "Best Estimate" Information About the Spectral Distribution and Total Values of Hydrometeor Number Concentration and Liquid-Water-Content Along the Missile Trajectory of Flight No. Q2-6360 (Unit No. R487101) of 2 February 1973, Launched at 1408:00 GMT	186
G3.	Summary and "Best Estimate" Information About the Spectral Distribution and Total Values of Hydrometeor Number Concentration and Liquid-Water-Content Along the Missile Trajectory of Flight No. Q2-6361 (Unit No. R487102) of 2 February 1973, Launched at 1408:30 GMT	188
G4.	Summary and "Best Estimate" Information About the Spectral Distribution and Total Values of Hydrometeor Number Concentration and Liquid-Water-Content Along the Missile Trajectory of Flight No. Q2-6362 (Unit No. R487103) of 27 February 1973, Launched at 1040:00 GMT	190
G5.	Summary and "Best Estimate" Information About the Spectral Distribution and Total Values of Hydrometeor Number Concentration and Liquid-Water-Content Along the Missile Trajectory of Flight No. Q2-6363 (Unit No. R487104) of 27 February 1973, Launched at 1040:30 GMT	192
G6.	Values and Comparison of Certain of the Distribution Parameters for Four Examples of Hydrometeor Populations Which are Diameter-Truncated or Non-Truncated	210

Tables

G7.	Distribution of Number Concentration, Liquid-Water-Content and Radar Reflectivity Factor Computed From the Precipitation Model for Conditions of Matching Correspondence With the Disdrometer and Filter-Paper Samples of Rain, of Table D2, Appendix D, Lower Truncation Diameter Equal to 0.07943 mm	213
G8.	Distribution of Number Concentration, Liquid-Water-Content and Radar Reflectivity Factor Computed From the Precipitation Model for Conditions of Matching Correspondence With the Disdrometer and Filter Paper Samples of Rain, of Table D2, Appendix D, Lower Truncation Diameter Equal to Sample-Observed	214
G9.	Comparisons Parameters of Hydrometeor Data and Precipitation Model	219
H1.	Parameters and Equations of the " ℓ Distributions", Parameters of ℓ to D Conversion and the Resultant Parameters of the "D Distributions"	235
H2.	Term, Total and Ratio Uncertainties in M, Z and k Resulting From the Uncertainties of γ and ϕ , in ℓ to D Conversion	236
H3.	Values of k_{ℓ} , k, Δk_{ℓ} and $\Delta k_{\ell}/\bar{k}$	237
H4.	Values of k_D , k, Δk_D and $\Delta k_D/\bar{k}$	239

**Hydrometeor Data and Analytical - Theoretical
Investigations Pertaining to the SAMS Rain Erosion Program
of the 1972-73 Season at Wallops Island, Virginia
AFGL/SAMS Report No.5**

I. INTRODUCTION

The liquid-water-content values and other associated hydrometeorological information for the trajectories of the SAMS missiles launched in the 1972-73 season that are presented in this report, were determined from radar, surface, and aircraft data obtained at Wallops Island, Virginia on the days of firing.

The dates, times, and circumstances of the missile launch operations are noted in the main text of this report and the general weather conditions at the times of firing are indicated. The profiles of liquid-water-content and the integral of liquid-water-content for the trajectory paths of the missiles that are presented were determined from radar measurements. Comments are made about the cloud liquid-water-content measurements obtained from the AFGL (formerly AFCRL) C-130A and the Meteorology Research Inc. (MRI) Navajo aircraft. Reference is made to the summary data tabulations and hydrometeor size-distribution information presented in Appendix G.

The report is organized such that the analytical results of immediate, direct pertinence to the erosion problem are presented in the main text. All background material and supplementary information are included in appendices. This format of presentation conforms with the agreement of the SAMS-ABRES conference at AFCRL on 7 and 8 March 1974.

(Received for publication 30 June 1977)

There are eight appendices to the report, as identified in the Table of Contents. The weather, cloud, and precipitation situations on the days of the missile flights are discussed in Appendix A. The radar structure of the storms, in the launch directions, is illustrated in Appendix B. Values of the radar and hydrometeor parameters along the missile trajectories are described and tabulated in Appendix C. Surface measurements of precipitation rate and liquid-water-content are presented in Appendix D. Certain aircraft storm data acquired by the AFGL C130A aircraft, also particular empirical and theoretical analyses, are discussed in Appendix E. The data obtained by the MRI Navajo aircraft are referenced in Appendix F. Spectral information concerning the number concentrations and liquid-water-content contributions of the various size classes and types of hydrometeors along the missile trajectories is provided in Appendix G. Additionally presented therein are the equations of the double truncated, exponential model that describes the spectral characteristics of precipitation size hydrometeors. Special background studies are included in Appendix H.

The figures and tables of these appendices are presented in numerical order by "common subject", rather than by "storm date". This is advantageous, in fact almost necessary, for the logical discussion of the subject matter, but it poses difficulties for the reader who wishes to inspect and intercompare all of the measurement results pertaining to a single missile flight, or a single storm. The large number of the text figures and tables add to the difficulty. The author has attempted to alleviate these problems somewhat by having the "thumb edge pages" of the separate appendices indexed by "bleed printing". The beginning page number of each appendix, and the page number of each figure and table, are also listed in the front of the report, in the Table of Contents, and in the List of Illustrations and Tables.

Note is made of the previous reports of the AFCRL/SAMS series. The Wallops Island radars, the radar measurement techniques, and the calibration procedures were described in AFCRL/SAMS Report No. 1. The methods used to obtain liquid-water-content values from the radar data for the missile trajectories were explained in AFCRL/SAMS Report No. 2. Liquid-water-content and size-distribution information for the SAMS missile flights of the 1971-72 season were provided in AFCRL/SAMS Report No. 3. Climatological data for selected Wallops storms were presented in AFGL/SAMS Report No. 4. These reports will subsequently be referenced as R No. 1, R No. 2, R No. 3, and R No. 4.^{1,2,3,4}

1. Plank, V.G. (1974) A Summary of the Radar Equations and Measurement Techniques Used in the SAMS Rain Program at Wallops Island, Virginia, AFCRL-SAMS Report No. 1, AFCRL-TR-74-0053, Special Reports No. 172.
2. Plank, V.G. (1974) Hydrometeor Parameters Determined From the Radar Data of the SAMS Rain Erosion Program, AFCRL/SAMS Report No. 2, AFCRL-TR-74-0249, ERP No. 477.
3. Plank, V.G. (1974) Liquid-Water-Content and Hydrometeor Size-Distribution Information for the SAMS Missile Flights of the 1971-1972 Season at Wallops Island, Virginia, AFCRL/SAMS Report No. 3, AFCRL-TR-74-0296, Special Reports No. 178.
4. Berthel, R.O. (1976) A Climatology of Selected Storms for Wallops Island, Virginia, 1971-1975, SAMS Report No. 4, AFGL-TR-76-0118, ERP No. 563.

2. FLIGHT CIRCUMSTANCES AND WEATHER CONDITIONS

Four missiles were launched during the 1972-73 season. The first and second (Q2-6360 and Q2-6361, Unit Nos. R487101 and R487102) were fired on 2 February 1973, at the times 1408:00 and 1408:30 GMT. They were launched into a storm associated with an occluded frontal system and warm front which had extensive cloudiness and a large area of surface precipitation. The third and fourth missiles (Q2-6362 and Q2-6363, Unit Nos. R487103 and R487104) were fired on 27 February 1973, at 1040:00 and 1040:30 GMT, through the clouds and precipitation of a dissipating open wave system that was passing the Wallops area, about 200 miles to the south.

The missiles were of the two-stage, Terrier-Recruit type. They were fired from "Launch Pad Zero" in the 146° azimuth direction, see the map of Figure D1, Appendix D. The erosion objectives and results of the flights have been reported by Cole, Church and Marshall.

The storm conditions at the launch times, and before and after launch, are discussed in Appendix A. Surface weather maps, satellite photographs, and storm cross-sections are presented that reveal the general cloud and precipitation conditions. The radar echo-structure of the storms in the 146° launch direction of the missiles is shown in Appendix B. The surface rainfall-rates and liquid-water-content values during the launch periods are illustrated in Appendix D.

3. PROFILES OF LIQUID-WATER-CONTENT AND INTEGRAL OF LIQUID-WATER-CONTENT FOR THE MISSILE TRAJECTORIES AS DETERMINED FROM RADAR DATA

The solid-line profiles of Figures 1 through 4 show the radar-determined values of liquid-water-content (M) vs altitude for the four missile flights of the 1972-73 season. The values pertain to the missile trajectories but they are plotted vs the altitude of the trajectory points above the ground (or sea) level.

The dashed-line profiles of Figures 1 through 4 show the values of the integral of liquid-water-content ($\int M d R_s$) which have been integrated, cumulatively, from the launch pad upward, along the course of the missile trajectories, to the storm top altitudes. The maximum, "total storm passage" value of the integral is indicated at the top of each profile, by the drafted numbers. The units of the integral are $gm\ m^{-2}$. The assumptions and equations used to compute the values of the integral were discussed in R No. 2.

*Sandia Corporation, Albuquerque, New Mexico.

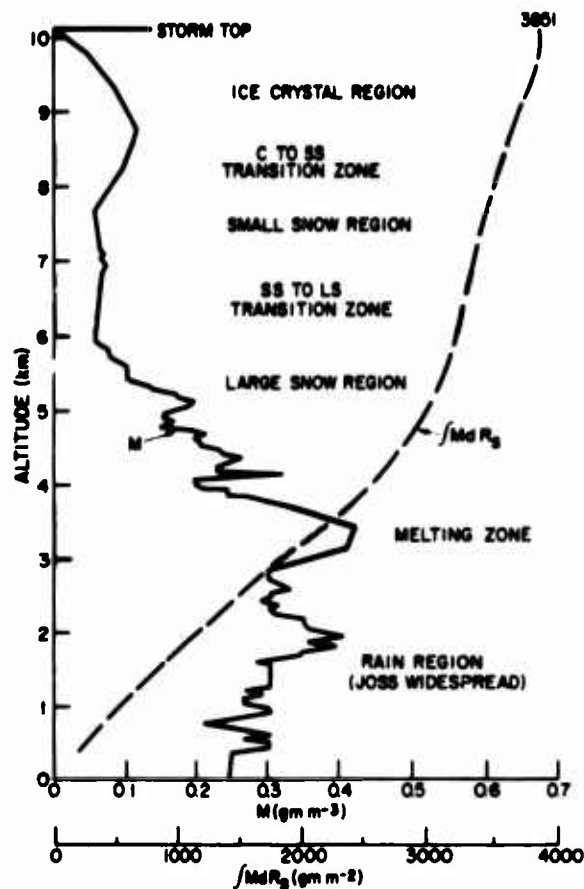


Figure 1. Profiles of Liquid-Water-Content (M) and Integral of Liquid-Water-Content ($\int M dR_3$) for the Missile Trajectory of Flight No. Q2-6360 (Unit No. R487101) of 2 February 1973, Launched at 1408:00 GMT

The hydrometeor regions and transition zones of the storms are also indicated in Figures 1 through 4. These regions and zones were established from aircraft observations and/or radiosonde temperatures. The letter symbols used in the figure are identified in Table 1. This table additionally lists the empirical equations, relating P vs Z , M vs Z and M vs P , see R No. 2, that were employed in the liquid-water-content computations for the different hydrometeor categories and types defined for the 1972-73 season. The definitions are consistent with those of Table 2, R No. 2.

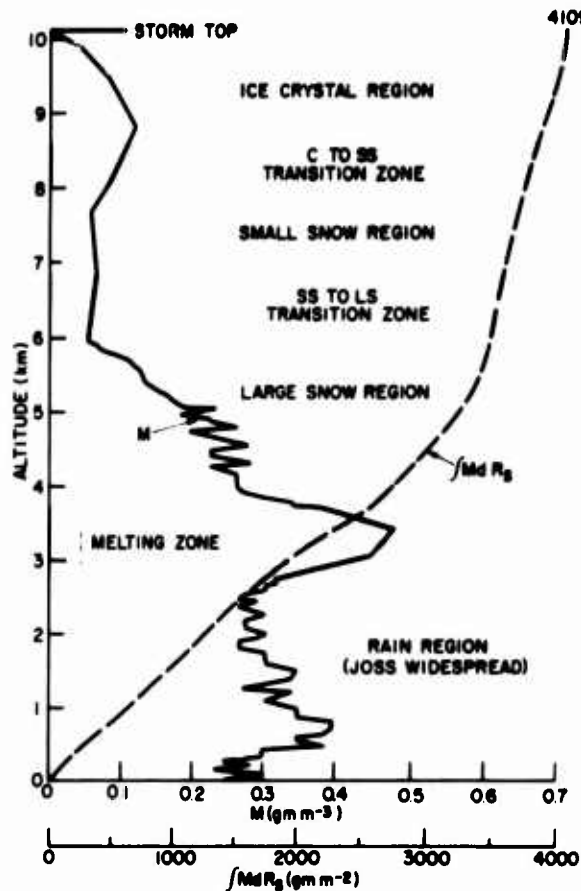


Figure 2. Profiles of Liquid-Water-Content (M) and Integral of Liquid-Water-Content ($\int M d R_g$) for the Missile Trajectory of Flight No. Q2-6361 (Unit No. R487102) of 2 February 1973, Launched at 1408:30 GMT

Background and auxiliary information about the radar and hydrometeor conditions along the missile trajectories is supplied in Appendix C. Diagrams and profiles of the radar integration signal, \underline{I} , are presented in Figures C1 through C6 of this appendix. Profiles of the radar reflectivity factors for water and ice hydrometeors, Z_W and Z_I , are presented in Figures C7 through C10. Profiles of the precipitation rate, P , are presented in Figures C11 through C14.

The numerical values of the radar and hydrometeor parameters for the missile trajectories are listed in Tables C1 through C4, for each data point altitude.

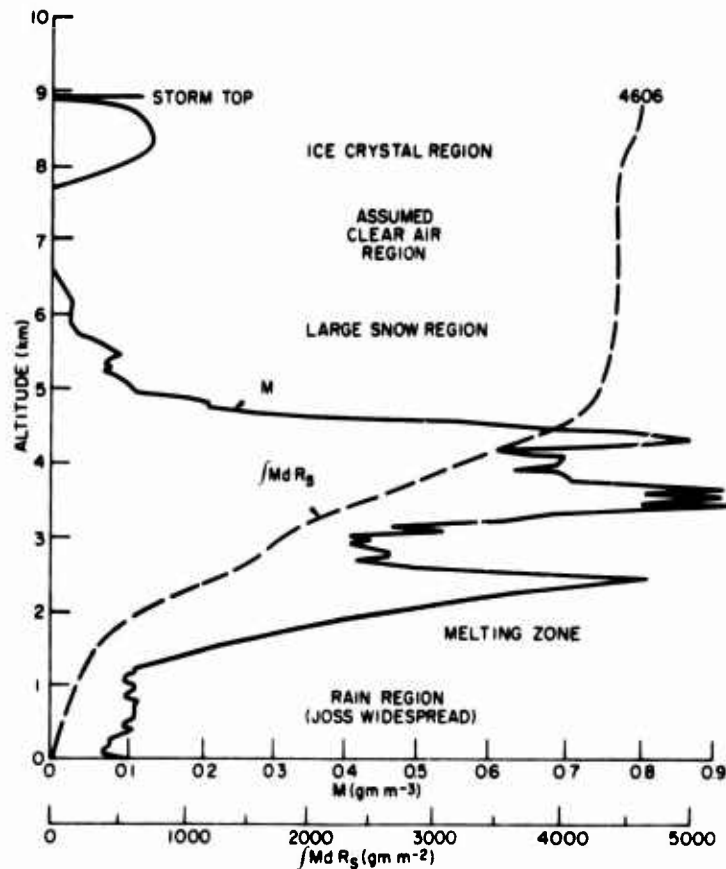


Figure 3. Profiles of Liquid-Water-Content (M) and Integral of Liquid-Water-Content ($\int Md R_g$) for the Missile Trajectory of Flight No. Q2-6362 (Unit No. R487103) of 27 February 1973, Launched at 1040:00 GMT. The M values for the upper cirrus deck are maximum values; the actual values are something indeterminate smaller

4. CLOUD LIQUID-WATER-CONTENT VALUES FOR THE MISSILE TRAJECTORIES

In addition to the liquid-water-content values measured by the radar, which pertain to hydrometeors of precipitation size (those having drop diameters, or equivalent melted diameters, larger than about 80 microns) there is substantial liquid-water-content present in the Wallops storms in the cloud size-range of the hydrometeor spectrum (those having drop diameters smaller than about 80 microns). Aircraft measurements are required to determine the liquid-water-content values for these cloud-size droplets and particles.

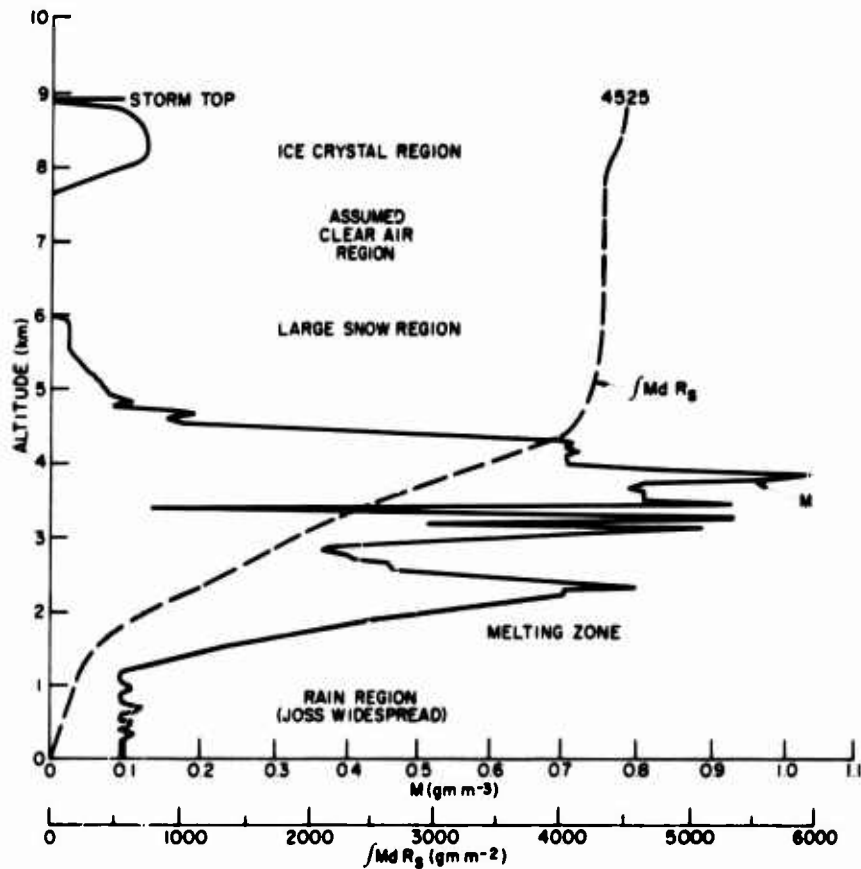


Figure 4. Profiles of Liquid-Water-Content (M) and Integral of Liquid-Water-Content ($\int M dR_g$) for the Missile Trajectory of Flight No. Q2-6363 (Unit No. R487104) of 27 February 1973, Launched at 1040:30 GMT. The M values for the upper cirrus deck are maximum values; the actual values are something indeterminately smaller

Aircraft measurement information about cloud liquid-water-contents was obtained by the AFGL C-130A aircraft for the Wallops storm of 2 February 1973. These liquid-water-content values are illustrated in Figure 5. The 50th percentile, frequency of occurrence values were presumed to be representative of the cloud conditions along the missile trajectories at the launch times. The particular values are listed in Tables C1 and C2 (for the altitude points of the radar measurements and in Tables G2 and G3 (for each 250 meters of altitude where clouds were present).

Table 1. Hydrometeor Regions, Types and Equations Used in the 1972-73 Season. See R No. 2 for description of how equations were interpolated across the melting zone and the other transition zones. Note that a cirrus layer existed above the top of the convective element penetrated by the missiles in the storm of 27 February 1973 and that the layer between the top of the element and the base of the cirrus deck was either clear or virtually devoid of hydrometeors

Date of Storm	Hydrometeor Region or Zone	Symbol	Altitude Limits km	Equation Relating P and Z (i.e., $P=K \cdot Z^p$)	Equation Relating M and P (i.e., $M=kP^c$)	Equation Relating M and Z (i.e., $M=K_M Z^{E_M}$)
2 February 1973 Missile No. Q2-6360	Rain Region	R	Sfc. to 2.80	$P = .0252 Z^{.667}$	$M = .0756 P^{.864}$	$M = .00314 Z^{.576}$
	Melting Zone	MZ	2.80 to 3.69			
	Large Snow Region	LS	3.69 to 5.94	$P = .0169 Z^{.631}$	$M = .233 P^{.944}$	$M = .00495 Z^{.596}$
	SS to LS Transition Zone	SS-LS	5.94 to 6.60			
	Small Snow Region	SS	6.60 to 8.08	$P = .0365 Z^{.625}$	$M = .250 P^{.860}$	$M = .0145 Z^{.538}$
	C to SS Transition Zone	C-SS	8.08 to 8.53			
2 February 1973 Missile No. Q2-6361	Crystal Region	C	8.53 to 10.07	$P = .100 Z^{.719}$	$M = .206 P^{.735}$	$M = .038 Z^{.529}$
	Rain Region	R	Sfc. to 2.68			
	Melting Zone	MZ	2.68 to 3.66			
	Large Snow Region	LS	3.66 to 5.94			
	SS to LS Transition Zone	SS-LS	5.94 to 6.80			
	Small Snow Region	SS	6.80 to 8.02			
27 February 1973 Missile No. Q2-6362	C to SS Transition Zone	C-SS	8.02 to 8.53			
	Crystal Region	C	8.53 to 10.07			
	Rain Region	R	Sfc. to 1.19	$P = .0252 Z^{.667}$	$M = .0756 P^{.864}$	$M = .00314 Z^{.576}$
	Melting Zone	MZ	1.19 to 2.19			
	Large Snow Region	LS	2.19 to 6.50	$P = .0169 Z^{.631}$	$M = .233 P^{.944}$	$M = .00495 Z^{.596}$
	Assumed Clear Layer	--	6.50 to 7.62			
27 February 1973 Missile No. Q2-6363	Upper Cirrus Deck	C	7.62 to 8.84	$P = .100 Z^{.719}$	$M = .206 P^{.735}$	$M = .038 Z^{.529}$
	Rain Region	R	Sfc. to 1.19			
	Melting Zone	MZ	1.19 to 2.19			
	Large Snow Region	LS	2.19 to 6.50			
27 February 1973 Missile No. Q2-6363	Assumed Clear Layer	--	6.50 to 7.62			
	Upper Cirrus Deck	C	7.62 to 8.84			

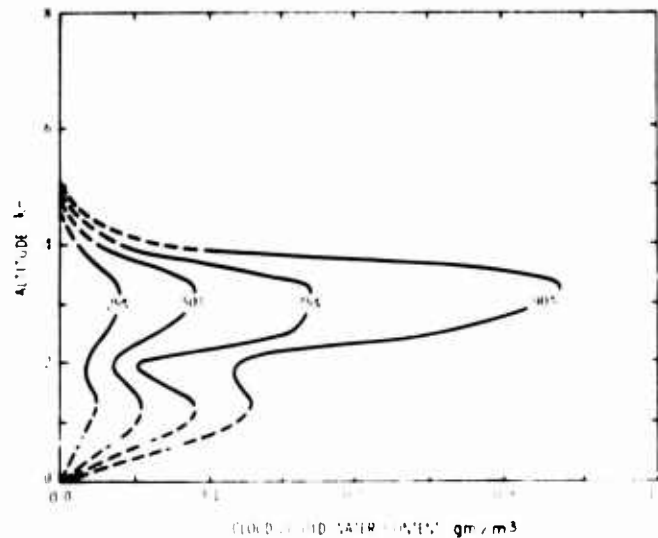


Figure 5. Percent Frequency of Occurrence Isolines of Cloud Liquid-Water-Content, as Determined From the Johnson-Williams (JW) Instrument of the AFGL C-130A Aircraft

Aircraft measurements of cloud-liquid-water-content in the storm of 27 February 1973 were made by the Meteorology Research Inc. (MRI) Navajo aircraft, see Appendix F. Relatively few of the measurements were analytically reduced and only "broad range" information is available for several particular altitudes in the storm. Our "best estimates" of the possible cloud liquid-water-contents for this storm are listed in Tables C3 and C4 (for the radar data points) and in Tables G4 and G5 (for the 250 meter points).

5. COMMENTS

Aircraft measurement information concerning the size-distribution of the hydrometeors was rather sparse and qualitative in the 1972-73 season. Thus, as in the case of the 1971-72 season discussed in R No. 3, spectral information regarding the size-distribution of the number concentration and liquid-water-content (contribution) of the hydrometeors along the missile trajectories was estimated from theoretical distribution functions, of double truncated type. The models providing the bases for the computations were the same as used in R No. 3. The computational results, which are believed to be reasonably descriptive of the probable conditions along the missile trajectories are presented in Tables G2 through G5, of

Appendix G. The mathematics and assumptions of the "precipitation model" are also presented in this appendix, as an addendum, and the descriptivity of the model is discussed relative to data results.

References

1. Plank, V.G. (1974) A Summary of the Radar Equations and Measurement Techniques Used in the SAMS Rain Program at Wallops Island, Virginia, AFCRL-SAMS Report No. 1, AFCRL-TR-74-0053, Special Report No. 172.
2. Plank, V.G. (1974) Hydrometeor Parameters Determined From the Radar Data of the SAMS Rain Erosion Program, AFCRL/SAMS Report No. 2, AFCRL-TR-74-0249, ERP No. 477.
3. Plank, V.G. (1974) Liquid-Water-Content and Hydrometeor Size-Distribution Information for the SAMS Missile Flights of the 1971-72 Season at Wallops Island, Virginia, AFCRL/SAMS Report No. 3, AFCRL-TR-74-0296, Special Report No. 178.
4. Berthel, R.O. (1976) A Climatology of Selected Storms for Wallops Island Virginia, 1971-1975, SAMS Report No. 4, AFGL-TR-76-0118, ERP No. 563.
5. Marshall, J.S., Langille, R.C., and Palmer, W. McK. (1947) Measurements of rainfall by radar, J. Meteor. 4:186-192.
6. Joss, J., and Waldvogel, A. (1970) Disdrometer RD69 Instruction Manual, Marc. Weibel Dipl. Ing., ETH, Kapellenstrasse 20, 4000, Basel, Switzerland.
7. Gunn, R., and Kinzer, G.D. (1949) The terminal velocity of fall for water droplets in stagnant air, J. Meteorol. 6:243(565, 594, 596-97).
8. Smithsonian Meteorological Tables, 1951: Sixth revised edition, Smithsonian Institution, Washington, D.C.
9. Joss, J., and Waldvogel, A. (1969) Raindrops size distribution and sampling size errors, J. Atmos. Sci. 26:566-569.
10. Church, J.F., Pocs, K.K., and Spatola, A.A. (1975) The Continuous Aluminum-Foil Hydrometeor Sampler; Design, Operation, Data Analysis Procedures, and Operating Instructions, AFCRL-TR-75-0370, Instrumentation Papers, No. 235.
11. Auer, A., and Veal, D. (1970) The dimensions of ice crystals in natural clouds, J. Atmos. Sci. 27:919-926.

References

12. Heymsfield, A. J., and Knollenberg, R. G. (1972) Properties of cirrus-generating cells, J. Atmos. Sci. 29(7):1358-1366.
13. Kajikawa, M. (1972) Measurement of falling velocity of individual snow crystals, J. Meteor. Soc. Japan. 50:577-584.
14. Heymsfield, A. (1972) Ice Crystal Terminal Velocities, Technical Note No. 41, Cloud Physics Laboratory, Department of the Geophysical Sciences, University of Chicago.
15. Ohtake, T., and Henmi, T. (1970) Radar Reflectivity of Aggregated Snowflakes preprints of papers presented at the 14th Radar Meteorology Conference, Tucson, Arizona, 17-20 November 1970, pp 209-211.
16. Barnes, A. A., Nelson, L. D., and Metcalf, J. I. (1974) Weather Documentation at Kwajalein Missile Range, AFSG, No. 292, AFCRL-TR-74-0439.
17. Joss, J., Thoms, J. C., and Waldvogel, A. (1968) The variation of raindrop size distributions at Locarno, Proc. Internatl. Conf. on Cloud Physics, Toronto, Amer. Meteorol. Soc., Boston, p. 369
18. Takeuchi, D. M., Knuth, W. R., and Green, W. D. (1974) Meteorological Support for the SAMS/ABRES Program and the DNA HEART Program, Final Report under Contract DNA 001-72-C-0130 (P00002), Meteorology Research, Inc., Altadena, California
19. Marshall, J. S., and Palmer, W. McK. (1948) The distribution of raindrops with size, J. Meteorol. 5:165-166.
20. Marshall, J. S., and Gunn, K. I. S. (1952) Measurement of snow parameters by radar, J. Meteorol. 9:322.
21. Imai, I., Fujiwara, M., Ichimura, I., and Toyama, Y. (1955) Radar reflectivity of falling snow, Pap. in Meteorol. and Geophys. (Japan)6:130-139.
22. Sekhon, R. S., and Srivastava, R. C. (1970) Snow size spectra and radar reflectivity, J. Atmos. Sci. 27:299-307.



Appendix A

Synoptic Weather Maps, Satellite Photographs and Storm Cross Sections

Surface weather maps for the Eastern United States are presented in Figures A1 and A2 for the two storms of the 1972-73 season through which missiles were fired. There are three maps in each figure, for the times closest to the launch times and for times 3 hr previous and 3 hr subsequent. The isobars, fronts, and precipitation areas are shown on these maps.

Satellite photographs (Figures A3 through A6) reveal the appearance of the cloud shields associated with the storms. The dates and times are indicated and the location of Wallops Island is shown on each photograph by a drafted "X". The photographs of Figures A3 and A5 were obtained from the synchronous satellite ATS-3; those of Figures A4 and A6 were acquired from the polar-orbiting DAAP (Data Acquisition and Processing Program) satellite. The photographs for the storm of 2 February 1973 were taken about 10 min prior to launch and about 3 hr and 30 min following launch. Those for the storm of 27 February 1973 were taken about 3 hr after launch and about 6 hr after launch.

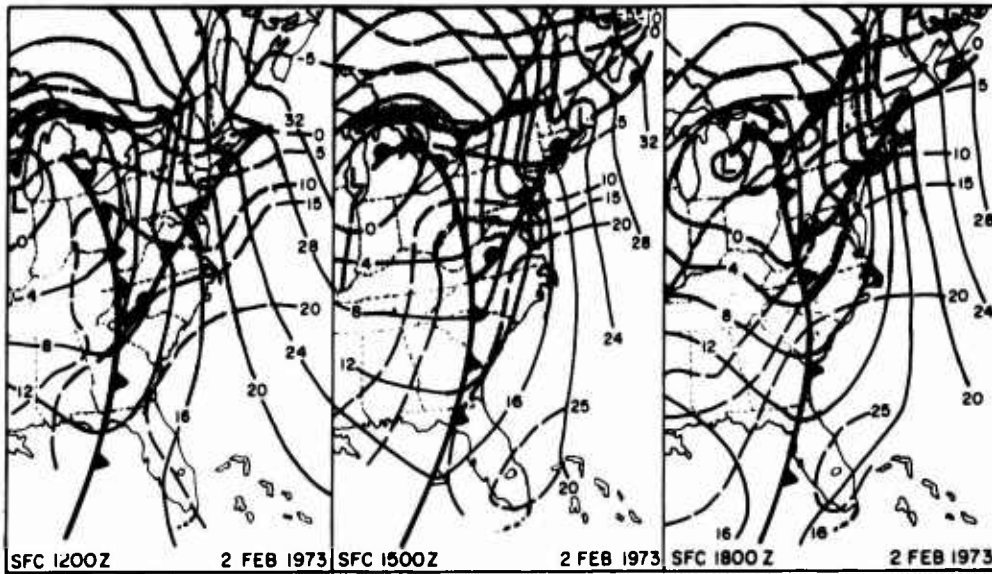


Figure A1. Surface Weather Maps for the Eastern United States for 1200, 1500, and 1800 GMT, 2 February 1973

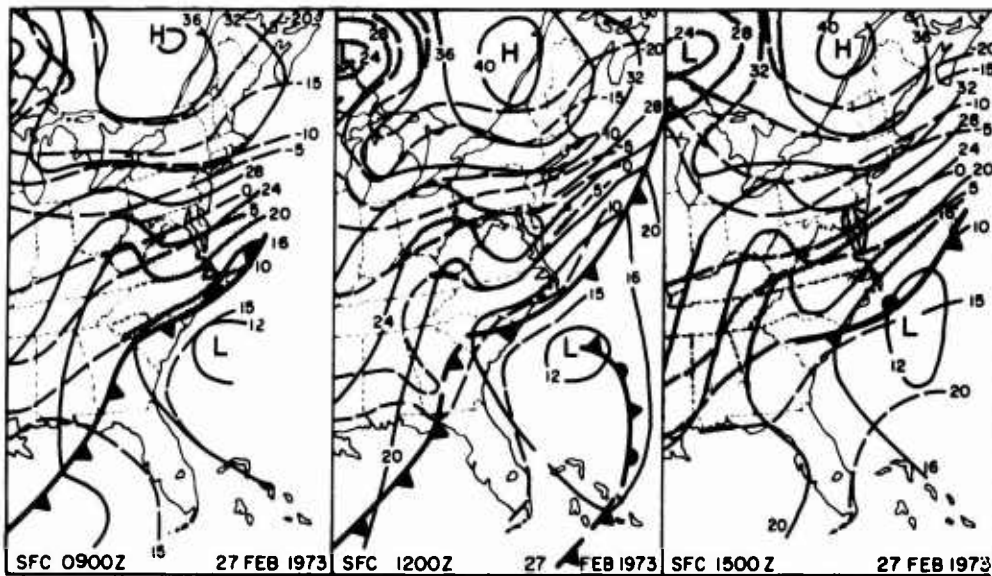


Figure A2. Surface Weather Maps for the Eastern United States for 0900, 1200, and 1500 GMT, 27 February 1973

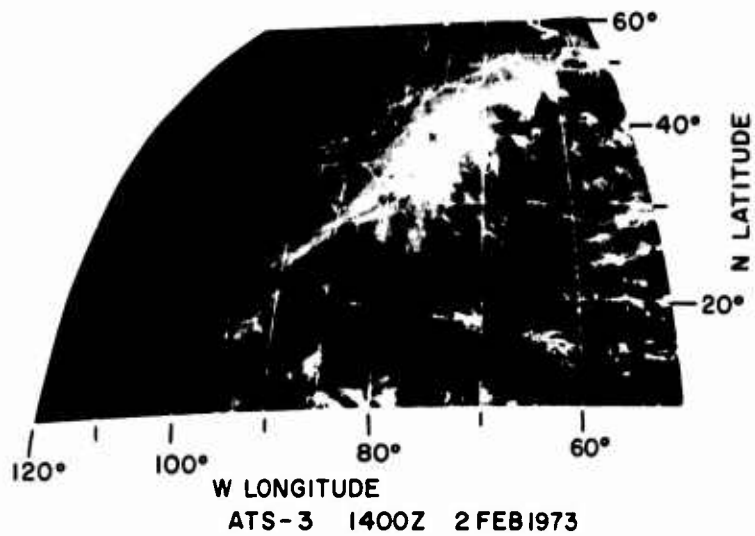


Figure A3. Photograph Obtained From the Synchronous Satellite. ATS-3, Showing the Cloud System Associated With the Storm of 2 February 1973, 1400Z.



Figure A4. Photograph Obtained From the Polar-Orbiting Satellite DAPP, Showing the Cloud System Associated With the Storm of 2 February 1973, Approximately 1730Z

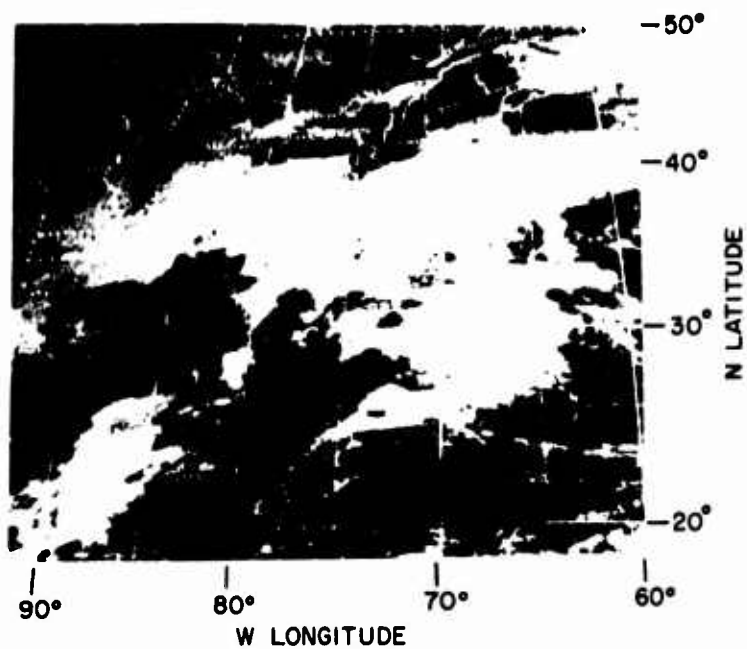


Figure A5. Photograph Obtained From the Synchronous Satellite ATS-3, Showing the Cloud System Associated With the Storm of 27 February 1973, 1356Z.

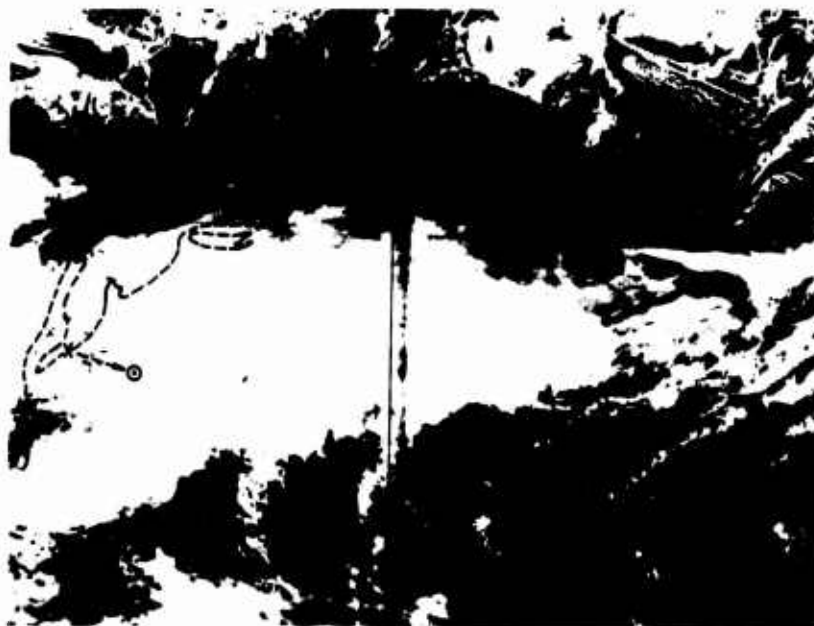


Figure A6. Photograph Obtained From the Polar-Orbiting Satellite DAPP, Showing the Cloud System Associated With the Storm of 27 February 1973, Approximately 1630Z.

Time-altitude cross sections are shown in Figures A7 and A8 which depict the general cloud and precipitation structure of the two storms that passed across the Wallops Island location. The cross sections pertain to 24-hr periods beginning at 00 Z on the days of the missile firings, and ending at 00 Z on the days after the firings. Time increases from right to left across the abscissa scales of the figures and the particular times of missile launching are indicated by drafted arrows. The isotherms, winds, and surface weather reports are also shown on the figures; the latter two being coded in accord with standard meteorological convention (see Federal Meteorological Handbooks of Surface and Winds Aloft Observations, Circulars N and O, U.S. Department of Commerce, Washington, D.C.).

Aircraft observations and measurements were obtained for both storms of the 1972-73 season. Two aircraft, the AFGL C-130A and the MRI (Meteorology Research, Inc.) Navajo, were flown in the storm of 2 February 1973. Just the Navajo aircraft was flown in the storm of 27 February 1973. Summary information and certain of the data results of these flights are presented in Appendices E and F.

The general characteristics of the two storms of the 1972-73 season may be summarized as follows:

The storm of 2 February 1973 was associated with a cold-frontal occlusion. The primary low center at the surface level at the launch times of the two missiles fired on this day was located in central Michigan. The cold front extended outward from this low center and passed through Lake Erie, central West Virginia, and eastern Georgia. The warm front at the surface level began in southern Virginia and extended northeastward through New Jersey and Massachusetts. This warm front, at the firing times of the missiles, was located about 150 miles WNW of Wallops Island.

The cloud shield associated with the storm was very extensive, as can be seen from Figures A3 and A4. The clouds covered most of the eastern seaboard from Florida to Maine and had an east-west extent of some 500 miles, or so.

The storm top at the launch times of the missiles was about 33,000 feet. The top structure was uniform and the interior of the storm was very homogeneous in character, at least down to the base level of the melting layer at 9200 ft (2.8 km). Below the melting layer, in the rain region, there were streamers of precipitation that caused the surface rain rates to be somewhat variable in space and time (from about 2 to 6 mm hr⁻¹ during the general pre-launch period of the missiles, see Appendix D). This storm, except for the variability in the rain region, was the most homogeneous one of all previous Wallops storms of SAMS missile launchings.

Wallops Island, VA.

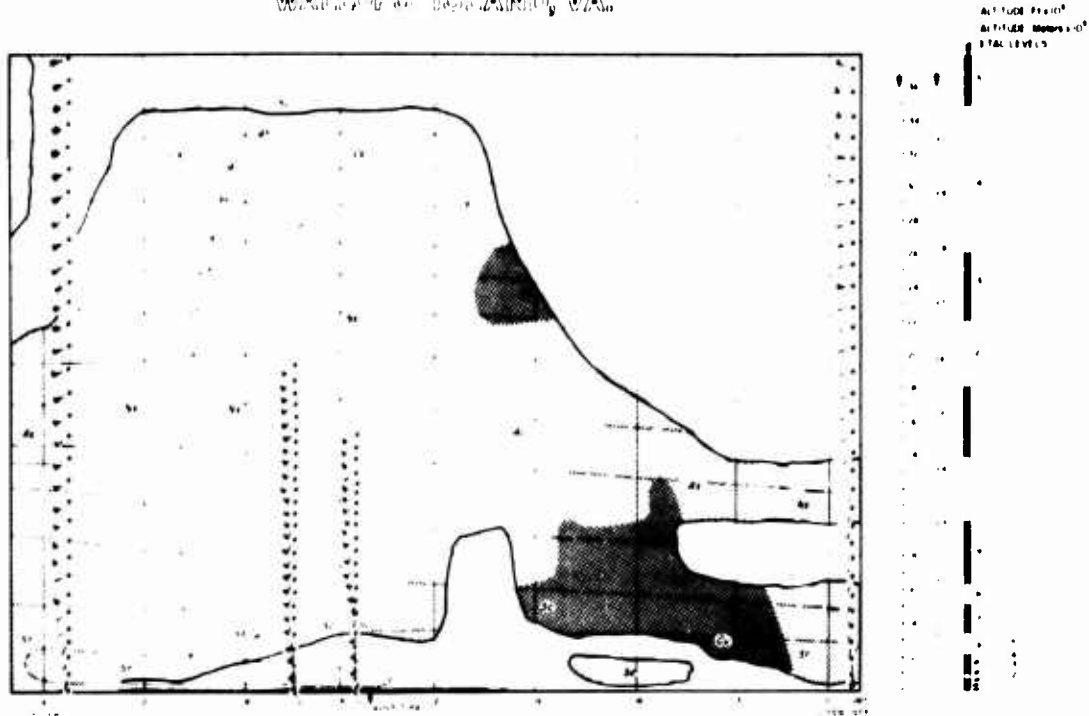


Figure A7. Time-Altitude Cross-Section for the Wallops Storm of 2 February 1973, for the Time Period 00 GMT to 2400 GMT. The time-height cross-section depicts a vertical section through the storm as it passed over the Wallops Island area. Although not all of the data used to perform the analysis of the cross-section are shown, certain of the more pertinent data are plotted. The wind direction and speed, the ambient temperatures, and the dew-point temperatures, taken from the radiosonde data are plotted. Isotherms for each 10°C are shown plotted as dashed lines. Cloud coverage and types, frontal zones, squall lines, precipitation areas, and type and hydrometeor type are also entered. The numerical values shown in addition to the radiosonde values represent average liquid-water-contents (in gm/m³) within the clouds. The three-hourly synoptic data are shown plotted beneath the cross section

WALLOPS ISLAND, VA.

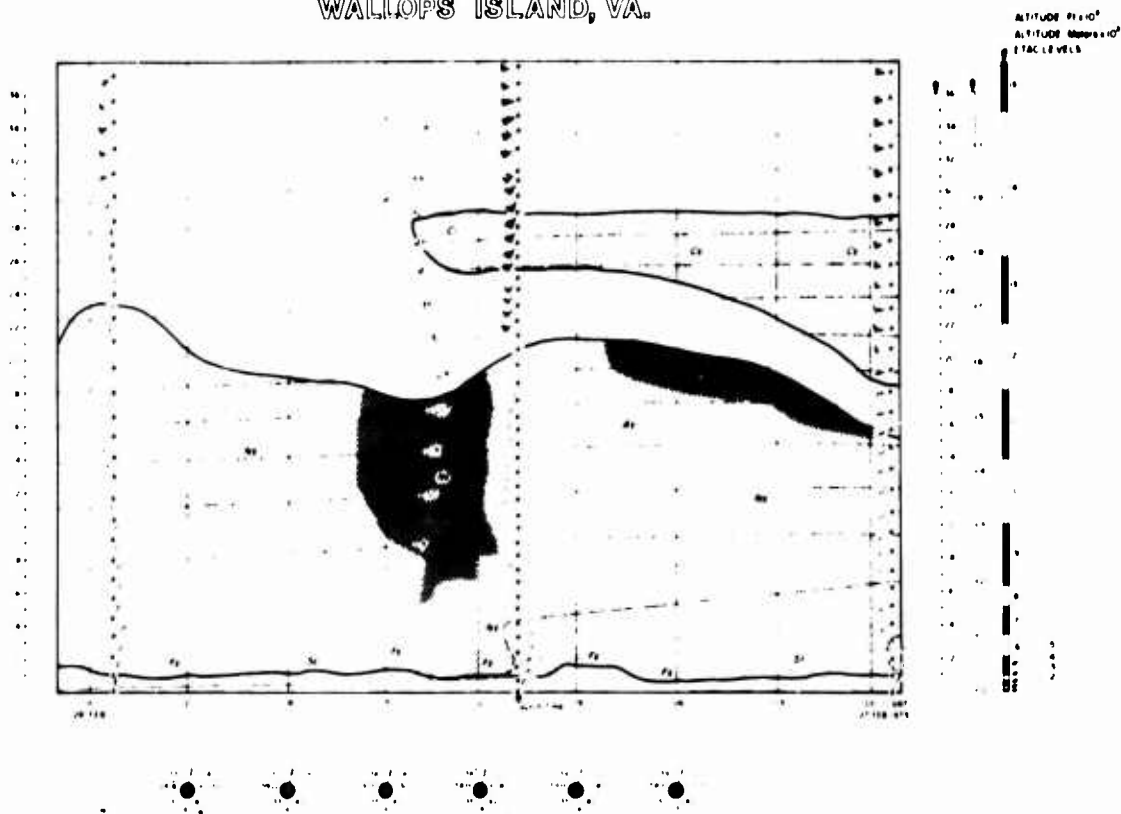


Figure A8. Time-Altitude Cross-Section for the Wallops Storm of 27 February 1973, for the Time Period 00 GMT to 2400 GMT. The time-height cross-section depicts a vertical section through the storm as it passed over the Wallops Island area. Although not all of the data used to perform the analysis of the cross-section are shown, certain of the more pertinent data are plotted. The wind direction and speed, the ambient temperatures, and the dew-point temperatures, taken from the radiosonde data are plotted. Isotherms for each 10°C are shown plotted as dashed lines. Cloud coverage and types, frontal zones, squall lines, precipitation areas, and type and hydrometeor type are also entered. The numerical values shown in addition to the radiosonde values represent average liquid-water-content (in gm/m^3) within the clouds. The three-hourly synoptic data are shown plotted beneath the cross-section

The precipitation area of the storm at the surface level at the synoptic scale (see Figure A1) was widespread and virtually continuous along the entire Atlantic seaboard. Light rain began at Wallops at about 0515 EST at an average rate of 0.5 mm hr^{-1} . The rain rate intensified to 2 mm hr^{-1} at 0625 EST and to 4 mm hr^{-1} at 0715 EST. The rain rate remained moderate for several hours thereafter, although there was appreciable variability, as shown in Figures D2 and D3 of Appendix D. At the launch time of the first missile, at 0908:00 EST, the rain rate was 3.9 mm hr^{-1} and the liquid-water-content of the precipitation was 0.245 gm m^{-3} . At the launch time of the second missile, fired 30 sec later, the rain rate was 4.2 mm hr^{-1} ; the liquid-water-content was 0.26 gm m^{-3} .

The rain rates at the launch site and "South site" gauges on this day increased and decreased more-or-less in concert with time. Thus, the horizontal scale of the precipitation streamers in the rain region was something in excess of the one-half mile spacing between gauges. (Radar data, see Figures B1 and B2, revealed a spacing of the order of one mile.)

The second, and last, storm of the 1972-73 season occurred on 27 February 1973. The storm clouds and precipitation occurred behind a cold front that had passed Wallops about 2200 EST on 26 February 1973. The front, at the launch times of the missiles, was oriented NE-SW and was located about 100 miles SE of Wallops. There were bands of cumulus congestus clouds and precipitation behind the front that roughly paralleled the front and the two missiles were fired into one of the largest, most-active of these bands. The trailing edge of a cirrostratus deck was also present above the lower, cumuliform clouds at the launch times of the missiles. Hence, the missiles penetrated both the cumulus congestus clouds of the precipitation band and the overlying ice crystal clouds of the cirrus deck. (The cumulus congestus bands and overlying cirrus deck can be seen in the DAAP photograph of Figure A6. This photograph was taken about 6 hr after the missile launch times and the frontal displacement during the intervening period is estimated to be about as indicated by the dashed arrow shown drawn on the photograph. In view of this displacement, and assuming no major temporal changes, the cloud situation over Wallops at the launch times would presumably have been approximately that illustrated at the point "©", also shown drafted on the photograph.)

The radar RHI diagrams and photographs for 27 February 1973, which were taken during the general launch period (see Appendix B), show that the echo structure of the clouds and precipitation was quite variable in space and time. Convective cells were present which had appreciable vertical development. The missiles were fired into a trough between convective cells. The cloud top at the exit points was about 21,000 feet. The missiles next passed through a clear-air layer (as best could be ascertained) and then intersected the cirrostratus deck in the altitude range 25,000 to 28,000 feet. The surface rain rate at the time the first missile was fired, at 0540:00 EST, was 1.3 mm hr^{-1} and the liquid-water-content of the precipitation was 0.095 gm m^{-3} . These same rain-rate and liquid-water-content values also prevailed at the time of the second missile firing 30 sec later.

It should be noted that the time cross-section of Figure A8 fails to depict the details of the storm situation of 27 February 1972. The convective nature of the situation is not indicated and the clouds, at least near the launch times, are incorrectly identified as nimbostratus, rather than cumulus congestus.

Appendix B

Radar Structures of the Storms at the Missile Launch Times

The radar equations and measurement techniques used in the SAMS rain erosion program at Wallops Island, Virginia were summarized in R No. 1. The radar and video-integration procedures employed during the 1972-73 season were indicated in Section 4.3 of that report. The calibration methods were explained in Sections 3.3 and 3.4 and calibration data for the 1972-73 season were supplied in Tables 4, 6 and 9.

Photographic and tape-recorded video-integration data were obtained with the FPS-18 radar for both of the missile-launch storms of the 1972-73 season. The polaroid RHI photographs for the first storm of 2 February 1973 were unusable, however, because of integrator problems; hence all launch period information for this storm had to be acquired from the tape-recorded data. Good quality data of both types, photographic and recorded, were acquired for the second storm of 27 February 1973.

The tape recorded data were processed by computer and "reconstructed RHI diagrams" were produced for the radar antenna sweeps made just prior to the missile launchings and during, or just after, the launchings. These diagrams for the storm of 2 February are shown in Figures B1 and B2. The diagrams for the storm of 27 February are shown in Figures B3 and B4. The trajectory paths (approximate) of the first missiles fired into the storms are indicated on the first of the respective figures; the trajectory paths of the second missiles are indicated on the second figures.

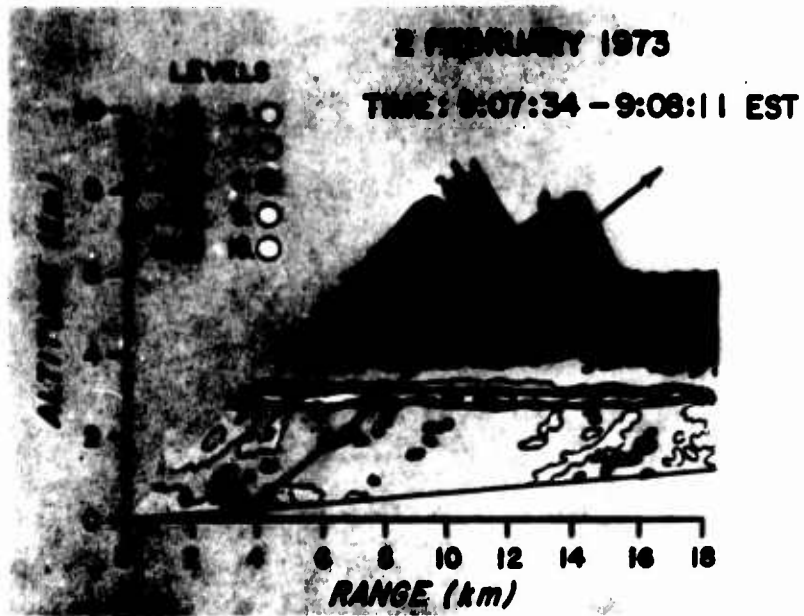


Figure B1. RHI Diagram With Colored, Contoured Regions of 5 dB Signal Differential Which Illustrate the Radar Structure of the Storm of 2 February 1973 in the 146° Azimuth Direction About 30 sec Prior to the Launch Time of the First Missile Fired on This Day. The approximate trajectory path of the missile is indicated by the arrow. The \bar{Z} and dBZ_e values of the nine signal levels of the color code are specified in Table B1

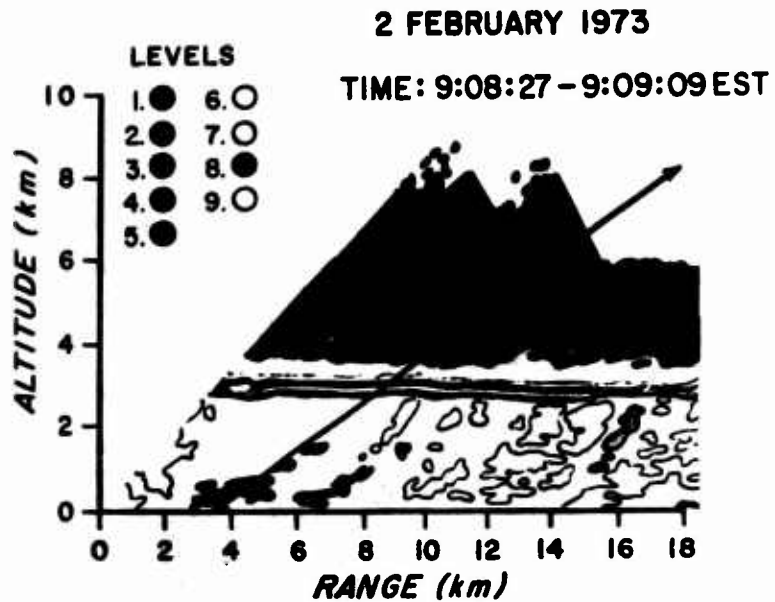


Figure B2. RHI Diagram With Colored, Contoured Regions of 5 dB Signal Differential Which Illustrate the Radar Structure of the Storm of 2 February 1973 in the 146° Azimuth Direction at About the Launch Time of the Second Missile Fired on This Day. The approximate trajectory path of the missile is indicated by the arrow. The \underline{I} and dBZ_e values of the eight signal levels of the color code are specified in Table B1

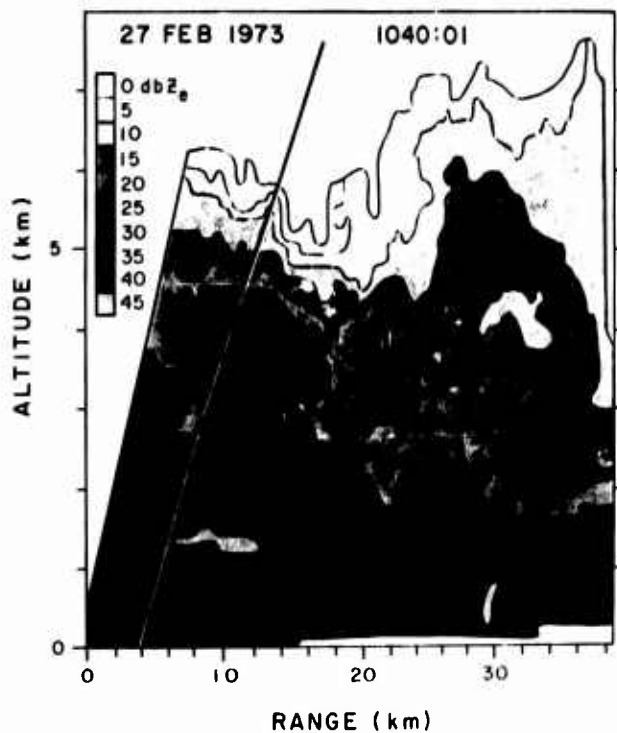


Figure B3. RHI Diagram With Colored, Contoured Regions of 5 dB Signal Differential Which Illustrate the Radar Structure of the Storm of 27 February 1973 in the 146° Azimuth Direction at About the Launch Time of the First Missile Fired on This day. The approximate trajectory path of the missile is indicated by the black line. The dBZ_e values of the color code (the "water equivalent" Z values in dB) pertain specifically to the boundary lines separating the colored regions

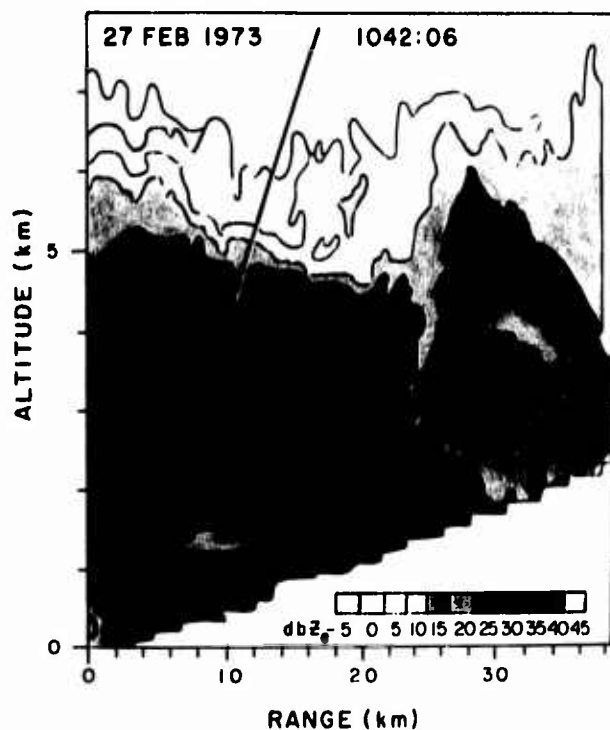


Figure B4. RHI Diagram With Colored, Contoured Regions of 5 dB Signal Differential Which Illustrate the Radar Structure of the Storm of 27 February 1973 in the 146° Azimuth Direction About 1 min and 30 sec After the Launch Time of the Second Missile Fired on This day. The approximate trajectory path of the missile is indicated by the black line. The dBZ_e values of the color code (the "water equivalent" Z values, in dB) pertain specifically to the boundary lines separating the colored regions

No additional RHI information (other than presented in Figures B1 and B2) is available to illustrate the radar structure of the storm of 2 February 1973. Computer RHI diagrams were prepared only for the missile launch times. No useable polaroid photographs were acquired for the storm.

Table B1. Color code of Signal Intensity Used With the Computer RHI Diagrams of Figures B1 and B2. The \bar{I} values of integration signal are dB above -92.3 dBm. The dBZ_e values are the "water equivalent" values of Z, in dB

Signal Level	dB Range of Signal Level	
	\bar{I} dB	dBZ _e dB
1	45.8-47	3.2 to 4.4
2	47-52	4.4 to 9.4
3	52-57	9.4 to 14.4
4	57-62	14.4 to 19.4
5	62-67	19.4 to 24.4
6	67-74	24.4 to 31.4
7	74-79	31.4 to 36.4
8	79-84	36.4 to 41.4
9	84-89	41.4 to 46.4
10	89-94	46.4 to 51.4

Polaroid RHI photographs for the storm of 27 February are shown in Figures B5 through B7. Photographs for the missile launch times are presented in Figure B5. These photographs pertain to the same times, that is, to the same up-sweep-down-sweep scans of the radar antenna, as the RHI diagrams of Figures B3 and B4. The trajectory paths of the missiles across the photographs are indicated. The threshold settings of the video integrator and the "gray scale shading information" pertaining to the photographs are noted in Table B2.

The photographs of Figure B7 illustrate the general echo conditions that prevailed along the launch azimuth on 27 February during the period of aircraft measurements following the missile firings. The first photograph illustrates the typical conditions at a time about mid-way through the aircraft measurement period. The second reveals the conditions at a time near the end of the aircraft measurement period.

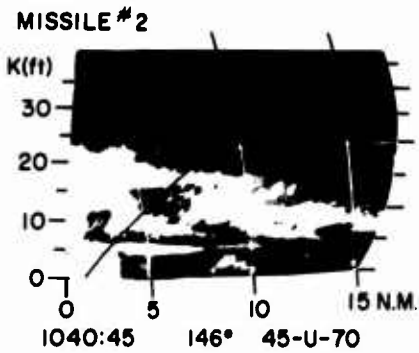
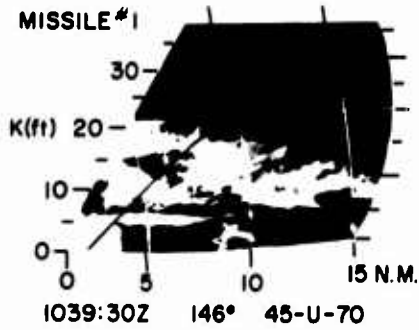


Figure B5. RHI Photographs Obtained With the FPS-18 Radar on 27 February 1973 at the Launch Times of the Two Missiles Fired on This Day. The first missile was launched at 1040:00 GMT; its trajectory path is indicated by the arrow of the upper photograph. The second missile was launched at 1040:30; its trajectory path is shown by the arrow of the lower photograph. The photographs were obtained using video integration of the gray scale type "45-U-70", specified in Table B2

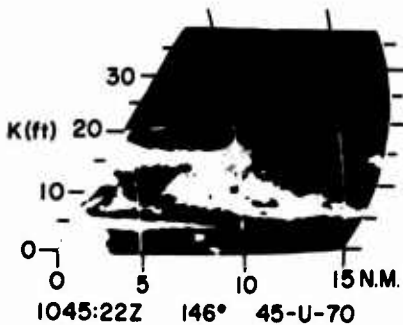
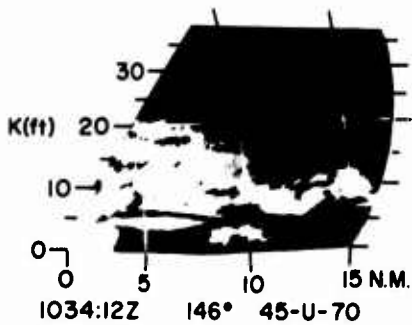


Figure B6. RHI Photographs Obtained With the FPS-18 Radar on 27 February 1973 Which Were Taken in the Launch Direction Approximately 6 min Before Launch (upper photograph) and 5 min After Launch (lower photograph). See Table B2 for specification of the type of gray-scale integration used (45-U-70)

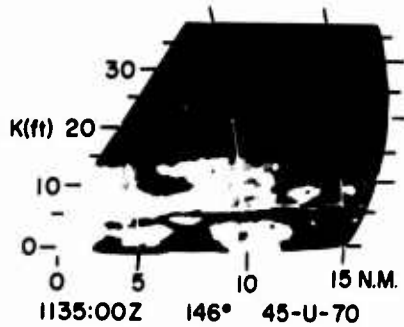


Figure B7. RHI Photographs Obtained With the FPS-18 Radar on 27 February 1973 Which Were Taken in the Launch Direction at the Approximate Mid-Time Point of the Aircraft Measurement Period (upper photograph) and Near the End of the Aircraft Measurement Period (lower photograph). See Table B2 for specification of the type of gray scale integration used

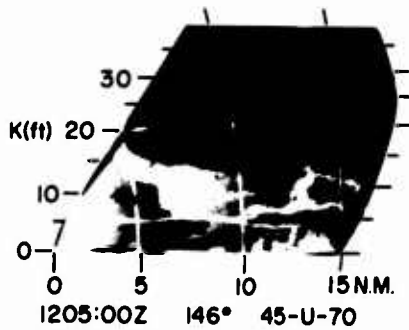


Table B2. Shading Code Used With the Video-Integrated RHI Photographs of Figures B5 through B7. The dB values listed are dB above -92.3 dBm

Gray Shade on RHI Photograph	Threshold Signal Levels Employed for Gray Scale Type 45-U-70 dB
Black	≤ 45
Dark Gray	55
Light Gray	65
White	70
Black	75
Dark Gray	80
Light Gray	≥ 80

The radar structure of the two storms of the 1972-73 season may be summarized as follows:

The echo structure of the storm of 2 February 1973, as shown by Figures B1 and B2, was quite uniform and horizontally homogeneous during the launch period of the missiles, particularly in the upper portions of the storm above the bright band. The storm top was located at 33,000 ft (10.06 km), from observations made from the AFGL C-130A aircraft. The radar echo tops (ATPVITS)* extended to about 24,000 ft (7.3 km). The base level of the bright band in the storm ranged from about 9100 to 9800 ft (2.8 to 3.0 km); the top level varied from about 9800 to 10,500 ft (3.0 to 3.2 km). Sloping "echo streamers" existed in the rain region below the bright band, some of which extended from the base of the bright band to the surface level. It can be seen, with reference to Figure B1, that the first missile launched on 2 February passed through a portion of one of the smaller of these streamer echoes. This explains the maximum of liquid-water-content that is shown at about the 1.8 km level in the profile plot of Figure 1 of the main text. The second missile, see Figure B2, also passed through a small echo region having signal intensities larger than the surroundings. This caused the maximum of liquid-water-content shown near the 0.5 km level in the profile plot of Figure 2.

The radar echo structure of the storm of 27 February 1973 was considerably different than that of 2 February. The storm portion that passed Wallops at launch time was essentially a squall line and there was substantial spatial-temporal variability of the radar echo patterns both within the squall line and associated with its passage across the 146° launch plane of the missiles. The missiles were fired into a trough between convective cells. The cloud tops, in the trough at the missile exit points, were about 6.5 km (21,000 ft). There was an apparent clear region, devoid of detectable radar echo, along the trajectory paths of the missiles in the altitude zone from about 6.5 km to 7.6 km (25,000 ft). Above this, likewise along the trajectory paths, there was an overlying cirrus deck, with top estimated to be about 8.5 km (28,000 ft). This estimate was obtained from specially-processed radar data. It could not be verified by aircraft observation, since the ceiling altitude of the MRI Navajo aircraft was only about 23,000 feet.

A radar bright-band was present at the launch time of the missiles which had a base variable from about 3 to 4 km (9800 to 13,000 ft) and a top ranging from about 5 to 6 km (16,400 to 19,700 ft).

The echo structure of this storm changed appreciably along the 146° azimuth direction from the time of the missile launchings until the end of the aircraft

*ATPVITS stands for "at the particular video-integrator threshold settings". The echo tops of the storm will be higher or lower, within an approximate 5 dB signal sensitivity range, dependent on the threshold settings and dB spacing of the particular "integration gate", or "gray scale level"; which is the receptor of the weakest storm signals of minimum detectability.

measurement period following the launchings. This can be seen by comparing Figure B7 with Figures B5 and B6. The radar echo tops of the storm clouds (ATPVITS) varied considerably throughout the period, dependent on which convective clouds of the storm band were intersected by the radar. In general, though, the echo tops decreased during the aircraft measurement period and the intensity of the radar echoes also decreased. There was little correlation or consistency between the echo patterns present at launch time and those present later on. It may be reported that the MRI Navajo aircraft on this day was barely able to make measurement passes and descend rapidly enough to "keep up with" the advective or dissipative diminishment of the cloud top altitudes along the 146° azimuth line of the measurements. Consequently, the aircraft measurements, level for level within the storm, were generally made in regions of less intense radar signal than had been present at the firing times of the missiles. The measurements were simply non-representative of the launch time conditions.

Appendix C

Computation of Hydrometeor Parameters from the Radar Data

The trajectory values of the radar integration signal, \int , in the 1972-73 season, were obtained from computer-processed RHI diagrams that were acquired from tape-recorded video-integrator data for the radar antenna sweeps made immediately before and after the missile launchings. These diagrams and the methods whereby the trajectory \int values were determined from the diagrams were discussed and illustrated in R No. 1.

Portions of the RHI diagrams for the four missile launches of the 1972-73 season are presented in Figures C1 and C2 which show the detailed \int signal-structure of the Wallops storms in the immediate vicinity of the trajectory paths of the missiles. The paths are shown superimposed over colored, contoured regions of 1 dB signal differential. The diagrams reveal the micro-structure that was intercepted by the missiles during their travel from the launch pad to near the storm top level. It should be noted that the clouds and hydrometeors of the storm of 2 February 1973 extended continuously upward from the surface to a storm top level of 33,000 feet. In the storm of 27 February, on the other hand, the missiles were fired through a particular convective element of the storm, which at the time of firing, and along the trajectory lines, had a top at about 19,500 ft that was surmounted by a cirrus layer that extended from about 26,000 ft to 29,000 feet. It was presumed, from the MRI Navajo observations, and from the fact that the radar returns were below the minimum detectable by the video integrator, that the layer between 19,500 ft and 26,000 ft was a "clear layer".

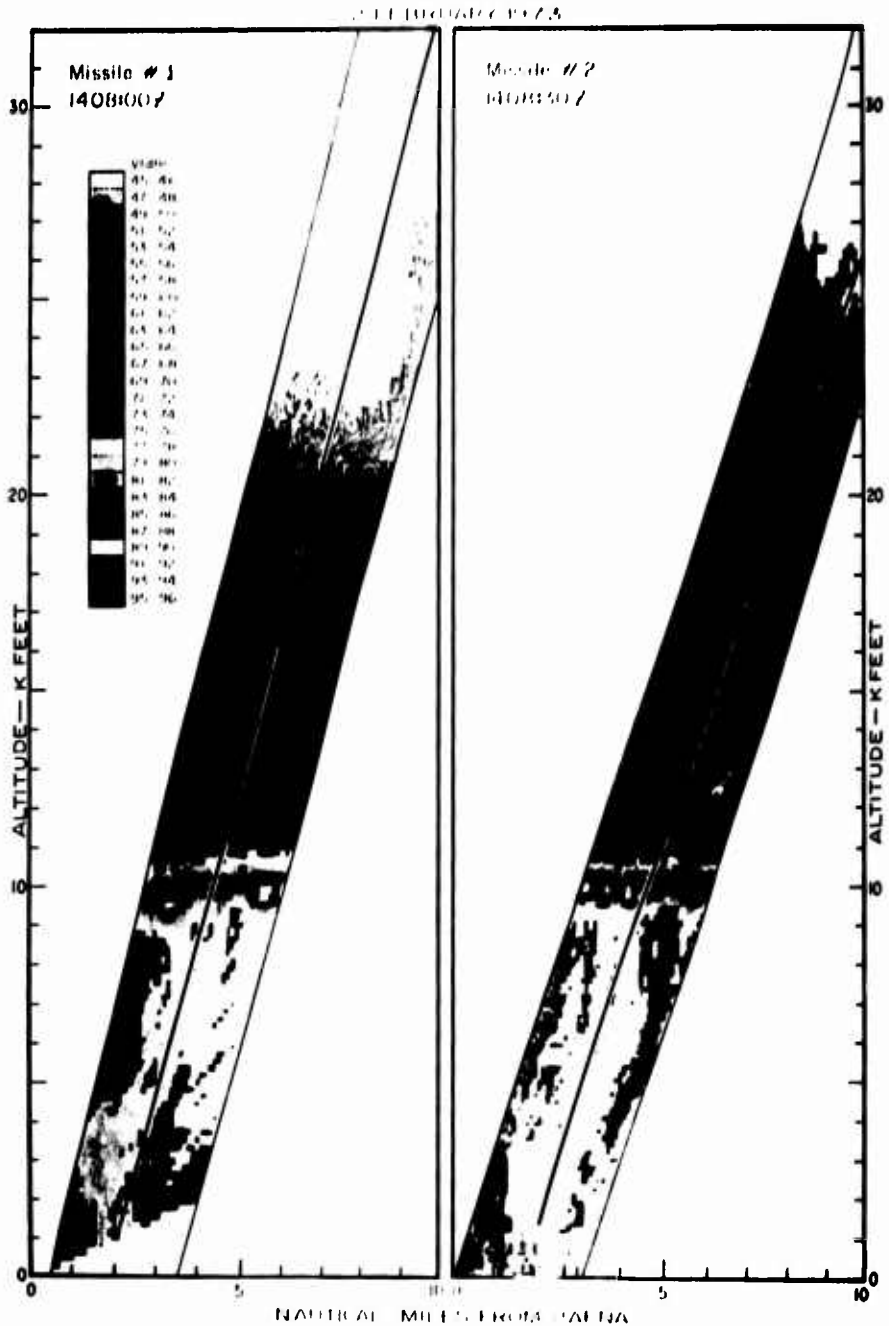


Figure C1. Portions of the RHI Diagrams for the Two Missile Launches of 2 February 1973 Which Show the Detailed \perp Signal-Structure of the Storm in the Immediate Vicinity of the Trajectory Paths. The paths are shown superimposed over colored, contoured regions of 1 dB signal differential. The dBZ_e (the "water equivalent" Z values, in dB) are related to the \perp values of the color code by a dB constant of -42.5. In other words, $\perp - 42.5 = \text{dBZ}_e$

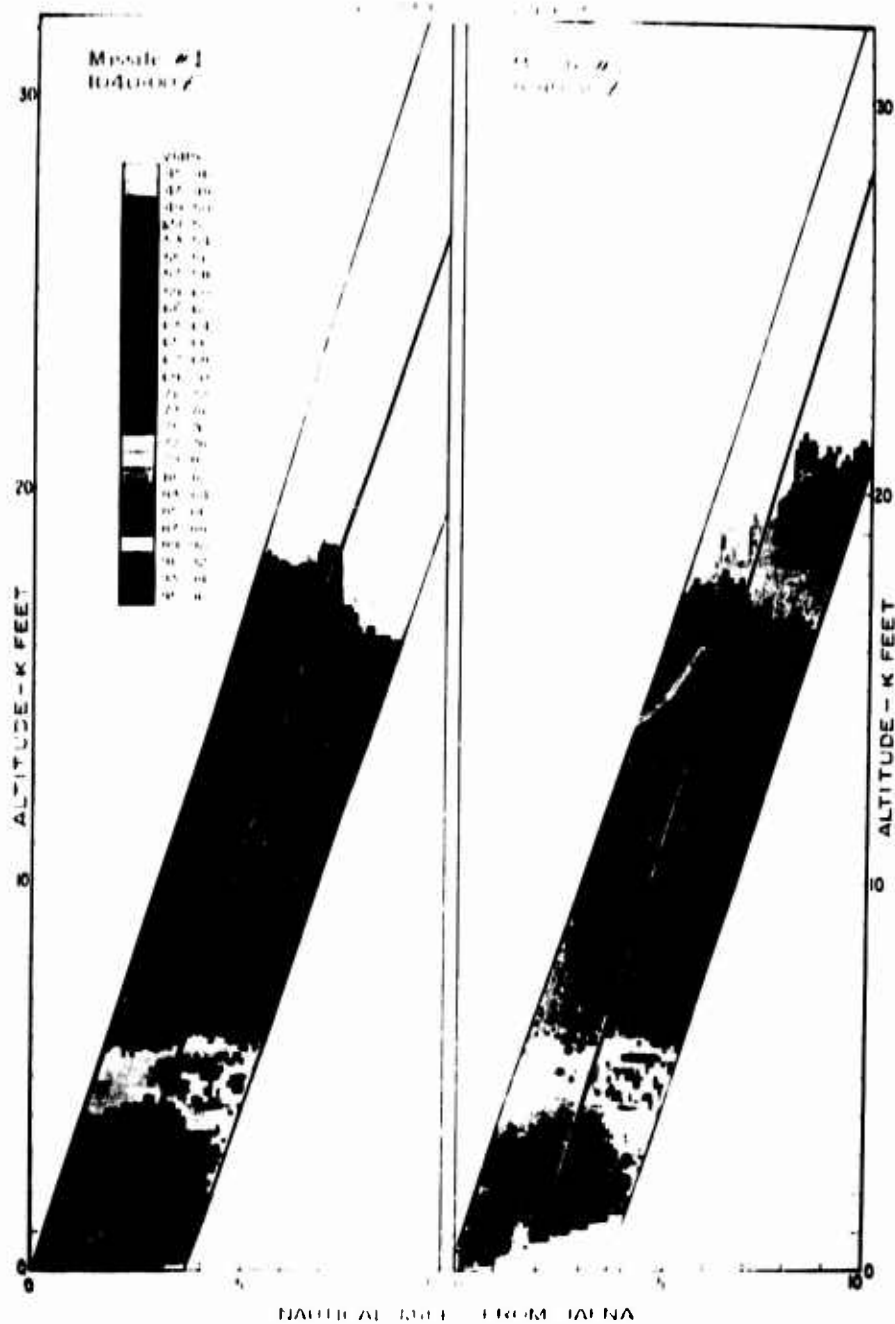


Figure C2. Portions of the RHI Diagrams for the Two Missile Launches of 27 February 1973 Which Show the Detailed \int Signal-Structure of the Storm in the Immediate Vicinity of the Trajectory Paths. The paths are shown superimposed over colored, contoured regions of 1 dB signal differential. The dBZ_e (the "water equivalent" Z values, in dB) are related to the \int values of the color code by a dB constant of -42.3 . In other words, $\int -42.3 = \text{dBZ}_e$.

The particular "profile values" of \bar{Z} that existed along the trajectory lines of the missiles are shown in Figures C3 through C6. The solid, middle portions of the profiles show the \bar{Z} values that were determined from the RHI diagrams within those altitude regions of the storms extending from above the radar ground-clutter-layer near the surface level to the storm altitudes aloft, where the \bar{Z} values became minimum detectable. The dashed portion of the profiles, at the bottom, show the \bar{Z} values which are presumed to be representative of the ground clutter layer (with the non-hydrometeor, clutter-part of the signal eliminated) and which are also consistent with the measured precipitation rates at the launch times of the missiles (see R No. 2). The dotted portions of the profiles, at the top, show the \bar{Z} values that were assumed to apply to the uppermost part of the missile trajectories where the radar returns were below the minimum detectable by the video integrator. (A linear decrease of \bar{Z} with altitude was assumed for the storm of 2 February 1973, from the altitude points of first minimum detectability to the storm top altitudes, as discussed in R No. 2. The \bar{Z} values for the upper cirrus layer for the storm of 27 February 1973 were obtained by "special processing" of the recorded radar data, as also discussed in R No. 2. It should be emphasized that the \bar{Z} values for this upper cirrus layer—those shown in Figures C5 and C6, and listed in Tables C3 and C4—are the maximum possible values. The actual values are something indeterminate smaller than these maxima.)

Two abscissa scales have been drafted on the diagrams of Figures C3 through C6. The second, lower scale indicates the decibel values of the radar volume reflectivity, $\bar{\eta}$, defined in R No. 1. The scales of \bar{Z} and $\bar{\eta}$ are related as described by Eq. (47) of R No. 1. The scale relationships differ from one storm day to another, dependent on the calibration constants of the radar.

Profiles of the radar reflectivity factors Z_W and Z_I , for water and ice hydrometeors, are presented in Figures C7 through C10. The profile values were computed from those of \bar{Z} using Eqs. (70) and (71), of R No. 1. The melting zone of the storms are indicated in the figures and both the Z_W and Z_I profiles are shown extended across the zones. The reflectivity factor is indeterminate within the melting zone, as explained in R No. 1, pp 66, but the two profiles provide some indication of this indeterminacy.

The hydrometeor regions and transition zones of the Wallop's storms of the 1972-73 season are identified in Figures C11 through C14. The regions and zones for the storm of 2 February 1973 were determined from measurements and observations made from the AFGL C-130A aircraft (see Appendix E). The regions and zones for the storm of 27 February 1973 were established from the observations of the MRI Navajo aircraft (see Appendix F). Radiosonde temperatures and radar data were also used in decisions regarding the altitude limits of the different regions and zones. The symbol code used in Figures C11 through C14 (also in Tables C1 through C4) was specified in Table 2, R No. 2. Rain is "R"; large-snow is "LS"; small-snow is "SS"; ice-crystals are "C". The subscripts indicate the observed or assumed types of these hydrometeors.

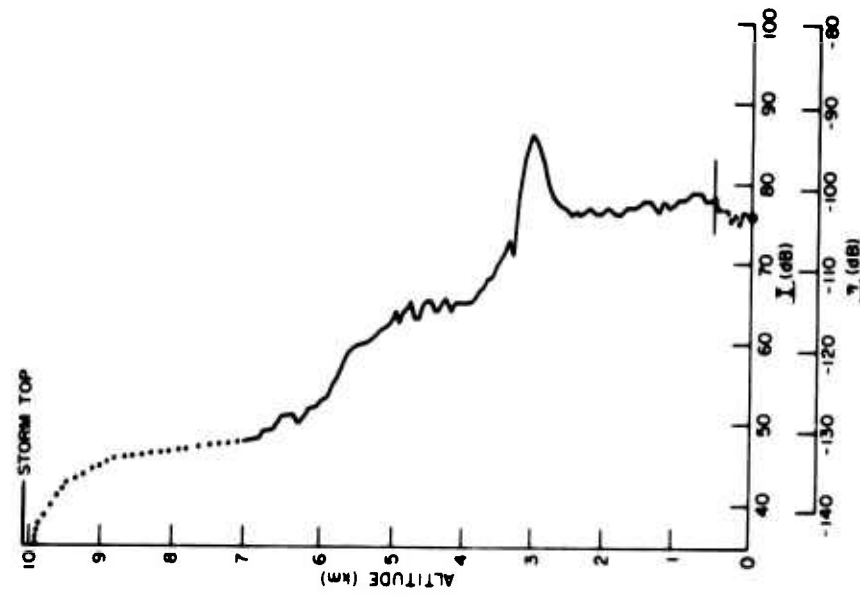


Figure C-4. Profiles of the Radar Integration Signal, I (upper abscissa scale) and of the Radar Volume Reflectivity, Z (lower abscissa scale) for the Missile Trajectory of Flight No. Q2-6361 (Unit No. R487 102) of 2 February 1973, Launched at 1408:30 GMT. The solid, dashed and dotted portions of the profile are explained in the text.

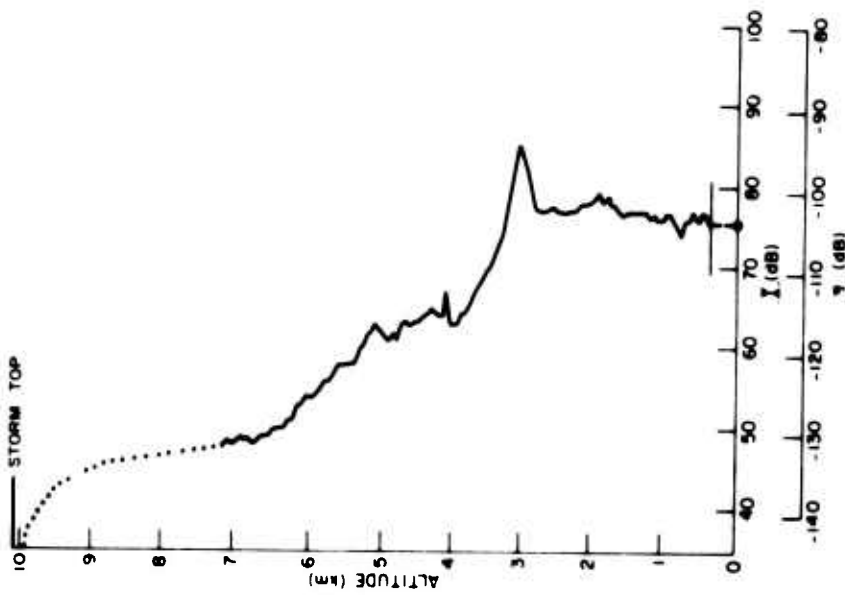


Figure C-3. Profiles of the Radar Integration Signal, I (upper abscissa scale), and of the Radar Volume Reflectivity, Z (lower abscissa scale) for the Missile Trajectory of Flight No. Q2-6360 (Unit No. 487 101) of 2 February 1973, Launched at 1408:00 GMT. The solid, dashed and dotted portions of the profile are explained in the text.

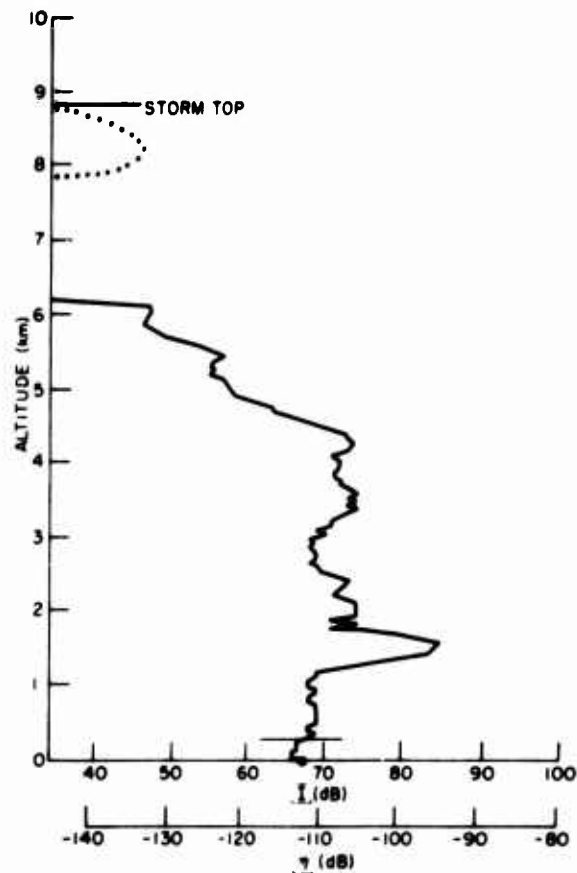


Figure C5. Profiles of the Radar Integration Signal, \bar{I} (upper abscissa scale), and of the Radar Volume Reflectivity, \bar{Z} (lower abscissa scale) for the Missile Trajectory of Flight No. Q2-8362 (Unit No. R487103) of 27 February 1973, Launched at 1040:00 GMT. The missile was launched through a convective cell which had a top at approximately 6.5 km. There was a presumed clear layer between 6.5 km and 7.6 km, with an overlying cirrus deck between 7.6 km and 8.5 km. It should be noted that the \bar{I} values for the cirrus deck, shown dotted, were obtained by special processing of the recorded radar data. They are maximum values. The actual values are something indeterminately smaller

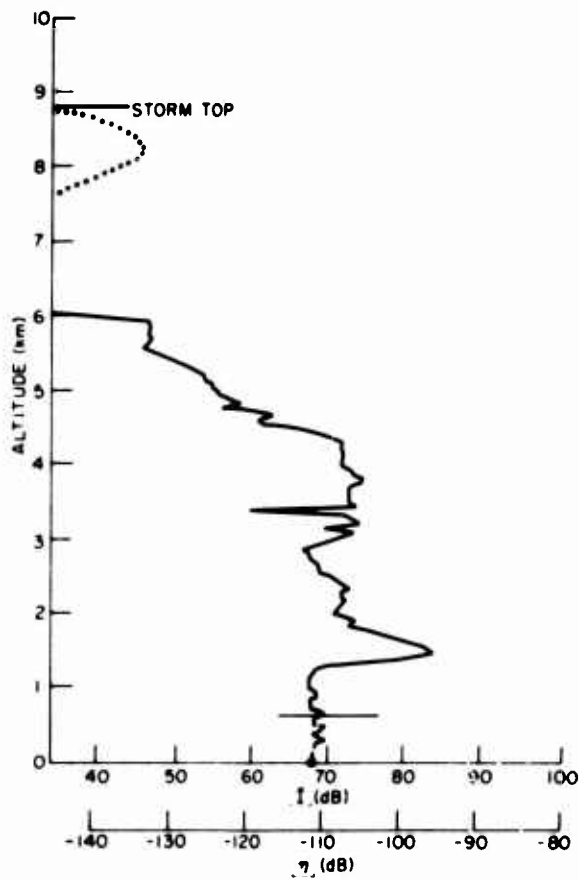


Figure C6. Profiles of the Radar Integration Signal, I (upper abscissa scale) and of the Radar Volume Reflectivity, η (lower abscissa scale) for the Missile Trajectory of Flight No. Q2-6363 (Unit No. R487104) of 27 February 1973, Launched at 1040:30 GMT. The missile was launched through a convective cell which had a top at approximately 6.5 km. There was a presumed clear layer between 6.5 km and 7.6 km, with an overlying cirrus deck between 7.6 km and 8.8 km. It should be noted that the I values for the cirrus deck, shown dotted, were obtained by special processing of the recorded radar data. They are maximum values. The actual values are something indeterminately smaller

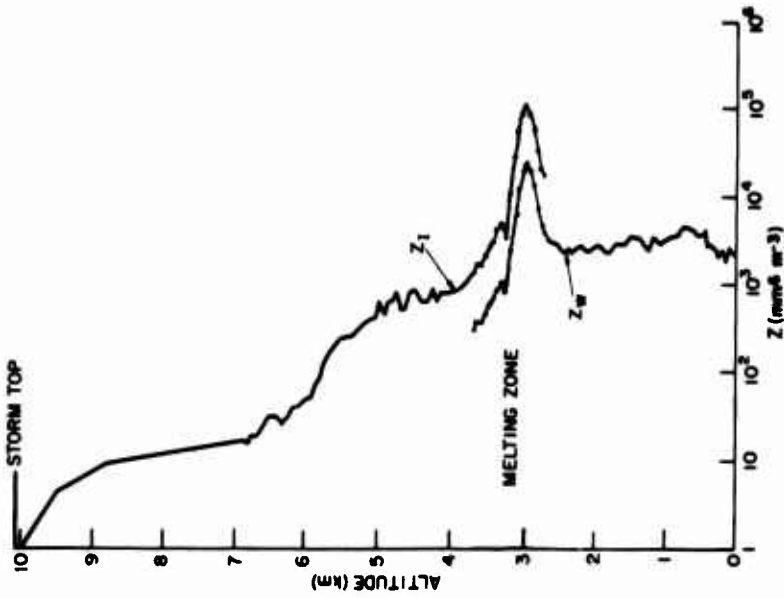


Figure C8. Profiles of the Radar Reflectivity Factor, Z_w , for Water Hydrometeors, and Z_i , for Ice Hydrometeors, for the Missile Trajectory of Flight No. Q2-6361 (Unit No. R487102) of 2 February 1973, Launched at 1408:30 GMT

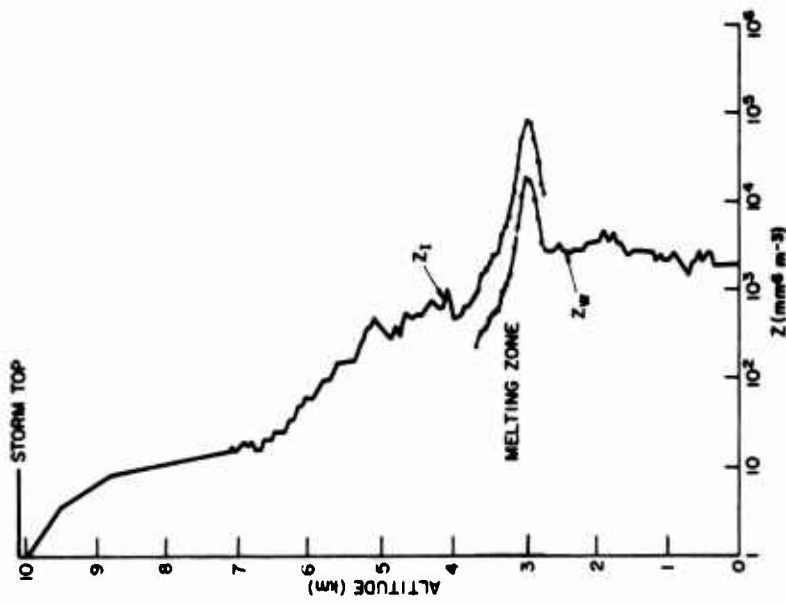


Figure C7. Profiles of the Radar Reflectivity Factor Z_w , for Water Hydrometeors, and Z_i , for Ice Hydrometeors, for the Missile Trajectory of Flight No. Q2-6360 (Unit No. R487101) of 2 February 1973, Launched at 1408:00 GMT

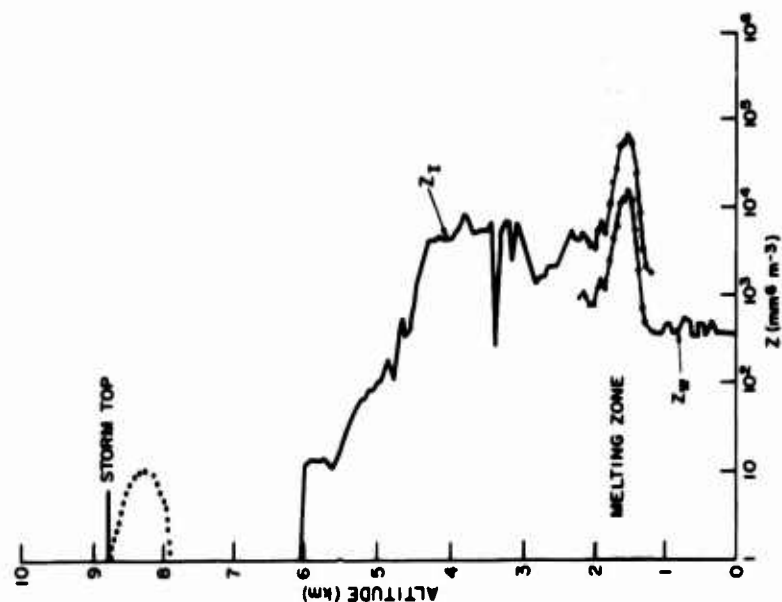


Figure C10. Profiles of the Radar Reflectivity Factor, Z_w , for Water Hydrometeors, and Z_I , for Ice Hydrometeors, for the Missile Trajectory of Flight No. Q2-6363 (Unit No. R487104) of 27 February 1973, Launched at 1040:30 GMT. The Z_I values for the upper cirrus deck, shown dotted, are maximum values

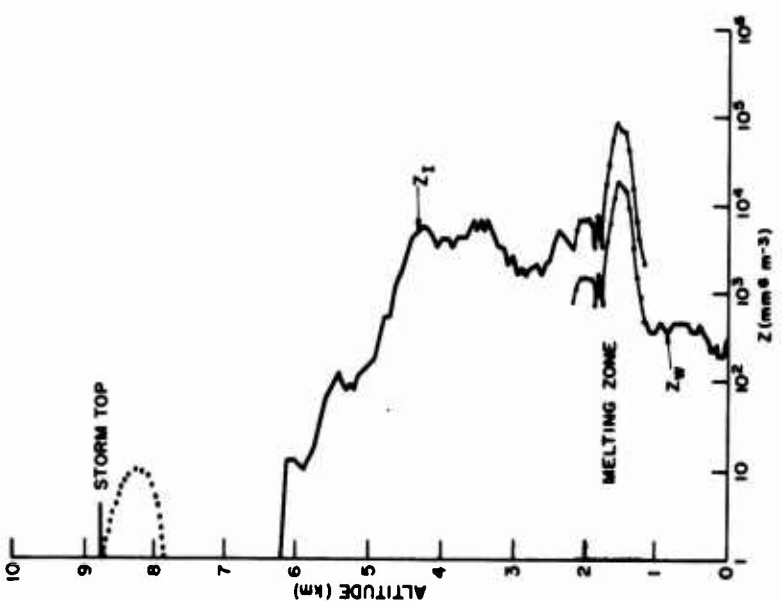


Figure C9. Profiles of the Radar Reflectivity Factor Z_w , for Water Hydrometeors, and Z_I , for Ice Hydrometeors, for the Missile Trajectory of Flight No. Q2-6362 (Unit No. R487103) of 27 February 1973, Launched at 1040:00 GMT. The Z_I values for the upper cirrus deck, shown dotted, are maximum values



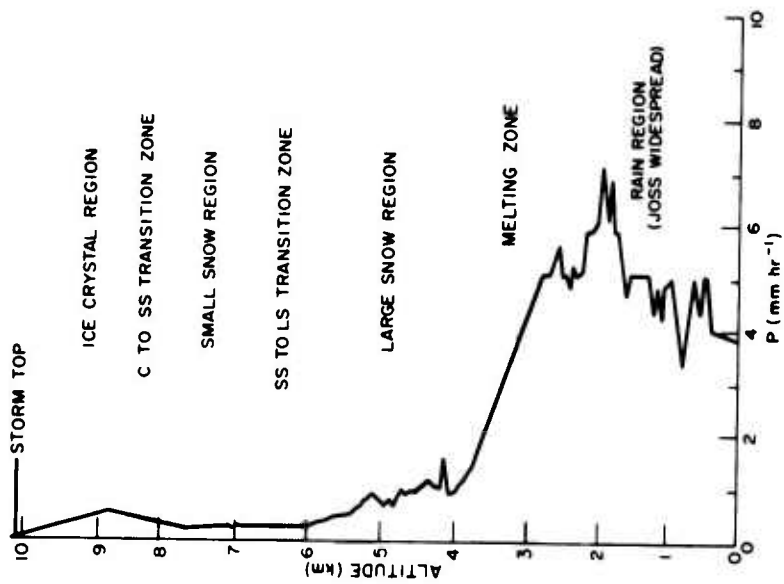


Figure C11. The Hydrometeor Regions and Zones Within the Storm of 2 February 1973 and the Profile of Precipitation Rate for the Missile Trajectory of Flight No. Q2-6360 (Unit No. R487101) Launched at 1408:00 GMT

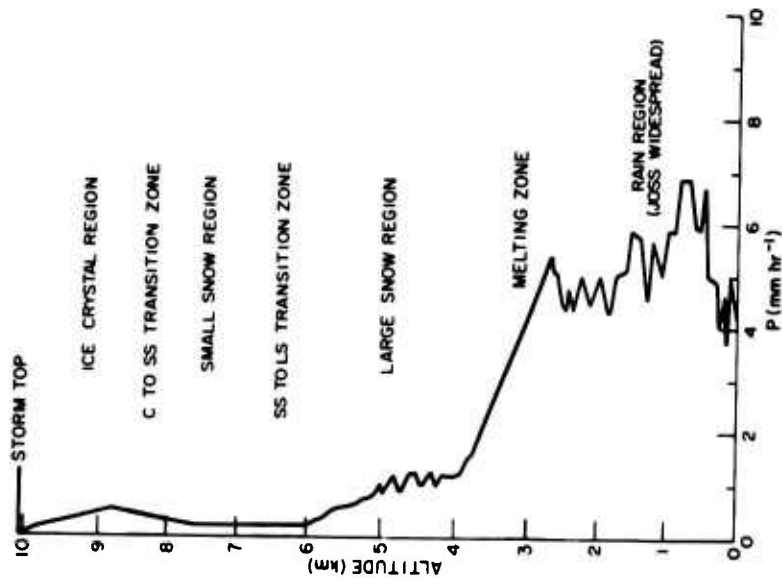


Figure C12. The Hydrometeor Regions and Zones Within the Storm of 2 February 1973 and the Profile of Precipitation Rate for the Missile Trajectory of Flight No. Q2-6361 (Unit No. R487102), Launched at 1408:30 GMT

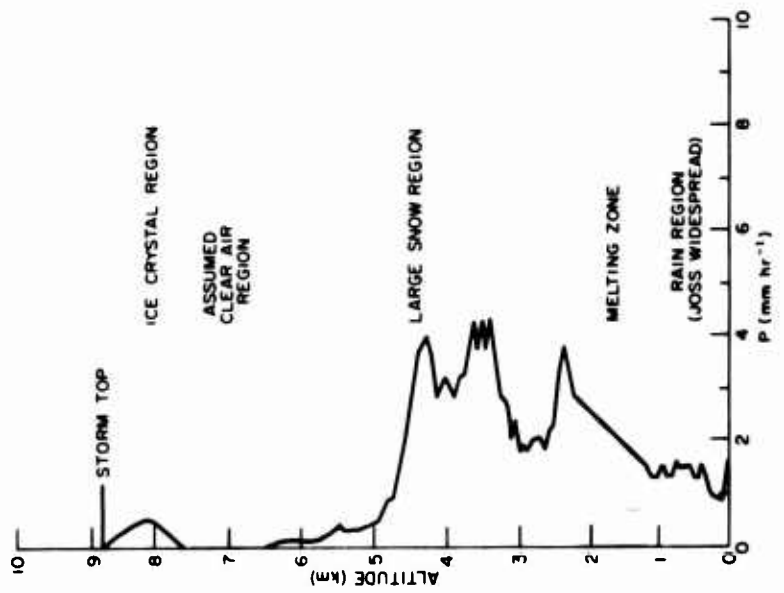


Figure C13. The Hydrometeor Regions and Zones Within the Storm of 27 February 1973 and the Profile of Precipitation Rate for the Missile Trajectory of Flight No. Q2-6362 (Unit No. R487103), Launched at 1040:00 GMT. The P values for the upper cirrus deck are maximum values

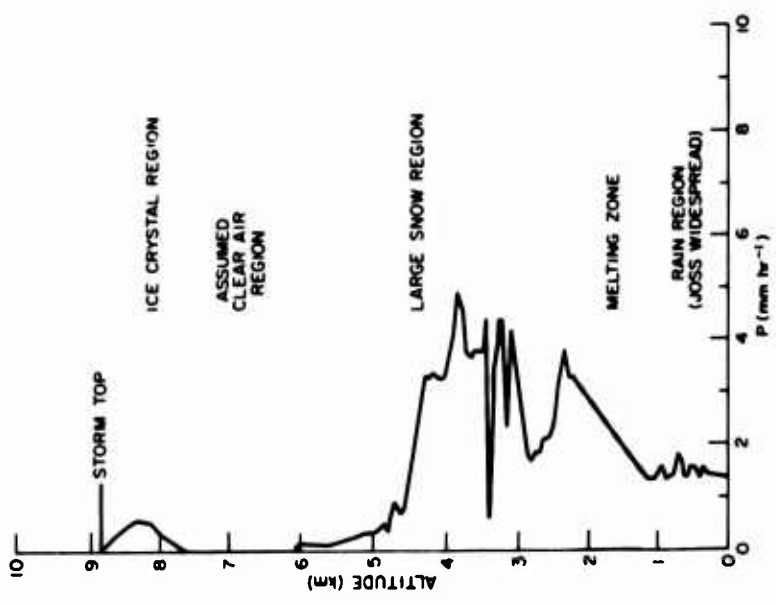


Figure C14. The Hydrometeor Regions and Zones Within the Storm of 27 February 1973 and the Profile of Precipitation Rate for the Missile Trajectory of Flight No. Q2-6363 (Unit No. R487104), Launched at 1040:30 GMT. The P values for the upper cirrus deck are maximum values



This information about the hydrometeor regions within the storms, combined with the Table 1 information concerning the P vs Z equations pertaining to the particular hydrometeor types, permitted the trajectory profiles of precipitation rate, P , to be computed from the Z_W and Z_I profiles of Figures C7 through C10. The techniques were described in Section 4.5 of R No. 2. The resultant profiles of P are shown in Figures C11 through C14.

The trajectory values of the liquid-water-content, M , and of the integral of liquid-water-content, $\int M dR_g$, which were presented in Figures 1 through 4 of the main text, were computed from the Z profiles of Figures C7 through C10, utilizing procedures that were also described in Section 4.5 of R No. 2.

The numerical data for all of the profiles shown in Figures C3 through C14, and Figures 1 through 4, are listed in Tables C1 through C4. The altitudes of the data points are identified in these tables and the radiosonde temperatures are indicated. The \bar{U} , \bar{V} , Z_W (or Z_I), P , M and $\int M dR_g$ values are tabulated for each altitude. These are listed under the table sections labeled "radar measured parameters". The tables additionally list the cloud liquid-water-content values, w , measured by the Johnson Williams instruments of the C-130A and Navajo aircraft, which, in our judgement, best typify, or bound, the cloud conditions along the missile trajectories at the launch times. The last columns of the tables give the values, or value limits, of the total liquid-water-content, contributed by both the precipitation-size drops or particles plus the cloud-size drops of liquid form, either warm or supercooled.

There is an unresolved problem of nomenclature in Tables C1 through C4 that should be noted (as it was noted in R No. 3). The radar, in the rain, large-snow and small-snow regions primarily detects drops or snow particles of precipitation size and the liquid-water-content values for these regions are listed in Tables C1 through C4 under the columns labeled "M". The radar, in the ice crystal region, however, detects particles which, at least in terms of their equivalent melted diameters, are partly in the cloud-size range. For this reason, the liquid-water-content values for ice crystals are listed in a separate column of the tables, labeled "ice cloud".

Note Concerning a Changed Analytical Assumption

Since this appendix is concerned with the computation of the hydrometeor parameters from radar data, it is appropriate to mention a particular analytical change that differs from that described in R No. 2. The change concerns the method whereby the liquid-water-content, or M , values were determined for the ice-crystal to small-snow transition zone and for the small-snow to large-snow transition zone. In R No. 2 it was stated that the precipitation rate was assumed to be linearly variable through these zones. This was the assumption used in some of the early, preliminary storm analyses of the SAMS-1 through SAMS-3 seasons. However, the assumption was changed for the final storm analyses which provided the tabular and profile values of M that have been submitted to SAMSO and published to date.

With the early assumption cited above, the radar-measured values of Z in the two transition zones were not used in the analyses. Only the Z values at the lower and upper boundaries of the zones were used. It became apparent that our zone analyses would have greater validity if we made use of the radar-measured Z values in the zones and simply assumed that the constant and exponent of the M vs Z equations were linearly variable within the zones (between the equation values pertaining to the hydrometeor region below the zone and those pertaining to the hydrometeor region above the zone). We have used this analytical technique in all of the final SAMS data provided thus far.

It should be emphasized that the assumption of a linearly-variable precipitation rate is still used in our analyses of the melting zone.

The author's failure to note the changed assumptions about the two mentioned transition zones has apparently caused some confusion among persons who have tried to repeat our results. The author apologizes for this oversight.

Table C1. Tabulation of the Numerical Values of the Radar and Hydrometeor Parameters for Missile Flight No. Q2-6360 (Unit No. R487101) of 2 February 1973, Launched at 1408:00 GMT

Missile Altitude	Horizontal Range from JAFNA	Radio-sonde Temperature	Hydro-meteor Region or Zone	Precipitation Type	Integrator Signal Values	Radar-Measured Parameters						Total Liquid Water Content
						Volume Reflectivity	Reflectivity Factor	Precipitation Rate	Liquid-Water Content of Precipitation	Integral of M Along Missile Path	Cloud Liquid Water Content	
km	k ft	°C			dB	η	Z	P	gm m ⁻³	$\int_0^7 M dr$	gm m ⁻³	gm m ⁻³
0	1.80	9.4			75.3	41.6×10^{-12}	1918	3.9	.245	0		.245
.36	1.17	2.10	Rain Region	R _{JW}	75.5	43.2×10^{-12}	1989	4.00	.250	180		.250
.41	1.35	2.15			77.0	61.0×10^{-12}	2810	5.03	.305	211		.305
.47	1.53	2.20			77.0	61.0×10^{-12}	2810	5.03	.305	245		.305
.52	1.71	2.26			76.0	48.4×10^{-12}	2232	4.31	.267	278		.267
.58	1.89	2.31			77.0	61.0×10^{-12}	2810	5.03	.305	310		.305
.63	2.07	2.35			75.0	48.4×10^{-12}	2232	4.31	.267	342		.267
.69	2.25	2.41			75.7	45.2×10^{-12}	2083	4.12	.257	371		.257
.74	2.43	2.46			74.2	32.0×10^{-12}	1475	3.27	.211	397		.211
.80	2.61	2.51			75.2	40.3×10^{-12}	1857	3.82	.240	422		.240
.85	2.79	2.55			76.0	48.4×10^{-12}	2232	4.31	.267	451		.267
.91	2.97	2.60			77.0	61.0×10^{-12}	2810	5.03	.305	483		.305
.96	3.15	2.65			76.8	58.2×10^{-12}	2683	4.88	.297	517		.297
1.01	3.33	2.71			76.0	48.4×10^{-12}	2232	4.31	.267	548	0	.267
1.07	3.51	2.77			76.0	48.4×10^{-12}	2232	4.31	.267	578	.028	.295
1.12	3.69	2.81			76.7	56.9×10^{-12}	2622	4.80	.293	609	.041	.334
1.18	3.87	2.86			76.1	49.5×10^{-12}	2284	4.38	.271	641	.048	.319
1.23	4.05	2.92			77.0	61.0×10^{-12}	2810	5.03	.305	673	.051	.356
1.29	4.23	2.97			77.0	61.0×10^{-12}	2810	5.03	.305	707	.049	.354
1.34	4.41	3.03			77.0	61.0×10^{-12}	2810	5.03	.305	742	.047	.352
1.40	4.59	3.07			77.0	61.0×10^{-12}	2810	5.03	.305	776	.045	.350
1.45	4.77	3.12			77.0	61.0×10^{-12}	2810	5.03	.305	810	.044	.349
1.51	4.95	3.16			77.0	61.0×10^{-12}	2810	5.03	.305	844	.042	.328
1.56	5.13	3.22			76.5	54.3×10^{-12}	2504	4.66	.286	877	.039	.344
1.62	5.31	3.25			77.0	61.0×10^{-12}	2810	5.03	.305	910	.038	.387
1.67	5.49	3.30			78.0	76.7×10^{-12}	3538	5.87	.349	947	.037	.386
1.73	5.67	3.35			78.0	76.7×10^{-12}	3538	5.87	.349	986	.037	.386
1.78	5.85	3.40			79.0	96.6×10^{-12}	4453	6.84	.398	1028	.037	.435

Table C1. Tabulation of the Numerical Values of the Radar and Hydrometeor Parameters for Missile Flight No. Q2-6360 (Unit No. R487101) of 2 February 1973, Launched at 1408:00 GMT (Cont)

Missile Altitude		Horizontal Range from JAFNA	Radio-sonde Temperature	Hydro-meteor Region or Zone	Precipitation Type	Integrator Signal Values	Volume Reflectivity	Reflectivity Factor	Precipitation Rate	Liquid-Water-Content of Precipitation	Integral of M Along Missile Path	Cloud Liquid Water Content	Total Liquid Water Content
km	k ft	nmi	°C			dB	cm ⁻¹	mm m ⁻³	mm hr ⁻¹	gm m ⁻³	gm m ⁻²	gm m ⁻³	gm m ⁻³
1.84	6.03	3.45	6.1			76.2	80.4×10^{-12}	3704	6.05	.358	1070	.038	.396
1.89	6.21	3.50	5.8	Rain Region	R _{1W}	79.2	101.2×10^{-12}	4663	7.05	.409	1113	.04	.449
1.95	6.39	3.55	5.6			79.0	96.6×10^{-12}	4453	6.84	.398	1158	.042	.440
2.00	6.57	3.61	5.3			78.2	80.4×10^{-12}	3704	6.05	.358	1200	.044	.402
2.06	6.75	3.65	5.0			78.0	76.7×10^{-12}	3538	5.87	.349	1240	.049	.398
2.11	6.93	3.68	4.7			78.0	76.7×10^{-12}	3538	5.87	.349	1279	.052	.351
2.17	7.11	3.72	4.5			78.0	76.7×10^{-12}	3538	5.87	.349	1318	.055	.354
2.22	7.29	3.76	4.1			77.1	62.4×10^{-12}	2875	5.11	.309	1355	.058	.367
2.28	7.47	3.80	3.9			77.0	61.0×10^{-12}	2810	5.03	.305	1389	.063	.368
2.33	7.65	3.86	3.6			77.2	63.8×10^{-12}	2942	5.19	.314	1424	.066	.380
2.39	7.83	3.90	3.3			76.7	56.9×10^{-12}	2622	4.80	.293	1458	.07	.363
2.44	8.01	3.95	3.0			77.0	61.0×10^{-12}	2810	5.03	.305	1491	.073	.378
2.50	8.19	3.98	2.7			77.0	61.0×10^{-12}	2810	5.03	.305	1526	.075	.380
2.55	8.37	4.02	2.5			77.7	71.6×10^{-12}	3301	5.60	.335	1561	.077	.412
2.61	8.55	4.07	2.2			77.3	65.3×10^{-12}	3011	5.27	.318	1598	.079	.397
2.66	8.73	4.12	1.9			77.0	61.0×10^{-12}	2810	5.03	.305	1633	.08	.385
2.72	8.91	4.16	1.6			77.0	61.0×10^{-12}	2810	5.03	.305	1667	.082	.387
2.77	9.09	4.20	1.3			77.0	61.0×10^{-12}	2810	5.03	.305	1701	.083	.388
2.80	9.20	4.23	1.2	Melting	L ₃ and R _{1W}	77.7	72.17×10^{-12}		4.90	.298	1722	.084	.382
3.10	10.17	4.47	-0.2			83.	242.7×10^{-12}		3.72	.413	1936	.086	.499
3.39	11.13	4.70	-0.4	Zone		71.3	16.53×10^{-12}		2.55	.426	2188	.053	.479
3.67	12.10	4.93	-2.1			66.4	5.36×10^{-12}		1.38	.315	2410	.033	.348
3.70	12.15	4.96	-2.2	Large Snow Region	L ₃	66.0	4.84×10^{-12}	693	1.31	.302	2420	.031	.333
3.76	12.33	5.00	-2.5			65.6	4.42×10^{-12}	605	1.24	.286	2453	.022	.308
3.81	12.51	5.05	-2.8			64.4	3.35×10^{-12}	687	1.04	.242	2482	.018	.260
3.87	12.69	5.10	-3.0			64.4	3.35×10^{-12}	687	1.04	.242	2509	.014	.256
3.92	12.87	5.13	-3.4			63.4	2.66×10^{-12}	545	.90	.211	2535	.011	.222
3.98	13.05	5.17	-3.8			63.0	2.42×10^{-12}	497	.85	.200	2558	0	.200

Table C.1. Tabulation of the Numerical Values of the Radar and Hydrometeor Parameters for Missile Flight Q2-6360 (Unit No. R487101) of 2 February 1973, Launched at 1408:00 GMT (Cont)

Missile Altitude	Horizontal Range from JAFNA	Radio-sonde Temperature	Hydro-meteor Region or Zone	Precipitation Type	Integrator Signal Values	Radar-Measured Parameters						Cloud Liquid Water Content	Total Liquid Water Content
						Volume Reflectivity	Reflectivity Factor	Precipitation Rate	Liquid-Water-Content of Precipitation	Integral of M Along Missile Path			
km	km	°C			dB	η	Z	P	gm m ⁻³	$\int_0^7 M dr$	gm m ⁻³	gm m ⁻³	
4.03	14.23	5.23			63.0	2.42×10^{-12}	497	.85	.200	2580		.200	
4.09	14.41	5.27	Large Snow Region	LS ₃	66.4	5.31×10^{-12}	1088	1.30	.310	2600		.319	
4.14	13.50	5.12			64.0	3.05×10^{-12}	626	.98	.220	2640		.229	
4.20	13.77	5.16			64.0	3.05×10^{-12}	626	.98	.220	2666		.229	
4.25	13.95	5.40			64.5	3.43×10^{-12}	703	1.06	.246	2692		.246	
4.31	14.13	5.44			65.0	3.85×10^{-12}	788	1.14	.263	2721		.263	
4.36	14.31	5.40			64.3	3.27×10^{-12}	671	1.03	.230	2749		.239	
4.42	14.49	5.53			64.0	3.05×10^{-12}	626	.98	.220	2775		.229	
4.47	14.67	5.58			63.3	2.60×10^{-12}	533	.80	.208	2790		.208	
4.53	14.85	5.63			63.3	2.60×10^{-12}	533	.80	.208	2823		.208	
4.58	15.03	5.67			63.0	2.43×10^{-12}	497	.85	.200	2846		.200	
4.64	15.21	5.72			63.5	2.72×10^{-12}	558	.91	.214	2869		.214	
4.69	15.39	5.75			63.0	2.43×10^{-12}	497	.85	.200	2892		.200	
4.75	15.57	5.78			61.0	1.53×10^{-12}	314	.64	.152	2912		.152	
4.80	15.75	5.85			61.9	1.88×10^{-12}	386	.73	.172	2930		.172	
4.86	15.93	5.89			61.0	1.53×10^{-12}	314	.64	.152	2948		.152	
4.91	16.11	5.95			61.2	1.60×10^{-12}	320	.66	.156	2965		.156	
4.97	16.29	5.98			61.8	1.84×10^{-12}	377	.71	.170	2983		.170	
5.02	16.47	6.03			62.6	2.21×10^{-12}	454	.80	.190	3003		.190	
5.07	16.65	6.07			63.0	2.43×10^{-12}	497	.85	.200	3025		.200	
5.13	16.83	6.11			62.0	1.93×10^{-12}	395	.74	.174	3046		.174	
5.19	17.01	6.16			61.9	1.88×10^{-12}	386	.73	.172	3065		.172	
5.24	17.19	6.20			60.3	1.30×10^{-12}	267	.57	.138	3083		.138	
5.29	17.37	6.25			59.8	1.16×10^{-12}	238	.53	.129	3098		.129	
5.35	17.55	6.28			58.0	$.767 \times 10^{-12}$	157	.41	.101	3111		.101	
5.40	17.73	6.34			58.0	$.767 \times 10^{-12}$	157	.41	.101	3122		.101	
5.46	17.91	6.37			58.0	$.767 \times 10^{-12}$	157	.41	.101	3133		.101	
5.51	18.09	6.42			58.0	$.767 \times 10^{-12}$	157	.41	.101	3144		.101	

Table C1. Tabulation of the Numerical Values of the Radar and Hydrometeor Parameters for Missile Flight No. Q2-6360 (Unit No. R487101) of 2 February 1973, Launched at 1408:00 GMT (Cont)

Missile Altitude		Horizontal Range from JAFNA	Radio sonde Temperature	Hydro-meteor Region or Zone	Precipitation Type	Integrator Signal Values	Radar-Measured Parameters							Total Liquid Water Content
km	k ft						Volume Reflectivity	Reflectivity Factor	Precipitation Rate	Liquid-Water Content of Precipitation	Integral of M Along Missile Path	Cloud Liquid Water Content	Total Liquid Water Content	
		nm1	°C			dB	η	Z	P	gm m ⁻³	$\int_0^z M dr$	gm m ⁻³	gm m ⁻³	
5.57	18.27	6.47	-11.5	Large Snow Region	LS ₃	58.0	$.767 \times 10^{-12}$	157	.41	.101	3156	.101	.101	
5.62	18.45	6.50	-11.8			57.0	$.610 \times 10^{-12}$	125	.36	.088	3166	.088	.088	
5.68	18.63	6.56	-12.2			56.0	$.484 \times 10^{-12}$	99.2	.31	.077	3175	.077	.077	
5.73	18.81	6.60	-12.5			56.0	$.484 \times 10^{-12}$	99.2	.31	.077	3184	.077	.077	
5.77	18.99	6.65	-12.8			55.9	$.473 \times 10^{-12}$	97.0	.30	.075	3192	.075	.075	
5.84	19.17	6.68	-13.2			54.7	$.359 \times 10^{-12}$	73.6	.26	.064	3200	.064	.064	
5.90	19.35	6.74	-13.6			54.0	$.305 \times 10^{-12}$	62.6	.23	.058	3207	.058	.058	
6.23	20.43	7.01	-15.8	SS to LS Transition Zone	SS A and LS ₃	53.8	$.288 \times 10^{-12}$	60.0	.23	.058	3213	.058	.058	
6.51	21.37	7.22	-17.7			51.0	$.153 \times 10^{-12}$	31.5	.23	.061	3247	.061	.061	
6.80	22.3	7.46	-19.6			49.0	$.097 \times 10^{-12}$	19.8	.22	.064	3284	.064	.064	
6.83	22.41	7.50	-19.9	Small Snow Region	SS A	48.7	$.090 \times 10^{-12}$	18.5	.22	.068	3322	.068	.068	
6.87	22.59	7.53	-20.1			48.5	$.0861 \times 10^{-12}$	17.7	.22	.068	3327	.068	.068	
6.94	22.77	7.58	-20.6			49.0	$.0366 \times 10^{-12}$	19.8	.24	.072	3335	.072	.072	
7.00	22.95	7.62	-20.9			48.5	$.0861 \times 10^{-12}$	17.7	.22	.068	3342	.068	.068	
7.05	23.13	7.67	-21.4			48.0	$.0767 \times 10^{-12}$	15.7	.20	.064	3350	.064	.064	
7.10	23.31	7.71	-21.7			48.4	$.0841 \times 10^{-12}$	17.3	.22	.067	3357	.067	.067	
7.6	24.95	8.12	-25.0			48.0	$.0767 \times 10^{-12}$	15.7	.20	.064	3364	.064	.064	
8.07	26.5	8.54	-28.8	Ice Crystal to S ₃ Transition Zone	C ₁	47.2	$.0638 \times 10^{-12}$	13.1	.18	.058	3426	.058	.058	
8.23	27.0	8.66	-30.0			46.5	$.055 \times 10^{-12}$	11.2	.30	.089	3497	.089	.089	
8.38	27.5	8.79	-31.3			46.3	$.052 \times 10^{-12}$	10.7	.34	.097	3526	.097	.097	
8.53	28.0	8.93	-32.7			46.1	$.049 \times 10^{-12}$	10.2	.38	.104	3557	.104	.104	
8.58	28.1	9.13	-34.7	Ice Crystal Region	C ₁	45.9	$.047 \times 10^{-12}$	9.72	.42	.108	3590	.108	.108	
9.49	31.13	9.74	-40.7			45.5	$.0432 \times 10^{-12}$	8.85	.48	.120	3648	.120	.120	
9.89	32.43	10.07	-44.2			42.0	$.0193 \times 10^{-12}$	3.95	.27	.079	3791	.079	.079	
10.02	32.88	10.19	-45.5			37.0	$.0061 \times 10^{-12}$	1.25	.12	.043	3840	.043	.043	
10.06	33.03	10.43	-45.9			30.0	$.0012 \times 10^{-12}$	0.25	.04	.018	3849	.018	.018	
						0	0	0	0	0	3851	0	0	

Table C2. Tabulation of the Numerical Values of the Radar and Hydrometeor Parameters for Missile Flight No. Q2-6361 (Unit No. R487102) of 2 February 1973, Launched at 1408:30 GMT

Missile Altitude	Horizontal Range from JAFNA	Radio-sonde Temperature	Hydro-meteor Region or Zone	Precipitation Type	Radar-Measured Parameters							Total Liquid Water Content
					Integrator Signal Values	Volume Reflectivity	Reflectivity Factor	Precipitation Rate	Liquid-Water-Content of M of Precipitation	Integral of M Along Missile Path	Cloud Liquid Water Content	
km	k ft	°C			I_s	η	Z	P	gm m ⁻³	$\int_0^z M dr$	gm m ⁻³	gm m ⁻³
0	1.80	9.4	Rain Region	R _{0W}	75.8	46.5×10^{-12}	2143	4.2	.261	0	.261	.261
.08	.27	12.8			76.8	58.2×10^{-12}	2683	4.88	.297	46.9	.297	.297
.14	.45	15.1			75.0	38.5×10^{-12}	1773	3.70	.234	76.6	.234	.234
.19	.63	15.3			76.4	53.1×10^{-12}	2447	4.59	.282	106	.282	.282
.25	.81	15.4			75.6	44.2×10^{-12}	2036	4.06	.254	136	.254	.254
.30	.99	15.2			76.8	58.2×10^{-12}	2683	4.88	.297	166	.297	.297
.36	1.17	14.8			76.9	59.6×10^{-12}	2746	4.95	.301	200	.301	.301
.41	1.35	14.5			76.9	59.6×10^{-12}	2746	4.95	.301	234	.301	.301
.47	1.53	14.1			78.7	90.2×10^{-12}	4156	6.53	.383	272	.383	.383
.52	1.71	13.8			78.0	76.7×10^{-12}	3538	5.87	.349	313	.349	.349
.58	1.89	13.3			78.0	76.7×10^{-12}	3538	5.87	.349	349	.349	.349
.63	2.07	13.1			78.8	92.2×10^{-12}	4253	6.63	.388	393	.388	.388
.69	2.25	12.8			78.8	92.2×10^{-12}	4253	6.63	.388	437	.388	.388
.74	2.43	12.4			79.0	96.6×10^{-12}	4453	6.84	.398	482	.398	.398
.80	2.61	12.1			79.0	96.6×10^{-12}	4453	6.84	.398	526	.398	.398
.85	2.79	11.8			79.0	96.6×10^{-12}	4453	6.84	.398	568	.398	.398
.91	2.97	11.5			78.0	76.7×10^{-12}	3538	5.87	.349	607	.349	.349
.96	3.15	11.1			78.0	76.7×10^{-12}	3538	5.87	.349	646	.349	.349
1.01	3.33	10.8			78.0	76.7×10^{-12}	3538	5.87	.349	683	.349	.349
1.07	3.51	10.4			77.4	66.8×10^{-12}	3081	5.35	.322	719	.322	.322
1.12	3.69	10.2			77.0	61.0×10^{-12}	2810	5.03	.305	754	.305	.305
1.18	3.87	9.8			77.4	66.8×10^{-12}	3081	5.35	.322	791	.322	.322
1.23	4.05	9.4			77.8	73.3×10^{-12}	3378	5.69	.340	825	.340	.340
1.29	4.23	9.1			76.3	51.9×10^{-12}	2392	4.52	.278	858	.278	.278
1.34	4.41	8.8			77.0	61.0×10^{-12}	2810	5.03	.305	894	.305	.305
1.40	4.59	8.5			77.8	73.3×10^{-12}	3378	5.69	.340	932	.340	.340
1.45	4.77	8.1			77.9	75.0×10^{-12}	3457	5.78	.344	971	.344	.344
1.51	4.95	7.8			78.0	76.7×10^{-12}	3538	5.87	.349	1009	.349	.349
					77.7	71.6×10^{-12}	3301	5.60	.335		.335	.335

Table C2. Tabulation of the Numerical Values of the Radar and Hydrometeor Parameters for Missile Flight No. Q2-6361 (Unit No. R487102) of 2 February 1973, Launched at 1408:30 GMT (Cont)

Missile Altitude	Horizontal Range from JAFNA	Radio-sonde Temperature	Hydro-meteor Region or Zone	Precipitation Type	Integrator Signal Values	Radar-Measured Parameters							Total Liquid Water Content
						Volume Reflectivity	Reflectivity Factor	Precipitation Rate	Liquid-Water-Content of Precipitation of Ice Cloud	Integral of M Along Missile Path	Cloud Liquid Water Content		
km	k ft	°C			dB	η	Z	P	gm m^{-3}	$\int_0^z M \text{ dr}$	gm m^{-3}	gm m^{-3}	
1.56	5.13	3.20			77.0	61.0×10^{-12}	2810	5.03	.305	1045	.042	.347	
1.62	5.31	3.24	Rain Region	R _{01W}	77.0	61.0×10^{-12}	2810	5.03	.305	1079	.039	.344	
1.67	5.49	3.27			77.0	61.0×10^{-12}	2810	5.03	.305	1113	.038	.343	
1.73	5.67	3.35			76.9	59.6×10^{-12}	2746	4.95	.301	1147	.037	.338	
1.78	5.85	3.39			76.0	48.4×10^{-12}	2232	4.31	.267	1179	.037	.304	
1.84	6.03	3.46			76.0	48.4×10^{-12}	2232	4.31	.267	1209	.038	.305	
1.89	6.21	3.50			76.6	55.6×10^{-12}	2563	4.73	.290	1240	.040	.330	
1.95	6.39	3.56			77.0	61.0×10^{-12}	2810	5.03	.305	1274	.042	.347	
2.00	6.57	3.62			76.8	58.2×10^{-12}	2683	4.88	.297	1307	.044	.341	
2.06	6.75	3.68			76.2	50.7×10^{-12}	2337	4.45	.275	1339	.049	.324	
2.11	6.93	3.74			76.2	50.7×10^{-12}	2337	4.45	.275	1370	.052	.327	
2.17	7.11	3.79			76.7	56.9×10^{-12}	2622	4.86	.293	1402	.055	.348	
2.22	7.29	3.85			76.9	59.6×10^{-12}	2746	4.95	.301	1435	.058	.357	
2.28	7.47	3.90			76.4	53.1×10^{-12}	2447	4.59	.282	1468	.063	.345	
2.33	7.65	3.97			76.0	48.4×10^{-12}	2232	4.32	.267	1500	.066	.333	
2.39	7.83	4.02			76.6	55.6×10^{-12}	2563	4.73	.290	1530	.070	.360	
2.44	8.01	4.08			76.0	48.4×10^{-12}	2232	4.32	.267	1561	.073	.340	
2.50	8.19	4.13			76.3	51.9×10^{-12}	2392	4.52	.278	1591	.075	.353	
2.55	8.37	4.19			77.0	61.0×10^{-12}	2810	5.03	.305	1624	.077	.382	
2.61	8.55	4.25			77.0	61.0×10^{-12}	2810	5.03	.305	1658	.079	.384	
2.66	8.73	4.31			77.4	66.8×10^{-12}	3081	5.35	.322	1693	.080	.402	
2.68	8.80	4.33	Melting Zone	L ₃ and R _{01W}	77.6	70.52×10^{-12}		5.27	.318	1707	.080	.398	
3.01	9.87	4.67			85.7	448.4×10^{-12}		4.08	.448	1961	.089	.537	
3.33	10.93	5.00			72.5	21.74×10^{-12}		2.88	.477	2268	.058	.535	
3.66	12.00	5.35			67.8	7.38×10^{-12}		1.69	.382	2553	.035	.417	
3.70	12.15	5.40	Large Snow Region	L ₃	67.0	6.10×10^{-12}	1250	1.52	.346	2587	.031	.377	
3.76	12.33	5.46			66.8	5.82×10^{-12}	1193	1.48	.337	2625	.022	.359	
3.81	12.51	5.51			66.0	4.84×10^{-12}	993	1.31	.302	2661	.018	.320	

Table C2. Tabulation of the Numerical Values of the Radar and Hydrometeor Parameters for Missile Flight No. Q2-6361 (Unit No. R487102) of 2 February 1973, Launched at 1408:00 GMT (Cont)

Missile Altitude	Horizontal Range from JAFNA	Radio-sonde Temperature	Hydro-meteor Region or Zone	Precipitation Type	Radar-Measured Parameters						Cloud Liquid Water Content	Total Liquid Water Content
					Integrator Signal Values	Volume Reflectivity	Reflectivity Factor	Precipitation Rate	Liquid-Water-Content of M of Precipitation-Cloud	Integral of M Along Missile Path		
km	k ft	°C			I_S	η	Z	P	of M	$\int_0^L M dr$	$gm m^{-3}$	$gm m^{-3}$
3.87	12.69	-3.0			65.3	4.12×10^{-12}	845	1.19	.274	2693	.014	.288
3.92	12.87	-3.4	Large Snow Region	I_S3	65.0	3.85×10^{-12}	788	1.14		2723	.011	.274
3.98	13.05	-3.8			65.0	3.85×10^{-12}	788	1.14	.263	2752	0	.263
4.03	13.23	-4.1			65.0	3.85×10^{-12}	788	1.14	.263	2782		.263
4.09	13.41	-4.3			65.0	3.85×10^{-12}	788	1.14	.263	2811		.263
4.14	13.59	-4.5			65.0	3.85×10^{-12}	788	1.14	.263	2841		.263
4.20	13.77	-4.8			64.0	3.05×10^{-12}	626	.98	.229	2868		.229
4.25	13.95	-5.0			65.5	4.31×10^{-12}	884	1.22	.282	2897		.282
4.31	14.13	-5.3			65.0	3.85×10^{-12}	788	1.14	.263	2927		.263
4.36	14.31	-5.5			64.0	3.05×10^{-12}	626	.98	.229	2955		.229
4.42	14.49	-5.8			64.0	3.05×10^{-12}	626	.98	.229	2980		.229
4.47	14.67	-6.0			65.3	4.12×10^{-12}	845	1.19	.274	3009		.274
4.53	14.85	-6.3			65.2	4.03×10^{-12}	826	1.17	.270	3039		.270
4.58	15.03	-6.5			63.0	3.50×10^{-12}	719	1.07	.249	3068		.249
4.64	15.21	-6.8			63.0	2.43×10^{-12}	497	.85	.200	3093		.200
4.69	15.39	-7.0			65.0	3.85×10^{-12}	788	1.14	.263	3116		.263
4.75	15.57	-7.2			64.0	3.05×10^{-12}	626	.98	.229	3141		.229
4.80	15.75	-7.5			63.6	2.79×10^{-12}	571	.93	.217	3169		.217
4.86	15.93	-7.7			62.5	2.16×10^{-12}	443	.79	.187	3194		.187
4.91	16.11	-7.9			64.0	3.05×10^{-12}	626	.98	.229	3217		.229
4.97	16.29	-8.1			62.4	2.11×10^{-12}	433	.78	.184	3240		.184
5.02	16.47	-8.4			61.9	1.88×10^{-12}	386	.72	.172	3263		.172
5.07	16.65	-8.7			61.7	1.80×10^{-12}	369	.70	.167	3283		.167
5.13	16.83	-9.0			61.5	1.72×10^{-12}	352	.68	.163	3302		.163
5.19	17.01	-9.3			60.8	1.46×10^{-12}	300	.62	.148	3320		.148
5.24	17.19	-9.6			60.5	1.36×10^{-12}	280	.59	.142	3338		.142
5.29	17.37	-9.9			60.0	1.22×10^{-12}	249	.55	.132	3354		.132
5.35	17.55	-10.3								3369		.132

Table C2. Tabulation of the Numerical Values of the Radar and Hydrometeor Parameters for Missile Flight No. Q2-6361 (Unit No. R487102) of 2 February 1973, Launched at 1408.30 GMT (Cont)

Missile Altitude Kilometers	Horizontal Range from JAFNA nautical miles	Radio-sonde Temperature °C	Hydro-meteor Region or Zone	Precipitation Type	Integrator Signal Values dB	Radar-Measured Parameters						Total Liquid Water Content gm m ⁻³
						Volume Reflectivity cm ⁻¹	Reflectivity Factor mm ⁶ m ⁻³	Precipitation Rate mm hr ⁻¹	Liquid-Water Content of Precipitation gm m ⁻³	Integral Along Missile Path $\int_0^7 M dR$ gm m ⁻²	Cloud Liquid Water Content gm m ⁻³	
5.40	17.73	-10.6	Large Snow Region	L _s	60.0	1.22×10^{-12}	249	.55	.132	3384		.132
5.46	17.91	-10.9			59.8	1.16×10^{-12}	238	.53	.129	3399		.129
5.51	18.09	-11.2			59.9	1.16×10^{-12}	238	.53	.129	3413		.129
5.57	18.27	-11.5			59.0	$.966 \times 10^{-12}$	198	.48	.115	3427		.115
5.62	18.45	-11.8			58.7	$.902 \times 10^{-12}$	185	.46	.111	3440		.111
5.68	18.63	-12.2			57.4	$.668 \times 10^{-12}$	137	.38	.093	3451		.093
5.73	18.81	-12.5			56.6	$.556 \times 10^{-12}$	114	.34	.083	3461		.083
5.79	18.99	-12.8			55.2	$.403 \times 10^{-12}$	82.6	.27	.069	3469		.069
5.84	19.17	-13.2			54.7	$.359 \times 10^{-12}$	73.6	.25	.064	3477		.064
5.90	19.35	-13.6			53.0	$.243 \times 10^{-12}$	49.7	.20	.051	3483		.051
5.94	19.50	-13.9			51.0	$.243 \times 10^{-12}$	49.7	.20	.051	3488		.051
6.23	20.43	-15.8	Small Snow to Ice Trans. Zone	SSA and LS _s	50.4	$.133 \times 10^{-12}$	27.4	.20	.055	3519		.055
6.51	21.37	-17.7			50.5	$.138 \times 10^{-12}$	28.0	.20	.059	3552		.059
6.80	22.30	-19.6			48.0	$.077 \times 10^{-12}$	15.7	.20	.064	3587		.064
6.83	22.41	-19.9	Small Snow Region	SSA	48.0	$.077 \times 10^{-12}$	15.7	.20	.064	3592		.064
7.6	24.95	-25.0			47.0	$.061 \times 10^{-12}$	12.5	.18	.056	3687		.056
8.01	26.30	-28.3			46.5	$.054 \times 10^{-12}$	11.2	.28	.084	3746		.084
8.19	26.86	-29.7			46.3	$.051 \times 10^{-12}$	10.7	.33	.094	3777		.094
8.36	27.43	-31.2			46.0	$.049 \times 10^{-12}$	9.95	.37	.102	3812		.102
8.53	28.0	-32.7			45.8	$.046 \times 10^{-12}$	9.50	.42	.108	3849		.108
8.78	28.81	-34.7			45.5	$.0432 \times 10^{-12}$	8.85	.48	.120	3906		.120
9.49	31.13	-40.7			42.0	$.0193 \times 10^{-12}$	3.95	.27	.079	4049		.079
9.89	32.43	-44.2			37.0	$.0061 \times 10^{-12}$	1.25	.12	.043	4098		.043
10.02	32.88	-45.5			30.0	$.0012 \times 10^{-12}$	0.25	.04	.018	4107		.018
10.06	33.03	-45.9			0	0	0	0	0	4109		0

Table C3. Tabulation of the Numerical Values of the Radar and Hydrometeor Parameters for Missile Flight No. Q2-6362 (Unit No. R487103) of 27 February 1973, Launched at 1040:00 GMT. Note that the parameter values for the upper cirrus deck are maximum values

Missile Altitude	Horizontal Range from JAFNA	Radio-sonde Temperature	Hydro-meteor Region or Zone	Precipitation Type	Integrator Signal Values	Radar-Measured Parameters							Total Liquid Water Content
						Volume Reflectivity	Reflectivity Factor	Precipitation Rate	Liquid-Water-Content of Precipitation	Integral of M Along Missile Path	Cloud Liquid Water Content		
km	x ft	°C			dB	η	Z	P	gm m ⁻³	$\int_0^z M dz$	gm m ⁻³	gm m ⁻³	
0	1.80	3.5	Rain Region	R _{1W}	68.0	8.01×10^{-12}	371.	1.30	.095	0		.095	
0.3	1.82	3.2			65.7	4.73×10^{-12}	218.	.92	.070	4.6		.070	
0.8	1.87	2.3			65.7	4.73×10^{-12}	218.	.92	.070	12.4		.070	
1.4	1.93	1.5			66.2	5.31×10^{-12}	245.	.99	.075	20.5		.075	
1.9	1.98	0.7			66.2	5.31×10^{-12}	245.	.99	.075	28.9		.075	
2.5	2.03	0.2			66.7	5.96×10^{-12}	275.	1.07	.080	37.5		.080	
3.0	2.10	-0.2			67.5	7.16×10^{-12}	330.	1.21	.085	56.6		.085	
3.6	2.14	-0.7			69.0	10.12×10^{-12}	466.	1.52	.108	67.6		.108	
4.1	2.20	-1.1			68.0	8.04×10^{-12}	370.	1.30	.095	79.0		.095	
4.7	2.26	-1.5			68.1	8.22×10^{-12}	379.	1.32	.096	89.7		.096	
5.2	2.32	-1.9			69.0	10.16×10^{-12}	466.	1.52	.108	101		.108	
5.8	2.37	-1.4			69.0	10.16×10^{-12}	466.	1.52	.108	113		.108	
6.3	2.42	-0.8			69.0	10.16×10^{-12}	466.	1.52	.108	125		.108	
6.9	2.47	-0.2			69.0	10.16×10^{-12}	466.	1.52	.108	138		.108	
7.4	2.53	0.5			69.2	10.59×10^{-12}	488.	1.57	.111	150		.111	
8.0	2.61	1.2			68.0	8.34×10^{-12}	370.	1.30	.095	161		.095	
8.5	2.70	1.6			65.2	8.41×10^{-12}	388.	1.34	.098	172		.098	
9.1	2.70	1.4			69.0	10.16×10^{-12}	466.	1.52	.108	184		.108	
9.6	2.76	1.2			69.0	10.16×10^{-12}	466.	1.52	.108	196		.108	
1.01	2.80	1.1			68.0	8.04×10^{-12}	370.	1.30	.095	207		.095	
1.07	2.85	0.9			68.0	8.04×10^{-12}	370.	1.30	.095	218		.095	
1.12	2.91	0.7			69.0	10.16×10^{-12}	466.	1.52	.108	229		.108	
1.18	2.97	0.5			69.1	10.35×10^{-12}	477.	1.54	.110	242		.110	
1.19	2.98	0.4	Melting Zone	R _{1W}	69.6	11.57×10^{-12}		1.55	.111	244		.111	
1.52	3.31	-0.5			84.4	$348. \times 10^{-12}$		1.97	.234	362		.234	
1.86	3.63	-0.7			73.1	26.24×10^{-12}		2.39	.401	579		.401	
2.10	3.96	-2.0			72.0	19.95×10^{-12}		2.81	.617	927		.617	
2.22	3.99	-2.1	Large Snow Region	L ₃	71.1	16.40×10^{-12}	3363.	2.84	.624	962		.624	
2.28	4.05	-2.4			71.9	19.72×10^{-12}	4044.	3.19	.506	1036		.506	

Table C3. Tabulation of the Numerical Values of the Radar and Hydrometeor Parameters for Missile Flight No. Q2-6362 (Unit No. R487103) of 27 February 1973, Launched at 1040:00 GMT (Cont)

Missile Altitude	Horizontal Range from JAFNA	Radio-sonde Temperature	Hydro-meteor Region or Zone	Precipitation Type	Radar-Measured Parameters						Integral of M Along Missile Path $\int_0^M dRS$	Cloud Liquid Water Content	Total Liquid Water Content
					Integrator Signal Values I_S	Volume Reflectivity η	Reflectivity Factor Z	Precipitation Rate P	Liquid-Water-Content of M of Precipitation-ice Cloud	gm m ⁻³			
km	k ft	°C			cm ⁻¹	mm m ⁻³	mm hr ⁻¹	gm m ⁻³	mm hr ⁻¹	gm m ⁻³	gm m ⁻²	gm m ⁻³	gm m ⁻³
2.33	7.65	4.10		LS ₃	72.4	22.13×10^{-12}	4537	3.43	.746	1116	.746	.746	
2.39	7.83	4.15	Large Snow Region		73.0	25.41×10^{-12}	5209	3.74	.810	1204	.810	.810	
2.44	8.01	4.21			72.4	22.13×10^{-12}	4537	3.43	.746	1291	.746	.746	
2.5	8.19	4.27			71.0	16.03×10^{-12}	3287	2.80	.616	1367	.616	.616	
2.55	8.37	4.31			69.5	11.35×10^{-12}	2327	2.25	.501	1429	.501	.501	
2.61	8.55	4.37			69.1	10.35×10^{-12}	2122	2.12	.474	1484	.474	.474	
2.66	8.73	4.43			68.1	8.22×10^{-12}	1686	1.84	.414	1554	.414	.414	
2.72	8.91	4.48			68.9	9.89×10^{-12}	2027	2.06	.462	1582	.462	.462	
2.77	9.09	4.54			68.9	9.89×10^{-12}	2027	2.06	.462	1634	.462	.462	
2.83	9.27	4.58			68.5	9.02×10^{-12}	1848	1.95	.437	1684	.437	.437	
2.88	9.45	4.64			68.0	8.04×10^{-12}	1647	1.81	.408	1732	.408	.408	
2.94	9.63	4.70			68.5	9.02×10^{-12}	1848	1.95	.437	1779	.437	.437	
2.99	9.81	4.76			68.0	8.04×10^{-12}	1647	1.81	.408	1826	.408	.408	
3.04	9.99	4.80			70.0	12.74×10^{-12}	2611	2.42	.537	1879	.537	.537	
3.10	10.17	4.86			69.0	10.12×10^{-12}	2074	2.09	.468	1935	.468	.468	
3.15	10.35	4.92			70.9	15.67×10^{-12}	3212	2.76	.607	1955	.607	.607	
3.21	10.53	4.98			71.1	16.41×10^{-12}	3363	2.84	.624	2064	.624	.624	
3.26	10.71	5.03			71.8	19.28×10^{-12}	3951	3.14	.687	2138	.687	.687	
3.32	10.89	5.08			73.0	25.41×10^{-12}	5209	3.74	.810	2222	.810	.810	
3.37	11.07	5.14			74.0	31.99×10^{-12}	6558	4.33	.929	2319	.929	.929	
3.43	11.25	5.19			73.9	31.26×10^{-12}	6409	4.27	.916	2416	.916	.916	
3.48	11.43	5.24			73.0	25.41×10^{-12}	5209	3.74	.810	2513	.810	.810	
3.54	11.61	5.30			73.9	31.26×10^{-12}	6409	4.27	.916	2609	.916	.916	
3.59	11.79	5.35			73.0	25.41×10^{-12}	5209	3.74	.810	2706	.810	.810	
3.65	11.97	5.40			73.0	25.41×10^{-12}	5209	3.74	.810	2803	.810	.810	
3.70	12.15	5.46			72.0	20.18×10^{-12}	4138	3.24	.706	2887	.706	.706	
3.76	12.33	5.52			72.0	20.18×10^{-12}	4138	3.24	.706	2966	.706	.706	
3.81	12.51	5.57			71.9	19.72×10^{-12}	4044	3.19	.697	3045	.697	.697	
3.87	12.69	5.62			71.2	16.79×10^{-12}	3442	2.88	.633	3119	.633	.633	

Table C3. Tabulation of the Numerical Values of the Radar and Hydrometeor Parameters for Missile Flight No. Q2-6362 (Unit No. R487103) of 27 February 1973, Launched at 1040:00 GMT. (Cont)

Missile Altitude		Horizontal Range from JAFNA	Radio-sonde Temperature °C	Hydro-meteor Region or Zone	Precipitation Type	Integrating Signal Values I_s dB	Volume Reflectivity η cm^{-1}	Reflectivity Factor Z $mm^6 m^{-3}$	Precipitation Rate P $mm hr^{-1}$	Liquid-Water-Content of Precipitation of Ice Cloud $gm m^{-3}$	Integral of M Along Missile Path $\int M drs$ $gm m^{-2}$	Cloud Liquid Water Content $gm m^{-3}$	Total Liquid Water Content $gm m^{-3}$
km	ft												
3.92	12.87	5.68	11.4	Large Snow Region	LS ₃	71.8	19.28×10^{-12}	3951	3.14	.687	3193	.057	.744
3.98	13.05	5.74	-11.7			71.9	19.72×10^{-12}	4044	3.19	.697	3271	.060	.757
4.03	13.23	5.79	-12.0			71.9	19.72×10^{-12}	4044	3.19	.697	3348	.059	.756
4.09	13.41	5.84	-12.4			71.0	16.03×10^{-12}	3287	2.80	.616	3422	.057	.673
4.14	13.59	5.89	-12.7			72.0	20.18×10^{-12}	4138	3.24	.706	3496	.055	.761
4.20	13.77	5.95	-13.0			73.0	25.41×10^{-12}	5209	3.74	.810	3581	.052	.862
4.25	13.95	6.00	-13.3			73.5	28.51×10^{-12}	5845	4.02	.867	3675	.050	.917
4.31	14.13	6.06	-13.7			73.0	25.41×10^{-12}	5209	3.74	.810	3768	.048	.858
4.36	14.31	6.11	-14.0			72.8	24.27×10^{-12}	4975	3.64	.788	3858	.045	.833
4.42	14.49	6.16	-14.3			72.0	20.18×10^{-12}	4138	3.24	.706	3941	.043	.749
4.47	14.67	6.22	-14.6			71.0	16.03×10^{-12}	3287	2.80	.616	4015	.040	.656
4.53	14.85	6.28	-15.0			68.6	9.23×10^{-12}	1891	1.98	.443	4075	.037	.480
4.58	15.03	6.33	-15.3			67.0	6.38×10^{-12}	1308	1.57	.356	4110	.035	.391
4.64	15.21	6.38	-15.6			64.9	3.94×10^{-12}	807	1.15	.267	4154	.033	.300
4.69	15.39	6.44	-16.0			63.0	2.54×10^{-12}	521	.88	.205	4181	.031	.236
4.75	15.57	6.50	-16.3			63.1	2.60×10^{-12}	533	.89	.208	4204	.030	.238
4.80	15.75	6.56	-16.6	62.0	2.02×10^{-12}	414	.76	.179	4225	.029	.206		
4.86	15.93	6.62	-17.0	59.7	1.19×10^{-12}	244	.54	.131	4243	.028	.159		
4.91	16.11	6.67	-17.3	58.2	$.84 \times 10^{-12}$	173	.44	.106	4256	.027	.133		
4.97	16.29	6.72	-17.6	58.0	$.80 \times 10^{-12}$	165	.42	.104	4268	.026	.130		
5.02	16.47	6.78	-17.9	57.4	$.70 \times 10^{-12}$	144	.39	.095	4279	.025	.120		
5.07	16.65	6.84	-18.3	57.0	$.64 \times 10^{-12}$	131	.37	.090	4280	.024	.114		
5.13	16.83	6.90	-18.7	56.5	$.57 \times 10^{-12}$	117	.34	.084	4299	.023	.107		
5.19	17.01	6.96	-19.1	55.0	$.40 \times 10^{-12}$	82.6	.27	.069	4308	.021	.090		
5.24	17.19	7.00	-19.4	55.5	$.45 \times 10^{-12}$	92.6	.29	.073	4316	.020	.093		
5.29	17.37	7.06	-19.8	55.0	$.40 \times 10^{-12}$	82.6	.27	.069	4323	.019	.088		
5.35	17.55	7.13	-20.3	55.6	$.46 \times 10^{-12}$	94.8	.30	.075	4331	.018	.093		
5.40	17.73	7.18	-20.7	57.0	$.64 \times 10^{-12}$	131	.37	.090	4341	.017	.107		

Table C3. Tabulation of the Numerical Values of the Radar and Hydrometeor Parameters for Missile Flight No. Q2-6362 (Unit No. R487103) of 27 February 1973, Launched at 1040:00 GMT (Cont)

Missile Altitude		Horizontal Range from IAFNA	Radio Sonda Temperature	Hydro-meteor Region or Zone	Precipitation Type	Integrator Signal Values	Radar-Measured Parameters						Cloud Liquid Water Content	Total Liquid Water Content
km	s. ft.						Volume Reflectivity	Reflectivity Factor	Precipitation Rate	Liquid-Water-Content of Precipitation	Integral of M Along Missile Path	Cloud Liquid Water Content		
		mm	°C			I _h	η	Z	P	g m ⁻³	$\int_0^z M dr$	g m ⁻³	g m ⁻³	
5.46	17.91	7.24	21.1			56.1	$.52 \times 10^{-12}$	105	.32	.080	4350	.018	.096	
5.51	18.09	7.29	21.4	Large Snow Region	LS ₃	55.0	$.40 \times 10^{-12}$	82.6	.27	.069	4359	.015	.084	
5.57	18.27	7.35	-21.8			54.0	$.32 \times 10^{-12}$	65.6	.24	.060	4366	.013	.073	
5.68	18.63	7.47	-22.8			49.0	$.10 \times 10^{-12}$	20.7	.11	.030	4376	.011	.041	
5.73	18.81	7.52	-23.2			48.0	$.08 \times 10^{-12}$	16.5	.099	.026	4379	.010	.036	
5.79	18.99	7.57	-23.6			47.0	$.064 \times 10^{-12}$	13.1	.086	.023	4382	.008	.031	
5.84	19.17	7.63	-24.1			46.0	$.051 \times 10^{-12}$	10.4	.074	.020	4384	.007	.027	
6.01	19.71	7.80	-25.5			47.0	$.064 \times 10^{-12}$	13.1	.086	.023	4391	.005	.028	
6.06	19.89	7.85	-26.0			47.0	$.064 \times 10^{-12}$	13.1	.086	.023	4394	.004	.027	
6.12	20.07	7.91	-26.4			47.0	$.064 \times 10^{-12}$	13.1	.086	.023	4396	.003	.026	
6.50	21.33	8.50	-29.6	Assumed Clear	None	0	0	0	0	0	4405	0	0	
7.00	22.97	8.81	-33.6			0	0	0	0	0	4405	0	0	
7.50	24.61	9.35	-37.5			0	0	0	0	0	4405	0	0	
7.92	25.00	9.47	-38.4			0	0	0	0	0	4405	0	0	
7.93	26.00	9.79	-41.0	File-validated Ice Crystal Layer	C ₁	42.0	$.02 \times 10^{-12}$	4.14	.280	.080	4431	.080	.060	
8.08	26.50	9.96	-42.4			45.4	$.04 \times 10^{-12}$	9.05	.490	.122	4463	.122	.122	
8.23	27.00	10.13	-43.9			46.0	$.05 \times 10^{-12}$	10.4	.540	.131	4502	.131	.131	
8.38	27.50	10.29	-45.3			45.4	$.04 \times 10^{-12}$	9.05	.490	.122	4541	.122	.122	
8.53	28.00	10.45	-46.7			43.0	$.03 \times 10^{-12}$	5.21	.328	.091	4571	.091	.091	
8.76	28.73	10.69	-48.7			37.0	$.006 \times 10^{-12}$	1.31	.121	.044	4601	.044	.044	
8.82	28.95	10.74	-49.2			30.0	$.001 \times 10^{-12}$.261	.038	.019	4606	.019	.019	
8.84	29.00	10.78	-49.5			0	0	0	0	0	4606	0	0	

Table C4. Tabulation of the Numerical Values of the Radar and Hydrometeor Parameters for Missile Flight No. Q2-6363 (Unit No. R487104) of 27 February 1973, Launched at 1040:30 GMT. Note that the parameter values for the upper cirrus deck are maximum values

Missile Altitude		Horizontal Range from JAFNA	Radio-sonde Temperature	Hydro-meteor Region or Zone	Precipitation Type	Radar-Measured Parameters						Cloud Liquid Water Content	Total Liquid Water Content
km	k ft	nmi	°C			Integrator Signal Values	Volume Reflectivity	Reflectivity Factor	Precipitation Rate	Liquid-Water Content of Precipitation	Integral of M Along Missile Path	gm m ⁻³	gm m ⁻³
						I _S	η	Z	P		$\int_0^7 M dR_S$		
						dB	cm ⁻¹	mm ⁶ m ⁻³	mm hr ⁻¹	gm m ⁻³	gm m ⁻²	gm m ⁻³	gm m ⁻³
0	0	1.80	3.5	Rain Region	R _{1W}	67.9	8.01 × 10 ⁻¹²	369	1.30	.065	0	.095	
.25	.81	2.02	1.9			68.3	8.61 × 10 ⁻¹²	397	1.36	.066	61	.099	
.50	.99	2.07	1.5			69.2	10.6 × 10 ⁻¹²	488	1.57	.111	72	.111	
.36	1.17	2.12	1.1			68.2	8.41 × 10 ⁻¹²	388	1.34	.097	84	.097	
.41	1.35	2.17	0.7			69.0	10.1 × 10 ⁻¹²	466	1.52	.108	96	.108	
.47	1.53	2.22	0.3			69.2	10.6 × 10 ⁻¹²	488	1.57	.111	108	.111	
.52	1.71	2.27	-0.1			68.1	8.22 × 10 ⁻¹²	379	1.32	.096	118	.096	
.58	1.89	2.31	-0.4			68.2	8.41 × 10 ⁻¹²	388	1.34	.097	130	.097	
.63	2.07	2.37	-0.8			69.5	11.4 × 10 ⁻¹²	523	1.64	.116	136	.116	
.69	2.25	2.47	-0.2			70.0	12.7 × 10 ⁻¹²	587	1.77	.124	149	.124	
.74	2.43	2.49	-0.5			68.5	9.02 × 10 ⁻¹²	416	1.41	.101	162	.101	
.80	2.61	2.53	1.2			68.1	8.22 × 10 ⁻¹²	379	1.32	.096	173	.096	
.85	2.79	2.57	1.6			68.0	8.04 × 10 ⁻¹²	370	1.30	.095	183	.095	
.91	2.97	2.62	1.4			69.0	16.1 × 10 ⁻¹²	466	1.52	.108	195	.108	
.96	3.15	2.68	1.2			69.0	10.1 × 10 ⁻¹²	466	1.52	.108	207	.108	
1.01	3.33	2.74	1.1			68.0	8.03 × 10 ⁻¹²	370	1.30	.095	218	.095	
1.07	3.51	2.78	0.9			68.0	8.03 × 10 ⁻¹²	370	1.30	.095	229	.095	
1.12	3.69	2.82	0.7			68.0	8.03 × 10 ⁻¹²	370	1.30	.095	240	.095	
1.18	3.87	2.87	0.5			68.5	9.02 × 10 ⁻¹²	416	1.41	.101	251	.101	
1.19	3.90	2.90	0.4	Melting Zone	R _{1W} and L _{S3}	68.6	9.19 × 10 ⁻¹²		1.42	.102	253	.102	
1.52	5.00	3.20	-0.5			83.7	300. × 10 ⁻¹²		2.01	.239	369	.239	
1.86	6.10	3.51	-0.7			73.3	27.4 × 10 ⁻¹²		2.60	.434	599	.434	
2.19	7.20	3.83	-2.0			72.3	21.6 × 10 ⁻¹²		3.19	.696	985	.696	
2.22	7.29	3.85	-2.1	Large Snow Region	L _{S3}	72.0	20.2 × 10 ⁻¹²	4138	3.24	.706	1025	.706	
2.28	7.47	3.90	-2.4			72.0	20.2 × 10 ⁻¹²	4138	3.24	.706	1104	.706	
2.33	7.65	3.96	-2.7			72.9	24.8 × 10 ⁻¹²	5090	3.69	.799	1188	.799	
2.39	7.83	4.01	-2.9			72.2	21.1 × 10 ⁻¹²	4333	3.33	.726	1273	.726	
2.44	8.01	4.06	-3.2			71.1	16.4 × 10 ⁻¹²	3363	2.84	.624	1349	.624	

Table C4. Tabulation of the Numerical Values of the Radar and Hydrometeor Parameters for Missile Flight No. Q2-6363 (Unit No. R487104) of 27 February 1973, Launched at 1040:30 GMT (Cont)

Missile Altitude		Horizontal Range from JAFNA	Radio-sonde Temperature	Hydro-meteor Region or Zone	Precipitation Type	Integrator Signal Values	Volume Reflectivity	Reflectivity Factor	Precipitation Rate	Liquid-Water-Content of Precipitation of Ice Cloud	Integral of M Along Missile Path	Cloud Liquid Water Content	Total Liquid Water Content	
km	k ft	nmi	°C			LS	η	Z	P	gm m^{-3}	$\int_0^z M dr$	gm m^{-3}	gm m^{-3}	
2.50	8.19	4.10	-3.5	Large Snow Region	LS ₃	70.0	12.7×10^{-12}	2611	2.42	.537	1414	.537	.537	
2.55	8.37	4.15	-3.7			69.0	10.1×10^{-12}	2074	2.09	2.06	.468	1470	.468	.468
2.61	8.55	4.21	-4.0			68.9	9.89×10^{-12}	2027	2.06	2.06	.461	1522	.461	.461
2.66	8.73	4.26	-4.3			68.9	9.89×10^{-12}	2027	2.06	2.06	.461	1574	.461	.461
2.72	8.91	4.32	-4.6			68.0	8.04×10^{-12}	1647	1.81	1.81	.408	1622	.408	.408
2.77	9.09	4.36	-4.8			67.8	7.67×10^{-12}	1573	1.76	1.76	.397	1667	.397	.397
2.83	9.27	4.41	-5.0			67.2	6.68×10^{-12}	1370	1.61	1.61	.366	1710	.366	.366
2.88	9.45	4.47	-5.3			68.0	8.04×10^{-12}	1647	1.81	1.81	.408	1753	.408	.408
2.94	9.63	4.52	-5.6			69.7	11.9×10^{-12}	2436	2.32	2.32	.515	1805	.515	.515
2.99	9.81	4.57	-5.8			71.0	16.0×10^{-12}	3287	2.80	2.80	.616	1868	.616	.616
3.04	9.99	4.62	-6.1			72.6	23.2×10^{-12}	4751	3.53	3.53	.767	1946	.767	.767
3.10	10.17	4.67	-6.4			73.7	29.9×10^{-12}	6120	4.14	4.14	.891	2038	.891	.891
3.15	10.35	4.73	-6.7			69.7	11.9×10^{-12}	2436	2.32	2.32	.515	2117	.515	.515
3.21	10.53	4.78	-7.0			74.0	32.0×10^{-12}	6558	4.33	4.33	.929	2198	.929	.929
3.26	10.71	4.82	-7.3	74.0	32.0×10^{-12}	6558	4.33	4.33	.929	2302	.929	.929		
3.32	10.89	4.87	-7.7	72.5	22.7×10^{-12}	4643	3.48	3.48	.756	2396	.756	.756		
3.37	11.07	4.92	-8.0	60.0	1.27×10^{-12}	2611	0.57	0.57	.136	2446	.136	.136		
3.43	11.25	4.98	-8.4	74.0	32.0×10^{-12}	6558	4.33	4.33	.929	2506	.929	.929		
3.48	11.43	5.03	-8.7	73.0	25.4×10^{-12}	5209	3.74	3.74	.810	2603	.810	.810		
3.54	11.61	5.08	-9.0	73.0	25.4×10^{-12}	5209	3.74	3.74	.810	2694	.810	.810		
3.59	11.79	5.13	-9.4	73.0	25.4×10^{-12}	5209	3.74	3.74	.810	2784	.810	.810		
3.65	11.97	5.18	-9.7	72.8	24.3×10^{-12}	4975	3.64	3.64	.788	2874	.788	.788		
3.70	12.15	5.24	-10.0	73.0	25.4×10^{-12}	5209	3.74	3.74	.810	2963	.810	.810		
3.76	12.33	5.29	-10.4	74.4	35.1×10^{-12}	7190	4.59	4.59	.981	3063	0	.981		
3.81	12.51	5.34	-10.7	74.8	38.5×10^{-12}	7884	4.86	4.86	1.037	3176	.040	1.077		
3.87	12.69	5.38	-11.0	73.4	27.9×10^{-12}	5712	3.97	3.97	.856	3282	.054	.910		
3.92	12.87	5.44	-11.4	73.0	25.4×10^{-12}	5209	3.74	3.74	.810	3375	.057	.867		
3.98	13.05	5.50	-11.7	72.0	20.2×10^{-12}	4138	3.24	3.24	.706	3460	.060	.766		

Table C4. Tabulation of the Numerical Values of the Radar and Hydrometeor Parameters for Missile Flight No. Q2-6363 (Unit No. R487104) of 27 February 1973, Launched at 1040:30 GMT (Cont)

Missile Altitude km	Horizontal Range from AFNA km	Ratio sonde Temperature to True C	Hydro- meteor Region or Zone	Pre- cipitation Type	Radar-Measured Parameters						Cloud Liquid Water Content gm m ⁻³	Total Liquid Water Content gm m ⁻³
					Inter- ceptor Signal Values dB	Volume Reflectivity Z mm ⁶ m ⁻³	Reflectivity Factor Z/R mm ⁶ m ⁻³	Precipi- tation Rate P mm hr ⁻¹	Liquid-Water- Content of Precipi- tation Cloud gm m ⁻³	Integral of M Along Missile Path $\int_0^M \text{MARS}$ gm m ⁻²		
4.03	13.23	5.55			-2.0	$20.2 \cdot 10^{-12}$	4138	3.24	.706	3539	.059	.765
4.09	13.41	5.60	Large Snow Region	1-2	-2.0	$20.2 \cdot 10^{-12}$	4138	3.24	.706	3618	.057	.763
4.14	13.59	5.65			-2.2	$21.1 \cdot 10^{-12}$	4133	3.33	.726	3698	.055	.761
4.20	13.77	5.70			-2.0	$20.2 \cdot 10^{-12}$	4138	3.24	.706	3779	.052	.758
4.25	13.95	5.75			-2.1	$20.7 \cdot 10^{-12}$	4234	3.28	.716	3858	.050	.766
4.31	14.13	5.80			-2.0	$20.2 \cdot 10^{-12}$	4138	3.24	.706	3938	.048	.754
4.36	14.31	5.86			-0.1	$13.0 \cdot 10^{-12}$	2672	2.46	.544	4008	.045	.589
4.42	14.49	5.90			98.8	$5.95 \cdot 10^{-12}$	1380	2.03	.455	4064	.043	.498
4.47	14.67	5.96			96.0	$5.07 \cdot 10^{-12}$	1039	1.35	.310	4106	.040	.350
4.53	14.85	6.02			92.0	$2.02 \cdot 10^{-12}$	4138	.76	.179	4134	.037	.216
4.58	15.01	6.07			91.0	$1.50 \cdot 10^{-12}$	429	.65	.156	4153	.035	.191
4.64	15.21	6.12			82.8	$2.43 \cdot 10^{-12}$	498	.85	.200	4172	.033	.233
4.69	15.39	6.16			91.3	$1.72 \cdot 10^{-12}$	352	.68	.163	4193	.031	.194
4.75	15.57	6.22			58.4	$5.56 \cdot 10^{-12}$	114	.34	.083	4206	.030	.113
4.80	15.75	6.27			58.6	$9.23 \cdot 10^{-12}$	189	.46	.112	4217	.028	.140
4.86	15.93	6.32			55.0	$5.38 \cdot 10^{-12}$	131	.37	.090	4229	.026	.116
4.91	16.11	6.37			56.0	$5.07 \cdot 10^{-12}$	104	.32	.079	4238	.023	.102
4.97	16.29	6.41			55.9	$4.95 \cdot 10^{-12}$	102	.31	.078	4247	.021	.099
5.02	16.47	6.47			55.0	$4.03 \cdot 10^{-12}$	82.6	.27	.069	4255	.019	.088
5.07	16.65	6.52			55.0	$4.03 \cdot 10^{-12}$	82.6	.27	.069	4263	.017	.086
5.13	16.83	6.56			54.0	$4.20 \cdot 10^{-12}$	65.6	.24	.060	4270	.015	.075
5.19	17.01	6.61			54.0	$3.02 \cdot 10^{-12}$	95.6	.24	.060	4277	.012	.072
5.24	17.19	6.68			53.0	$2.54 \cdot 10^{-12}$	52.1	.20	.052	4283	.010	.062
5.29	17.37	6.73			52.0	$2.02 \cdot 10^{-12}$	41.4	.18	.044	4288	.009	.053
5.31	18.09	6.94			47.0	$0.64 \cdot 10^{-12}$	13.1	.086	.023	4304	.005	.028
5.37	18.27	6.98			46.1	$0.52 \cdot 10^{-12}$	10.6	.075	.020	4306	.004	.024
5.62	18.45	7.03			46.8	$0.61 \cdot 10^{-12}$	12.5	.083	.022	4309	.003	.025
5.68	18.63	7.09			47.2	$0.67 \cdot 10^{-12}$	13.7	.088	.024	4311	.0015	.026

Table C4. Tabulation of the Numerical Values of the Radar and Hydrometeor Parameters for Missile Flight No. Q2-6363 (Unit No. R487104) of 27 February 1973, Launched at 1040:30 GMT (Cont)

Missile Altitude km	Horizontal Range from AFNA mi	Radio-sonde Temperature C	Hydro-meteor Region or Zone	Precipitation Type	Inter-grator Signal Values dB	Volume Reflectivity Z mm^{-1}	Reflectivity Factor Z mm^{-1}	Precipitation Rate P mm hr^{-1}	Radar-Measured Parameters			Total Liquid Water Content gm m^{-3}
									Liquid-Water-Content of Precipitation of Cloud gm m^{-3}	Integral of M Along Missile Path $\int_0^7 \text{M dRS}$ gm m^{-2}	Cloud Liquid Water Content gm m^{-3}	
5.73	18.81	-23.2	Large Snow Region	LS ₃	47.0	$.064 \cdot 10^{-12}$	13.1	.086	.023	4314	0	.023
5.79	18.00	-23.6			47.0	$.064 \cdot 10^{-12}$	13.1	.086	.023	4316		.023
5.84	17.11	-24.1			47.0	$.064 \cdot 10^{-12}$	13.1	.086	.023	4319		.023
5.90	16.35	-24.6			46.8	$.061 \cdot 10^{-12}$	12.5	.083	.022	4121		.022
5.95	15.53	-25.1			46.0	$.051 \cdot 10^{-12}$	10.4	.074	.020	4324		.020
5.97	14.69	-25.4			0	0	0	0	0	4325		0
6.50	21.33	-29.6	Assumed Clear	None	0	0	0	0	0	4325		0
7.00	22.97	-33.6			0	0	0	0	0	4325		0
7.50	24.61	-37.5			0	0	0	0	0	4325		0
7.52	25.0	-38.4			0	0	0	0	0	4325		0
7.93	26.00	-41.0			42.0	$.020 \cdot 10^{-12}$	4.1	.26	.080	4351		.080
8.08	26.50	-42.4	Elemented Ice Crystal Layer	C ₁	45.4	$.044 \cdot 10^{-12}$	9.1	.49	.122	4382		.122
8.23	27.00	-43.9			-6.0	$.051 \cdot 10^{-12}$	10.4	.54	.131	4421		.131
8.38	27.50	-45.3			45.4	$.044 \cdot 10^{-12}$	9.05	.49	.122	4460		.122
8.53	28.00	-46.7			43.0	$.03 \cdot 10^{-12}$	5.21	.33	.091	4490		.091
8.76	28.73	-48.7			31.0	$.006 \cdot 10^{-12}$	1.11	.12	.044	4521		.044
8.82	28.95	-49.2			30	$.001 \cdot 10^{-12}$.251	.038	.019	4524		.019
8.84	29.00	-49.5			0	0	0	0	0	4525		0

Appendix D

Precipitation Measurements at the Surface Level

D1. SURFACE MEASUREMENTS OF PRECIPITATION RATE AND LIQUID-WATER-CONTENT

The precipitation rate (rain rate) at the launch site of the missiles and in the nearby vicinity was measured by tipping-bucket and weighing gauges and was also determined indirectly from disdrometer instruments, as explained in R No. 1 and R No. 2. The sites of the measurements are indicated in Figure D1.

The precipitation-rate and liquid-water-content values measured by the two disdrometer instruments (Numbers 1 and 3) located at the launch site are shown by the time plots of Figures D2 and D4. The plots of the first figure pertain to the storm of 2 February 1973; those of the second figure pertain to the storm of 27 February 1973. The plots are for 3-hr periods centered approximately about the launch times of the missiles. The launch times are indicated.

The ordinate scales at the left in these figures give the precipitation rate (P), in mm hr^{-1} . The ordinate scales at the right give the liquid-water-content of the precipitation (M), in gm m^{-3} . The M and P scales are related by the power-function equations that are shown drafted at the lower right in each of the diagrams. These equations were determined from regression analyses (non-linear) that were performed on the size-distribution data acquired from the disdrometers (see R No. 1, R No. 2, and R No. 3). The equations differ somewhat, due to the different rain-rates sensed by the tipping-bucket instruments as opposed to the disdrometers.

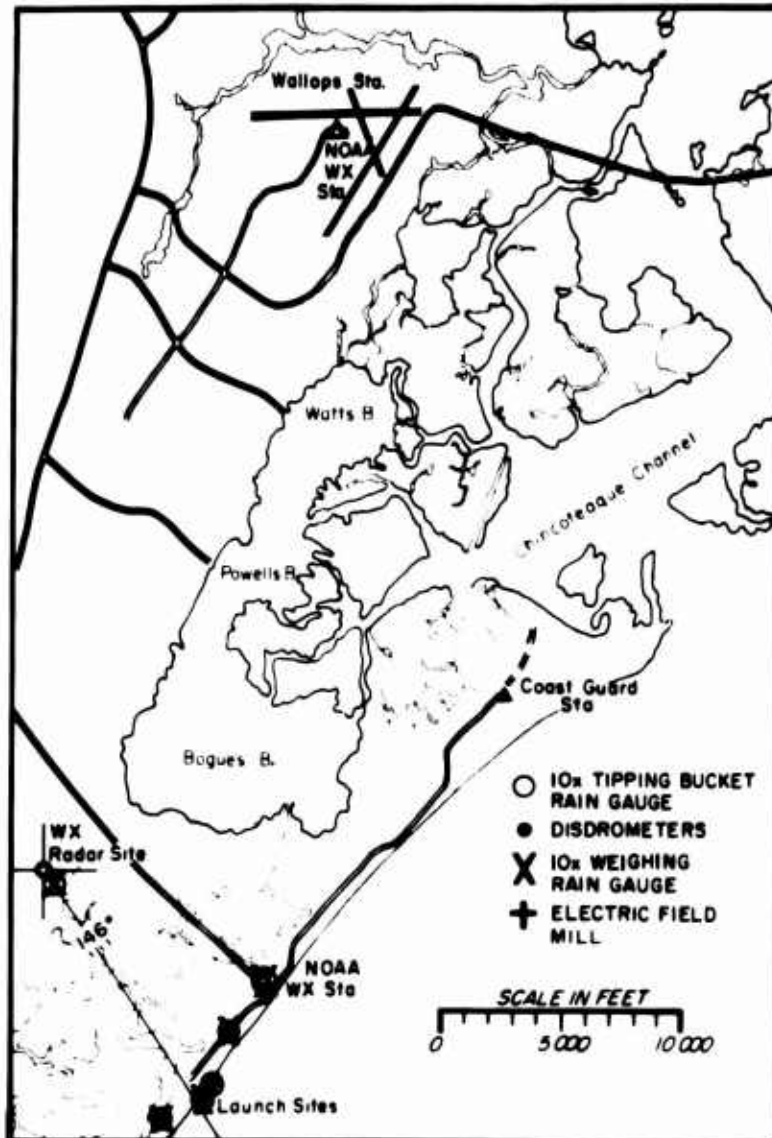


Figure D1. Map Showing Siting Locations of Rain Gauges and Disdrometers Relative to the Missile Launch Pads

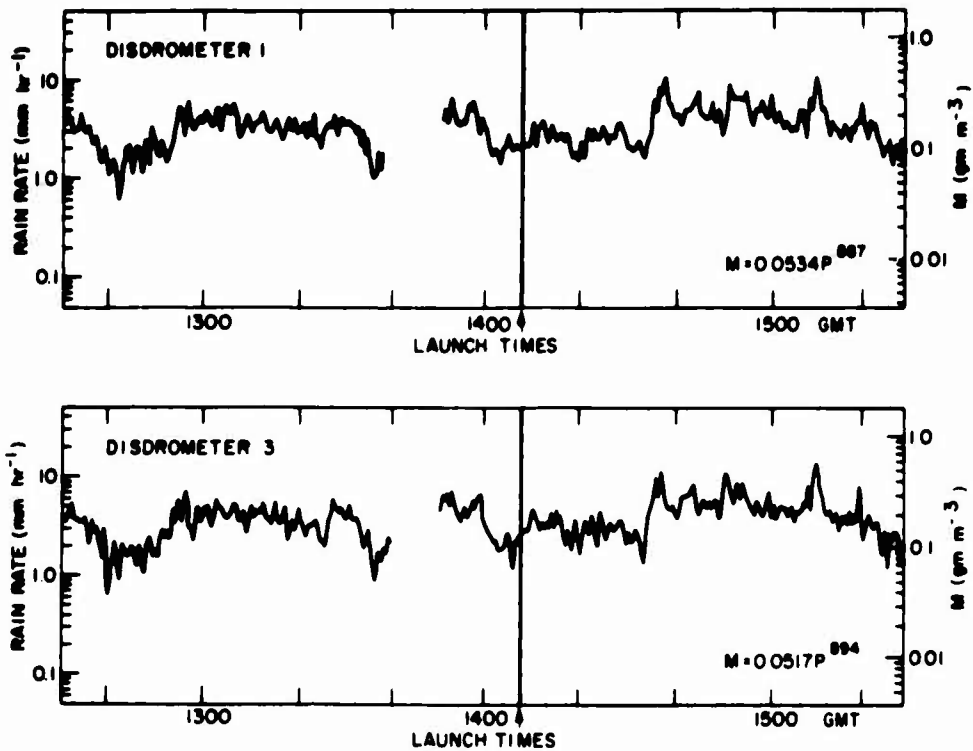


Figure D2. Time-Plots of Precipitation Rate and Liquid-Water-Content at the Surface Level for the 3-hr Period Centered About the Launch Times of the Missiles, From Disdrometer Data Acquired at the Launch Site on 2 February 1973

The precipitation rates and liquid-water-content values that were measured by (or determined from) the tipping-bucket gauges at the launch site and at the so-called "South Site" (located approximately one-half mile south of the launch site (see Figure D1)) are shown by the time plots of Figures D3 and D5. The plots of the first figure pertain to the storm of 2 February; those of the second figure pertain to the storm of 27 February. The upper diagrams in each figure show the plots for the tipping-bucket gauge located at the launch site. The lower diagrams show the plots for the gauge located at the South Site. Ordinate scales of both P and M have been drafted on these diagrams, as in the case of the disdrometer diagrams. The equations of relationship are noted. (It might be mentioned that these equations are based on the combined data for the two disdrometers at the launch site.)

* Tipping-bucket gauges were also operated at the North Site and the RARF Site shown on the map. These gauges were of a non-standard type, however, and there were associated data analysis problems. The data were never reduced to final form for presentation.

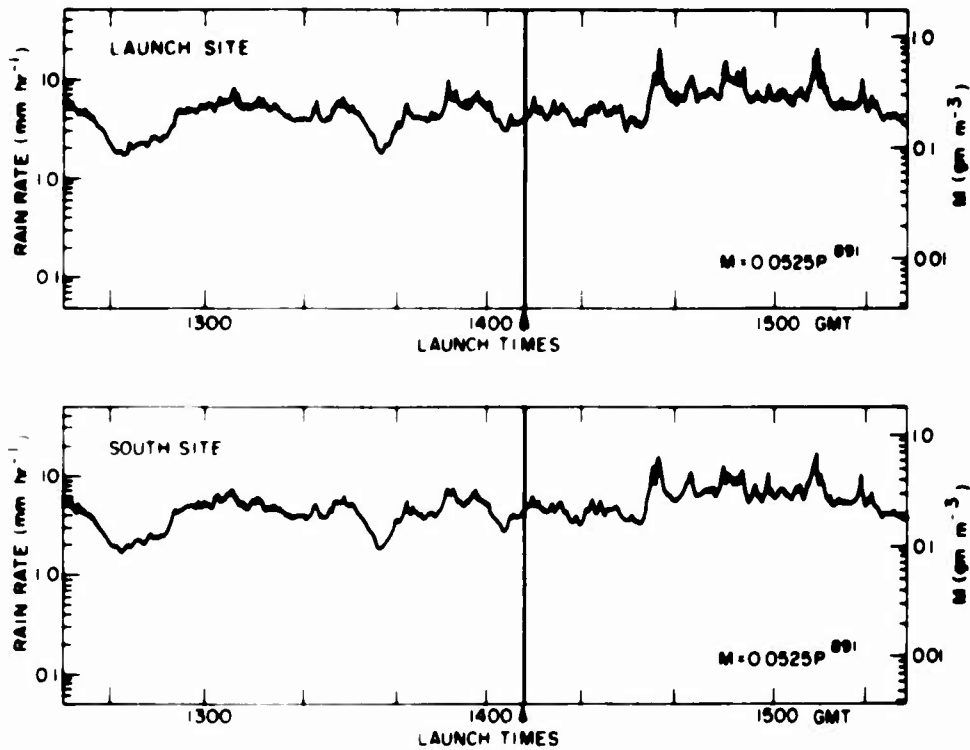


Figure D3. Time-Plots of Precipitation Rate and Liquid-Water-Content at the Surface Level for the 3-hr Period Centered About the Launch Times of the Missiles, From Tipping-Bucket Data Acquired at the Launch Site and South Site on 2 February 1973.

An examination and comparison of Figures D2 and D3, for the storm of 2 February 1973, reveals that the precipitation rates at the surface level during the period illustrated ranged generally from about 1 to 10 mm hr^{-1} . The liquid-water-contents ranged from about 0.05 to 0.40 gm m^{-3} . The figures also reveal that the precipitation rates and liquid-water-content values increased and decreased more-or-less in concert, at all gauges at both sites, throughout the measurement period. This indicates that the storm precipitation at the surface level was relatively homogeneous in its spatial characteristics, at least at horizontal scale somewhat exceeding the one-half mile spacing between the launch site and South Site gauges.

The launch site gauges at the times of the missile firings on this date (the two missiles were launched 30 sec apart) gave precipitation-rate values varying from about 2 to 4 mm hr⁻¹, with liquid-water-contents varying from about 0.1 to 0.2 gm m⁻³, depending on which of the gauge values one chooses to believe.

With regard to the Figures D4 and D5 plots for the storm of 27 February 1973, it should be explained that the disdrometer instruments at the launch site were not "turned on" until 1010 GMT, hence data were available only for the latter portion of the illustrated time period. The tipping-bucket gauges at the launch site and south site were operated throughout the total period, however.

Inspection and inter-comparison of the diagrams of Figures D4 and D5 show that the precipitation rates at the surface level during the 1-hr period centered about the launch times of the missiles (the two missiles on this day were also launched 30 sec apart) ranged generally from about 0.6 to 4 mm hr⁻¹. The liquid-water-contents ranged from about 0.03 to 0.19 gm m⁻³. The peaks and troughs of the time plots for the different gauges during this period were well correlated and the rainfall was reasonably homogeneous over the horizontal area of the two site locations. However, it is also seen from the diagrams that the precipitation rates and liquid-water-content values determined from the disdrometer instruments were substantially smaller than the tipping-bucket values from about 1130 GMT onward, during the dissipating phase of the storm when the precipitation rates were generally less than 0.5 mm hr⁻¹. The disdrometer instruments, during this phase, were apparently insensitive to the smallest of the falling raindrops and the precipitation-rate and liquid-water-content values computed from the data were, consequently, erroneously small. The disdrometer precipitation-rates were also appreciably smaller than the tipping-bucket rates during the immediate launch period of the missiles.

*The surface values of precipitation rate assumed for the trajectory computations of Tables C1 and C2, of Appendix C, were 3.9 mm hr⁻¹, for the first missile, and 4.2 mm hr⁻¹, for the second. The liquid-water-content values at the surface level for the trajectories were computed from the "Joss Widespread" equation relating M and P, see Table 2, R No. 2, which gave 0.245 gm m⁻³, for the first missile, and 0.261 gm m⁻³, for the second. The disdrometer relationships between M and P, shown in Figure D2 were not used in the trajectory computations, because disdrometer calibration problems existed that delayed the equation determinations until many months following the completion of the trajectory computations. Use of the disdrometer equations in place of the "Joss Widespread" would increase the liquid-water-content in the rain regions by approximately 35 percent.

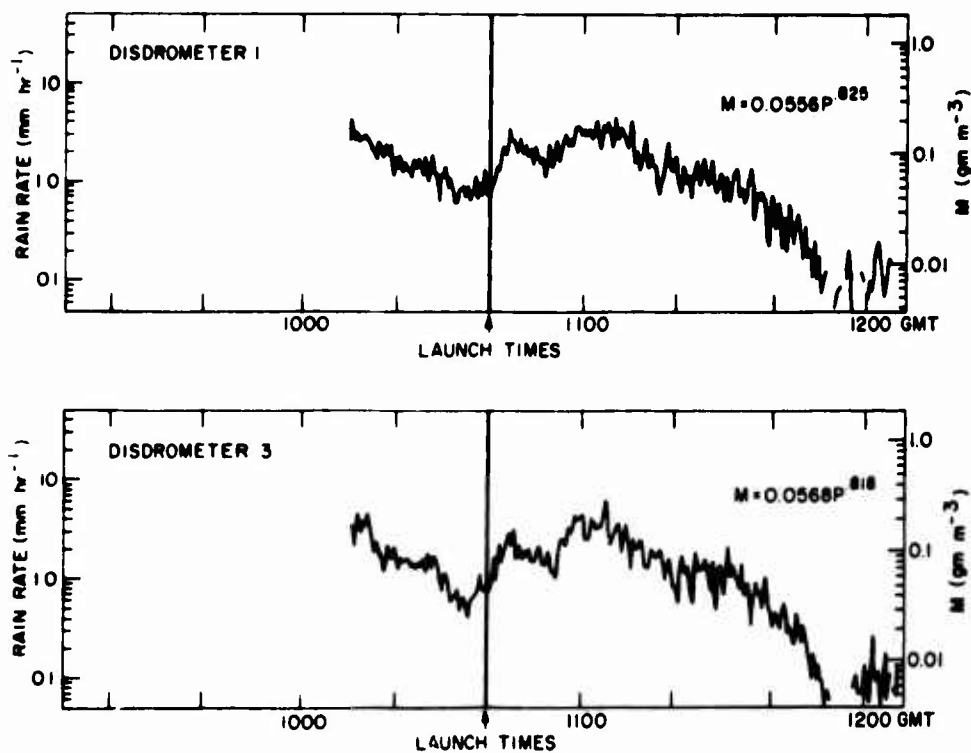


Figure D4. Time-Plots of Precipitation Rate and Liquid-Water-Content at the Surface Level for the Period 1/2-hr Prior to Launch Time to 1-1/2-hr Subsequent to Launch Time, From Disdrometer Data Acquired at the Launch Site on 27 February 1973. The disdrometer instruments were not "turned on" until 1/2 hr Before Launch Time on This Day

Thus, although the disdrometer results for 27 February 1973 are presented herein, for completeness, it should be emphasized that questions exist concerning the instrument calibrations and the accuracy and significance of the results.* (The disdrometer problems of this day were mentioned in R No. 1 and R No. 2, in the context of our inability to use the disdrometer data to secure a meaningful calibration constant for the FPS-18 radar).

*The disdrometer instruments are essentially "relative indicators" which have to be set or "calibrated" in order to provide quantitative results. There are several methods of calibration. A sensitivity check, or "electronic calibration method", is provided as part of the instrument circuitry. Water drops of known sizes can be dropped on the sensing heads of the instruments, from heights assuring terminal velocities, and the disdrometer readings of drop size can be adjusted for conformance with the actual. The total rainfall computed from the disdrometer data for a period of relatively-long duration, some 2 to 3 hr or so, can be "adjusted", by recomputation, to correspond to the total rainfall measured by the tipping-bucket gauges, and/or weighing gauges, for the same, common period. The disdrometer precipitation-rates can also be adjusted, during computations, so that the computed rates agree with the tipping-bucket rates for any given time or time interval of choice. The particular calibration method or combinations used for the data of 27 February 1973 is unknown to the author.

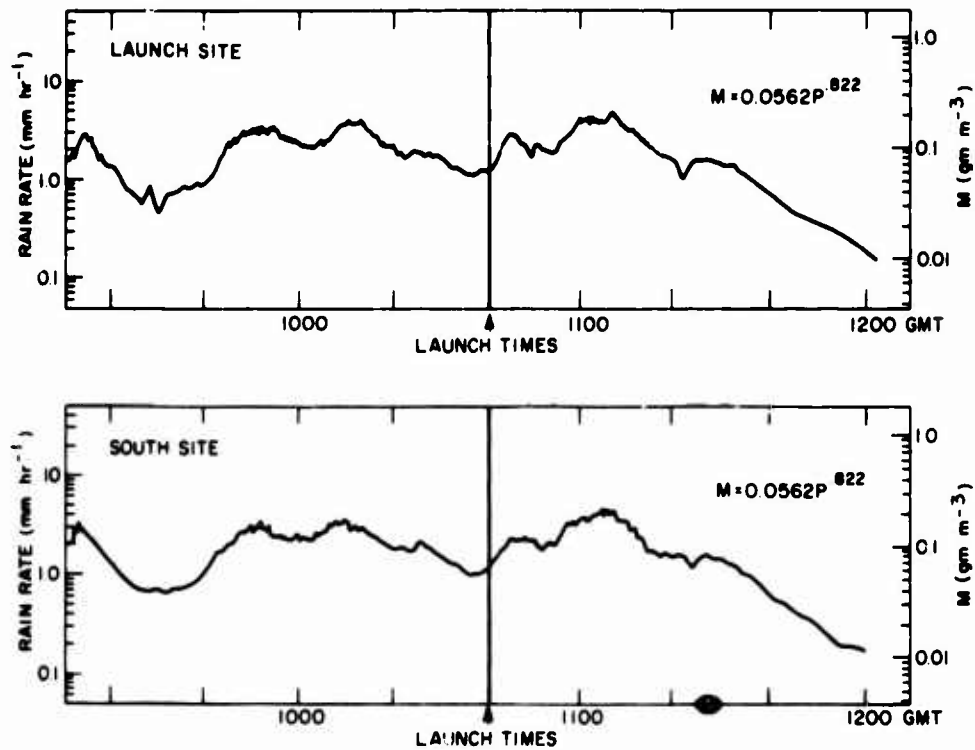


Figure D5. Time-Plots of Precipitation Rate and Liquid-Water-Content at the Surface Level for the 3-hr Period Centered About the Launch Times of the Missiles, From Tipping-Bucket Data Acquired at the Launch Site and South Site on 27 February 1973

The tipping-bucket gauge at the launch site at the firing times of the missiles on 27 February gave a precipitation rate of 1.26 mm hr^{-1} . A value of 1.3 mm hr^{-1} was used for the trajectory computations discussed in Appendix C.

D2. COMPARATIVE SIZE-DISTRIBUTION MEASUREMENTS OBTAINED ON 26 FEBRUARY 1973

The size variation of the number concentration of the raindrops recorded by the disdrometer instruments was "checked and compared", on 26 February 1973, with measurements made, at common sites and times, by a "dyed filter-paper" technique.

The rainstorm of 26 February 1973 was not a launch day for the SAMS missiles. However, the comparison data obtained on this date are quite pertinent to the SAMS objectives of accuracy and uncertainty assessment.

In the filter paper technique, which is a conventional meteorological technique, large filter-paper disks (24 cm in diameter), which are impregnated with methylene-blue powder, are exposed to the falling rain for carefully timed intervals (which vary inversely with the rainrate). The raindrops that fall on the filter paper during the exposure interval wet the paper and dissolve the methylene-blue powder at the places where they strike the paper. Thus, they leave "blue colored signatures", or patches, on the paper which can be manually sized and counted in later analyses. The general relationships between the "patch diameters" and the "physical diameters" of the raindrops have been established through various calibration studies performed in the past.⁵ The specific relationships, for the AFRL tests of 26 February 1973, were established by calibrations performed by Mr. A. A. [unclear].

The first set of comparisons were made during the rainstorm of 26 February. In the first, which was performed at the launch site, two filter papers were exposed for 15 sec each, in quick succession, during the particular time interval 1249:00 to 1249:30 EST, which corresponded to the recording interval of the two disdrometers, Numbers 1 and 3, that were located at the site and operating at the time. The two disdrometers were spaced about 4-ft apart. The filter paper samples were obtained from a location mid-way between the disdrometers. The papers were exposed at ground height in the "bottom half of a film can", the top cover of which was removed at the beginning of the exposure and replaced at the end. A 15-sec exposure of the filter paper was required because of the rainrate. This meant that two papers had to be exposed to cover the 30-sec recording interval of the disdrometers. The person who placed and exposed the paper of the second sample approached the disdrometer vicinity from the downwind side and was only briefly present, for about 1 to 2 sec, at arms length distance from the disdrometers. Thus, he did not interfere with the measurements in any material way.

The second set of comparisons was made at the South Site location during the time interval 1341:00 to 1341:30 EST. Two filter papers were exposed in the same manner described above, while the disdrometer instrument at the site was operating and recording size distribution information.

The precipitation rates for the disdrometer and filter-paper measurements at the two sites were determined for the 30-sec intervals cited previously, using methods described in R No. 1 and R No. 2. These precipitation rates are shown listed in Table D1. Also shown are the precipitation rates that were measured directly by the tipping-bucket gauges at the sites. These are the "calibrated precipitation rates" of the tipping-bucket gauges, which have been corrected for "bucket spillage as a function of rainrate". (The corrections were established by laboratory calibration of the instruments. The values are small, less than 5 percent, for rainrates below 5 mm hr^{-1}).

5. Marshall, J.S., Langille, R.C., and Palmer, W. McK. (1947) Measurements of rainfall by radar, J. Meteor. 4:186-192.

Table D1. Comparison Rainrates Determined for Two Sites and Time Intervals During the Storm of 26 February 1973

Site	Time Interval	Method of Measurement	Rainrate mm hr ⁻¹
Launch Site	30 sec (1249:00 to 1249:30 EST)	Disdrometer No. 1	1.72
		Disdrometer No. 3	1.24
		Filter Paper	2.5
		Tipping-Bucket Raingauge	2.2
South Site	30 sec (1341:00 to 1341:30 EST)	Disdrometer No. 4	1.86
		Filter Paper	4.1
		Tipping-Bucket Raingauge	3.4

It is seen, from the table, that the disdrometer rainrates at the individual sites were substantially smaller than those determined from the filter paper or measured by the tipping-bucket gauges. Comparisons of the rates for the filter-paper vs those for the tipping-bucket reveals reasonable correspondence at the launch site but appreciable difference at the south site.

Size distribution information for the disdrometers and filter-paper samples is presented in Table D2. The number concentrations of the drops are shown in the first lines of the table, which pertain to the individual samples. The number concentrations are listed in the particular diameter classes which are the "counting classes" of the disdrometer instruments. The concentrations for the filter-paper samples are listed in these same classes, for comparability.

The class contributions to the liquid-water-content and to the radar reflectivity factor are shown in the second and third lines of the table, for the individual samples. The total number concentrations of the drops, of all sizes in the populations, are presented under the column labeled " N_T ". Likewise, the total liquid-water-content, M , and the total radar reflectivity factor, Z , are listed in the columns immediately following. (It should be noted that the parameters tabulated in the last five columns will not be discussed in the present appendix. They pertain to subjects considered in Appendix E, and will be described therein).

With regard to the number concentration values shown in Table D2, it is seen that much-larger numbers of raindrops were detected by the filter papers than were recorded by the disdrometers (by a factor of 3 to a factor of 6.7). The disdrometers failed to detect the smallest drops and/or detected them in number concentrations less than were actually present. For drops from about 0.75 mm to 1.7 mm, the concentrations were roughly the same for the disdrometers and filter papers. Then, again, for drops of the largest sizes, the disdrometers generally failed to detect drops as large as were captured on the papers. There is a logical explanation for this, in that the sampling area of the filter papers ($\sim 452 \text{ cm}^2$) is some 9 times larger than the sampling area of the disdrometer instruments (50 cm^2). Hence, a greater number of the largest raindrops, which were present in the storm in relatively-small concentration, would logically be detected by the filter papers and not by the disdrometers. (Probability arguments can be advanced that these largest drops should also be detected by the disdrometers within sampling intervals that were 9 times larger than the basic 30-sec counting-interval of the instruments, that is, within a 4-1/2 min period of record. It may be reported that drops as large as detected on the filter papers were recorded on all disdrometers during the 4-1/2 min periods centered about the mid-times of the Table D2 intervals).

The disdrometer instruments and their mode of operation were described in R No. 1. In theory, the instruments have a threshold of momentum detection corresponding to that of a gravitationally-falling drop of 0.3 mm diameter.⁶ Under operational conditions, though, this "sensitivity threshold" is modified appreciably, over short term periods, at least, by the updraft-downdraft motions associated with atmospheric turbulence. The extent of such modifications, and of the turbulent effects on the instrumental sizing and counting of drops of even larger sizes, is dependent on the storm conditions of the particular day and on the locations and methods of siting the disdrometers.

With due regard to these influences, it was still apparent that the disdrometers in the tests of 26 February 1973, as the instruments were calibrated and operated on this day, had severely diminished sensitivity of number count for drop sizes smaller than about 0.75 mm. Drops smaller than this were counted, down to the 0.3 mm threshold on two of the three disdrometers, but the recorded concentrations were obviously deficient. It was equally obvious (see Table D2) that the counts of the Number 1 disdrometer at the launch site were so grossly deficient for small drops as to warrant a conclusion that the instrument was malfunctioning and inoperative.

The liquid-water-content and radar reflectivity factor values of Table D2 were derived from the number concentration data using the fall-velocity relationships for

6. Joss, J., and Waldvogel, A. (1970) Disdrometer RD 69 Instruction Manual, Marc. Weibel Dipl. Ing., ETH, Kapellenstrasse 20, 4000, Basel, Switzerland.

raindrops of Gunn and Kinzer⁷ which also appear in Table 114 of the Smithsonian Meteorological Tables (8th Edition, 1951).⁸ These are the fall-velocity relationships that are used in the "disdrometer computational program" of AFCRL, which is based on a program developed by Joss.

With reference to Table D2, it is seen that the M values determined from the filter-paper samples were about twice as large as those derived from the disdrometer data. (Disdrometer Number 1 is ignored in these comparisons, for the reasons stated above.) It is also seen that the Z values for the filter-paper were some 2 to 4 times larger than those for the disdrometers.

It might be pertinent to mention that Joss and Waldvogel⁹ have presented equations and information about the probabilities of determining the "true values" (or long-term average values) of precipitation rate, P, and radar reflectivity factor, Z, from measurements of drop size distributions in rain. The required sample sizes and probabilities vary with rainrate. For example, for a rainrate of 1 mm hr^{-1} , a sample size of $1.5 \text{ m}^2 \text{ sec}$ is required to measure a value of P that has a 0.95 probability of being within 10 percent of the true value; and a sample size of $19 \text{ m}^2 \text{ sec}$ is required to measure Z to these same probability-confidence levels. For the disdrometer instrument, with its sampling area of 50 cm^2 , this means that a measurement period of about 5 min is needed to determine P, with a 0.95 probability of 90 percent accuracy, and an approximate 1-hr period is needed to determine Z, to the same accuracy.

For a rainrate of 10 mm hr^{-1} , the sample sizes required to determine P and Z to this accuracy are 0.5 m^2 and $6.5 \text{ m}^2 \text{ sec}$, respectively. With the disdrometer, this means that a measurement period of 2 min is needed for P and a measurement period of 20 min is needed for Z.

7. Gunn, R., and Kinzer, G. D. (1949) The terminal velocity of fall for water droplets in stagnant air, J. Meteorol. 6:243(565, 594, 596-7).
8. Smithsonian Meteorological Tables, 1951: Sixth revised edition, Smithsonian Institution, Washington, D. C.
9. Joss, J., and Waldvogel, A. (1969) Raindrop size distribution and sampling size errors, J. Atmos. Sci. 26:566-569.

Appendix E

AFCRL Flights, Summary Notes and Particular Analyses, for the 1972-73 Season

The AFGL C-130A aircraft was based at Hanscom Field, Bedford, Massachusetts during the 1972-73 season. When storm conditions appropriate for SAMS operations were forecast for the Wallops area, the aircraft was flown from Hanscom Field to Wallops where: (1) it "stood by" in a holding pattern, awaiting the potential missile firing or; (2) it landed, usually either at Wallops Station, Virginia or Langley AFB, Virginia, where the flight crew awaited further instructions concerning the storm and missile launch conditions and maintained readiness for measurement sorties.

Twenty-three aircraft sorties were flown in support of SAMS during the 1972-73 season, as identified in Table E1. Flights were made in 13 potential storm situations. SAMS missiles were launched in two of the e situations, on 2 February 1973 and 27 February 1973. Measurements with the C-130A aircraft were made in the storms of 2 February. But measurements could not be made in the storm of 27 February, because of a propeller malfunction on the No. 3 engine of the aircraft.

Table E1. Dates and Times of AFGL C-130A Flights in Support of SAMS-ABRES During the 1972-73 Season. With Comments About Mission Results

Dates of Planned Missile Launches	AFGL C-130A Flight Information			Comments
	Airfield of Departure and Take-Off Time	Airfield of Landing and Landing Time	Airfield of Landing and Landing Time	
15 January 1973	Bedford, Mass. 1205 EST	Wallops Station, Va. 1358 EST	Wallops Station, Va. 1358 EST	Missile not fired.
15 January 1973	Wallops Station, Va. 1515 EST	Bedford, Mass. 1635 EST	Bedford, Mass. 1635 EST	Return flight from mission.
18 January 1973	Bedford, Mass. 0730 EST	Wallops Station, Va. 0900 EST	Wallops Station, Va. 0900 EST	Practice Mission
18 January 1973	Wallops Station, Va. 1054 EST	Bedford, Mass. 1357 EST	Bedford, Mass. 1357 EST	Return flight.
19 January 1973	Bedford, Mass. 1257 EST	Wallops Station, Va. 1445 EST	Wallops Station, Va. 1445 EST	Missile not fired.
19 January 1973	Wallops Station, Va. 1600 EST	Bedford, Mass. 1833 EST	Bedford, Mass. 1833 EST	Return flight.
22 January 1973	Bedford, Mass. 0927 EST	Wallops Station, Va. 1145 EST	Wallops Station, Va. 1145 EST	Missile not fired, flew to
22 January 1973	Wallops Station, Va. 1252 EST	Langley AFB, Va. 1507 EST	Langley AFB, Va. 1507 EST	Langley for fuel.
22 January 1973	Langley AFB, Va. 1630 EST	Bedford, Mass. 1816 EST	Bedford, Mass. 1816 EST	Return flight.
1 February 1973	Bedford, Mass. 1556 EST	Wallops Station, Va. 1632 EST	Wallops Station, Va. 1632 EST	RON at Wallops.
2 February 1973	Wallops Station, Va. 0824 EST	Langley AFB, Va. 1136 EST	Langley AFB, Va. 1136 EST	Missiles launched at 0908:00
2 February 1973	Langley AFB, Va. "	Bedford, Mass. 1513 EST	Bedford, Mass. 1513 EST	Return flight.
26 February 1973	Bedford, Mass. 1515 EST	Andrews AFB, Va. 1845 EST	Andrews AFB, Va. 1845 EST	Missile not fired, RON at Andrews.
27 February 1973	-----	-----	-----	Missiles launched at 0540:00
				and 0540:30 EST. C-130A
				unable to depart Andrews AFB,
				because of mechanical failure
				of No. 3 propeller.
15 March 1973	Bedford, Mass. 1312 EST	Langley AFB, Va. 1740 EST	Langley AFB, Va. 1740 EST	Missile not fired, RON at Langley.
16 March 1973	Langley AFB, Va. 1133 EST	Wallops Station, Va. 1208 EST	Wallops Station, Va. 1208 EST	Change of station.
17 March 1973	Wallops Station, Va. 1443 EST	Bedford, Mass. 1555 EST	Bedford, Mass. 1555 EST	Missile not fired.
20 March 1973	Bedford, Mass. 0840 EST	Wallops Station, Va. 1040 EST	Wallops Station, Va. 1040 EST	RON at Wallops Station
21 March 1973	Wallops Station, Va. 1315 EST	Bedford, Mass. 1512 EST	Bedford, Mass. 1512 EST	Missile not fired.
26 March 1973	Bedford, Mass. 1521 EST	Wallops Station, Va. 1806 EST	Wallops Station, Va. 1806 EST	Missile not fired.
26 March 1973	Wallops Station, Va. 1822 EST	Bedford, Mass. 1855 EST	Bedford, Mass. 1855 EST	Return flight.
4 April 1973	Bedford, Mass. 0923 EST	Wallops Station, Va. 1126 EST	Wallops Station, Va. 1126 EST	Missile not fired.
5 April 1973	Wallops Station, Va. 1554 EST	Bedford, Mass. 1720 EST	Bedford, Mass. 1720 EST	Return flight.
10 April 1973	Bedford, Mass. 0938 EST	Bedford, Mass. 1210 EST	Bedford, Mass. 1210 EST	Round robin flight, missile not fired.

E1. OBSERVATIONS AND DATA ACQUIRED DURING THE STORM OF 2 FEBRUARY 1973

Observations and measurements were made at 12 different flight levels in the storm of 2 February 1973. The observations and measurements of the storm conditions along the missile trajectories began at about 1410 Z, at an altitude of 32,000 ft (True Altitude, corrected from Pressure Altitude), and they were terminated at approximately 1554 Z, at an altitude of about 500 ft.

Comments about the general hydrometeor conditions at the various altitudes in the storm are presented in Table E2. These are the edited notes of the AFGL Flight Director, Lt. Col. James E. Church. (They have been edited only to delete references to non-meteorological matters, such as comments regarding navigation, positioning, radio communications, etc.)

Table E2. Flight Director's Notes Concerning the General Hydrometeor Conditions at the Different Flight Levels in the Storm of 2 February 1973. The notes have been edited to delete references to non-meteorological matters, such as navigation, positioning, radio communications, etc.

Time GMT	Altitude k ft	Remarks
1325:00	0.3	Moderate rain, 2-3 mm size on climbout.
1325:41	1.5	Below cloud base, fog below, visibility 2-1/2-3 mile slant.
1326:43	3.4	Entering new cloud now.
1328:17	6.0	Still below main cloud base, have stratus below me.
1328:29	6.2	In and out tops of stratus or stratocumulus.
1328:40	6.4	Into base of main cloud.
1328:55	7.1	Still have occasional 4-5 mm rain.
1329:02	7.3	In clear above stratus and below altostratus.
1330:12	8.	Between layers, precip. lighter now, most drops 2-3 mm.
1331:00	10.0	Getting small snow crystals hitting snow stick.
1331:06	10.2	Getting 1 mm snow crystals now, rain has stopped, getting little stellars up to 2 mm.
1331:44	10.0	In snow now.
1332:02	11.5	I see only small snow crystals, stellars, still melting but not sticking, 1-2 mm crystals, no big agglomerates hitting stick, can see agglomerates going by near spinner.

*"Flight track diagrams" for the C-130A sortie of 2 February 1973 exist at AFGL which have been related to the path trajectories of the missiles. But these are not presented because of their complexity and marginal utility.

Table E2. Flight Director's Notes Concerning the General Hydrometeor Conditions at the Different Flight Levels in the Storm of 2 February 1973 (Cont)

Time GMT	Altitude k ft	Remarks
1334:07	14.3	Still getting small ice crystals 1-2 mm, no big agglomerates, but still see big agglomerates going by spinner, not hitting snow stick, moderate intensity.
1336:11	16.5	In all snow now, small dendrites stellars 1-2 mm size.
1337:28	17.8	Getting small stellars 2-3 mm size, occasional 3 mm but seeing bigger agglomerates going by spinner, riming slight bit on leading edge of wing, all snow now.
1338:09	18.4	Still in moderate snow, small ice crystals, appear to be stellars, size decreasing, 1 mm mostly, occasional 2 mm crystals now. Still see bigger agglomerates going by spinner, but none hitting snow stick.
1339:04	19.1	Still getting very small ice crystals about 1 mm, very uniform size, agglomerates going by spinner getting smaller too.
1339:27	19.4	Crystals going to needles now or possibly columns, about 1 mm size.
1339:38	19.4	Crystals getting smaller and smaller.
1340:56	20.7	In cirrus now, crystal size 1-2 mm occasional 1 mm in size.
1341:46	21.1	Small ice crystals about 1/2 mm in size.
1342:00	21.3	We've had absolutely no turbulence.
1324:42	21.7	Light, small crystals, 1/2 mm size columns or needles.
1344:24	22.6	Clouds pretty dry up here. No riming at all on snow stick, ice crystals changing to platelets now. About 1/2 mm occasional 1 mm.
1345:25	23.6	I see agglomerates going by spinner, seeing hexagonal plates about 1/2 mm, occasional 1 mm.
1346:12	24.0	Intensity definitely tapering off on snow, crystal size very small, about 1/2 mm size average.
1347:16	25.0	Ice crystals about 1/2 mm, light intensity, no riming on stick at all. Saw 1 mm particle hit stick but most about 1/4-1/2 mm, very tiny crystals.
1348:32	25.3	Slightly bigger platelets now, about 1/2 mm size.
1349:56	26.2	Sun dimly visible. Snow size continues to decrease in size as we climb. Now down to 1/4 mm in plates.
1350:13	26.4	Less than 1/4 mm; very light intensity.

Table E2. Flight Director's Notes Concerning the General Hydrometeor Conditions at the Different Flight Levels in the Storm of 2 February 1973 (Cont)

Time GMT	Altitude k ft	Remarks
1353:48	27.8	Ice crystals still 1/4 mm size, little stellars or dendrites. No agglomerates going by spinner.
1355:56	28.7	Very tiny needles now, 1/4 mm. Still in clouds with several k ft of clouds still above.
1356:42	29.0	Getting small columns now about or less than 1/4 mm.
1359:42	30.0	Very tiny crystals, back to hexagonal platelets again, 1/4 mm size.
1405:50	30.8	Sun fairly bright. still not at cloud tops. Still in very small ice crystals.
1409:30	31.7	Still in clouds.
1410:35	32.0	Still in clouds with very small ice crystals, size about 1/10 mm and stable cloud, very smooth flying. Estimate cloud tops still 2-3 k ft above us.
1414:00	31.0	Can see halo around sun, still in clouds, ice crystals about 1/10 mm size.
1417:19	29.3	Still very tiny ice crystals, appear to be platelets. Sun is bright, lost halo, crystals very uniform size on snow stick.
1417:55	28.4	Intensity increasing but still light, uniform crystal size.
1418:08	28.0	Ice crystal size slowly increasing 1/4 - 1/2 mm size.
1418:36	27.2	Descending. Seeing hexagonal plates 1/4 - 1/2 mm size.
1419:18	26.1	Still in cirrus.
1420:35	25.5	Light intensity ice crystals, sun very dim. 1/4 - 1/2 mm size, all platelets, no agglomerates.
1423:00	25.7	Getting 1/4 - 1/2 mm ice crystals, platelets, no agglomerates.
1424:08	25.5	1/4 - 1/2 mm crystal size. Sun dimly visible above, very stable flying.
1424:50	25.1	Still in ice crystals 1/2 - 1 mm size, descending to 20 K, very uniform size, light intensity.
1425:22	24.5	Descending, 1/2 - 1 mm size, still platelets.
1426:05	22.9	1/2 - 1 mm size now, uniform crystal sizes.
1426:25	22.4	Number frequency of crystals increasing now 1/2 - 1 mm.
1426:50	21.8	Ice crystals getting bigger, about 1 mm size now, light-moderate intensity. No riming of stick. Starting to see occasional agglomerate going by now.
1427:21	21.0	Occasional agglomerate going by, 1 mm ice crystals, still appear as platelets.

Table E2. Flight Director's Notes Concerning the General Hydrometeor Conditions at the Different Flight Levels in the Storm of 2 February 1973 (Cont)

Time GMT	Altitude k ft	Remarks
1428:31	20.5	Getting light turbulence chop now, some agglomerates going by spinner, ice crystals 1 mm size.
1429:34	20.4	1 mm size, seeing needles now mixed with platelets. Agglomerates going by spinner that are larger.
1430:00	20.6	1 mm platelets now, moderate intensity, no chop now.
1431:30	20.7	Back to platelets, 1 - 1.5 mm size.
1432:00	20.6	Have three size crystals now. Most are 1 - 1.5 mm platelets, another size 2 mm much less frequent than agglomerates, 3 - 4 mm going by spinner.
1433:16	20.5	Moderate intensity crystals or size 1.5 mm, no riming of stick yet. see large agglomerates going by spinner.
1434:45	19.3	Still getting small platelets, 1 - 1.5 mm size, moderate intensity, no riming, smooth flight, see big agglomerates going by spinner, moderate intensity.
1435:19	18.5	Stick starting to rime up now.
1435:38	18.2	Moderate intensity of crystals.
1436:06	17.5	Getting into snow flake region now, picking up 2 - 3 mm agglomerates on snow stick.
1436:17	17.2	Size increasing, moderate intensity, 1 - 2 mm flakes with some agglomerates, getting into stellars and dendrites, riming on snowstick.
1436:49	16.4	No cloud drops on windshield.
1436:57	16.3	Moderate intensity, crystals 1 - 2 mm, larger in agglomerates.
1437:25	15.8	Still getting 1 - 2 mm separate crystals (flakes). No agglomerates hitting stick, 2 - 3 mm size. Much bigger agglomerates blowing by spinner.
1438:48	15.2	Definitely in snow, lots of big agglomerates, moderate to heavy intensity, 2 mm average size crystal, no real riming of stick.
1439:57	15.2	Agglomerates sizes 3 - 4 to even 5 mm sizes.
1440:00	15.2	Average size 2 mm, agglomerates from 3 - 5 mm sizes.
1441:56	15.2	Moderate-heavy in snow, 2 - 3 mm with much larger agglomerates going by 3 - 5 mm, no riming on snow stick, snow nice and dry.
1443:05	15.1	Big agglomerates going by 3 - 5 mm sizes, 2 - 3 mm sizes hitting snow stick but do not appear to be individual crystals.

Table E2. Flight Director's Notes Concerning the General Hydrometeor Conditions at the Different Flight Levels in the Storm of 2 February 1973 (Cont)

Time GMT	Altitude k ft	Remarks
1444:00	14.3	Flake sizes 2 - 3 mm.
1444:07	14.1	Starting to rime on leading edge of wing.
1444:57	12.9	Getting into heavy snow now, large agglomerates 3 - 5 mm, no snow sticking on windshield 2 - 3 mm sizes, appear to be dendrites.
1445:48	12.2	Occasional cloud top now, getting towards melting zone.
1446:20	12.2	2 - 3 mm size agglomerates, definitely not individual snow flakes now.
1447:08	11.9	2 - 3 mm size flakes, melting as they hit snow stick.
1447:43	12.1	Moderate-heavy snow agglomerates, 2 - 3 mm sizes, with bigger ones 4 - 5 mm, no rime riming, in and out cloud tops.
1449:15	12.1	Seeing dendrites, moderate intensity, across most abundant class, lot of agglomerates blowing by spinner, no liquid droplets at this altitude, all dendrites.
1450:53	11.8	Snow stick riming up, 2 - 3 mm agglomerates.
1451:40	11.1	Definite dendrites, moderate intensity, large agglomerates going by snow stick, flakes hit and melt immediately at this altitude, 2 - 3 mm average size, large ones 4 - 5 mm.
1452:19	10.5	No precip hitting windshield, in and out of clouds now.
1453:00	10.3	Now in rain.
1453:13	10.2	See large agglomerates going by at 5 - 6 mm sizes with rain, rain moderate intensity.
1453:33	10.1	Some small snow mixed with rain.
1453:51	10.1	Getting large rain drops now, size 2 - 3 mm, occasional burst of larger droplets 3 - 4 mm, some snow mixed in (10 percent), mostly rain in light cloud.
1454:29	10.1	Some light chop, drops 2 - 3 mm in rain, some riming yet.
1454:56	10.2	Bursts of rain but some small flakes.
1455:13	10.1	Occasional big rain drops, melting snow flakes 1 - 2 mm sizes, occasional 3 - 4 mm drops.
1455:44	9.9	In mixed cloud, rain and snow.
1456:15	9.9	In convective cell, moderate intensity, heavy shower, 4 - 5 mm rain, no snow.
1459:07	10.0	In showers now, light chop, large rain 4 - 5 mm drops, many more smaller 2 - 3 mm size, seeing no snow hitting stick.

Table E2. Flight Director's Notes Concerning the General Hydrometeor Conditions at the Different Flight Levels in the Storm of 2 February 1973 (Cont)

Time GMT	Altitude k ft	Remarks
1500:05	10.1	Very heavy showers, very big drops 5 - 6 mm, most rain 3 mm size, no snow.
1501:10	8.9	Continue in convective showers, 5 - 6 mm drops on windshield, or precip size 3 mm.
1501:40	8.1	Clouds very thin.
1502:02	8.1	Moderate showers, 4 - 5 mm drop size, majority of rain 2 - 3 mm drops.
1503:15	8.0	Moderate showers, 2 - 3 mm drop size predominately, occasional 3 - 4 - 5 mm drops mixed in.
1504:18	7.9	Steady rain, 2 - 3 mm size predominately.
1504:49	8.0	Occasional light chop at altitude.
1507:35	7.9	In steady moderate rain, light chop.
1508:20	8.0	Just above cloud tops, very ragged.
1508:29	8.0	Rain continues moderate intensity.
1509:00	7.9	Rain continues, (moderate rain).
1509:23	7.9	Below altostratus deck and above stratocumulus deck, no real turbulence.
1510:37	7.8	In ragged cloud.
1513:43	5.9	See broken stratus below me.
1514:00	5.9	Occasionally flicking through top of stratus.
1515:21	5.8	Moderate showers now.
1515:39	5.8	Steady rain, no turbulence, essentially between decks.
1521:48	4.2	Steady rain, down to light intensity.
1522:24	4.0	Very thin cloud, very little turbulence.
1522:30	4.0	Now in moderate showers.
1524:46	3.9	Back to light intensity precip.
1527:08	3.8	Still in light to moderate rain, uniform rain.
1528:22	3.8	Just above tops of stratus. Rain is steady, light - moderate intensity.
1533:43	1.8	Appear to be below stratus deck now.
1534:28	1.7	Light - moderate rain now, maximum drop size about 3 mm, maybe occasional 4 mm, mostly 2 mm sizes.
1537:31	1.9	Below most of stratus clouds, in light - moderate rain.

The C-130A flight of 2 February 1973 was plagued with instrumental difficulties and malfunctions involving three of the four primary cloud-physics sensors. The chloroform-formvar solution used for the replicator instrument was unavailable, hence, this instrument was not operated during the flight. The shutter on the foil-sampler instrument "froze open" at 1415 Z, during the first SAMS measurement pass at the 32,000-ft level, and the aluminum foil of the recording roll tore and separated about 6 min later. The recording system for the raindrop spectrometer instrument malfunctioned and, although the instrument itself operated properly throughout the flight, no data record was available for analysis.

The Johnson-Williams (JW) liquid-water-content meter functioned well during the flight and provided the data, concerning cloud liquid-water-contents, which were previously referenced and illustrated in Figure 5 of the main text. These data were also used in the summary tables of Appendix G, Tables G2 and G3.

E2. ANALYSES OF FOIL REPLICATOR DATA

Two types of analyses were performed on the useable portion of the foil replicator record (obtained before the foil broke). The first was performed on the "ascent portion" of the record to establish the maximum sizes of the snow and ice particles that were present in the storm at the different altitudes, also to estimate the approximate number concentrations of the particles, when possible. Independent analyses were performed by two, skilled persons, to determine if subjective differences existed and to assess their nature.¹⁰ The analyses were performed directly on the foil record using a "measuring magnifier". About three man days of time was required by each analyst. The data results are shown in Table E3. Summary information is presented in the table concerning the "snow stick observations" of the flight director. The sampling volumes are also listed in the table. These are large, compared to normal sampling volumes for aircraft instruments, but are still very-small, relative to the atmospheric volumes observed by the RARF radars used for SAMS.

*The aircraft ascended over the "holding pattern location" (about 20 to 35 miles SE of Wallops). The foil-sampler instrument was "turned on" during ascent at approximately 1331 Z, at the 11,000-ft level, and the aircraft reached its maximum flight altitude, of 32,000 ft, at about 1410 Z. The "ascent portion" of the foil record, mentioned above, was obtained during this period, which was somewhat prior to, and including, the times of the missile launchings. The storm on this day was quite homogeneous (see Appendices A and B), therefore, the foil data obtained over the holding area are probably representative of the general storm conditions over the launch area.

10. Church, J. F., Pocs, K. K., and Spatola, A. A. (1975) The Continuous Aluminum-Foil Hydrometeor Sampler; Design, Operation, Data Analysis Procedures and Operating Instructions, AFCRL-TR-75-0370, Instrumentation Papers No. 235.

Table E3. The Sizes, by Altitude Layer, of the Ten Largest Snow or Ice Particles Measured by Two Analysts, A1 and A2, From the Foil Record of the "Ascent Portion" of the C-130A Sortie of 2 February 1973. The largest particle sizes observed from the "snow stick" are also indicated and the ice-crystal type is noted. The average particle sizes measured by the separate analysts are listed, as are the approximate number concentrations of the largest particles

Sizes of Largest Measured or Observed Particles mm	Altitude Range of Measurements or Observations												Storm Top Altitude		
	11,000 to 14,000 ft	14,000 to 17,000 ft	17,000 to 20,000 ft	20,000 to 23,000 ft	23,000 to 26,000 ft	26,000 to 29,000 ft	29,000 to 32,000 ft	Storm Top Altitude							
	Foil A1	S.S. A2	Obs	Foil A1	S.S. A2	Obs	Foil A1	S.S. A2	Obs	Foil A1	S.S. A2	Obs	Foil A1	S.S. A2	Obs
	6.0 5.5 2	5.5 5.5	5.5 5.5	5.0 6.0 2*	5.5 5.5	5.5 5.5	3.5 4.0 2*	3.0 3.5	3.0 3.5	1.0 2.2 1*	1.2 2.5 .5	1.4 2.0 1*	1.4 2.0 1*	1.2 2.0	1.2 2.0
	5.5 5.5	5.5 5.5	5.5 5.5	5.5 5.5	5.5 5.5	5.5 5.5	3.0 3.5	3.0 3.5	3.0 3.5	1.0 2.2 1*	1.0 2.2 1*	1.0 2.2 1*	1.0 2.2 1*	1.0 2.2 1*	1.0 2.2 1*
	5.5 5.5	5.5 5.5	5.5 5.5	5.5 5.5	5.5 5.5	5.5 5.5	3.0 3.5	3.0 3.5	3.0 3.5	1.0 2.2 1*	1.0 2.2 1*	1.0 2.2 1*	1.0 2.2 1*	1.0 2.2 1*	1.0 2.2 1*
	6.0 7.0	6.0 6.5	6.0 5.0	6.0 5.0	6.0 5.0	6.0 5.0	2.5 3.0	2.5 3.0	2.5 3.0	1.0 2.2 1*	1.0 2.2 1*	1.0 2.2 1*	1.0 2.2 1*	1.0 2.2 1*	1.0 2.2 1*
	6.0 6.5	6.0 6.5	6.0 6.5	6.5 5.0	6.5 5.0	6.5 5.0	3.0 3.0	3.0 3.0	3.0 3.0	1.0 2.2 1*	1.0 2.2 1*	1.0 2.2 1*	1.0 2.2 1*	1.0 2.2 1*	1.0 2.2 1*
	5.5 6.0	5.5 6.0	5.5 6.0	5.5 5.0	5.5 5.0	5.5 5.0	3.0 3.0	3.0 3.0	3.0 3.0	1.0 2.2 1*	1.0 2.2 1*	1.0 2.2 1*	1.0 2.2 1*	1.0 2.2 1*	1.0 2.2 1*
	7.0 5.5	6.0 5.5	6.0 4.0	5.5 4.5 3*	5.5 4.5	5.5 4.5	3.0 3.0	3.0 3.0	3.0 3.0	1.0 2.2 1*	1.0 2.2 1*	1.0 2.2 1*	1.0 2.2 1*	1.0 2.2 1*	1.0 2.2 1*
	6.0 5.5	6.0 5.5	6.0 5.5	6.0 4.0	6.0 4.0	6.0 4.0	3.0 2.8 2*	3.0 2.8 2*	3.0 2.8 2*	1.0 2.2 1*	1.0 2.2 1*	1.0 2.2 1*	1.0 2.2 1*	1.0 2.2 1*	1.0 2.2 1*
	6.5 5.5	6.5 5.5	6.5 5.5	6.5 4.0	6.5 4.0	6.5 4.0	3.0 2.8	3.0 2.8	3.0 2.8	1.0 2.2 1*	1.0 2.2 1*	1.0 2.2 1*	1.0 2.2 1*	1.0 2.2 1*	1.0 2.2 1*
	6.2 5.0	6.2 5.0	6.2 5.0	6.0 4.0	6.0 4.0	6.0 4.0	3.0 3.2	3.0 3.2	3.0 3.2	1.2 2.2	1.1 2.2	1.1 2.1	1.1 2.1	1.1 2.1	1.1 2.1
Ave. Largest Size mm															
Sample Volume m ³	20	25	30	35	45	60	60	60	60	60	60	60	60	60	60
Approx. Number Concentration No. m ⁻³ mm ⁻¹	.1-.3	.1-.3	.1-.3	.1-.3	.2-.5	.2-.5	.2-.5	.2-.5	.2-.5	.2-.5	.2-.5	.2-.5	.2-.5	.2-.5	.2-.5

* Crystal aggregates larger than the size indicated were observed passing by the aircraft spinner and/or on the spectrometer instrument.

It is seen that the snow aggregates in the lowest altitude layer of the table, between 11,000 and 14,000 ft, had sizes (physical sizes) as large as 7.5 mm and that the maximum particle sizes generally decreased upward from this altitude layer to the storm top level. The table reveals that the separate analysts differed substantially in their measurements of the maximum sizes in the altitude range from 20,000 to 32,000 ft. The table also shows that the maximum sizes observed on the "snow stick" were appreciably smaller than those measured from the foil. This is to be anticipated, since the "sampling volume" of the snow stick (the air volume that "impinges" on the snow stick, the contained particles of which are observed by the human eye during its "intensity interval") is considerably smaller than that of the foil sampler instrument. It should be noted that larger-size particles, than observed on the snow stick, were frequently seen passing in front of the "black background" of the aircraft spinners (the propeller hub assemblies) and/or were detected by the spectrometer instrument of the C-130A aircraft. These instances are indicated in Table E3 by the asterisks.

In the second type of analysis performed on the foil record, four particular samples of the record were selected for the SAMS measurement portion of the flight (following the missile firings). The sample times and altitudes are noted in Tables E4 and E5. The portions of the foil record containing the selected samples were photographically enlarged and printed using optimum contrast lighting and processing. The magnification varied but ranged from 6× to 6.5×. For three of the samples, those of Table E4, the numbers of the ice particle impressions shown on the prints were counted in size-classes of the largest particle dimension. For two of the samples (one common), those of Table E5, the numbers of the particles were counted in size-classes of the average particle dimension, which was an average of the length and breadth dimensions of the particle images shown on the prints. (The 1416:48 Z sample for the 30,000 ft level was "counted both ways", hence, the data for this sample as counted by the first method are shown in Table E5). Subjective allowance was made in the analyses for the differences between the images of the "dent sizes" of the particles and their "physical sizes". It might additionally be noted that the minimum particle size that could be reliably and consistently counted by the analyst was about 0.2 mm; the absolute threshold of size detectability was about 0.05 mm. Approximately two man weeks of photographic and analytic effort were required to obtain the presented data.

Table E4. Number Concentration of Ice Particles as Counted in Classes of Maximum Particle Dimension, for Three Foil Samples Obtained on 2 February 1973

Maximum Particle Dimension mm	Sample No. 1 1407:00 Z --- 30,800 ft Foil Speed = .868 cm sec ⁻¹ Acft. Speed = 118.6 m sec ⁻¹ Sample Volume = .0521 m ³		Sample No. 3 1416:48 Z --- 30,000 ft Foil Speed = .868 cm sec ⁻¹ Acft. Speed = 112.5 m sec ⁻¹ Sample Volume = .0494 m ³		Sample No. 4 1418:45 Z --- 26,900 ft Foil Speed = .868 cm sec ⁻¹ Acft. Speed = 110.0 m sec ⁻¹ Sample Volume = .0483 m ³	
	No. of Particles per 1 cm ² of Foil	No. of Particles per m ³	No. of Particles per 1 cm ² of Foil	No. of Particles per m ³	No. of Particles per 1 cm ² of Foil	No. of Particles per m ³
< .039	---	---	3	61	---	---
.039 to .116	2	38	28	567	8	166
.116 to .192	26	490	128	2591	17	352
.192 to .270	48	921	86	1741	18	373
.270 to .346	98	1881	73	1478	36	745
.346 to .426	77	1478	19	385	23	476
.426 to .500	77	1478	32	648	38	787
.500 to .578	39	740	5	101	6	124
.578 to .655	35	672	9	182	22	455
.655 to .731	5	96	1	20	7	145
.731 to .809	7	134	1	20	9	186
	N _T = 7946 m ⁻³		N _T = 7794 m ⁻³		N _T = 4079 m ⁻³	
	√N _T = 89.1		√N _T = 88.3		√N _T = 63.9	
	F = .695		F = .502		F = .570	
	k = .0325		k = .0232		k = .0191	

Table E5. Number Concentration of Ice Particles as Counted in Classes of Average Particle Dimension, for Two Foil Samples Obtained on 2 February 1973

Average Particle Dimension mm	Sample No. 2 1412:54 Z --- 32,000 ft Foil Speed = .868 cm sec ⁻¹ Acft. Speed = 116.4 m sec ⁻¹ Sample Volume = .0511 m ³		Sample No. 3 1416:48 Z --- 30,000 ft Foil Speed = .868 cm sec ⁻¹ Acft. Speed = 112.5 m sec ⁻¹ Sample Volume = .0494 m ³	
	No. of Particles per 1 cm ² of Foil	No. of Particles per m ³	No. of Particles per 1 cm ² of Foil	No. of Particles per m ³
< .040	23	450	41	830
.040 to .121	50	978	75	1518
.121 to .202	132	2583	157	3178
.202 to .283	70	1370	70	1417
.283 to .365	42	822	28	567
.365 to .446	5	98	4	81
.446 to .526	3	59	2	40
		$N_T = 6360 \text{ m}^{-3}$	$N_T = 7631 \text{ m}^{-3}$	
		$\sqrt{N_T} = 79.7$	$\sqrt{N_T} = 87.4$	
		F = .572	F = .529	
		k = .0239	k = .0242	



The "actual count" data for the foil samples are listed in the left hand columns of Tables E4 and E5, under the identified sample headings. The normalized number concentrations of the ice particles, per counting class, per cubic meter of atmospheric volume, are shown in the right hand columns. The total, normalized numbers of the particles, N_T , are also shown. The normalizations were accomplished through knowledge of the volumes of air, containing particles, that impinged on the sample areas of the foil during their exposure to the airstream of the aircraft. (The "sample volume", in other words, is the product of sample-area times airspeed times exposure interval. A correction for the "aerodynamic collection efficiency", of the sensing-probe-of-the-foil-sampling-instrument for ice particles of the different sizes, should also be applied, but was not, because of lack of knowledge.)

It is seen from Tables E4 and E5 that the total number concentrations of the ice particles ranged from about 4100 to 8000 per cubic meter. It is also seen that the maximum dimensions of the largest particles of Table E4 are somewhat smaller than the maximum sizes reported in Table E3. This is to be anticipated, since the sample volumes of the Table E3 samples are much smaller (by a factor of 200, or so) than the average "per particle" volumes of Table E4.

With regard to Sample No. 3, of Tables E4 and E5, it may be noted that the sizes of the particles, as measured in terms of their maximum dimensions, span a range that is about twice that for the particles sized according to their average dimensions. This might be indicative that the particles that "hit the foil" were generally "elongated particles", as opposed to symmetrical particles. However, a close inspection of the original foil records and photographs reveals that, at least for three of the four samples, the direction of elongation was preferentially "along the direction of the foil strip", rather than across the strip. This suggests possible instrumental-analytical problems of the types indicated below.

* The revolving drum of the foil-sampler instrument, ¹⁰ upon which the foil rests as it is carried past the opening exposed to the airstream, has "lathe-turned ridges" around its circumference which are spaced 0.25 mm apart and which serve to "elevate the foil" and provide "denting space" for the particles that impact. When particles strike the foil at aircraft speeds, it is suspected that the resulting dents in the foil are extended preferentially along the circumferal "troughs" between these ridges. For large particles, the circumferal elongation would be relatively slight, compared with the orthogonal dimensions of the dents. But, for small particles, such as ice crystals, the distortion might conceivably be rather substantial. It might also be noted that the aluminum foil itself, when manufactured and during its passage through the instrument, has, or develops, various scratches and lines that are predominantly oriented in the direction of the strip, rather than crossways. The presence of such scratches and lines on the foil complicate the dimensional determinations for small particles (the dents of which are very difficult to see on the foil and assess). A careful analyst, irrespective of these problems, can usually judge the true particle dimensions fairly well, if he works on the original foil record and uses various magnifying devices and lighting from different angles. With a photographic print of the foil, however, the analyst loses an appreciable amount of his judgement ability, since particular contrasts, exposures, shadows, illumination angles, etc. have been incorporated into the print, once and for all, in the photographic processing.

The sample data of Tables E4 and E5 were further employed to estimate, by different comparative methods, the distributed and total values of the liquid-water-content (M), and radar reflectivity factor (Z) of the ice particles. It will be instructive to describe these methods and results in some detail. We will then summarize and draw conclusions.

It may be noted initially that three assumptive steps are required in any estimates of M (or Z) from particle-size data concerning ice crystals. First, it is necessary to know or assume the type (three-dimensional shape) of the ice crystals that are present in the storm at the given altitude. Furthermore, even if measurements or observations indicate that a given type crystal is occasionally present in a population, or is present only in certain size ranges, it is necessary to assume that all the crystals of the population have the same, common shape. Second, it is necessary to estimate the probable, or typical, length, breadth and thickness dimensions of the crystals of the particular type. Third, it is necessary to estimate the effective water-density of the ice-air mixture contained within the volume defined by these dimensions such that the water-mass of the crystals can be assessed. These are the three essential assumptions. Additionally, it is conventional to compute the "equivalent melted diameters" of the crystals corresponding to the water-mass values. From this point on, the determination of the distributed and total values of M and Z is straightforward, as will be demonstrated later herein.

Previous investigators have made a variety of assumptions about how the geometry and/or density of different ice-crystal types might best be approximated. These assumptions, in general, are based on theoretical reasoning applied to experimental data. Such work has been reported by Auer and Veal, Heymsfield and Knollenberg and Kajikawa, for example. 11, 12, 13

As concerns our estimations herein, we therefore have various choices about which literature methods and results we might wish to employ. We elected to follow the work of just two investigations, however, for reasons that are explained below.

For the storm of 2 February 1973, we are primarily interested in two different types of ice crystals. We are interested in the platelet type of crystals, because (see Tables E2 and E3) this was the observed crystal type in the upper portion of the storm above 26,000 ft. We are also interested in the bullet-columnar-rosette type of crystal, because this is the type that has been implicitly assumed, to date,

11. Auer, A., and Veal, D. (1970) The dimensions of ice crystals in natural clouds, J. Atmos. Sci. 27:919-926.
12. Heymsfield, A. J., and Knollenberg, R. G. (1972) Properties of cirrus-generating cells, J. Atmos. Sci. 29(7):1358-1366.
13. Kajikawa, M. (1972) Measurement of falling velocity of individual snow crystals. J. Meteor. Soc. Japan, 50:577-584.

for all of the AFCRL computations (from radar data) of the liquid-water-content for the SAMS missile paths through the ice-crystal regions of the Wallops storms.

It is convenient, for illustration, first to consider ice crystals of the bullet-columnar type and reference the work of Heymsfield and Knollenberg.¹² Then we will consider columnar crystals, and also platelets, referencing the work of Kajikawa.¹³ It should be reiterated that these investigators are merely two of many who have reported crystal studies in the literature; however, they are regarded as "typical studies".

Heymsfield and Knollenberg¹² found that for bullet crystals with length $l \geq 0.3$ mm, the width of the crystal w was related to the length as

$$w = 0.185 l^{0.53} \text{ mm.} \quad (\text{E1})$$

They also stated that the water-density of the crystals (in cirrostratus at temperatures $\leq -22^\circ\text{C}$) was related to the length as

$$\rho = 0.81 l^{-0.054} \text{ gm cm}^{-3} \quad (\text{E2})$$

and that the mass of the bullet crystals (nearly the same for columnar crystals) was given by

$$m = 1.65 \times 10^{-5} l^{1.74} \text{ gm m}^{-3}. \quad (\text{E3})$$

The data supporting these equations were presented earlier by Heymsfield.¹⁴ The data reveals considerable scatter.

* In the AFCRL analyses of the radar data for the SAMS missile trajectories through the ice-crystal regions of the Wallops storms, we have been forced to assume that the ice-crystals were of the bullet-columnar-rosette type (rosettes are combinations of bullets or columns). This was because, as discussed in R No. 2, the only available equation relating the measured values of the radar reflectivity factor in ice crystals to the liquid-water-content of the crystals is an unpublished equation of Cunningham which is based on certain aircraft-measurement data for the bullet-rosette type of crystals that were obtained by A.J. Heymsfield, while at the University of Chicago. The equation was deemed to be the only one appropriate for SAMS application, since it stemmed from aircraft data, rather than surface data. The use of this equation, in the SAMS storm analyses, implicitly presumes that the ice crystals are of the bullet-rosette type, irrespective of whatever the observed type might be.

14. Heymsfield, A. (1972) Ice Crystal Terminal Velocities, Technical Note No. 41, Cloud Physics Laboratory, Department of the Geophysical Sciences, University of Chicago.

With the mass of the bullet (or columnar) crystal defined by Eq. (E3), it follows that the equivalent-melted-diameter of such crystals is related to the length of the crystals as

$$D_e = 0.316 l^{0.58} \text{ mm.} \quad (\text{E4})$$

This equation is shown plotted in Figure E1.

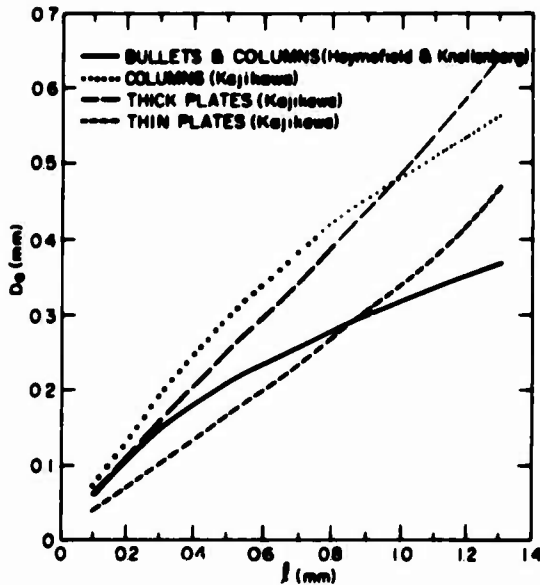


Figure E1. The Relationship, for Different Crystal Types, Between the Length Measures Defined by Heymsfield and Knollenberg¹² and Kajikawa¹³ and the Equivalent-Melted-Diameters

Kajikawa¹³ has presented a contrasting relationship for columnar type ice-crystals, in which the dimensional length of the "c axis" of the columns (the length of the axis of symmetry) is related to the equivalent-melted-diameter. This relationship is also shown plotted in Figure E1. Kajikawa additionally presented relationships for platelet-type crystals, which, as mentioned, was the observed crystal type on 2 February 1973. He presented relationships for thick-hexagonal-plates and thin-hexagonal-plates, in which the "diameter" of the plates is related to the equivalent-melted-diameter. Both of these relationships are also illustrated in Figure E1. It was impossible to distinguish between thick and thin plates from the snow-stick observations of 2 February; hence, the actual crystals could have been either, or some combination.

We can use these relationships of Heymsfield, Knollenberg, and Kajikawa^{12, 13} to determine the equivalent-melted-diameters of the ice particles of the four foil samples cited earlier. The principal problem is to establish an equivalence

between the size measured obtained from the analyses and the measures defined by these authors.

Ice crystals of the regular geometric types under discussion (bullets, columns, plates) will tend to fall gravitationally through a static atmosphere with preferential orientation. When entering the sensing orifice of the foil sampling instrument, however, it is logical to suspect that the crystals would be "tumbled" by the "streamline divergence" around the sensing probe, such that the crystals would impinge on the foil with a variety of orientations, probably of random type. If this is true, the signatures of the crystals, left on the foil in the form of dent impressions, would not be directly, or easily, relatable to the geometric dimensions of the individual crystals, which are the size measures used by the theorists and experimentalists. Probability considerations are involved which cannot be defined without full and complete knowledge of the nature of the ice crystal population in the atmosphere and of the aerodynamic flow field around the aircraft sensing probe. (We are at an impasse regarding the first requirement, because, if we knew the nature of the ice-crystal population, we would not need the foil sampling instrument, but would, instead, use the instrument that provided such knowledge.)

Because of our inabilities to specify how the ice-crystals might "tumble", or "tilt", as they enter the sensing probe of the aircraft, we are left with no choice but to assume that the length and/or breadth dimensions of the ice-crystal signatures measured from the foil record can, somehow, be related to the particular dimensions of the individual crystals, as defined by Heymsfield, Knollenberg, and Kajikawa, for example. We make this assumption and presume that we might be able to establish the rough bounds of possibility, first, by relating the maximum signature lengths measured from the foil to the length measures of the above authors and, second, by relating the average signature dimensions from the foil to the length measures of these authors.

If the maximum particle dimensions of the foil samples of Table E4 are assumed to be identifiable with the length measures of Heymsfield, Knollenberg, and Kajikawa, for bullet-columnar crystals, and with the diameter measure of Kajikawa, for thick plates and thin plates, then the data of Table E4 can be converted through use of the curves of Figure E1, to the data shown in the upper part of Table E6, which lists the number concentrations of the ice particles in size classes of equivalent-melted-diameter. In contrast, if the average particle dimensions of the foil samples of Table E5 are assumed to be identifiable with the length measures of these authors, the Table E5 data can be converted to that shown in the lower part of Table E6. (It should be mentioned that "normalization adjustments" were performed on the Table E4 and E5 data to convert to the common class diameters of Table E6. Such normalizations were necessary to permit the comparison of the table results, between samples and between the different ice-crystal types.)

Table E6. Distributions of Ice-Particle Number-Concentration for Different Sizing Methods, Different Samples, and Different Assumptions About Ice-Crystal Type and Analytical Procedures

Method of Sampling From Pool	Sample No.	Assumed Ice-Crystal Type	Investigator Procedure Used	D _v Equivalent Melting Diameter, μm											N _T m^{-3}			
				.025	.075	.125	.175	.225	.275	.325	.375	.425	.475	.525		.625	.675	
Max. Dip en.	1	Bullets & Col. Collarins	Hevys A. Knoll, Kulkawa	23	415	1628	3327	2341	212									7946
Max. Dip en.	1	Thin Plates	Hevys A. Knoll, Kulkawa	15	203	680	1596	1946	1920	1040	436	110						7946
Max. Dip en.	1	Thin Plates	Hevys A. Knoll, Kulkawa	23	415	1298	2421	2055	1014	553	167							7946
Max. Dip en.	3	Bullets & Col. Collarins	Hevys A. Knoll, Kulkawa	5	2305	2736	1638	683	37									7794
Max. Dip en.	3	Thin Plates	Hevys A. Knoll, Kulkawa	5	2305	2476	1473	703	188	146	27							7794
Max. Dip en.	3	Thin Plates	Hevys A. Knoll, Kulkawa	1588	3335	1650	433	115	13									7794
Max. Dip en.	4	Bullets & Col. Collarins	Hevys A. Knoll, Kulkawa	73	204	435	1152	1141	676	227	27							4079
Max. Dip en.	4	Thin Plates	Hevys A. Knoll, Kulkawa	62	174	411	400	283	682	580	513	275	224	75				4079
Max. Dip en.	4	Thin Plates	Hevys A. Knoll, Kulkawa	77	283	435	838	663	653	384	277	216	130	63	46	11		4079
Max. Dip en.	4	Thin Plates	Hevys A. Knoll, Kulkawa	224	666	1186	405	542	258	182	70	46						4079
Ave. Dip en.	2	Bullets & Col. Collarins	Hevys A. Knoll, Kulkawa	1007	2270	2143	841	53										6360
Ave. Dip en.	2	Thin Plates	Hevys A. Knoll, Kulkawa	806	1368	2201	1268	608	96	13								6360
Ave. Dip en.	2	Thin Plates	Hevys A. Knoll, Kulkawa	1007	2270	2040	917	108	72									6360
Ave. Dip en.	2	Thin Plates	Hevys A. Knoll, Kulkawa	2068	3436	792	44											6360
Ave. Dip en.	3	Bullets & Col. Collarins	Hevys A. Knoll, Kulkawa	1688	2970	2384	503	76										7631
Ave. Dip en.	3	Thin Plates	Hevys A. Knoll, Kulkawa	1382	1887	2637	1221	426	73									7631
Ave. Dip en.	3	Thin Plates	Hevys A. Knoll, Kulkawa	1688	2970	2254	660	84	15									7631
Ave. Dip en.	3	Thin Plates	Hevys A. Knoll, Kulkawa	3172	3870	557	30											7631

From Table E6, it is seen that substantial differences in the spectral distribution of the number concentrations of the ice particles of the samples occur in association with the different assumptions that are made about the ice-crystal type, with the different literature treatments of common crystal types (that is, Heymsfield and Knollenberg bullets and columns vs Kajikawa columns) and with the different methods of assessing the particle sizes from the foil signatures and associating these dimensions with the particular ones of the cited authors. It is also seen that the total number concentrations of the particles in the samples are unchanged from those of Tables E4 and E5. This must be true, of course, since the re-classification of the particles in classes of equivalent-melted-diameter does not affect the total number concentration.

The number concentration data of Table E6 are readily converted into the corresponding, higher-moment distributions of liquid-water-content, M , and radar reflectivity factor, Z . The liquid-water-content for any given size class of Table E6 data is given by

$$M_{c_i} = \frac{\pi \cdot 10^{-3} \rho N_i D_{e_i}^3}{6} \text{ gm m}^{-3} \quad (\text{E5})$$

where N_i is the number concentration of the ice crystals in the given class, in m^{-3} ; D_{e_i} is the mid-equivalent-melted-diameter of the class, in mm; and ρ is the density of liquid water, equal to 1.0 gm cm^{-3} . The total liquid-water-content, for all size classes of the distribution, is then given simply by

$$M = \sum_{i=1}^{i=n} M_{c_i} \text{ gm m}^{-3}, \quad (\text{E6})$$

where n is the total number of the classes.

Likewise, the class values of the radar reflectivity factor are given by

$$Z_{c_i} = N_i D_{e_i}^6 \text{ mm}^6 \text{ m}^{-3}, \quad (\text{E7})$$

and the total reflectivity factor is

$$Z = \sum_{i=1}^{i=n} Z_{c_i} \text{ mm}^6 \text{ m}^{-3}. \quad (\text{E8})$$

The distributed and total values of M corresponding to the number concentration data of Table E6 are presented in Table E7. The distributed and total values of Z are presented in Table E8.

Table E7. Distributions of Ice-Particle Liquid-Water-Contents for Different Sizing Methods, Different Samples, and Different Assumptions About Ice-Crystal Type and Analytical Procedures

Method of Sizing from Foil	Sample No.	Assumed Ice-Crystal Type	Investigator Procedure Used	D _e Equivalent-Melted-Diameter, μm															Total LWC gm m ⁻³		
				.025	.075	.125	.175	.225	.275	.325	.375	.425	.475	.525	.575	.625	.675				
Max. Dimen.	1	Bullets & Col.	Hevms & Knoll.	0	0	0.0017	0.0093	0.014	0.023												0.97
Max. Dimen.	1	Columns	Knikawa	0	0	0.0007	0.0045	0.012	0.021	0.010	0.012	0.0044									0.73
Max. Dimen.	1	Thin Plates	Knikawa	0	0	0.0013	0.0068	0.012	0.011	0.0090	0.0046										0.46
Max. Dimen.	3	Bullets & Col.	Hevms & Knoll.	0	0	0.0028	0.015	0.041	0.004												0.12
Max. Dimen.	3	Columns	Knikawa	0	0	0.003	0.024	0.051	0.082	0.034	0.030	0.007									0.25
Max. Dimen.	3	Thin Plates	Knikawa	0	0	0.005	0.025	0.01	0.047	0.020	0.026	0.008									0.11
Max. Dimen.	4	Bullets & Col.	Hevms & Knoll.	0	0	0.009	0.017	0.04	0.001												0.048
Max. Dimen.	4	Columns	Knikawa	0	0	0.001	0.005	0.032	0.068	0.074	0.041	0.007									0.23
Max. Dimen.	4	Thin Plates	Knikawa	0	0	0.003	0.011	0.047	0.074	0.010	0.014	0.011	0.0091	0.0058							0.64
Max. Dimen.	4	Thin Plates	Knikawa	0	0	0.001	0.004	0.024	0.040	0.071	0.066	0.077	0.008	0.054							0.54
Avg. Dimen.	2	Bullets & Col.	Hevms & Knoll.	0	0	0.005	0.022	0.024	0.003												0.054
Avg. Dimen.	2	Columns	Knikawa	0	0	0.003	0.023	0.036	0.036	0.010	0.002										0.11
Avg. Dimen.	2	Thin Plates	Knikawa	0	0	0.005	0.021	0.026	0.006	0.002											0.061
Avg. Dimen.	3	Bullets & Col.	Hevms & Knoll.	0	0	0.008	0.008	0.001													0.017
Avg. Dimen.	3	Columns	Knikawa	0	0	0.006	0.024	0.017	0.022												0.050
Avg. Dimen.	3	Thin Plates	Knikawa	0	0	0.004	0.027	0.034	0.025	0.008	0.002										0.10
Avg. Dimen.	4	Bullets & Col.	Hevms & Knoll.	0	0	0.006	0.023	0.019	0.005	0.002											0.054
Avg. Dimen.	4	Columns	Knikawa	0	0	0.009	0.006	0.005													0.015

Table E8. Distribution of Ice-Particle Radar-Reflectivity-Factors for Different Sizing Methods, Different Samples, and Different Assumptions About Ice-Crystal Type and Analytical Procedures

Method of Sizing from Foil	Sample No.	Assumed Ice-Crystal Type	Investigator Procedure Used	D _e Equivalent-Melted-Diameter, μm															Total Radar Reflectivity Factor gm m ⁻³			
				.025	.075	.125	.175	.225	.275	.325	.375	.425	.475	.525	.575	.625	.675					
Max. Dimen.	1	Bullets & Col.	Hevms & Knoll.	0	0	0.001	0.062	0.0	0.04	0.73												4.78
Max. Dimen.	1	Columns	Knikawa	0	0	0.0026	0.1	0.253	0.30	1.226	1.213	0.563										4.106
Max. Dimen.	1	Thin Plates	Knikawa	0	0	0.001	0.050	0.1	0.267	0.439	0.652	0.454										1.987
Max. Dimen.	3	Bullets & Col.	Hevms & Knoll.	0	0	0.003	0.13	0.1	0.60	0.26												1.151
Max. Dimen.	3	Columns	Knikawa	0	0	0.004	0.10	0.1	0.80	0.13												1.54
Max. Dimen.	3	Thin Plates	Knikawa	0	0	0.002	0.090	0.123	0.26	0.23	0.305	0.081										1.121
Max. Dimen.	4	Bullets & Col.	Hevms & Knoll.	0	0	0.007	0.063	0.14	0.15	0.040												0.481
Max. Dimen.	4	Columns	Knikawa	0	0	0.001	0.10	0.1	0.148	0.292	0.267	0.053										0.040
Max. Dimen.	4	Thin Plates	Knikawa	0	0	0.001	0.12	0.1	0.102	0.285	0.684	1.430	1.625	1.328	1.571							7.06
Max. Dimen.	4	Thin Plates	Knikawa	0	0	0.001	0.117	0.1	0.086	0.283	0.454	0.773	1.277	1.774	1.936	1.701	0.585					7.048
Max. Dimen.	4	Thin Plates	Knikawa	0	0	0.001	0.045	0.0	0.070	0.111	0.114	0.165	0.265									7.374
Avg. Dimen.	2	Bullets & Col.	Hevms & Knoll.	0	0	0.004	0.084	0.2	0.044													0.887
Avg. Dimen.	2	Columns	Knikawa	0	0	0.002	0.084	0.19	0.75	0.02	0.010											0.017
Avg. Dimen.	2	Thin Plates	Knikawa	0	0	0.004	0.078	0.15	0.14	0.064												0.176
Avg. Dimen.	3	Bullets & Col.	Hevms & Knoll.	0	0	0.006	0.010	0.007														0.055
Avg. Dimen.	3	Columns	Knikawa	0	0	0.005	0.001	0.1	0.030	0.032	0.006											0.0043
Avg. Dimen.	3	Thin Plates	Knikawa	0	0	0.003	0.010	0.05	0.055	0.011	0.0044											0.029
Avg. Dimen.	3	Thin Plates	Knikawa	0	0	0.005	0.006	0.013	0.011	0.001												0.140
Avg. Dimen.	4	Bullets & Col.	Hevms & Knoll.	0	0	0.007	0.021	0.0														0.044
Avg. Dimen.	4	Columns	Knikawa	0	0	0.007	0.021	0.0														0.0013

These tables show that large differences in the distributed and total values of M and Z occur dependent on the sizing methods used in the foil measurements, on the ice-crystal type, and on the crystal-geometry and density assumptions employed by the different investigators.

The differences in total M and total Z which are associated with the different foil-measurement-methods (and with the uncertainty of how to relate these measurements to those of the investigators cited herein) are illustrated by the particular data for Sample No. 3, of Tables E7 and E8. The particle sizes in this sample were measured both in terms of maximum particle dimensions and average particle dimensions. The different sizing methods, for common ice-crystal types, are seen to produce differences in total M ranging from about a factor of 2 to a factor of 3 (for the sample data listed in Table E7). The corresponding differences in total Z varied from about a factor of 5 to a factor of 12 (for the sample data listed in Table E8).

It will be recalled that the observed crystal-type at the storm altitudes where the foil samples were acquired was "plates". The data of Tables E7 and E8 (for the individual samples) reveal that lack of knowledge of whether these were "thick plates" or "thin plates" could cause differences of total M of the order of a factor of 3 to a factor of 4 and differences of total Z of the order of a factor of 8 to a factor of 13. These differences or "uncertainty factors", would be in addition to those cited in the paragraph preceding.

The differences between investigators concerning their treatments of a common ice-crystal type are illustrated by the table comparisons between the Heymsfield and Knollenberg "bullets and columns" and the "columns" of Kajikawa. The total M values differ by about a factor of 2 to a factor of 3; the total Z values differ by about a factor of 5 to a factor of 9.

If, on the day of this storm, we had had a complete lack of knowledge of the ice-crystal type and, hence, as in the case of other SAMS storms, had been forced to assume that they were "bullets, columns or rosettes" [(for consistency with the crystal type implicitly assumed in the M vs Z equation applied to the SAMS radar data (see footnote on page 106)] then we would have been subject to uncertainties of total M and total Z which could, conceivably, have been as large as any of the differences evidenced by Sample No. 3 (of Tables E7 and E8). The differences, for this sample, are seen to be as large as a factor of 19, for total M, and a factor of 340, for total Z. Actually, the normal, typical uncertainties for foil replicator data would not be as large as these maxima. But, from the evidence of this sample, plus the others investigated herein, it would seem logical to anticipate uncertainties of M ranging upward to perhaps as large as a factor of 10 and uncertainties of Z ranging upward to perhaps as large as a factor of 50.

The variability spread of the M and Z values of the foil samples is further illuminated in Figure E2. The four diagrams of this figure show, for each of the four samples, the plotted points of M and Z that correspond to the values listed in

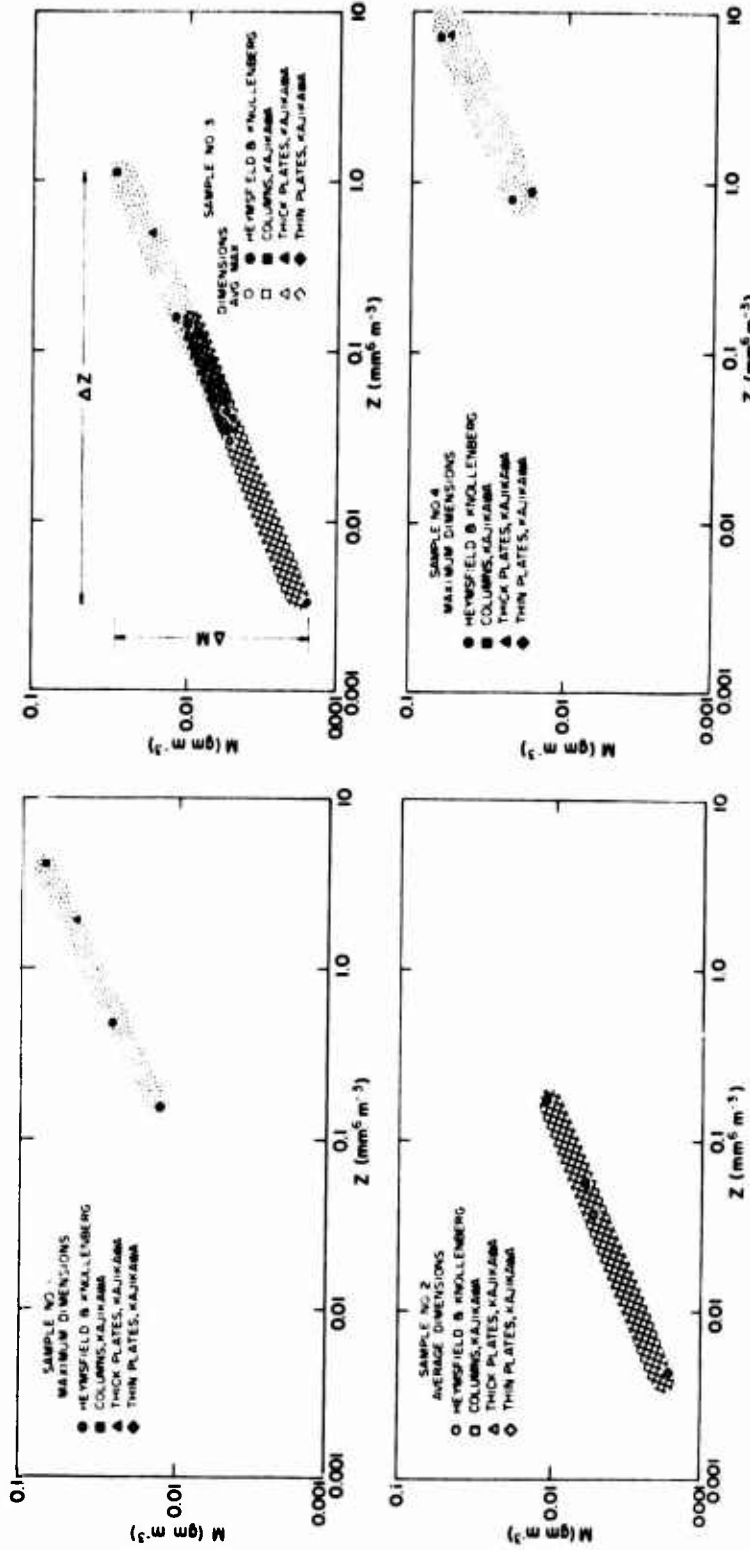


Figure E2. Plots of M vs Z for the Different Sizing Methods, Different Samples, and Different Assumptions About Ice-Crystal Type and Analytical Procedures. The spread of the values for the single samples is indicated by the shaded areas

Tables E7 and E8. The spread of the values derived from the different crystal-type and computational assumptions is indicated by the shaded areas. The spread for the samples (Numbers 1, 3, and 4) in which the ice particles were measured in terms of their maximum dimensions is indicated by the "dotted" shading. The spread for the samples (Numbers 2 and 3) in which the ice particles were measured in terms of their average dimensions is indicated by the "cross-hatched" shading. Both types of shading appear in the diagram for Sample Number 3, since the particles of this sample were measured by both methods.

It is only with reference to this Sample 3 diagram that the full range of the "uncertainty spread" of the M and Z values pertaining to the foil measurements may be illustrated. The uncertainty spread of the M values is delineated by the arrows labeled ΔM . The uncertainty spread of the Z values is delineated by the arrows labeled ΔZ . As mentioned previously, the spread of the M values is approximately a factor of 19; that of the Z values is approximately a factor of 340.

E3. DATA CORRESPONDENCE WITH THE SAMS M vs Z EQUATION FOR ICE CRYSTALS

It is of interest, at this point, to consider the M and Z differences that exist between the foil-sample values discussed above and the values that would be deduced from use of the power-function relationship that has been employed with the radar data for the SAMS missile trajectories.

The power-function relationship between M and Z that has been employed universally, to date, with all radar-measurement data for the ice-crystal regions of the Wallops Storm is

$$M = 0.038 Z^{0.529} \text{ gm m}^{-3} . \quad (\text{E9})$$

This equation was discussed in R No. 2 and was also presented in Table 1 herein.

A plot of Eq. (E9) is shown in Figure E3. Also shown in the figure are the plotted points of M vs Z for the foil samples of Tables E7 and E8. The points are identified by the same symbol coding used in Figure E2, except that the sample numbers are indicated by subscripts.

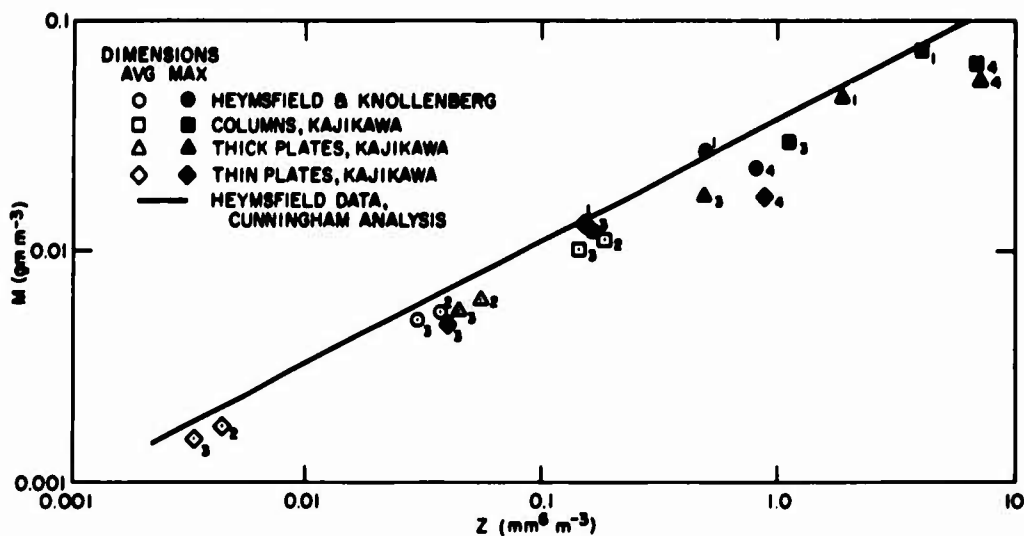


Figure E3. An Illustration of How the M vs Z Data of Tables E7 and E8 Fit the Heysfield-Cunningham Regression Equation for Bullet-Rossette Ice Crystals. The different sizing methods, samples and assumptions discussed in the text are indicated by the symbol coding of the plotted data points.

It is seen that the plotted points of the foil samples all lie reasonably close to the line of the equation relationship. The M values of the samples are somewhat smaller than predicted by the equation; the Z values are somewhat larger. The agreement is very good, however, with the M values departing from the equation generally by less than a factor of 1.4; the Z values departing generally by less than a factor of 2.

E4. A PARADOX

There is a paradox, here, that the reader will immediately detect. It may be elucidated in the form of a question. How is it possible that foil-sample data which evidence "uncertainty scatter" exceeding an order of magnitude in M and two orders of magnitude in Z can "conform to", and "agree with", the values of equation prediction to within less than a factor of two difference? Obviously, some parameter exists, other than M or Z , that is descriptive of the departure of these data points from the regression line. What is this parameter and what is the nature of the departure situation? The remainder of this appendix will be devoted to these questions and their implications for SAMS (Readers who might not be interested in the background and details of the explanations are referred directly to Section E6.)

E5. BACKGROUND CONSIDERATIONS

E5.1 The M vs Z Equations for Single Hydrometeor Samples

The reader will note from Figure E2 that, although the M and Z values of the foil-sample data scatter wildly, dependent on analyses methods and assumptions, the "scatter envelopes" for the samples, indicated by the shading, have a distinct "slope" which is essentially the same for all of the samples. This "comes about", in major part, because, irrespective of sampling methods and assumptions, there is a fundamental mathematical relationship that always prevails (for any single sample and all single samples) between the liquid-water-content derived for the sample, which is a function of D_e^3 , where D_e is the equivalent-melted-diameter, and the radar reflectivity value derived for the sample, which is a function of D_e^6 . Thus, $M = f(D_e^3)$ is related to $Z = f(D_e^6)$ as

$$M = k Z^{0.5} \text{ gm m}^{-3}, \quad (\text{E10})$$

where k is a coefficient that has a particular value for any single hydrometeor sample.

Therefore, for any sample data, for any type of hydrometeors (not necessarily ice-crystals, also including rain and snow), in which M and Z are both computed from the same size distribution data, the exponent of Z, in the power-function relation for single samples of Eq. (E10) is mathematically dictated to have the value of 0.5*.

To demonstrate this, consider the classified data of any hydrometeor sample, in which classification has been accomplished in terms of drop diameter, in the case of rain, or in terms of equivalent-melted-diameter, in the case of snow or ice crystals. For such data, we may write, with reference to Eqs. (E5) and (E6),

$$M_s = C \sum_{i=1}^{i=n} N_i D_i^3 + N_2 D_2^3 + N_3 D_3^3 + N_4 D_4^3 + \dots + N_n D_n^3, \quad (\text{E11})$$

where the subscript "s" on M signifies that this is a liquid-water-content value computed from a single, individual hydrometeor sample, where $N_1, N_2, N_3, \dots, N_n$ are the number concentrations of the drops or particles in the successive diameter

*This presumes that the diameter values of the size classes are properly defined for the particular moment of the distributed parameter. For example, the technically-accurate class diameter for M will differ from that for Z. For a large number of classes, say $n > 20$, such differences and their mathematical consequences are very slight. The differences are appreciable for $n < 10$ however. We also become involved with problems of non-representative sampling in such case, as discussed on page 151 and in Appendix H.

(or equivalent-melted-diameter) classes, where $D_1, D_2, D_3, \dots, D_n$ are the mid-diameters of the successive classes, where

$$C = \frac{\pi \times 10^{-3} \rho}{6} \text{ gm mm}^{-3}, \quad (\text{E12})$$

and ρ is the density of liquid water, equal to 1.0 gm cm^{-3} . It should be noted that the lower diameter boundary of the first size class is $D = 0$.

With reference to Eqs. (E7) and (E8), we may also write,

$$Z_s = \sum_{i=1}^{i=n} N_i D_i^6 + N_2 D_2^6 + N_3 D_3^6 + N_4 D_4^6 \dots + N_n D_n^6, \quad (\text{E13})$$

where the N_i 's and D_i 's are identical to those of Eq. (E11).

Consider that the data of any given hydrometeor sample described by Eqs. (E11), (E12), and (E13) are linearly-classified, such that the diameter widths of the classes are commonly the same across the entire diameter range of the sample. (Such classification is not necessary for the proofs following; it is merely a convenient example. The same results may be demonstrated for any method of classification, as, for instance, geometric classification, arithmetic or geometric progression, truncated distributions, etc).

With linear classification, assuming that there are n diameter classes of data, the mid-diameters of the successive classes, $i = 1$ through $i = n$, are given by

$$D_i = \frac{(2i - 1)}{(2n - 1)} D_n, \quad (\text{E14})$$

where D_n is the mid-diameter of the n 'th, or last, class, which contains the drops or particles of the largest size.*

* For "irregular classification", in which the diameter widths of the classes differ between classes, the D_i 's of the successive classes cannot be generally specified in terms of D_n . However, the ratios of D_i/D_n are, of course, known for each particular class.

For geometric classification, as used in the SAMS tables of Appendix G, the geometric mean diameter of the successive classes is given by

$$D_i = D_{1L} \left(\frac{D_n}{D_{1L}} \right)^{\left(\frac{2i-1}{2n-1} \right)}$$

where D_{1L} is the diameter at the lower boundary of the first size class and D_n is the geometric mean diameter of the n 'th or last, class. Equations for D_i for various other types of classification can also be written without particular difficulty.

Equation (E14) may be substituted into Eq. (E11), to replace the $D_1, D_2, D_3,$ etc. diameters of the latter with the D_n equivalents, with the result

$$M_s = \frac{C D_n^3}{(2n - 1)^3} \sum_{i=1}^{i=n} (2i - 1)^3 N_i. \quad (E15)$$

Similarly, Eq. (E14) may be substituted into Eq. (E13) to obtain

$$Z_s = \frac{D_n^6}{(2n - 1)^6} \sum_{i=1}^{i=n} (2i - 1)^6 N_i. \quad (E16)$$

If we solve Eq. (E16) for D_n^3 and substitute the result into Eq. (E15), we find that

$$M_s = k Z_s^{0.5}, \quad (E17)$$

where

$$k = \frac{C \sum_{i=1}^{i=n} (2i - 1)^3 N_i}{\left[\sum_{i=1}^{i=n} (2i - 1)^6 \right]^{0.5}} \quad (E18)$$

is a coefficient that depends on the particular values of the class number concentrations of the drops or particles in the diameter classes, $i = 1$ through $i = n$, of the given hydrometeor sample.

E5.2 The Form Factor and Examples

Actually, the coefficient k depends on two identifiable features of the number-concentration spectra of the sample, as will be demonstrated. It depends (1) on the total number-concentration of the drops or particles of all sizes in the sample and (2) on the "form of the distribution", as, for example, a monodispersed-type distribution vs a uniform-type distribution vs an exponential-type distribution, etc. We may illustrate this dependence in the following manner.

If N_T is the total number concentration of the drops or particles of the sample, then

$$N_T = \sum_{i=1}^{i=n} N_i. \quad (E19)$$

If we divide both sides of this equation by N_T , we may then write the reversed equation

$$\sum_{i=1}^{i=n} \alpha_i = 1.0 . \quad (E20)$$

where

$$\alpha_i = N_i / N_T . \quad (E21)$$

By the use of Eqs. (E20) and (E21), we are permitted to write the equation for k in the form

$$k = C \sqrt{N_T} F , \quad (E22)$$

where

$$F = \frac{\sum_{i=1}^{i=n} (2i - 1)^3 \alpha_i}{\left[\sum_{i=1}^{i=n} (2i - 1)^6 \alpha_i \right]^{0.5}} \quad (E23)$$

is the "form factor" of the distribution. Equation (E22), with F as defined by the above equation, demonstrates the dependence of k on the total number concentration of the drops or particles within the given sample, also its dependence on the non-dimensionalized, number-concentration coefficients, $\alpha_1, \alpha_2, \alpha_3$, etc., see Eq. (E21), which have different values of the distribution".*

*The "form of the distribution", in other words, describes the manner in which the number concentrations of the drops or particles in the different diameter classes are apportioned relative to each other, over the diameter range of the sample, and relative to the total number concentration value for the sample. Since numerous references to the "form factor" will be made in the succeeding paragraphs, it is pertinent to note that the form factor for irregularly classified data (in which the diameter widths of the classes differ between classes) is given by)

$$F = \frac{\sum_{i=1}^{i=n} D_i^3 \alpha_i}{\left[\sum_{i=1}^{i=n} D_i^6 \alpha_i \right]^{0.5}} . \quad (E23a)$$

where D_i is the algebraic mid-diameter of any given class and α_i is as defined by Eq. (E21). This is the most generalized form of the F equations.

For geometric classification, as used in the SAMS tables of Appendix G, the form factor is specified by

$$F = \frac{\sum_{i=1}^{i=n} (D_n / D_{1L})^{\frac{6i}{2n-1}} \alpha_i}{\left[\sum_{i=1}^{i=n} (D_n / D_{1L})^{\frac{12i}{2n-1}} \alpha_i \right]^{0.5}} . \quad (E23b)$$

where D_{1L} is the diameter at the lower boundary of the first size class and D_n is the geometric mean diameter of the last, or n th class. Again α_i is as defined by Eq. (E21).

A specific example might be helpful at this point. Consider a simple distribution of hydrometeors in which there are just three diameter classes. Assume that the number concentrations of the drops or particles in these classes decreases with increasing diameter, in an exponential-type manner, such that

$$N_1 = 4800. \quad (E24)$$

$$N_2 = 1100. \quad (E25)$$

and

$$N_3 = 46. \quad (E26)$$

The total number concentration of the drops or particles of the sample is

$$N_T = N_1 + N_2 + N_3, \quad (E27)$$

from Eq. (E19) or

$$N_T = 5946. \quad (E28)$$

for the N_i values cited. This number total is of the same order as those of the foil samples of Table E6.

The α coefficients for the three diameter classes are, respectively, from Eq. (E21)

$$\alpha_1 = 0.807, \quad (E29)$$

$$\alpha_2 = 0.185, \quad (E30)$$

and

$$\alpha_3 = 0.00774. \quad (E31)$$

These coefficients substituted in Eq. (E23) yield a value of

$$F = 0.423, \quad (E32)$$

for the "form factor". Then, since

$$\sqrt{N_T} = 77.11 \quad (E33)$$

and

$$C = \frac{\pi \times 10^{-3} \rho}{8} = 5.24 \times 10^{-4} , \quad (\text{E34})$$

the value of k , from Eq. (E22) becomes

$$k = 0.0171 . \quad (\text{E35})$$

A second example will illustrate how the values of the above parameters would change for a hydrometeor sample of completely different type. Consider a sample distribution consisting of three diameter classes, as before, but in which the number concentration of the drops or particles in the classes are

$$N_1 = 70 , \quad (\text{E36})$$

$$N_2 = 75 , \quad (\text{E37})$$

and

$$N_3 = 72 , \quad (\text{E38})$$

which gives a total number concentration of

$$N_T = 217 . \quad (\text{E39})$$

This distribution differs radically from the former, since the number total of the drops or particles is much smaller and since the class number concentrations are approximately the same in each of the three classes (a "uniform type" distribution), as compared with the "exponential type" distribution of the first example.

The α coefficients for this new sample are, respectively,

$$\alpha_1 = 0.323 , \quad (\text{E40})$$

$$\alpha_2 = 0.346 , \quad (\text{E41})$$

and

$$\alpha_3 = 0.332 , \quad (\text{E42})$$

which values, inserted in Eq. (E23), yield

$$F = 0.694 . \quad (\text{E43})$$

When this form-factor value and

$$\sqrt{N_T} = 14.73 \quad (E44)$$

are substituted into Eq. (E22) together with the C value of Eq. (E34) the k value for the sample becomes

$$k = 0.00530 . \quad (E45)$$

A comparison of the k values of the first and second samples described above shows that the values differ by about a factor of 3.2, in the ratio amount of the larger divided by the smaller. It is seen, moreover, that of the two equation terms, of Eq. (E22) that produced these differences, the $\sqrt{N_T}$ term differed in ratio amount by about a factor of 5.2 between the two samples; whereas the ratio difference in the form-factor term was approximately 0.610 (or a factor of 1.6, when inverted).

The salient point, here, is that, even for radically different assumptions about the characteristics of two, separate samples of precipitation-size hydrometeors, the differences in the form-factor term of Eq. (E22) will generally be much smaller than the differences in the $\sqrt{N_T}$ term (in causing differences of k between samples).*

This is further illustrated by reference to Table D2, of Appendix D, and to Tables E4, E5, and E9, of the present appendix. In each table, the values of $\sqrt{N_T}$, F and k are listed for the different hydrometeor distributions. The ranges of these values are summarized in Table E10. It is seen that the values and ranges of F are approximately the same for rain and ice crystals. But the values and ranges of $\sqrt{N_T}$ differ appreciably between the two hydrometeor types and these differences are directly reflected in the k value differences between types, see Eq. (E22).

* If cloud-size hydrometeors are included in the smallest size-class of a distribution of precipitation-size hydrometeors, these statements are no longer true. The inclusion of cloud-size hydrometeors, which have large number concentration, will materially increase the value of $\sqrt{N_T}$ (over that for precipitation-size hydrometeors alone) and will also materially decrease the value of F. However, the inclusion of the cloud-size hydrometeors does not change the k value, or, at most, only changes it slightly. This non-variance of k comes about because the $\sqrt{N_T}$ contribution of the cloud-size hydrometeors, in Eq. (E22), is almost perfectly counterbalanced by a compensating decrease in the F value, as computed from the series ratio of Eq. (E23) (or from the more-general Eq. (E23a)). This situation, of the inclusion-exclusion of the cloud-size hydrometeors, has been investigated extensively. It may be stated that the k values for rain and large-snow are insensitive to the inclusion of any hydrometeors smaller than about 80μ (equivalent-melted-diameter) and that the k values for small-snow and ice-crystals are insensitive for diameter sizes smaller than about 70μ and 30μ , respectively. These diameters cited are, in essence, the lower truncation limits of spectral significance (for any sample data or theoretical computations involving k, M or Z, or their interrelationships).

Table E9. Values of the α Coefficients and of $\sqrt{N_T}$, F, and k for the Number Concentration Data for Ice Crystals of Table E6

Method of Sizing From Fol	Sample No.	Assumed Ice-Crystal Type	Investigator Procedure Used	No. of Plates														$\sqrt{N_T}$	F	k ($m^{-1.5}$)
				1	2	3	4	5	6	7	8	9	10	11	12	13	14			
Max. Dimen.	1	Bullets & Col.	Hermes & Knoll.	.0025	.052	.205	.419	.294	.0267									89.140	.831	.0388
Max. Dimen.	1	Columns	Kajikawa	.0025	.052	.085	.301	.255	.12	.131	.055	.014						89.140	.760	.0355
Max. Dimen.	1	Thin Plates	Kajikawa	.0281	.246	.433	.223	.095	.011	.070	.021							89.140	.717	.0325
Max. Dimen.	3	Bullets & Col.	Hermes & Knoll.	.01	.296	.351	.210	.088	.0047									88.284	.665	.0307
Max. Dimen.	3	Columns	Kajikawa	.05	.284	.310	.180	.102	.024	.019	.0022							88.284	.596	.0271
Max. Dimen.	3	Thin Plates	Kajikawa	.204	.505	.212	.063	.015	.0017									88.284	.508	.0249
Max. Dimen.	4	Bullets & Col.	Hermes & Knoll.	.019	.043	.121	.282	.200	.166	.095	.0066							63.067	.754	.0252
Max. Dimen.	4	Columns	Kajikawa	.019	.063	.105	.205	.152	.180	.064	.067	.055	.018					63.067	.701	.0235
Max. Dimen.	4	Thin Plates	Kajikawa	.055	.153	.291	.222	.133	.063	.045	.017	.011	.012	.0027				63.067	.542	.0195
Avg. Dimen.	2	Bullets & Col.	Hermes & Knoll.	.158	.317	.245	.132	.033	.015	.0020								89.140	.652	.0272
Avg. Dimen.	2	Columns	Kajikawa	.127	.215	.245	.136	.098	.017	.0035								89.140	.621	.0259
Avg. Dimen.	2	Thin Plates	Kajikawa	.158	.357	.321	.144	.017										89.140	.582	.0231
Avg. Dimen.	3	Thin Plates	Kajikawa	.330	.530	.125	.069											89.140	.504	.0204
Avg. Dimen.	3	Bullets & Col.	Hermes & Knoll.	.221	.384	.312	.078	.0047										87.356	.615	.0201
Avg. Dimen.	3	Columns	Kajikawa	.181	.287	.346	.160	.046	.0096	.0012								87.356	.581	.0186
Avg. Dimen.	3	Thin Plates	Kajikawa	.221	.384	.275	.086	.011	.0020									87.356	.562	.0187
Avg. Dimen.	3	Thin Plates	Kajikawa	.418	.507	.073	.0039											87.356	.554	.0253

Table E10. Ranges of the Values of $\sqrt{N_T}$, F, and k for the R ϵ in Samples of Table D2, Appendix D, and for the Ice Particle Samples of Tables E4, E5, and E9 Herein

Type of Information	Where Presented	Range of $\sqrt{N_T}$ Values	Range of F Values	Range of k Values
Rain -- from disdrometers and filter papers	Table D2, Appendix D	9.5 to 24.5	.224 to .643	.00289 to .00647
Ice Particles -- from foil impactor				
a. Basic data, sized in terms of maximum particle dimensions	Table F4, Appendix E	63.9 to 89.1	.502 to .695	.0191 to .0325
b. Basic data, sized in terms of average particle dimensions	Table F5, Appendix E	79.7 to 87.4	.529 to .572	.0239 to .0242
c. Data converted to equivalent-melted-diameter, by assumptions and procedures discussed in text	Table E9, Appendix E	63.9 to 89.1	.506 to .831	.0180 to .0388

The Table E10 information also reveals that the values and ranges of $\sqrt{N_T}$, F , and k are approximately the same for the basic data and for the data converted into equivalent-melted-diameter. This suggests the possibility that the k values for distributions of ice hydrometeors might be deduced, to a reasonable first approximation, from the basic data themselves, without the assumptive necessity of converting the nebulous length measures for crystals into equivalent-melted-diameters.

E5.3 Values of the Form Factor for Various Types of Hydrometeor Distribution

The concept of the form factor and of the equation relationships pertaining to single hydrometeor samples can be exceedingly useful for SAMS purposes, as we will discuss. However, we must still provide additional background information for such discussions to be fruitful. In this vein, we have considered various different types of hydrometeor distributions and have computed the associated form factor values. Certain of these distributions are illustrated in Figures E4 and E5. Exponential and modified-exponential type distributions are shown in Figure E4; bi-modal distributions of different kinds are shown in Figure E5. Truncation effects on the F values are illustrated in both figures. It is seen that the F values for most distributions range generally from about 0.2 to 1.0. The values cannot exceed 1.0, which is the value for mono-dispersed distributions. Values smaller than 0.2 can exist, theoretically, but are unlikely to be of common occurrence in atmospheric distributions of precipitation-size hydrometeors. For example, small F values, approaching zero, can be obtained in bi-modal distributions having very-large spacing between the modal peaks. But these would be unusual distributions. It may be stated that the F values for exponential distributions will never be smaller than 0.222, irrespective of truncation (see Section H1 and Figure H1, of Appendix H). The F values for distributions in which the particle number concentrations in the classes decrease at a "rate" greater than exponential, with increasing particle size, can, under certain circumstances (see the fifth histogram from the left at the top in Figure E4, also the footnote on page 122) be smaller than 0.2.

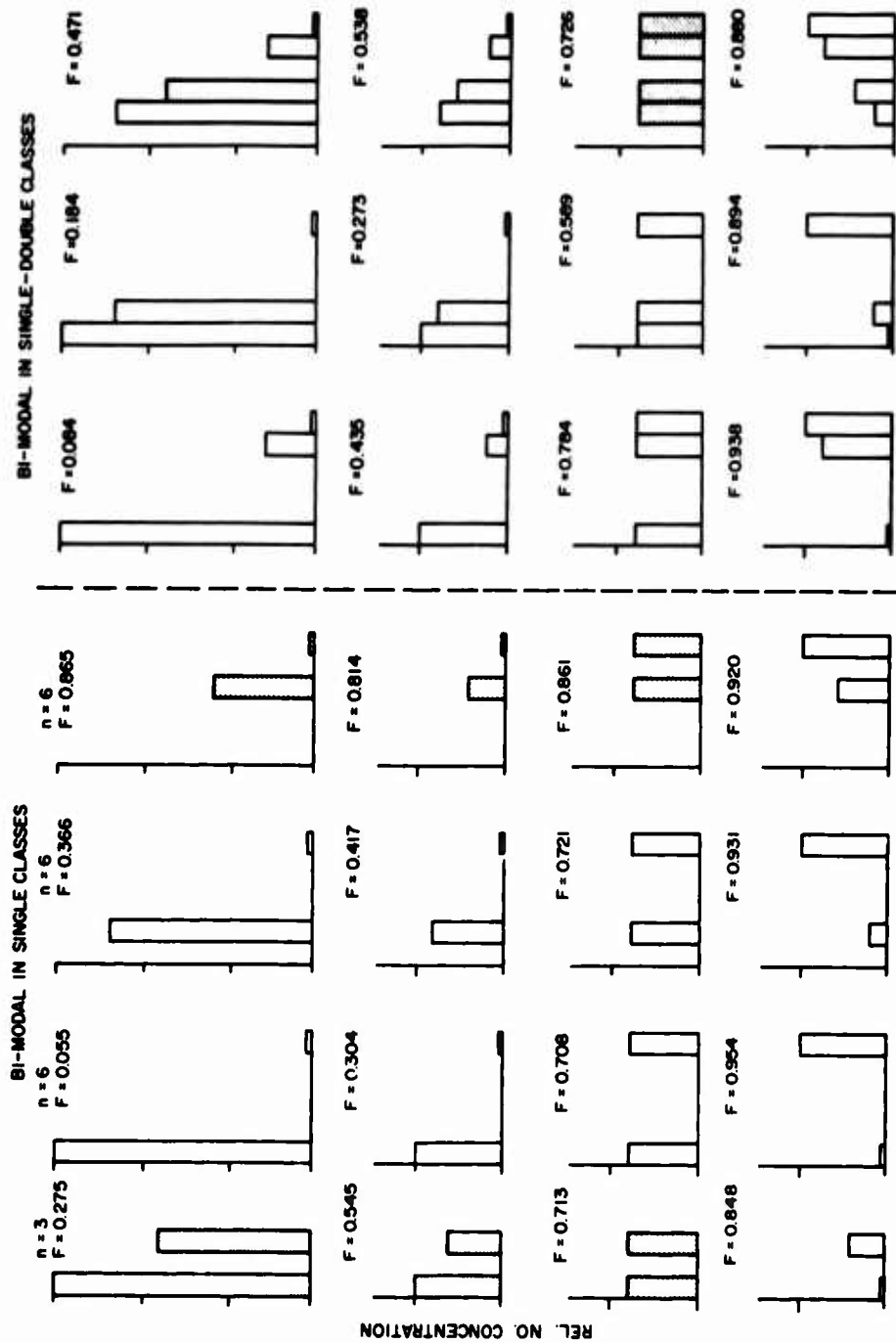


Figure E5. Illustrations of the Form-Factor Values Associated With Representative Hydrometeor Distributions of Bi-Modal and Truncated Bi-Modal Types. The n values and F values are indicated. The number concentration scales of the ordinate are in terms of relative concentrations. No diameter scale is indicated along the abscissa, since, with linear classification, the F values depend only on n and not on the absolute diameter widths of the classes or the absolute diameter range. (See Figure E8 and the associated text discussion if there are questions concerning the ordinate and abscissa scales)

To verify these statements, reference is made to the F values for disdrometer samples of rain which are shown plotted in the first diagrams of Figures E9 and E10, also to the values for the large-snow samples of Ohtake and Henmi¹⁵ of the first diagram of Figure E11,* and to the values for the ice crystal distributions of PVM-5¹⁶ shown in the first diagram of Figure E12.** It is seen that the F values for the rain samples range from about 0.3 to 0.9. The values for large-snow range from about 0.1 to 1.0, with only six of the samples (of 174 total) evidencing values smaller than 0.2. The values for ice-crystals range from about 0.35 to 0.7. Hence, at least for the samples of these data sets, the statements of the above paragraph are generally verified.

E5.4 Multiple Hydrometeor Samples and the M vs Z Regression Equations Expressed in Terms of k, N_p, and F

Part of the background required for the answer to the "paradox question" raised earlier has been established to this point. We now turn to a consideration of regression analyses, which is the essential "next step".

In any regression analysis, the equation line of "best fit" is sought that describes the "association trend" between the "sample values" of two variables (usually two). The "sample values", when cross plotted, may reveal linear, logarithmic, or other forms of relationship and least-squares methods are generally used to establish the criteria of "best fit" for the regression line, also to establish the particular values of the coefficients or exponents of the regression equation.

For the M and Z values determined from hydrometeor samples, it has been conventional to "fit" the cross-plotted M vs Z points of the multiple, individual samples with a regression equation of power-function form, that is,

$$M = KZ^E, \quad (E46)$$

15. Ohtake, T., and Henmi, T. (1970) Radar Reflectivity of Aggregated Snowflakes preprints of papers presented at the 14th Radar Meteorology Conference, Tucson, Arizona, 17-20 November 1970, pp 209-211.
16. Barnes, A. A., Nelson, L. D., and Metcalf, J. I. (1974) Weather Documentation at Kwajalein Missile Range, AFSG, No. 292, AFCRL-TR-74-0439.

*The reader may question why the F values for the large snow data of Ohtake and Henmi are presented without any comments about length to equivalent-melted-diameter conversions, which is one of the major problems of discursive concern in the present appendix. The answer is that Ohtake and Henmi obtained their data, at the surface level, by capturing snowflakes on angora wool (or Japanese silk wool) collectors. They then let the snowflakes melt before size determination and thus obtained direct measurements of equivalent-melted diameter.

**For the ice crystal data, the f to D conversions were accomplished as discussed by Barnes, Nelson and Metcalf. These methods are not questioned, here, since we are merely concerned with the general range of the form factor values.

where the values of the constant, K, and the exponent, E, are the values sought from the least squares analyses of fitting the regression line to the field of the data points. It may be noted that this equation, when plotted on log paper, is a straight line having a slope equal to the value of the exponent, E. Or, in other words, if we take the log of Eq. (E46) to obtain

$$\log M = \log K + E \log Z, \quad (E47)$$

it follows that the "log slope" of the regression equation is

$$E = \frac{\log M - \log K}{\log Z} \quad (E48)$$

Let us turn, now, to a consideration of the individual sample points, of $\log M_s$ vs $\log Z_s$, which are the data points that would be "fitted" by the regression line of Eq. (E47). Let us establish the requirements of the sample data that will yield particular values of the "log slope parameter", E, of Eq. (E48). It will be convenient, in this work, to use the subscript "s" to identify the M and Z values that pertain to individual hydrometeor samples and to use the M and Z letters, non-subscripted, to refer to the variable parameters of the regression equation.

For any individual hydrometeor sample, we have previously demonstrated that, irrespective of the type of hydrometeors, the form of the distribution, or the quantities of the drops or particles, the liquid-water-content of the sample is related to the radar reflectivity factor as

$$M_s = k Z_s^{0.5}. \quad (E49)$$

This is merely a repeat of Eq. (E10) with the "s" subscripts added. Particular isolines of k, plotted from this equation, are shown in Figure E6.

Suppose that we have two hydrometeor samples and that we wish to determine the "log slope" of the straight line connecting the $\log M_s$ vs $\log Z_s$ points of the samples. From Eq. (E49) we may write

$$M_{s_1} = k_1 Z_{s_1}^{0.5}, \quad (E50)$$

for the first sample, and

$$M_{s_2} = k_2 Z_{s_2}^{0.5}, \quad (E51)$$

for the second. The log forms of these equations are, respectively,

$$\log M_{S_1} = \log k_1 + 0.5 \log Z_{S_1}, \quad (\text{E52})$$

and

$$\log M_{S_2} = \log k_2 + 0.5 \log Z_{S_2}. \quad (\text{E53})$$

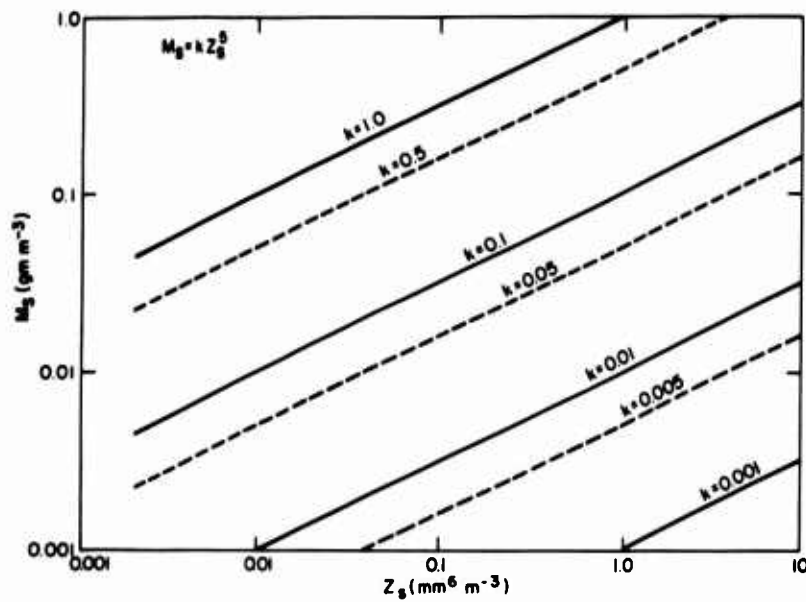


Figure E6. Particular Isolines of k , for Single Hydrometeor Samples, as Plotted from Eq. (E49)

If, for sign convention, we assume that $Z_{S_2} > Z_{S_1}$ (also implying that $M_{S_2} > M_{S_1}$), the slope of the straight line connecting the cross-plotted points of $\log M_s$ vs $\log Z_s$ for the two samples will, from Eqs. (E52) and (E53) be given by

$$\frac{\Delta \log M_s}{\Delta \log Z_s} = 0.5 + \frac{\Delta \log k}{\Delta \log Z_s}, \quad (\text{E54})$$

where

$$\Delta \log M_g = \log M_{g_2} - \log M_{g_1} , \quad (E55)$$

$$\Delta \log Z_g = \log Z_{g_2} - \log Z_{g_1} , \quad (E56)$$

and

$$\Delta \log k = \log k_2 - \log k_1 . \quad (E57)$$

The log-slope of the regression equation, specified by Eq. (E48) will equal the log-slope of the line connecting the two data points, specified by Eq. (E54) when

$$E = \frac{\Delta \log M_g}{\Delta \log Z_g} , \quad (E58)$$

which permits us to write Eq. (E54) as

$$E = 0.5 + \frac{\Delta \log k}{\Delta \log Z_g} . \quad (E59)$$

This last equation shows that the log-slope, E , of a regression equation that passes perfectly through the plotted data points of the two samples will have a particular value exceeding 0.5, or smaller than 0.5, which is "amount dependent" on the difference in the $\log k$ values of the two samples relative to the difference in their $\log Z_g$ values. The equation also shows that, if the samples have the same k value, hence $\Delta \log k = 0$, the slope of the regression line will be precisely equal to 0.5. This statement is not limited to two samples only; it may be generalized to the case of any number of hydrometeor samples having the same, common k value. All such samples, when their $\log M_g$ and $\log Z_g$ values are cross-plotted, will have data points that lie along one particular straight line, which has a log-slope equal to 0.5.

We might further generalize and state that, for any given set of hydrometeor samples that is used for regression purposes, the magnitude of the k values of the set, and their constantancy within the set, will dictate, a-priori, and in major degree, the particular values of the constant and exponent of the regression equation that "best fits" the data and will also establish the "range spread" of the M and Z values of the data set and the standard error of estimate. For example, the set of the isolines of k for the basic foil data (the isolines corresponding to the k values of Tables E4 and E5) are shown in Figure 7, in the upper diagram. The set of isolines of k for the analyzed foil data (corresponding to the k values of Table E9) are shown in the lower diagram of Figure E7. The isoline data of these diagrams do not really constitute independent sets, but they may be used for the purposes of illustration. Thus, we may state that it is axiomatic that the regression

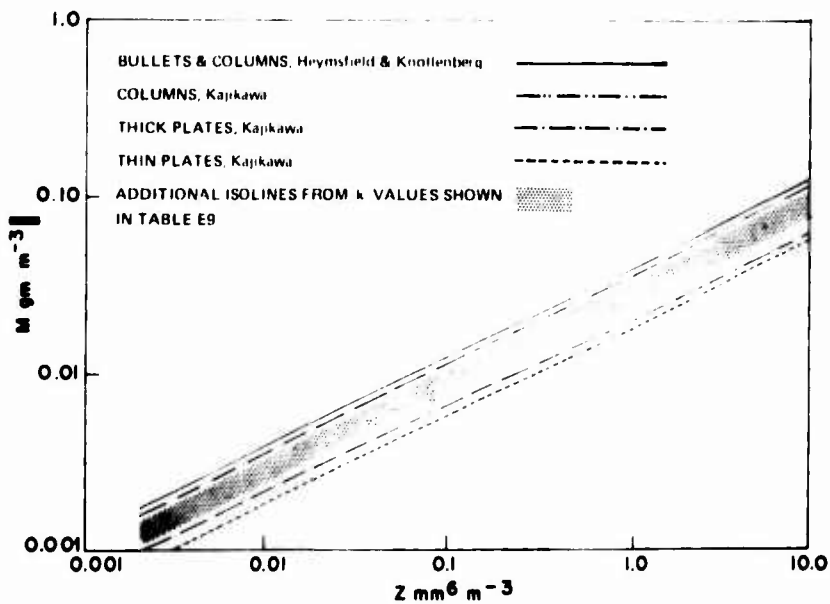
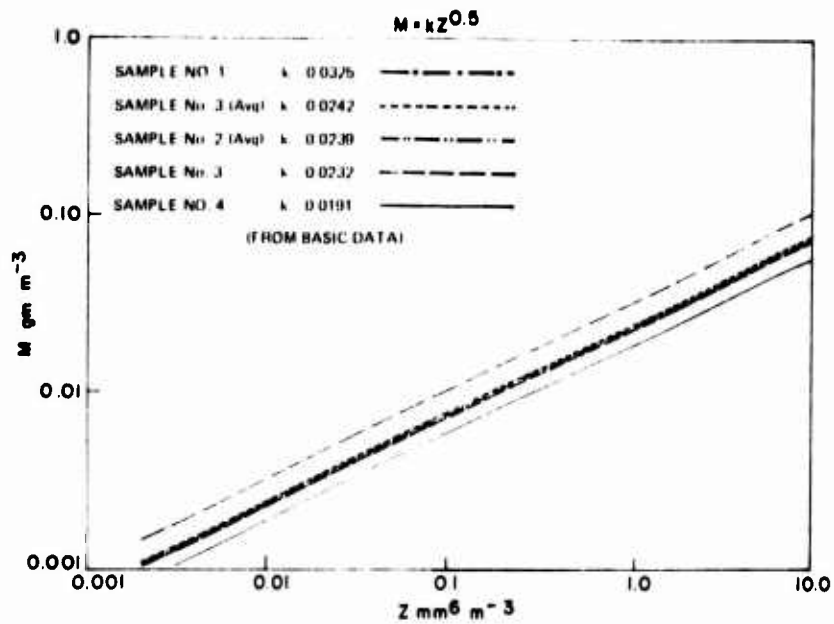


Figure E7. Isolines of k Corresponding to the Basic Foil Data of Tables E4 and E5 (upper diagram) and to the Data of Table E9, Which Have Been Converted Into Terms of Equivalent-Melted-Diameter by the Various Text-Discussed Methods and Assumptions (lower diagram). These two diagrams, if superimposed, reveal that the envelope of the k isolines for the basic data is contained within, and centered approximately within, the isoline envelope for the converted data

equations of log M vs log Z, that would fit these data, must necessarily lie somewhere within the boundaries of the k isolines of the two cited diagrams of Figure E7. The regression lines must also be entirely contained within the limiting isolines of k. We might state at this point that the equation for the coefficient, K, of the M vs Z equation, is given by

$$K = 10^{[\overline{\log k} - \overline{\log Z_g}(E - 0.5)]} \quad (E60)$$

where $\overline{\log k}$ is the average of the log k values of the data set, $\overline{\log Z_g}$ is the average of the log Z_g values of the set and E is the exponent of the M vs Z equation, as defined by Eq. (E59). The above equation for K is readily derived from the slope-intercept form of the regression equation, of k vs Z_g , see the bottom diagrams of Figures E9, E10, E11, and E12, for example, from knowledge that the regression line will pass through the "centroid point", of $\overline{\log k}$ and $\overline{\log Z_g}$, and that the slope of the equation is given by E - 0.5, see Eq. (E59).

Two things are apparent from the previous comments and the Figure E7 diagrams. First, for any reasonable spread of the M or Z values of the data sets, it is seen that there is relatively little latitude for the regression lines to have "log slope" values departing appreciably from 0.5. Second, the envelope of the k isolines obtained from the basic foil data "lies within and is centered approximately within" the envelope of the k isolines for the analyzed foil data that were determined from the various "length to equivalent-melted-diameter" assumptions and procedures discussed earlier. This second statement has important implications for the continuing SAMS program, for it implies (as will be explained) that, up to the present point of discussion herein, we could have deduced the k values of the foil samples to an excellent approximation, without ever having bothered to concern ourselves with questions of ice-crystal type or conversions of length to equivalent-melted-diameter.

Part of the answer to the paradox question raised earlier is now apparent. It is that "the highly uncertain" M and Z values of the foil samples, as estimated by different assumptions and procedures, fit the Heymsfield-Cunningham regression equation with considerable accuracy (see Figure E3) because there is strong mathematical predilection, in sets of hydrometeor data obtained from size-distribution measurements, for the regression equation to have a "log slope" close to 0.5, with the equation constant being functionally dependent on the log-average of the k values of the set, in accordance with Eq. (E60). In other words, when both M and Z are computed from the same, common size-distribution data, the resultant values are not independent values, rather they are dependent values; and the mathematical predilection for the 0.5 exponent is a direct reflection of this dependency.*

* It should also be emphasized that, in this situation, the uncertainty scatter of the data points is predominantly "back and forth", along the regression line, rather than orthogonal to the line. Compare Figures E2 and E3.

To illustrate the general predilection for log-slope values close to 0.5, we may reference Table 2 of R No. 2. The reader will see, from column 3 of this table, that the exponent of the M vs Z equation for ice crystals is 0.529; the exponent of the equation for small-snow is 0.538; the average exponent for the six types of large-snow listed is 0.499; the average exponent for the four disdrometer equations for rain is 0.590; the exponent used by Joss et al,¹⁷ for rain of all types, is 0.576. Thus, although all except one of the cited values exceed 0.5, by up to 17 percent, the essential point concerning the predilection should be apparent.

E5.5 Equations Specifying the Departure of the Exponent, E, of the M vs Z Equation, From the Particular Value 0.5

We might, at this point, examine the theoretical conditions that would cause slope departures of the regression lines from the particular value 0.5. If we symbolize these departures by " ΔE ", then their sign and magnitude will be specified by the last term of Eq. (E59) as mentioned, such that

$$\Delta E = \frac{\Delta \log k}{\Delta \log Z_s} . \quad (E61)$$

If we take the log of Eq. (E22) and presume that two hydrometeor samples exist which are identified by the subscripts "1" and "2", we may write the difference equation between sample 2 and sample 1 as

$$\Delta \log k = 0.5 \Delta \log N_T + \Delta \log F , \quad (E62)$$

where

$$\Delta \log N_T = \log N_{T_2} - \log N_{T_1} , \quad (E63)$$

and

$$\Delta \log F = \log F_2 - \log F_1 . \quad (E64)$$

Equation (E62) may be substituted in Eq. (E61) to write

$$\Delta E = \frac{0.5 \Delta \log N_T + \Delta \log F}{\Delta \log Z_s} , \quad (E65)$$

17. Joss, J., Thams, J. C., and Waldvogel, A. (1968) The variation of raindrop size distributions at Locarno, Proc. Internatl. Conf. on Cloud Physics, Toronto, Amer. Meteorol. Soc., Boston, p. 369.

which shows that the values of ΔE will depend on the log variation of the total number concentration, N_T , across the Z_n range of the given set of hydrometeor samples, and will also depend on the log variation of the form factor values, across the Z_s range of the set.

The significance of the first numerator terms of Eq. (E65) is completely apparent. However, the significance of the second numerator term requires explanation.

If we use Eqs. (E23) and E64) which define F and $\Delta \log F$, the second numerator term of Eq. (E65) may be expanded to

$$\Delta \log F = \left[\left(\log \sum_{i=1}^{i=n_2} (2i-1)^3 \alpha_{i_2} - \log \sum_{i=1}^{i=n_1} (2i-1)^3 \alpha_{i_1} \right) - 0.5 \left(\log \sum_{i=1}^{i=n_2} (2i-1)^6 \alpha_{i_2} - \log \sum_{i=1}^{i=n_1} (2i-1)^6 \alpha_{i_1} \right) \right] \quad (E66)$$

This equation shows that $\Delta \log F$ will have values and will contribute to the values of ΔE [(through Eq. (E65)], if (1) there are log differences in the series summations of the α coefficients between any comparative pair, or set of pairs, of the hydrometeor samples and if (2) there are differences in the n values of the comparative samples, which are differences in the number of the diameter classes contained in the samples, or, more fundamentally, differences in the diameter range, or spread, of the samples.

E5.6 Comparative Situations in Which the Form Factor Values are Non-Variant

There are two identifiable situations in which the terms of Eq. (E66) will have zero values or zero sum. It will be instructive to note these situations.

The individual terms of Eq. (E66) will have zero values if the drops or particles in any given atmospheric region are "monodispersed", such that only one diameter size, or class, of hydrometeors exists at any particular point in the region. (The diameter, itself, however, may vary within the region.) This statement is readily verified, most easily by a consideration of fundamentals. Thus, with reference to Eqs. (E11) and (E13) we may write, for any monodispersed sample,

$$M_s = C N_T D^3 \quad (E67)$$

and

$$Z_s = N_T D^6, \quad (E68)$$

since there is only one diameter class which contains the total number of the drops or particles. When Eq. (E68) is solved for D^3 and substituted in Eq. (E67)

$$M_g = k Z_g^{0.5}, \quad (E69)$$

where

$$k = C \sqrt{N_T}. \quad (E70)$$

Thus, it is seen that the k value for any monodispersed sample is functionally dependent on $\sqrt{N_T}$ alone, and is not dependent on the form factor, as in the case of Eq. (E22). In other words, the value of the form factor for any monodispersed sample is $F = 1.0$, which means that the value of $\Delta \log F$, in Eq. (E64) is identically equal to zero. (Each term of Eq. (E66) has zero value in such situations, although this is not specifically demonstrated herein.)

The two parenthesis terms of Eq. (E66) will have zero sum if there is a "class by class proportionality" of the drop or particle number concentrations between any two comparative hydrometeor samples. This is strictly true only if the diameter spread of the two samples is the same, that is, if the number of the classes, n_1 , of the first sample, is equal to the number of the classes, n_2 , of the second, and if the classification method is the same. (We are using linear classification, here, for the purposes of illustration. See the footnote on page 138 for comments about other methods of classification.)

With class by class proportionality, the number concentration of the drops or particles in any given class, $i = g$, of the first sample is proportional to the number concentration of the drops or particles in the same class, $i = g$, in the second sample, such that

$$N_{i_1} = \beta N_{i_2}, \quad (E71)$$

where N_{i_1} is the class number concentration of the first sample, N_{i_2} is the class number concentration of the second, comparative sample and β is the factor of proportionality. Additionally, from Eq. (E19) it follows that the total number concentration, of the drops or particles of all sizes in the two samples, are related as

$$N_{T_1} = \beta N_{T_2}, \quad (E72)$$

which means that, see Eq. (E21),

$$\alpha_{i_1} = \beta \alpha_{i_2} . \quad (E73)$$

This relationship, introduced into Eq. (E66) for

$$n_1 = n_2 \quad (E74)$$

yields

$$\Delta \log F = (- \log \beta + \log \beta) = 0 , \quad (E75)$$

which demonstrates that the two parenthesis terms of Eq. (E66) have zero sum.

Two additional things should be noted with regard to the situation of class by class proportionality. First, with reference to Eq. (E71) it should be pointed out that the N_i number concentrations of the comparative samples may have zero values in any given class, $i = g$. This given class, or these given classes, may be the first, second, or third, etc., in diameter size, extending upward from zero diameter, which corresponds to the situation of lower-diameter truncation of the distributions. The point, here, is that the principle of class by class proportionality (yielding identical F values between samples, or $\Delta \log F = 0$) also applies to comparative data which are commonly truncated at the same lower diameter limit, as in the case of data obtained with an instrument incapable of measurements below a particular threshold of diameter sensitivity.

Second, it should be mentioned that class by class proportionality additionally pertains to any comparative distributions in which the class widths of the first sample, ΔD_1 (commonly the same for all classes, with linear classification), are proportional to the class widths, ΔD_2 , of the second, that is,

$$\Delta D_1 = \gamma \Delta D_2 , \quad (E76)$$

where γ is the constant of proportionality. The truth of this statement can be seen by reference to Eq. (E66). There is nothing in this equation that depends on class width. It is merely the total number of the classes, n_1 vs n_2 , that would cause differences in the summation terms between the two samples. Hence, Eqs. (E71) through (E75) also apply to the additional proportionality condition of Eq. (E76).

These principles of class-by-class proportionality for linearly classified data are illustrated in Figure E8. (The principles also apply to irregularly-classified and geometrically-classified data, as well, see footnote below.)^{*} In this figure, it is seen that a change in the class width, as shown by a comparison of the two upper histograms, does not change the value of F (which happens to be 0.264). Similarly, a change in the absolute number concentrations of the drops or particles in corresponding classes of comparative samples does not change the F value, as illustrated by the contrasting histograms at the upper right and lower left in the figure. The general case situation is sketched at the lower right in the figure. The form factor value will remain constant in this general case for any number concentration value of reference, N_r , and any class width, ΔD , one chooses to specify.

We might summarize at this point before diverting to the next topic of essential background information. Thusfar, we have established the conditions which yield identical F values between comparative samples, which are the same conditions that yield zero values of $\Delta \log F$ in Eqs. (E64) or (E66). Under these conditions, the departure equation for the exponent of the M vs Z regression equation, that is, Eq. (E65) reduces to

$$\Delta E = \frac{0.5 \Delta \log N_T}{\Delta \log Z_s} \quad (E77)$$

*The principles of class-by-class-proportionality discussed above for linear classification also apply to irregularly-classified data (in which the diameter widths of the classes differ between classes) and geometrically-classified data, such as that of the SAMS tables of Appendix G. This can be seen by reference to the form factor equations for irregular classification and geometric classification which have been presented in the footnote on page 119. For irregular classification, the form factor values between any comparative samples will be the same providing that the D_i ratios of Eq. (E23a) are commonly the same, class by class, between the samples. In other words, the F values will be identical if

$$\Delta D_{i_1} = \gamma \Delta D_{i_2} \quad (E76a)$$

where ΔD_{i_1} and ΔD_{i_2} are the class widths of the comparative samples and γ is a constant of proportionality that pertains commonly to all classes, $i = 1$ through $i = n$.

With geometric classification, the F values between comparative samples will likewise be the same insofar as the ratios of D_n/D_{1L} of Eq. (E23b) are the same between samples. However, since D_{1L} (the lower limit of the first size class) is not zero, in geometric classification, as it is with irregular and linear classification, the form factor values between comparative samples will change if D_{1L} is specified to have a particular absolute value that is held constant.

which shows that the exponent departures are caused solely by differences in the total number concentrations of the ice hydrometeors contained in the different samples.

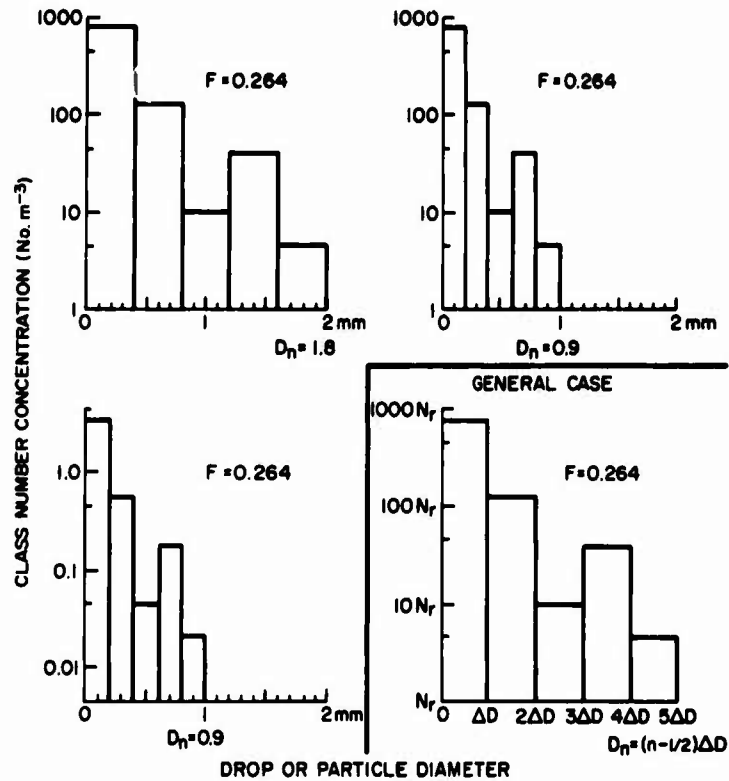


Figure E8. Illustrations of Class-By-Class Proportionality Which Yield Identical Values of the Form Factor, F . The general case situation is shown in the diagram at the lower right, which holds for any number concentration of reference, N_r , and any class width, ΔD , one chooses to specify

E5.7 Data Sets of Illustration and a Description of the "Physical Method" of Obtaining the M vs Z Equation

Reference is now made to the disdrometer, large-snow and ice-crystal data that are shown plotted in Figures E9, E10, E11, and E12. These data illustrate the typical values and trends (with $\log Z_g$) of the parameters of prior discussion and will permit us to demonstrate how the M vs Z regression equations for sets of hydrometeor data may be obtained in a manner that considers the physical nature of the spectral properties of the hydrometeors.

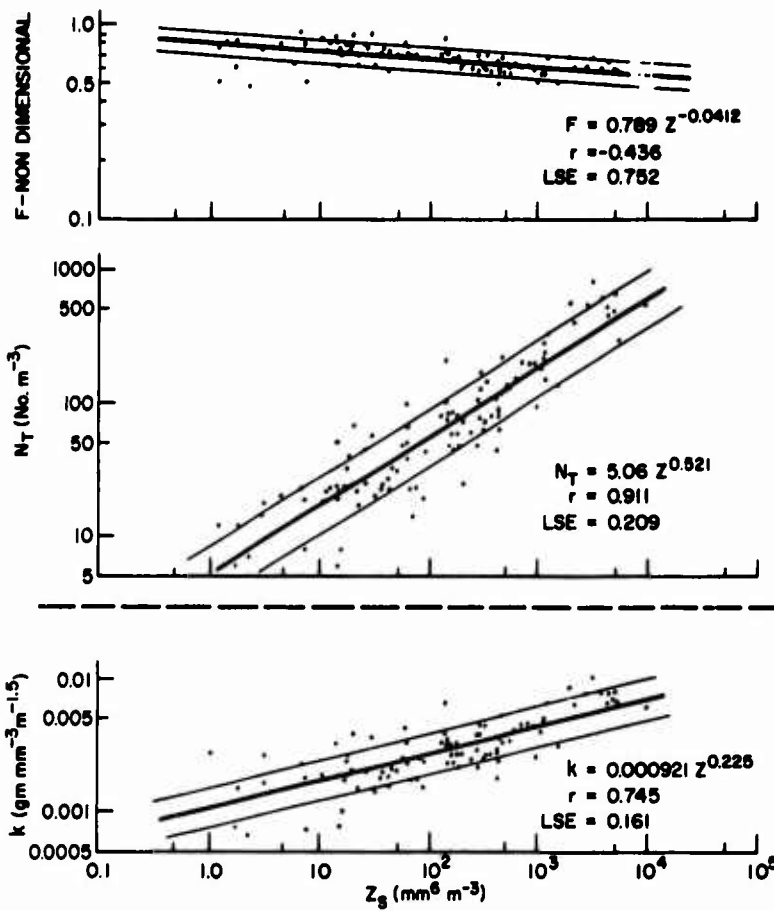


Figure E9. Plots of F, N_T and k, vs Z_s , for Rain Data From Disdrometer A Obtained on 22 March 1972. The regression lines, equations, correlation coefficients (r) and log standard errors (LSE) are indicated as are the error bounds of the LSE's (the lines bounding the regression line)

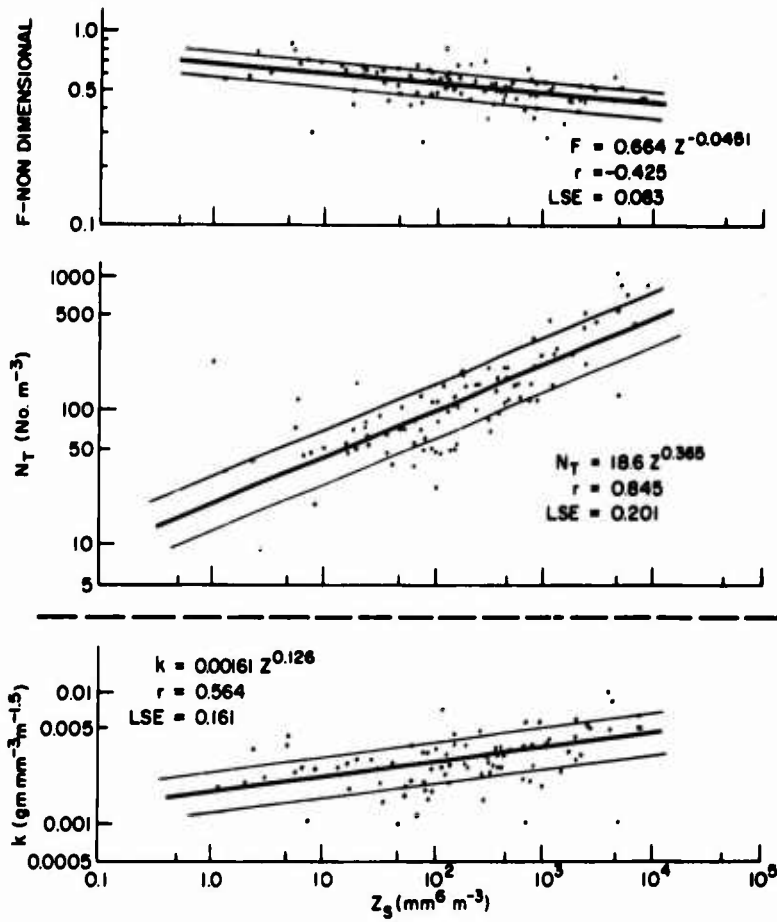


Figure E10. Plots of F , N_T and k , vs Z_g , for Rain Data From Disdrometer B Obtained on 22 March 1972. The regression lines, equations, correlation coefficients (r) and log standard errors (LSE) are indicated as are the error bounds of the LSE's (the lines bounding the regression line)

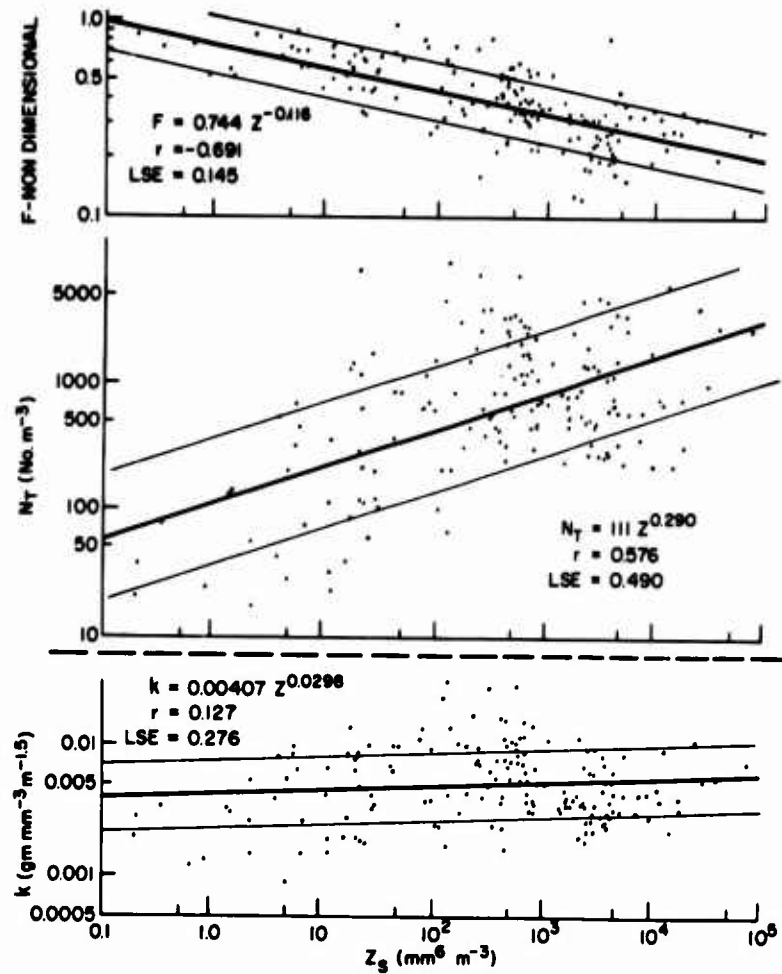


Figure E11. Plots of F , N_T and k , vs Z_g , for the Data of Ohtake and Henmi¹⁵ (1970) for Large-Snow of Dendritic-Stellar Type (LS₅). The regression lines, equations, correlation coefficients (r) and log standard errors (LSE) are indicated as are the error bounds of the LSE's (the lines bounding the regression line)

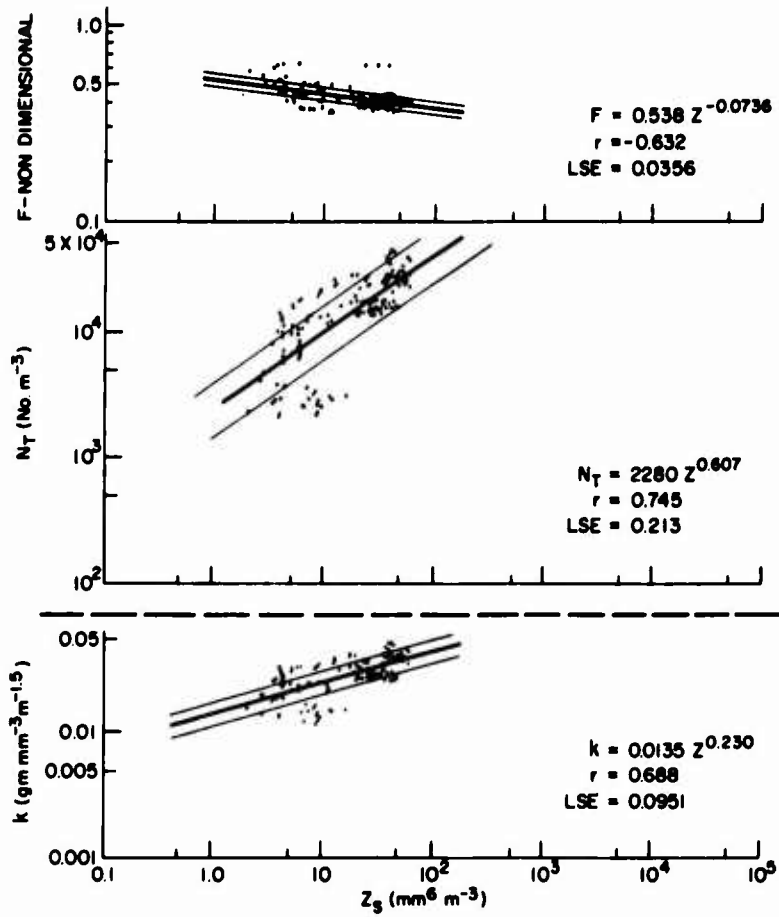


Figure E12. Plots of F , N_T and k , vs Z_g , for the Ice Crystal Data of PVM-5 (Barnes, Nelson and Metcalf)¹⁶. The regression lines, equations, correlation coefficients (r) and log standard errors (LSE) are indicated as are the error bounds of the LSE's (the lines bounding the regression line)

Disdrometer and large-snow data were presented in R No. 2 which showed cross-plots of the M vs Z values for two sets of disdrometer data obtained on 22 March 1972 (obtained from different instruments, identified as the A and B disdrometers) and for the data of Ohtake and Henmi¹⁵ as analyzed by Vardiman,^{*} for large snow of dendritic-steilar-type. From the original, basic data of these three sets, we determined the F values, the N_T values and the k values for each individual sample. ^{**} The values of these parameters, cross-plotted vs the Z_g values of the samples, are shown in the diagrams of Figures E9, E10, and E11. The plots of F vs Z_g are presented in the upper diagrams of each figure; those of N_T vs Z_g are presented in the middle diagrams; those of k vs Z_g are presented in the bottom diagrams. The regression lines that fit the data are shown and the regression equations, correlation coefficients, and log standard error values are indicated. It will be noted that the diagrams have logarithmic scales. Thus, the "slope" of the regression lines for the respective diagrams provide measures of the $\Delta \log F / \Delta \log Z_g$, $\Delta \log N_T / \Delta \log Z_g$, and $\Delta \log k / \Delta \log Z_g$ terms that enter into the "exponent", and "exponent departure", equations previously presented, that is, Eqs. (E59), (E61), and (E65).

The ice-crystal data of PVM-5 (Barnes, Nelson and Metcalf)¹⁶ are shown plotted in Figure E12, in the same format as for the other figures described above. These data are different than the disdrometer and large-snow data, however, in that particular f to D conversion assumptions were employed as discussed by the authors. This means, without going into details, which we will discuss later for ice hydrometeors in general, that the Z_g values of these ice-crystal samples are subject to much greater uncertainties, relatively, than are those of the disdrometer and large-snow samples of the other figures. Hence, again without detailed discussion, which is premature at this point, we may state that the "log slopes" of the regression lines of the Figure E12 diagrams provide valid measures of $\Delta \log F / \Delta \log Z_g$, $\Delta \log N_T / \Delta \log Z_g$, and $\Delta \log k / \Delta \log Z_g$ but that the coefficient, K , of the M vs Z equation [Eq. (E46)] is subject to important uncertainties, because of its dependence [see Eq. (E60)] on $\sqrt{\log Z_g}$, which is uncertain due to the Z_g uncertainties mentioned.

From the data of these figures, it is seen that the form factor values typically decrease with increasing Z_g and that $\Delta \log F / \Delta \log Z_g$ is negative, with values, for the four data sets, ranging from -0.041 to -0.118. The N_T values increase with Z_g and $\Delta \log N_T / \Delta \log Z_g$ is positive, with values ranging from 0.365 to 0.607. The k values [which are dependent on those of F and N_T see Eq. (E22)] increase with

* Unpublished work performed for AFCRL by L. Vardiman of Colorado State University (on reserve status from the Air Weather Service).

** The large-snow data of Ohtake and Henmi¹⁵ are devoid of f to D conversion problems, since, (see the footnote on page 128) their measurements were made directly in terms of equivalent-melted-diameter.

Z_g ; the $\Delta \log k / \Delta \log Z_g$ slope is positive; the slope values range from 0.037 to 0.230.

The diagrams of these figures effectively reveal some of the physical reasons why the M vs Z regression equations that are employed in SAMS have particular coefficient and exponent values. However, before discussing these, it is of interest to demonstrate specifically that the K and E values obtained by the "physical method" are the same as those obtained by the standard, conventional method, of direct M vs Z regression.

We may demonstrate the equivalence in two different ways. First, from Eq. (E10), we may solve for k to obtain

$$k = M Z^{-0.5} \quad (E78)$$

We may substitute for M in the above equation, from Eq. (E46), to write

$$k = K Z^{E-0.5} \quad (E79)$$

From Eqs. (E59) and (E61),

$$\Delta E = E - 0.5 \quad (E80)$$

which permits us to write the preceding equation as

$$k = K Z^{\Delta E} \quad (E81)$$

This last equation is the general equation that describes the regression of k with Z (or Z_g). In other words, it is the general equation that describes the regression lines shown in the bottom diagrams of Figures E9 through E12. Thus, it is apparent that the values of the coefficients of the equations of these diagrams (the equations have been typed thereon) are the values of K and that the exponent values of the equations are the values of ΔE , which are related to E in the manner prescribed by Eq. (E80), that is, $E = \Delta E + 0.5$.*

We may compare the K and E values of the bottom diagrams of Figures E9 through E12 with the K and E values obtained by the direct regression of the M_g and Z_g values of the data samples. Thus, for the rain data of the A Disdrometer of Figure E9, $K = 0.000921$, with $E = 0.725$ ($K = 0.000922$, with $E = 0.725$), where

*It might be noted with regard to Eq. (E81) that K is the particular value of k that exists for a Z (or Z_g) value of unity. Likewise, with regard to Eq. (E46) K is the particular value of M that exists for a Z value of unity. Therefore, when $Z = 1.0$, $k = M = K$.

the first values are those from the diagram equations and the values within the parentheses are the ones of standard, direct regression. For the rain data of the B Disdrometer of Figure E10, $K = 0.00161$, with $E = 0.626$ ($K = 0.00161$, with $E = 0.626$). For the large-snow data of Ohtake and Henmi of Figure E11, $K = 0.00407$, with $E = 0.530$ ($K = 0.00420$, with $E = 0.526$, see Table 2 of R No. 2, for large-snow of type LS_5). For the ice-crystal data of PVM-5 of Figure E12, $K = 0.0135$, with $E = 0.730$ ($K = 0.0135$, with $E = 0.731$).

With the exception of the Ohtake-Henmi data, see footnote below, * the agreement between methods is excellent, which demonstrates their equivalence.

The second demonstration of equivalence involves the data plots and regression equations of the two upper diagrams of Figures E9 through E12. With regard to the form factor data and equations of the first of these diagrams, it may be pointed out that the coefficient values of the equations are the particular values of F that "exist" at a Z (or Z_g) value of unity. We will symbolize these particular values as " F_1 ". The exponent values of the F equations are, of course, the values of the "log slope" of the regression lines. Likewise, with regard to the total number concentration data and equations of the second of the figure diagrams, the coefficient values of the regression equations are the particular values of N_T that exist at a Z value of unity, which we will symbolize as " N_{T1} ". The exponent values of the N_T equations are the "log slopes" of the regression lines.

The following relationships prevail, that relate the regression equations for F , N_T and k to the coefficient, K , and the exponent, E , of the M vs Z equations.

With regard to the coefficients, it is apparent, from Eqs. (E81) and (E22) that

$$K = k_1 = C \sqrt{N_{T1}} F_1 \quad (E82)$$

where k_1 is the particular k value corresponding to a Z (or Z_g) value of unity.

With regard to the exponents,

$$\Delta E = \frac{\Delta \log F}{\Delta \log Z_g} + \frac{0.5 \Delta \log N_T}{\Delta \log Z_g} \quad (E83)$$

from Eq. (E85) and, as mentioned earlier,

$$E = \Delta E + 0.5 \quad (E84)$$

* In our re-analysis of the Ohtake-Henmi data, we found various errors in the Vardiman-Ohtake-Henmi computations. These were corrected and this is the primary reason for the differences in the K and E values cited above.

The values of F_1 , N_{T1} , $\Delta \log F / \Delta \log Z_g$, and $\Delta \log N_T / \Delta \log Z_g$ are listed in the first four columns of Table E11 for each of the sets of hydrometeor data of Figures E9 through E12. Also listed, in the next three columns, are the values of K ($= k_1$), ΔE and E , which were computed from Eqs. (E82), (E83), and (E84) above.

A comparison of the K and E values of this table with those of the standard method of direct regression, cited earlier on page 145, shows good correspondence, which again verifies the equivalence of the regression techniques of the "physical method" and those of standard convention. There are some differences in the comparative values, larger than in the previous comparison, but these stem mostly from lack of perfect correlation (not to be expected) between the F and N_T values of the samples of the data sets, also from problems of computational "round off errors".

Before continuing, it might be noted that the centroid points of the data sets of the individual figures, E9 through E12, should be expected to obey the relationship of Eq. (E46) to a first approximation. For the convenience of future work herein, we will demonstrate that this is true.

The centroid values of $\overline{\log Z_g}$, $\overline{\log F}$, and $\overline{\log N_T}$ are listed in columns eight, nine, and ten, of Table E11, for each of the data sets of the first two diagrams of Figures E9 through E12. The values of

$$(\log k)_A = \log C + \overline{\log F} + 0.5 \overline{\log N_T}, \quad (E85)$$

which stems from the log form of Eq. (E46) are listed in column eleven of the table. The comparison values of $\overline{\log k}$, which are the direct average values of the sample data of the bottom diagrams of Figures E9 through E12, are listed in column twelve. The table reveals that the $(\log k)_A$ values determined from the equation are closely the same as the $\overline{\log k}$ values of direct averaging.

The prime advantage of the "physical method" of regression is that, by its use, we gain understanding of the spectral characteristics of hydrometeors which can cause the different K and E values of the various categories and types of precipitation. For example, it is seen, from the data sets and equation references made heretofore, that the major determinant of the K values, and their category and type differences, is the total number concentration of the drops or particles (for comparable Z_g values). With regard to the determinants of the E values, we observe, first of all, that the total number concentrations of the drops or particles increase appreciably with increasing Z_g . This is logical and to be expected. However, we also observe that the values of the form factor decrease with increasing Z_g . This means that the two terms, $\Delta \log N_T / \Delta \log Z_g$ and $\Delta \log F / \Delta \log Z_g$, of Eq. (E85) contribute counteractively to the values of ΔE [hence E through Eq. (E84)]. This is not a type of spectral behaviour we would have suspected a-priori.

Table E11. Values of the Regression Parameters for the Rain, Large-Snow and Ice-Crystal Data of Figures E9, E10, E11, and E12, see Text Discussion

Data Identity	F ₁	N _{T1}	$\frac{\Delta \log F}{\Delta \log Z_s}$	$\frac{\Delta \log N_T}{\Delta \log Z_s}$	K (-k ₁)	ΔE	E	log Z _s	log F	log N _T	(log F) _A	(log F)
Rain Data for Disdrometer A (See Figure E9)	0.789	5.06	-0.0412	0.521	0.000930	0.219	0.719	2.087	-0.189	1.792	-2.574	-2.565
Rain Data for Disdrometer B (See Figure E10)	0.664	18.6	-0.0451	0.365	0.00150	0.137	0.637	2.268	-0.280	2.098	-2.512	-2.507
Ohtake-Henmi Data for Large-Snow (see Figure E11)	0.744	111	-0.116	0.290	0.00411	0.0290	0.529	2.495	-0.419	2.771	-2.314	-2.316
PVM-5 Data for Ice-Crystals (See Figure E12)	0.434	2280	-0.0736	0.607	0.0109	0.230	0.730	1.267	-0.362	4.127	-1.579	-1.579

The spectral physics of the hydrometeors is not completely revealed by the diagrams plots of Figures E9 through E12. This is because the form factor values are not uniquely descriptive of the spectra. The same values, in other words, can be obtained from a variety of different distributions. This was demonstrated previously in the histograms of Figures E4 and F5.

We can conduct additional analyses, however, of the type illustrated in Figure E13, to establish the kind of spectral behavior that causes the decreasing trend in the form factor values. In this figure, the form-factor data of Ohtake and Henmi, of Figure F13, have been re-plotted at larger scale in the upper diagram. The bounds of the log standard error of estimate about the regression line are indicated and three rectangular "boxes" are shown, labeled "A", "B", and "C". The number concentration data for all of the samples within these boxes were combined and normalized in the conventional terms of class number concentration, N , per m^3 of atmospheric volume. The resulting composite spectra, of N vs the equivalent-melted-diameter, D , of the snow particles in the classes, are shown in the three diagrams immediately below the scatter plot. The form factor values for the composite distributions are noted. The spectral trends with increasing Z_g are apparent from these diagrams. The spectra are seen to be near-exponential and, for small values of Z_g , the maximum particle diameters are small and the decrease of $\log N$ with D (the "exponential slope") is very "steep". For intermediate values of Z_g , the maximum particle diameters and the exponential slope are likewise intermediate. For large values of Z_g , the maximum particle diameters are large (up to 3.2 mm) and the exponential slope is relatively shallow. These trends are not unexpected, since they have been reported previously and have been replicated in various spectral models, including the SAMS "Precipitation Model" described in Appendix G, see Figure G9. However, this may be the first time that such spectral trends have been demonstrated in the context of their specific influence on the coefficient and exponent values of the M vs Z equation.

There are three particular points in the scatter plot of Figure E13 which are labeled "D", "E", and "F". These points are far removed from the regression line and are at the extremities of the data scatter. It was of interest to ascertain how the spectra of these individual samples differed from the composite spectra of the samples within the A, B, and C boxes which lie within the standard error bounds. These particular spectra are illustrated in the three bottom diagrams of the figure. The reasons why the samples have anomalous F values are fairly apparent. The "D Sample" has a relative deficit of small particles and has a spectral form roughly similar to that of the last histogram of the top row of Figure E4, which yields a large F value. The "E Sample" has a spectrum similar to that of the fifth histogram from the left, at the top, in Figure E4, which was specifically mentioned, on page 125, as being of a type associated with small values of the

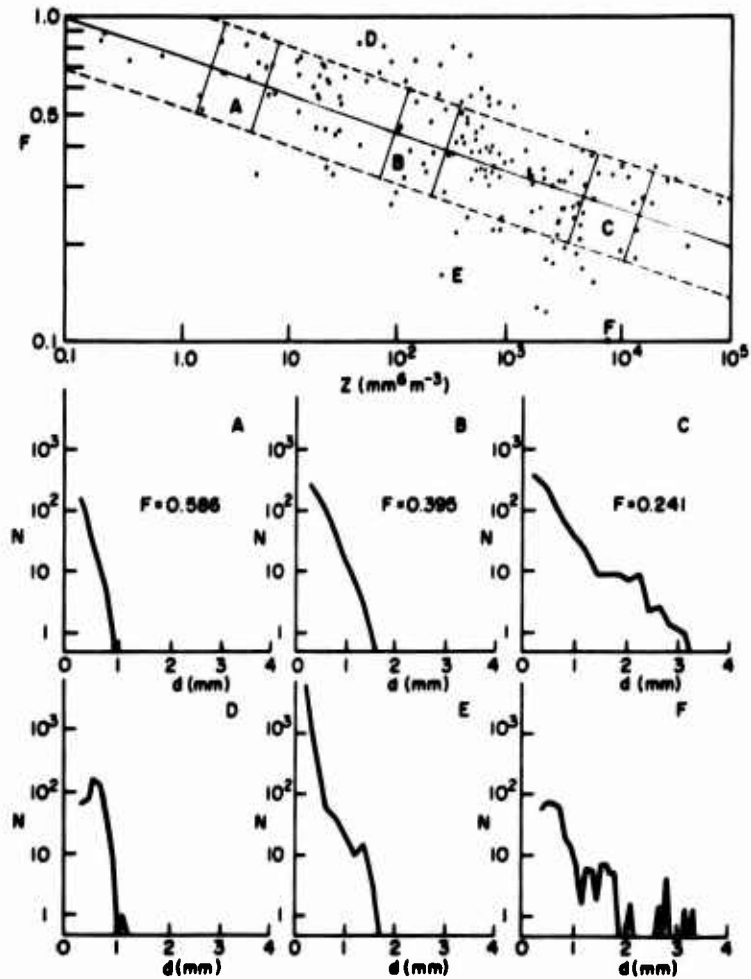


Figure E13. Illustrations of the Spectral Characteristics and Trends of the Form Factor Values for the Data of Ohtake and Henmi. The form factor values are shown plotted vs Z in the upper diagram and the regression line (solid) and lines of the log standard error of estimate (dashed) are indicated. These are the same data and lines shown plotted in the upper diagram of Figure E11. The composite spectrum, of particle number concentration (N) vs equivalent-melted-diameter (D), for all of the data samples whose points are contained within the rectangle labeled "A", is shown in the first of the smaller diagrams at the upper left. The composite spectra for the rectangles labeled "B" and "C" are shown in the next two diagrams. The particular spectra for the samples "D", "E", and "F", whose points lie at the extremities of the data scatter, are shown in the bottom diagrams

form factor. The "F Sample" is of a multi-modal type which, one suspects, is probably not a "representative sample" (that is, there are too few contained total particles to be representative). Multiple modes, depending on where they occur over the diameter range, can cause quite erratic behaviour of the form factor values, see the two upper rows of histograms of Figure F5. The modes of the "F Sample" are such as to cause a small value.

A general description of the form factor values for exponential distributions is presented in Appendix II and illustrated in Figures H1 through H5. From the first of these figures, it is seen that the form factor values for non-truncated distributions vary regularly with the descriptive parameters n (the number of classes) and ΔD_n (the non-dimensional product of the "exponential slope" times the diameter range of the distribution).^{*} The maximum F value (= 1.0) occurs with monodispersed distributions; the minimum value (≈ 0.222) occurs for very-large n ($\rightarrow \infty$) associated with very-large ΔD_n ($\rightarrow \infty$). This is a "theoretical minimum" only, since neither n nor ΔD_n would ever, in practice, have values much greater than about 50, for n , or 15, for ΔD_n . (ΔD_n is a parameter analogous to ΔD_m , which is discussed in Appendix G and shown to having limiting atmospheric values of the order of 12, or 15, at most.)

A uniform distribution (all class number concentrations equal) is a special case of an exponential distribution. The F values for uniform distributions decrease from 0.733, for $n = 2$, to 0.664, for $n = 10$, to 0.6615, for $n = 100$, to a limit of ≈ 0.6614 , for $n \rightarrow \infty$.

Certain general statements can also be made about how changes of spectra will affect the form factor values. Truncation, for instance, with either lower diameter truncation or upper diameter truncation (see Figures H1 through H5 of Appendix H) will increase the F values, relative to the non-truncated ones. With bi-modal spectra, increased diameter separation of the modes, other spectral characteristics being held the same, will result in decreased F values, and vice versa. Similarly, any number concentration increase in a model peak at small diameter, relative to one at larger diameter, will decrease the F values, and vice versa.

16. SUMMARY AND EXPLANATION OF THE PARADOX QUESTION

At this point, we have established sufficient background to enable us to return to the "paradox question" raised earlier and provide an explanation. However, before doing this, we will review the basis for the question and repeat the question itself.

^{*}It may be stated that, with the exception of monodispersed distributions, at least 10 classes ($n = 10$) or more are required, with classified data, to provide an adequate description of a theoretical distribution function, such as one of exponential type. The same is true, in general, concerning the number of classes needed to provide adequate description of any continuous spectra, either atmospherically observed or theoretical. Hence, the form factor values of the above-cited figures, for $n < 10$, are really a special category of values which pertain to classified data that lack adequate resolution (sufficient classes) to describe the true spectra. Admittedly, we have violated this rule ourselves, herein, primarily for the convenience of illustration.

In the analyses of the foil impactor records at the beginning of the appendix, M and Z values derived from individual samples of ice particles were found to evidence very-large variability dependent on the analysis methods used, the crystal-type selected and the particular assumptions about ℓ to D_e conversions. With presumed knowledge of crystal-type, it was found that the M values of a given sample could readily be uncertain, due to various causes which were identified and discussed, over a spread exceeding a factor of 3, with the Z values being uncertain over a spread exceeding a factor of 10. Without knowledge of crystal-type, or with the forced assumption of type, as has been necessary in numerous Wallops storms of past SAMS analysis, it was ascertained that the uncertainty spread of the M values could be as large as a factor of 19; that of the Z values as large as a factor of 340.

When the M and Z values of the samples, as determined by the different methods and assumptions; were cross-plotted and compared with the regression equation for C_1 ice crystals, which is the single equation used thus far in SAMS, it was discovered that the data corresponded quite nicely with the regression line. The departure of the M values from the line was generally less than a factor of 1.4; the departure of the Z values was generally less than a factor of 2. This raised the paradox question, "How is it possible that foil-sample data which evidence "uncertainty scatter" exceeding an order of magnitude in M and two orders of magnitude in Z can "conform to, and "agree with", the values of equation prediction to within less than a factor of two difference?"

Part of the answer was found in the work described on pages 116 through 133. The equation,

$$M_s = k Z_s^{0.5}, \quad (E17)$$

for "single samples" was developed and the coefficient k was shown to be dependent on

$$k = C \sqrt{N_T} F, \quad (E22)$$

where C is a particular number [see Eq. (E12)], N_T is the total number concentration, of the drops or particles of all sizes in the sample, and F is the form factor, which is a non-dimensional factor that describes how the number concentrations of the drops or particles in the different disdrometer classes are apportioned relative to each other, over the diameter range of the sample, and relative to the total number concentration value for the sample.

The k values of the foil samples were next computed which corresponded to the different analysis methods and assumptions about crystal type and ℓ to D conversions. These values were closely similar for the different analysis methods applied to individual samples, also between samples. The uncertainty spread of the k values

was about an order of magnitude smaller than the M value uncertainties cited above, and about two orders of magnitude smaller than the cited Z value uncertainties. The reason why the k values were relatively non-variant for the same samples analyzed by different methods is that N_T , for any given sample, remains constant irrespective of analysis method, also that the F values do not differ materially with method.* The reason that the k values between the different samples were similar for the foil data is that the N_T and F values of the separate samples were not importantly different, in their effect on k through Eq. (E22) (see Tables E4 and E5).

The isolines of k, from Eq. (E17) were shown to be "straight lines" plotted on a diagram having a log Z abscissa and a log M ordinate. The "log slope" of the isolines was 0.5 (see Figure E4).

The particular isolines of k for the basic foil data (before ℓ to D conversion) and for the equivalent-melted-diameter, or D, data (as analyzed by the different, stated methods and assumptions regarding ℓ to D conversions) were plotted in Figure E5. The envelope of the isolines for the basic data had very small "spread" and the "isoline envelope" for these data was contained within, and centered approximately within, the isoline envelope for the converted "D data". This revealed that, to reasonable accuracy (to be discussed further), the k values of the ice-particle samples could have been determined a-priori, without any knowledge or assumption of ice-crystal type.

The diagram also revealed (compare the isoline envelopes of Figure E5 with the regression line of Figure E3) that the M_g vs Z_g points of the samples necessarily had to correspond closely to the M vs Z values prescribed by the regression equation for C_1 ice crystals, because the k values of the samples were nearly the same as those of the equation. We will now demonstrate this specifically.

The k values for any given regression equation, of M vs Z, are readily determined by substituting for M, in Eq. (E46), the M_g value for single hydrometeor samples, of Eq. (E17) to obtain

$$k = K Z_g^{(E-0.5)}, \quad (E85)$$

or, from Eq. (E80),

$$k = K Z_g^{\Delta E}. \quad (E86)$$

*The F values will differ only insofar as there are non-linearities in the ℓ to D conversions, and these, in most cases, will be slight differences. Linear ℓ to D conversions fall in the category of "class by class proportionality", as discussed on pages 136 through 139, in which there are no changes of F resulting from conversion.

In this substitution, since k is defined only for single samples, the general regression variables, M and Z , are specifically equated to their single-sample counterparts, M_g and Z_g . Hence, in words, Eq. (E85) [or (E86)] prescribes the single-sample values of k that exist directly along the course of the equation line.

For C_1 ice-crystals, $K = 0.038$ and $E = 0.029$, see Table 2 of R No. 2, so that the above equation reduces to

$$k = 0.038 Z^{0.029} \quad (E87)$$

If we plot the above equation on a diagram having logarithmic scales, with k as ordinate and Z as abscissa, we obtain the slightly-sloping line shown in Figure E14. We can also plot the k vs Z_g points for the foil data (of Tables E8 and E9) on this same diagram. These points are shown in the diagram, coded similar to the ones of Figure E3.

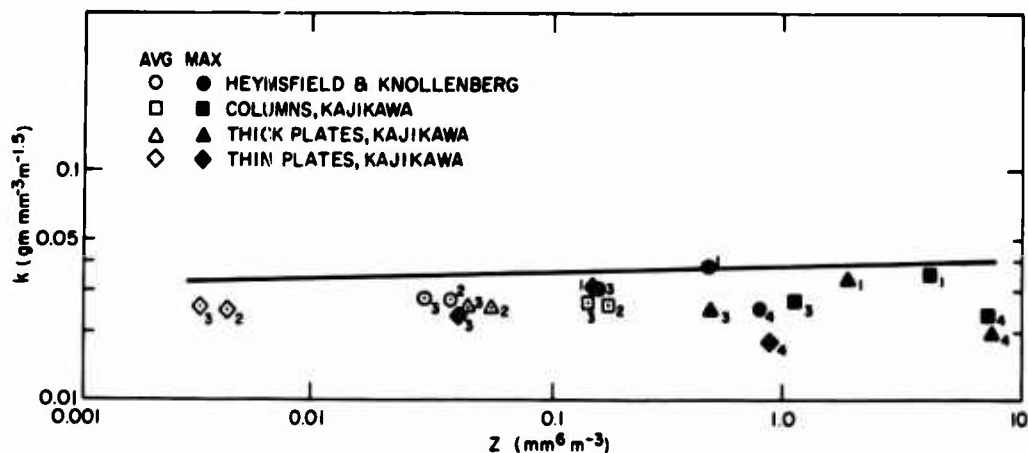


Figure E14. An Illustration of How the k vs Z_g Points of Tables E8 and E9 Fit the k vs Z Equation of Heymsfield and Cunningham, Which Pertains to C_1 Ice Crystals of Bullet-Rosette Type. The different sizing methods, samples, and assumptions discussed in the text are indicated by the symbol coding of the plotted data points. The coding is the same as used for Figure E3

A comparison of Figure E14 with Figure E3 reveals that the displacement of the data points from the equation lines is equivalent in the two diagrams. (The cycle spacing of the ordinate scales was deliberately "made equal" in both diagrams, to facilitate comparison.)

From this comparison, also see Figure E6, it is apparent that it is the "spectral parameter", k , that establishes the "quality of the correspondence" of the data

points to the equation lines. As noted previously, regarding Figure E3, the M vs Z points of this figure all lie within a factor of two displacement (in the orthogonal direction) from the equation line for C_1 ice-crystals. Likewise, the k vs Z points of Figure E14 lie within a factor of two displacement from the equation line. In the latter figure, however, it is clear that it is the parameter, k, and its variations, that is basically responsible for the orthogonal departure(s).

The paradox question is essentially answered at this point.

E7. POTENTIAL ANALYTICAL BENEFITS OF COMPUTING AND USING THE SPECTRAL PARAMETER, k

Not only has the paradox question been answered to this point but a spectral parameter has been discovered that can be computed from size-distribution data for ice hydrometeors with considerably greater accuracy than either the liquid-water-content, M, or the radar reflectivity factor, Z. This is the parameter k. Many procedures of the continuing programs can be materially simplified and made more accurate by computing and using this parameter in our analyses, as we will discuss and illustrate in the remainder of the appendix. We will first consider the absolute and relative accuracies of the three hydrometeor parameters, M, Z, and k, and illustrate the findings using particular nomograms. We will then draw conclusions, present verifying data and make recommendations for future analyses.

E7.1 Absolute and Relative Accuracies of the M, Z, and k

In considering the absolute and relative accuracies of M, Z, and k, we will first reference the foil data of previous discussion. Then, following, we will summarize the findings of certain theoretical treatments of the subject which are described in detail in Appendix H.

Previous consideration of the foil data analyzed by the different methods and l to D conversion assumptions revealed that the uncertainty spread of the M_g and Z_g values resulting from the diverse methods and assumptions was very large. Specifically, the uncertainties in the cases considered were the following: (see pages 110 through 115.

- (1) For differences in the method of measuring particle dimensions from the record of the foil impactor instrument, in terms of their "maximum dimensions", as opposed to their "average dimensions", the associated differences in M_g and Z_g , for the assumption of a given crystal type, ranged from about a factor of 2 to a factor of 5, for M_g , and from about a factor of 5 to a factor of 12, for Z_g .

- (2) For different l to D conversion methods, between investigators, for a given crystal type, the M_g differences ranged from about a factor of 2 to a factor of 3; the Z_g differences ranged from about a factor of 5 to a factor of 9,
- (3) For minor, observationally-subtle differences of ice-crystal type, as between "thin plates" and "thick plates", the M_g and Z_g differences, other assumptions held common, ranged from about a factor of 3 to a factor of 4 and from a factor of 8 to a factor of 13, respectively,
- (4) With complete lack of knowledge of crystal-type, or with the "forced assumption" of type, as has been necessary with most of the Wallops storms of previous SAMS analysis, the associated M_g and Z_g differences indicated by the foil data were as large as a factor of 19, in M_g , and a factor of 340, in Z_g .

In comparison with these cited uncertainty ranges of M_g and Z_g , the reader can see, by reference to Tables E4, E5, and E9, that the differences in the k values corresponding to the cases numbered above:

- (a) Ranged from a factor of 1.02 to a factor of 1.09 (2 to 9 percent), in Case 1,
- (b) Ranged from a factor of 1.05 to a factor of 1.13 (5 to 13 percent), in Case 2,
- (c) Ranged from a factor of 1.02 to a factor of 1.08 (2 to 8 percent) in Case 3, and
- (d) Were a factor of 1.31 (31 percent), in Case 4.

Thus, the k differences in these comparative instances were much smaller than either the M_g or Z_g differences; or, stating this conversely, the k values for the ice hydrometeors of the foil samples were determinable with considerably greater accuracy than either the M_g or Z_g values. The determination accuracy of k , for the instances noted above, was some 2 to 14 times better than that for M_g and some 5 to 260 times better than that for Z_g .

The reasons why the k values can be determined more accurately than either the M_g or Z_g values are readily demonstrated. Consider the single-sample equation for M_g , that is,

$$M_g = k Z_g^{0.5} \quad (E17)$$

If this equation is totally differentiated, regarding k as a variable,

$$\frac{dk}{k} = \frac{dM_g}{M_g} - \frac{dZ_g}{2Z_g} \quad (E88)$$

or, in finite difference form,

$$\frac{\Delta k}{k} = \frac{\Delta M_g}{M_g} - \frac{\Delta Z_g}{2Z_g}, \quad (\text{E89})$$

where \overline{M}_g and \overline{Z}_g are the mean values across the difference change.

The latter equation shows that the ratio changes in k (the uncertainty changes) will depend on the difference between two terms involving the ratio changes in M_g and Z_g . This means that, whereas the ratio changes in M_g and Z_g might be large, the associated ratio changes in k are not necessarily large; in fact they might be relatively small. That they are indeed small is shown by the evidence of the foil data (plus other evidence we will discuss next).

The first section of Table E12 shows the approximate average values of the terms of Eq. (E89) for the foil data and comparison cases described previously. The $\Delta M_g/M_g$ and $\Delta Z_g/2Z_g$ terms of the equation are seen to have values some 14 to 25 times larger than the $\Delta k/k$ values. (This is true of Cases 1, 2, and 3; Case 4 is an exception that is explained in the table.) The disparity is so large, in fact, that it is apparent that Eq. (E89) can never, in any general case situation, be used to assess the values of $\Delta k/k$.

The values of $\Delta k/k$ can be accurately assessed, however, from the k expression of Eq. (E22). Equation (E22), rewritten, is

$$k = C \sqrt{N_T} F, \quad (\text{E22})$$

which, when totally differentiated, yields

$$\frac{dk}{k} = \frac{dN_T}{2N_T} + \frac{dF}{F}, \quad (\text{E90})$$

or, in finite difference form,

$$\frac{\Delta k}{k} = \frac{\Delta N_T}{2N_T} + \frac{\Delta F}{F}. \quad (\text{E91})$$

This equation reveals that the ratio changes in k are fundamentally dependent on two summed terms involving the ratio changes of N_T (the total number concentration) and the ratio changes of F (the form factor).

Since M_g and Z_g are dependent parameters, when both are computed from the same common size-distribution-data, the negative sign of the second term in Eqs. (E88) and (E89) has significance and must be retained in any uncertainty investigation.

Table E12. Approximate Average Values of the Terms of Eq. (E89) and Average Values of the Terms of Eq. (E91) for the Comparative Cases Involving the Foil Samples That are Described in the Text, on Page 99. Also see the Footnote Comment on Page 104

Comparative Cases	Approximate Average Values of the Terms of Eq. (E89) [†]			Average Values of the Terms of Eq. (E91)		
	$\frac{\Delta M_s}{M_s}$	$\frac{\Delta Z_s}{2Z_s}$	$\frac{\Delta k}{k}$	$\frac{\Delta N_T}{2N_T}$	$\frac{\Delta F}{F}$	$\frac{\Delta k}{k}$
Case 1	~2.5	~2.4	~0.1	0.010	0.050	0.060
Case 2	~1.5	~1.4	~0.1	0	0.076	0.076
Case 3	~2.0	~1.9	~0.1	0	0.050	0.050
Case 4	~9 ^{**}	~85 ^{**}	?	0.010	0.055	0.065

[†]These can only be estimated, because of the very-large uncertainty spread of the M_s and Z_s values between methods, assumptions, and crystal types.

^{**}The entire mathematical concept of finite differences "breaks down" completely when dealing with such huge uncertainties of M_s and Z_s as are involved in this case; hence any consistent estimate of the term values of Eq. (E89) is impossible.

The second section of Table E12 shows the average values of the terms of Eq. (E91) for the foil samples and comparison cases of prior reference. It is apparent, both from the table and equation, that the $\Delta k/k$ values can be assessed much more accurately from Eq. (E91) than from Eq. (E89). The basic reason is that the right hand terms of Eq. (E91) are individually small, of the same order of magnitude as $\Delta k/k$, and that the terms are additive. In contrast, the right hand terms of Eq. (E89) are individually large and $\Delta k/k$ is the small subtractive difference between the terms.

The above equations and Table E12 results demonstrate why the k values of the foil data are, and should rationally be, inherently more accurate than either the M_s or Z_s values.

The reader might question whether generalized conclusions are warranted from such limited foil data. With this question in mind, a separate, theoretical investigation of ℓ to D conversion effects was conducted which is presented in the second section of Appendix H. This investigation considered the uncertainties of M_s , Z_s , and k that would result from the ℓ to D conversion of ice or snow particles that were sized in terms of their physical dimension, ℓ , and converted into equivalent melted diameter, D , in accord with the conventional, power-function relationship.

$$D = \gamma \ell^\phi \quad (E92)$$

under the assumptions that both the coefficient γ , and the exponent, ϕ , were subject to uncertainty.

The results of this investigation are summarized in Figures E15, E16, and E17. In each of these figures, the ratio uncertainties $\Delta Z_g / Z_g$ (solid curves), $\Delta M_g / M_g$ (dashed curves) and $\Delta k / k$ (dotted curves) are shown plotted vs the liquid-water-content, M_g . The uncertainties for large-snow of type LS_3 are shown in the first figure for four different uncertainty assumptions regarding γ and ϕ , see Tables H1 and H2, of Appendix H. The corresponding uncertainties for small-snow of type SS_g are shown in the second figure. Those for type C_1 ice-crystals are shown in the third. The figures show that the $\Delta Z_g / Z_g$ uncertainties range from about 1.4 to 5.2 (140 to 520 percent), dependent on hydrometeor type, liquid-water-content and γ , ϕ assumptions; the $\Delta M_g / M_g$ uncertainties range from about 0.071 to 2.0 (71 to 200 percent), whereas the $\Delta k / k$ uncertainties only range from about 0.10 to 0.34 (10 to 34 percent).

The figures also reveal (by forming the ratios of the decimal uncertainties) that the $\Delta k / k$ values are some 4 to 39 times less sensitive to ℓ to D conversion effects, than are the $\Delta Z_g / Z_g$ values and some 2 to 15 times less sensitive than are the $\Delta M_g / M_g$ values. Less sensitivity means, of course, that the k values for ice hydrometeors, for which ℓ to D conversions are required, can be determined more accurately, by these amounts, than either Z_g or M_g can be determined.

It is pertinent to note, see Eqs. (H40) and (H41) of Appendix H, that the decimal uncertainties of k depend only on the uncertainties of the exponent, ϕ , of Eq. (E92) whereas the decimal uncertainties of M_g and Z_g , besides being dependent on the exponent uncertainties, are also dependent on the uncertainties of the equation coefficient γ . The situation is discussed in Appendix H. Basically, however, the fact that $\Delta k / k$ does not depend on $\Delta \gamma$ stems from the principle of "class by class proportionality", that was described on pages 135 through 137. Only the non-linearities of conversion, which arise when $\phi \neq 1.0$, can cause changes or uncertainties in the k values. (Actually, it is the F values which contribute to k through Eq. (E22) that are specifically affected. The N_T values, which also contribute, remain unchanged with conversion.)

It should be emphasized, before leaving this section, that the $\Delta Z_g / Z_g$, $\Delta M_g / M_g$, and $\Delta k / k$ uncertainties indicated in Figures E15, E16, and E17 are strictly those pertaining to the effects of ℓ to D conversion. Other uncertain influences on Z_g , M_g , and k , such as discussed on pages 101 through 104, were not considered in the theoretical investigation.

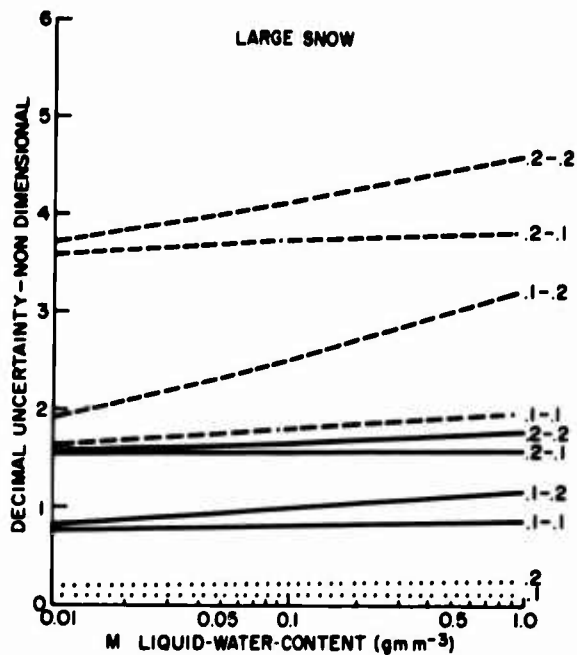


Figure E15. Equation Plots of the Decimal Uncertainties of Radar Reflectivity Factor, $\Delta Z_s/Z_s$ (dashed curves), of Liquid Water Content, $\Delta M_s/M_s$ (solid curves) and of the Spectral Parameter k , that is, $\Delta k/k$ (dotted curves), for Large Snow of Type I.S₃. The assumed uncertainties of ℓ to D conversion, that is, $\Delta\gamma$ and $\Delta\phi$, see Eqs. (H22), (H29), (H30), and (H38) of Appendix H, indicated for each of the curves. The first number is the assumed $\Delta\gamma$ uncertainty; the second is the assumed $\Delta\phi$ uncertainty. Since $\Delta k/k$ is functionally dependent on $\Delta\phi$ alone, only the $\Delta\phi$ assumptions are indicated for these curves

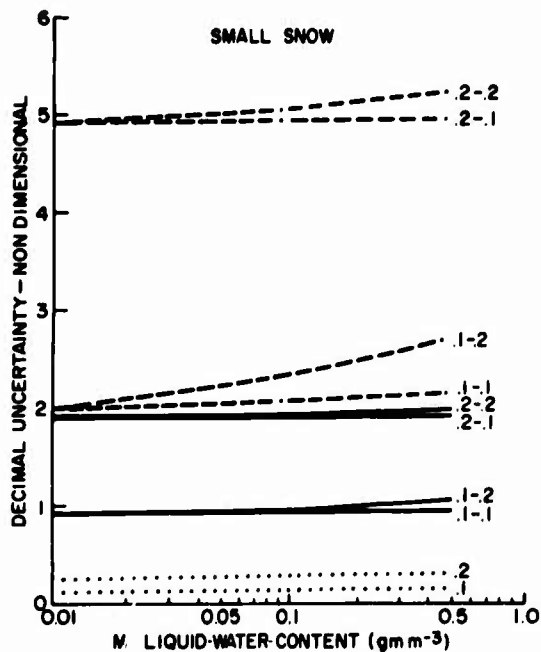


Figure E16. Equation Plots of the Decimal Uncertainties of Radar Reflectivity Factor, Liquid-Water-Content and the Spectral Parameter k , for Small Snow of Type SS_s (see caption of Figure E15 for a description of the curves)

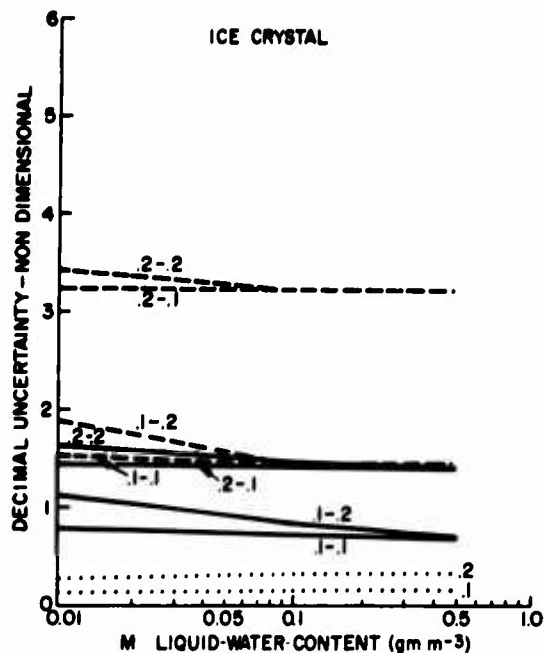


Figure E17. Equation Plots of the Decimal Uncertainties of Radar Reflectivity Factor, Liquid-Water-Content and the Spectral Parameter k , for Ice-Crystals of Type C_1 (see caption of Figure E15 for a description of the curves)

E7.2 Nomographic Illustrations of the Comparative Accuracies of the Spectral and Radar-Measured Parameters of the SAMS Program

The nomogram shown in Figure E18 has been found to be exceedingly useful for the consideration and illustration of the values, relationships, and uncertainties of the parameters of previous discussion. The ordinate scale of the nomogram is k ; the abscissa scale is Z . The isolines of M on the nomogram, as computed from Eq. (E17), are the lines that slope upward to the left. From value knowledge of any two of the parameters, M , Z , or k , the nomogram provides the value solution for the third.

For purposes of familiarizing the reader with this nomogram, the particular k vs Z equations are shown plotted thereon for C_1 ice-crystals, for small-snow, of type SS_s , for large-snow, of type LS_s and for widespread rain, of type R_{JW} . [The general equation is Eq. (E86)]. These are hydrometeor categories and types that have been commonly referenced in prior SAMS analyses and their equation lines on the nomogram show the relative k , Z differences between categories, for these types.

Type designations for hydrometeors were specified in R No. 2 and the particular M vs Z equations for the types were listed in Table 2. The k vs Z equations cited above are related to the M vs Z equations through Eqs. (E84) and (E86). The "M" subscript, applied to the K and E parameters of the cited table, has not been retained in the work herein.

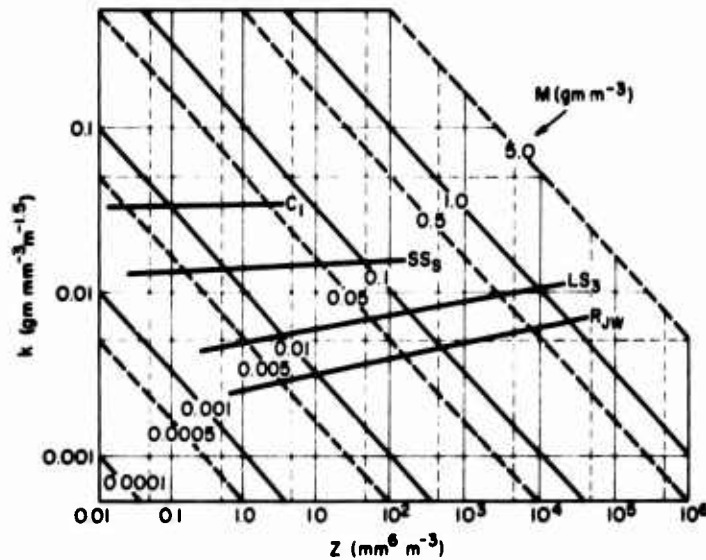


Figure E18. Example of Nomogram of k (ordinate) vs Z (abscissa) With Isolines of M . The particular equation plots, of k vs Z , are also shown for C_1 ice-crystals, for small-snow, of type SS_s , for large-snow, of type LS_s and for widespread rain, of type R_{jw} .

By use of this form of nomogram, we can progressively illustrate the SAMS situations, concerning ice hydrometeors, in which we (1) correlate the M and Z computed from spectral data, (2) correlate the M values computed from spectral data with the Z values measured by radar and (3) correlate the k values computed from spectral data with the Z values measured by radar. In each of these situations, it is assumed, for the convenience of illustration, that $Z = 25 \text{ mm}^6 \text{ m}^{-3}$, $M = 0.15 \text{ gm m}^{-3}$, and $k = 0.03 \text{ gm mm}^{-3} \text{ m}^{-1.5}$, which values are consistent with Eq. (E17).

In Situation 1, if the M and Z values are both computed from the same, common spectral data, the uncertainty bounds of the M and Z values will be approximately as indicated by the shaded areas of lightest tone in Figure E19. The specifics of

the uncertainty assumptions are explained in the footnote below. The overlapping area of the common M, Z uncertainties on the nomogram is the rhomboid indicated by the second stage of shading. If the M, Z values were independent values, this would be the "uncertainty rhomboid". However, the M, Z values computed from spectral data are not independent, hence, the actual uncertainty area on the nomogram is the horizontal, quasi-rectangular area indicated by the cross-hatching. (The vertical dimension of the rectangle is dictated by the k value uncertainties which are discussed below and illustrated in Figure E21.)

In Situation 2, in which the M values computed from spectral data are correlated with the Z values of radar measurement, the uncertainties are approximately as illustrated in Figure E20. The uncertainties of M are unchanged from the previous nomogram. However, the uncertainties of the radar-measured values of Z are substantially smaller than the uncertainties of the Z values of spectral computation. Radar-measured Z is uncertain to about ± 2 dB, with a carefully-calibrated, well-maintained radar, see Tables B1 through B4 of R No. 1, for example. This ± 2 dB of uncertainty is indicated in the Figure E20 nomogram. It is seen from the nomogram that the uncertainty area for spectral M correlated vs radar Z is a rhomboid that is "tall", vertically. This uncertainty area is orthogonally oriented, relative to that of Figure E19. It is pertinent to note that this method of correlation, here illustrated, is the one that is currently being employed in the SAMS program at Wallops Island, Virginia.

*The specific assumptions that were employed to obtain the M, Z and k uncertainties of Figures F19 and E21 were the following: It was assumed that the total number concentration of the ice hydrometeors would be measureable, in a proper-operating, well-maintained instrument of the Knollenberg type, to within a factor of two (approximately ± 1.5 dB). It was assumed, reference the theoretical work of Section 2, Appendix II, and Figures E15 through E17, that the uncertainties of f to D conversion would correspond approximately to a $\Delta\gamma = 0.2$ and a $\Delta\phi = 0.2$, which gives $\Delta Z_g/Z_g$, $\Delta M_g/M_g$, and $\Delta k/k$ uncertainties that are in approximate accord with those determined from the combined, comparable Case 2 and Case 3 situations of the foil data investigation, see page 156. It was also assumed that the differences of length-measure relationships between the physical measures of crystal or particle size and the sizes measured by the particular instrument, would cause component uncertainties of Z, M, and k of the order indicated under the Case 1 situation of the foil data investigation, that is, approximately \pm a factor of 2, for M and \pm a factor of 4, for Z).

The total uncertainties, of all combined components, were estimated, by mathematical-nomographic techniques, with probable error summation, to be \pm a factor of 10 (approximately ± 10 dB) for Z, \pm a factor of 5 (approximately ± 5 dB) for M and \pm a factor of 1.6 (approximately ± 2 dB) for k.

As mentioned in previous AFRL/SAMS Reports, the uncertainties, since they are large fractions or multiples of the basic values themselves, are highly non symmetric", in their positive vs their negative amounts. Thus, the above uncertainties quoted are not specifically relatable in terms of factors of difference, percent differences, or dB. Decibels are used in Figures E19, E20, and E21, to facilitate comparisons with the radar measurements.

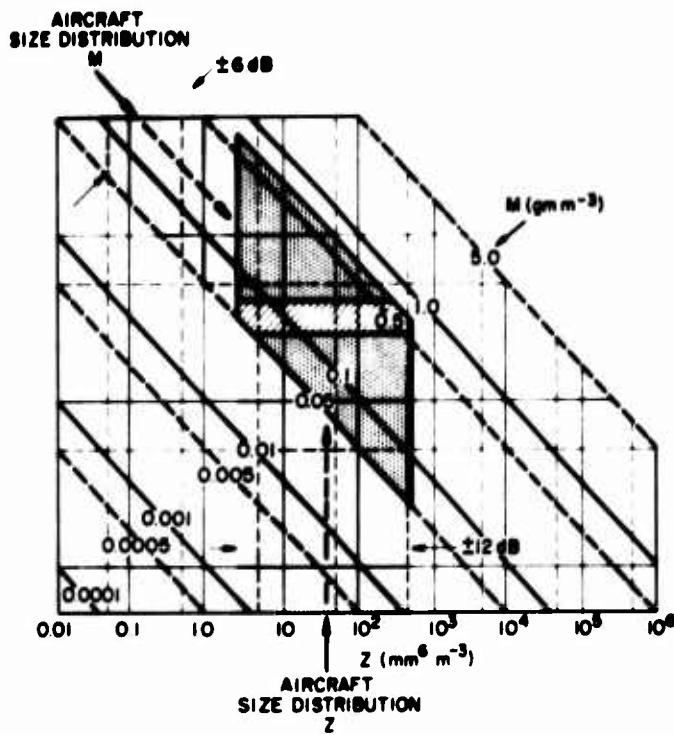


Figure E19. Nomographic Illustration of the Uncertainties and "Uncertainty Areas" of M and Z for the Case in Which These Parameters are Both Computed From Spectral Data

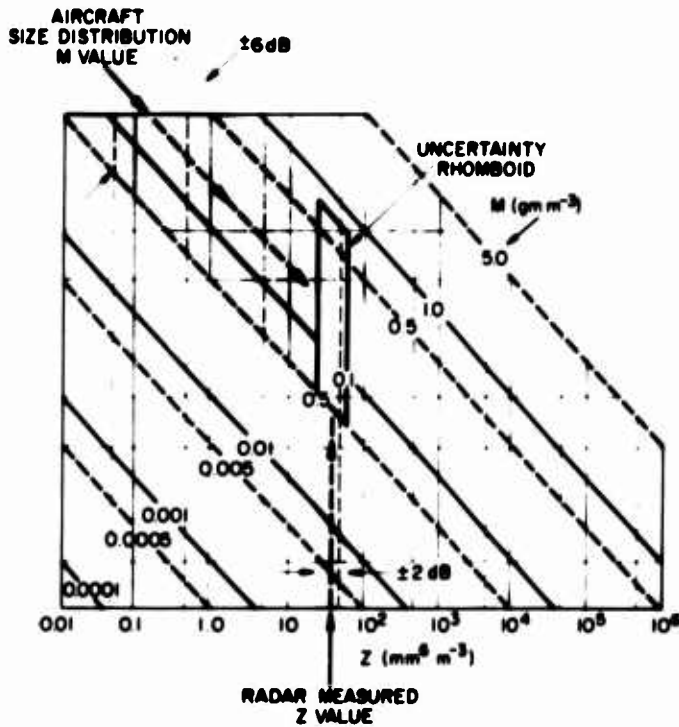


Figure E20. Nomographic Illustration of the Uncertainties and "Uncertainty Area" of M and Z for the Case in Which M is Computed From Spectral Data and Z is Measured by Radar

ICE HYDROMETEORS

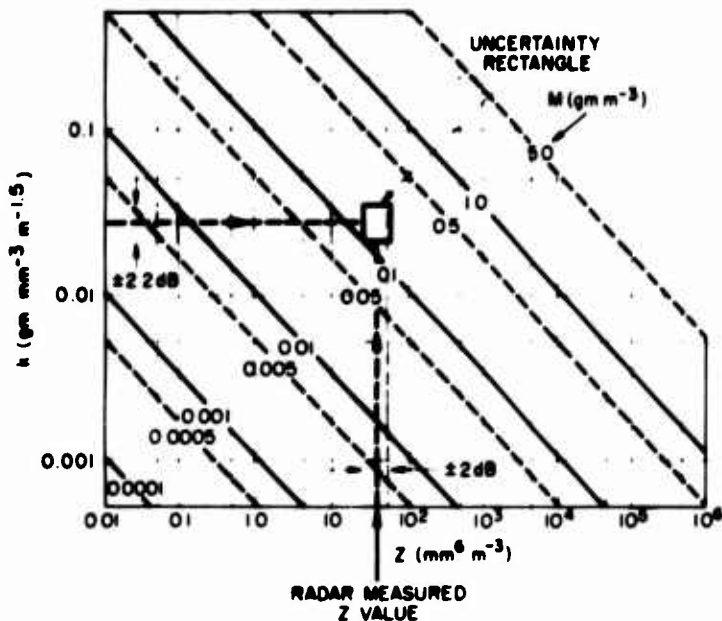


Figure E21. Nomographic Illustration of the Uncertainties and "Uncertainty Area" of k and Z for the Case in Which k is Computed From Spectral Data and Z is Measured by Radar

In Situation 3, in which the k values computed from spectral data are correlated with the Z values of radar measurement, the uncertainties are approximately as illustrated in Figure E21. The k value uncertainties, which are about ± 2 dB, were determined under the same set of uncertainty assumptions employed to estimate the uncertainties of spectral M and spectral Z , see the footnote on page 163. This nomogram reveals that the uncertainty area for spectral k correlated with radar Z is a rather-small, "square" area, which is considerably reduced in size, compared with the uncertainty areas of either Figure E19 or Figure E20.

This finding is important for SAMS, because it tells us that we can materially simplify and enhance the accuracy of our present analytical and correlation procedures by computing the spectral parameter k and employing it in correlations with radar Z (rather than, as now, correlating spectral M with radar Z).

E7.3 Verification of the Accuracy Enhancement of k vs Z Regression

If the previous suggestion has merit, it should be possible to design a data-test to prove that k vs Z regression yields more accurate results than M vs Z regression. The Z values, here, and in the subsequent discussion, are assumed to be those of radar measurement.

Such a test was designed using the ice-crystal data of PVM-5, Pass 8, which were previously referenced. These data were selected because the M values for the ice-crystal samples had been computed from Knollenberg spectral information using particular l to D conversion assumptions. The data were also selected because the spectral M values had been correlated with radar-measured Z values (as measured by the Alcor Radar on Roi-Namur Island, Kwajalein Atoll, M.I. ¹⁵).

The cross-plot of the aircraft, size-distribution M values vs the radar-measured Z values for Pass 8 of PVM-5 are shown in Figure E22. The points are plotted on the nomogram of prior description. The regression equation, of M vs Z, is shown and the regression line is indicated. The correlation coefficient for the data is 0.143; the log standard error of estimate is 0.197.

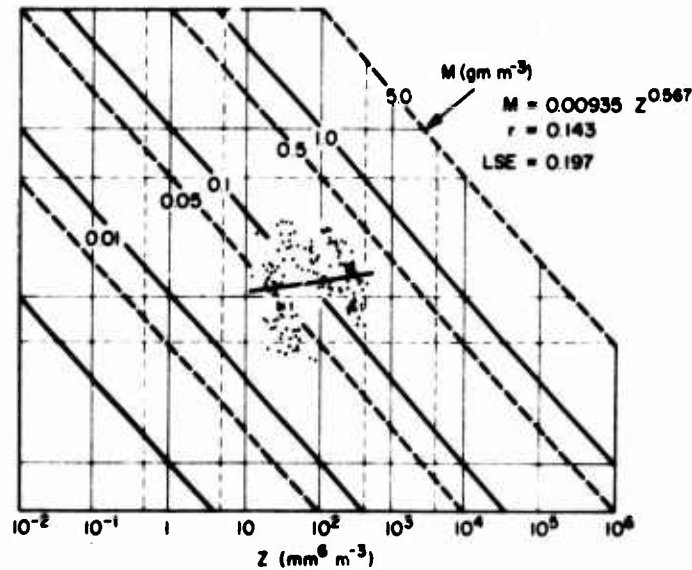


Figure E22. Cross-Plot of the Aircraft Spectral Values of M Plotted vs the Radar-Measured Values of Z, for the Data of PVM-5, Pass 8. The M vs Z regression equation is indicated, as are the correlation coefficient (r) and the log standard error of Estimate (LSE)

The k values for the size-distribution data of Pass 8 were computed and these are shown, in Figure E23, cross-plotted vs the radar Z values. The regression equation, of k vs Z, is noted and the corresponding M vs Z equation is shown, below the dashed line. The correlation coefficient for these data is 0.533; the log standard error of estimate is 0.110.

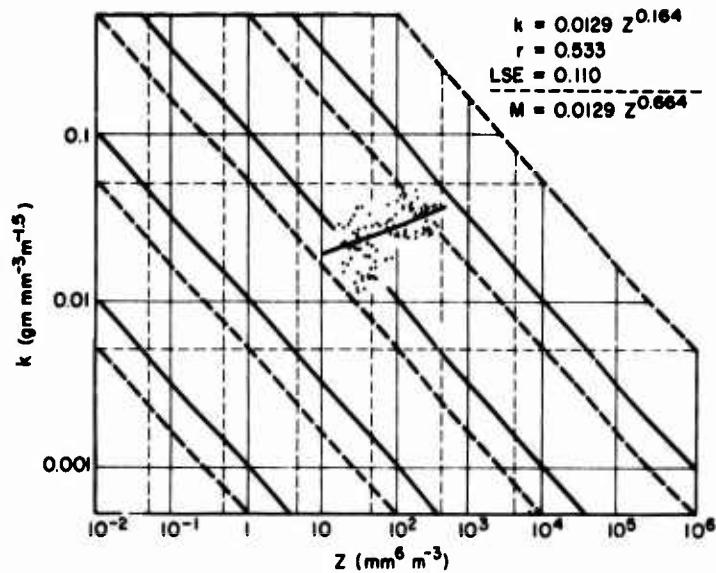


Figure E23. Cross-Plot of the Aircraft Spectral Values of k Plotted vs the Radar-Measured Values of Z , for the Data of PVM-5, Pass 8. The k vs Z regression equation is indicated, as are the correlation coefficient (R) and the log standard error of estimate (LSE). The M vs Z equation corresponding to that of k vs Z is noted below the dashed line

It is visually apparent that the k , Z data points of Figure E23 have less scatter and better fit the regression line, than the M , Z points of Figure E22. The correlation coefficient, by using k as a correlation parameter rather than M , has been improved from 0.143 to 0.533; the log standard error of estimate has been reduced from 0.197 to 0.110. These are substantial improvements of accuracy, which provide verification of the inherent superiority of the technique of k vs Z regression.

It is of interest to intercompare Figures E20 through E23. From Figure E22 it is seen that the PVM-5 data have large scatter in the vertical, or k , direction. This corresponds with the predicted direction and magnitude of the primary uncertainties, of Figure E20. Similarly, comparison of Figures E23 and E21, and intercomparison with Figures E22 and E20, reveals that the extent of the data scatter and predicted uncertainties has been commonly reduced, in the first cited pair of figures relative to the second.

Since Situation 1 and Situation 2 correlations have been performed previously in our SAMS work, we offer the following additional comments about the nature of the inaccuracies that are inherent in regression equations obtained by the two

methods. These comments will help identify and differentiate the "trustworthy" aspects of our previous correlation analyses from the "untrustworthy".

In Situation 1, when spectral M is correlated vs spectral Z, both the M and Z values are highly uncertain. However, the values of the spectral parameter k are known with fair accuracy. This implies, although we will not elaborate the details, that the exponent, E, of the M, Z regression equation, will also be known with reasonable accuracy, because

$$E = 0.5 + \frac{\Delta \log k}{\Delta \log Z_s} , \quad (E59)$$

and because the denominator of the second term can be evaluated from relative knowledge of the sample Z_s values, rather than absolute knowledge. With regard to the coefficient of the regression equation, which is given by

$$K = 10^{\frac{[\overline{\log k} - \overline{\log Z_s} (E - 0.5)]}{}} , \quad (E60)$$

see page 133, both the $\overline{\log k}$ and E terms of this equation are known moderately well, but the $\overline{\log Z_s}$ term is not. Hence, as can be seen from the equation, K can be accurately assessed, if E has a value equal to or close to 0.5; but the uncertainties of K will progressively increase and become substantial, as E departs from 0.5.

In Situation 2, when spectral M is correlated vs radar Z, the M values are highly uncertain but the Z values are known with optimum accuracy. There is an implication in this situation, which can be seen from Figure E20, that the k values are highly uncertain and that they are, in effect, being computed from the relationship

$$k = \frac{M_{\text{spectral}}}{\sqrt{Z_{\text{radar}}}} , \quad (E93)$$

rather than from the proper relationship of Eq. (E22) (in which both M and Z are spectrally determined). This implicit, fictitious uncertainty of the k values causes resultant, major uncertainty in the exponent, E, of the regression equation, because, see Eq. (E59), the term $\Delta \log k$ becomes highly uncertain, thereby affecting E. Likewise, the coefficient, K, of the regression equation, becomes highly uncertain, because both the $\overline{\log k}$ and E terms of Eq. (E60) are uncertain.

To summarize, then, the most-accurate regression equations will be obtained under Situation 3. The equations obtained under Situation 1 will be reasonably accurate, except that the K values will become progressively more uncertain as the E values depart from 0.5. The equations obtained under Situation 2 will be the least

accurate of all, since both E and K will be very uncertain. The latter type of regression should be avoided in the future.

EB. SUMMARY AND CONCLUSIONS

Certain factors were considered in this appendix (and in the support work of Appendix H) that would cause uncertainties in our ability to determine the values of liquid-water-content, M, and radar-reflectivity-factor, Z, from spectral data for ice hydrometeors (snow and ice crystals) obtained from aircraft instruments. Various analyses and investigations were performed to assess the uncertainties involved in (1) analyst subjectivity, in the case of foil impactor data, (2) the problems of relating the geometric dimensions of ice hydrometeors to the dimensions that are measured instrumentally or analytically and (3) the use of different l to D conversion assumptions applied to ice hydrometeors of a given category and type, when these are known, or to the category in general, when type is unknown.

It is concluded from this work that, due to these influences alone, the uncertainties in M, which are normal and to be expected, are of the order of \pm a factor of two to \pm a factor of five and the uncertainties of Z are of the order of \pm a factor of four to \pm a factor of ten. The precise nature of the data, and the diligence employed in analyses, will dictate whether the uncertainties will be larger or smaller, within these general ranges.

It should be emphasized that there were numerous other uncertainty influences of recognized importance that were not considered in the present investigation. Neglected were such things as (1) instrumental measurement inaccuracies, (2) problems of type differences, between the hydrometeors of different size within single samples, (3) instrumental truncation problems, and relative truncation problems, such as arise in the comparison or correlation of data from different instruments, or in comparisons or correlations with radar data, (4) problems of instrumental sampling-volumes, particle capture-probabilities and sample representativeness, between different instruments and relative to the "true" atmospheric conditions and to the atmospheric volumes sampled by radar, and (5) problems involving failures of space-time correspondence between comparative data samples. All of these uncertainty factors should be investigated in detail. They could not be, herein, because of limitations of resources and time.

In other work of the appendix, a spectral parameter was defined and described

*To verify these statements, reference is made to the data of PVM-5, Pass 8. For Situation 3, E = 0.664 and K = 0.0129. These are the values of optimum accuracy. For Situation 1, E = 0.731 and K = 0.0135. For Situation 2, E = 0.567 and K = 0.00935. It is apparent that the Situation 1 values better approximate those of Situation 3 than do the Situation 2 values.

that can be computed more accurately, from size-distribution data, than either M or Z can be computed. The accuracy enhancement achieved by use of the parameter ranges from about a factor of 2 to a factor of 15, relative to M, and from about a factor of 4 to a factor of 40, relative to Z, dependent on the particular circumstances. This spectral parameter was described in some detail and its values and trends (with Z) were demonstrated for rain, snow, and ice-crystals. The physical reasons for the characteristic values and trends were explained. Methods were also discussed whereby the parameter values could be employed in correlations with radar measurements of Z, to obtain more-accurate M vs Z equations, than formerly.

It is concluded, from this work, that various of the analytical procedures now being used in the AFCRL program of support for SAMS can be materially simplified and quantified by the routine computation and employment of this spectral parameter. The concepts and recommendations are explained and illustrated in the following section.

E9. RECOMMENDATIONS

By the routine computation of the spectral parameter, k, we can design analytical procedures that will reduce the fundamental problem of determining the liquid-water-content values for the SAMS missile trajectories into two essential data requirements and one computational step.

The concept involves the acquisition of two basic profiles for any given trajectory. The first is the trajectory-specific profile of the radar Z values, as obtained by the same SAMS methods employed in the past. The second is the trajectory-specific profile of the k values, as determined from aircraft spectral data (plus radar correlation data, as will be described). The desired trajectory values of liquid-water-content are immediately obtainable from these two profiles, because, for each height level in the storm, along the trajectory, except within the melting zone, the equation $M = k\sqrt{Z}$ applies and the M values are readily computed from those of Z and k.

For example, with reference to Figure E24, the dotted profile of this figure, labeled "No. 1", shows the radar Z values for the trajectory of the first SAMS missile launched into the storm of 2 February 1973. The solid profile, labeled "No. 2", shows the k values for the trajectory.* The values of liquid-water-

*The k values across the melting zone were determined from the AFCRL model of the melting zone, see Appendix G, by summing the spectral contributions of both the fully-melted water drops and the water-coated ice particles. The profile Z values shown in Figure E24, within the melting zone, are merely values that are consistent with these k values and with the assumption of a linear change of precipitation rate within the zone.

content for the trajectory, which were height computed from profiles 1 and 2, using the relation $M = k\sqrt{Z}$, are indicated by the dashed profile, labeled "No. 3".

The trajectory-specific profiles of the k values for the SAMS missiles cannot be obtained from aircraft spectral data alone, since k , when correlated with Z , does evidence some degree of variation, which is dependent on the storm conditions and hydrometeor type, see Figures E9 through E12, and Figure E18. Hence, either before a missile launch, or after, during storm periods that are representative of the launch time conditions, it is necessary to acquire combined radar and aircraft data at various storm levels to provide knowledge of the k vs Z relationships that specifically pertain to the particular storm and its contained hydrometeors. Such knowledge will be acquired for SAMS in the future by so-called "link mode" techniques, in which the weather radar is programmed to "look at" and obtain the Z values from a spatial volume located just ahead of (or very close to) the aircraft as it moves along its flight path through the storm. The variability of k with Z for various storm altitudes can be readily determined from such link-mode data and the trajectory-specific profiles of k , such as shown in Figure E24, can likewise be determined. [Alternately, or in addition, the particular M vs Z relationships for the different storm altitudes and hydrometeor types can be obtained, through the use of Eqs. (E78) and (E81)].

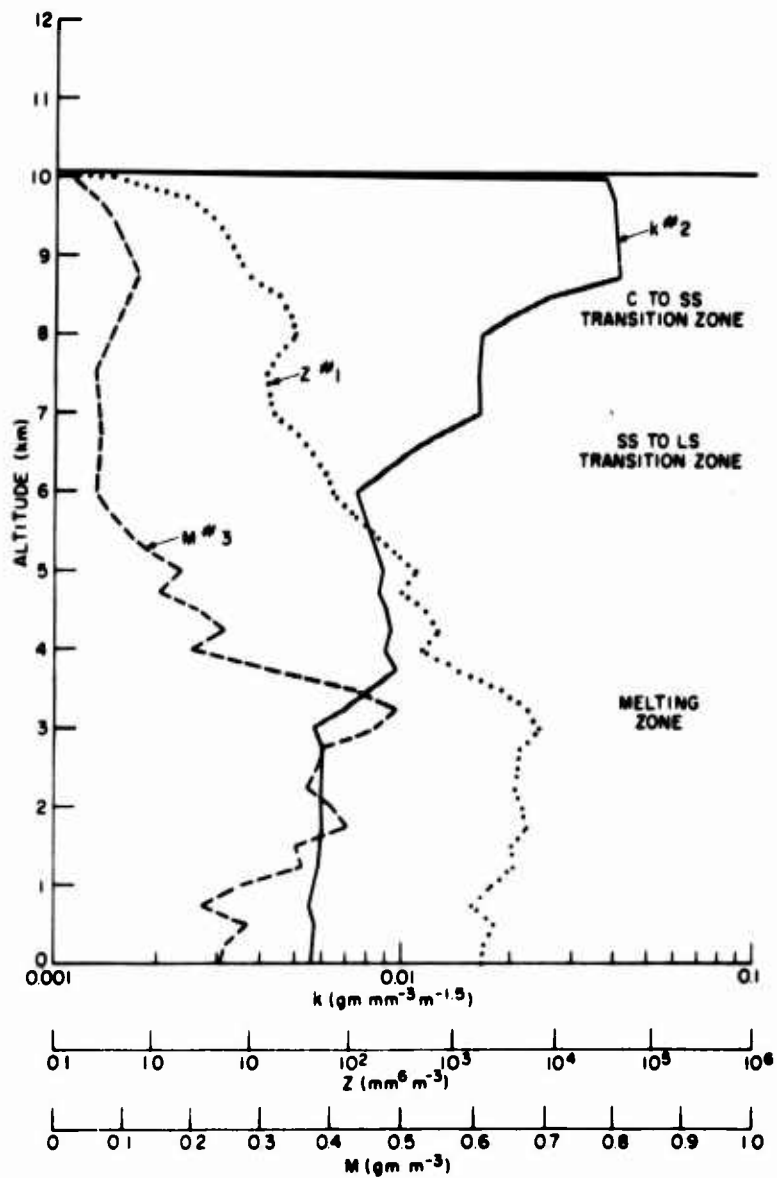


Figure E24. Examples of Trajectory Profiles of Radar Measured Z , of Aircraft-Radar Determined k and of the Resultant M Profile Computed from $M = k\sqrt{Z}$.

Appendix F

Liquid-Water-Content and Size Distribution Information Acquired from the MRI Navajo Aircraft

A Piper-Navajo aircraft was flown contractually for SAMS purposes in the 1972-73 season by Meteorology Research, Inc. (MRI). The aircraft was based at Wallops Station Airfield. The pilot was Mr. Alfonso Ollivares.

When appropriate storm conditions for missile launch operations existed at Wallops, the Navajo aircraft was usually flown into the storm to near its ceiling altitude of approximately 24,000 feet. It remained there in a holding pattern, together with the C-130 aircraft of AFGL (if present) until (a) the missile was fired, or (b) the launch operations were terminated for one of a variety of technical or meteorological reasons. If a missile was fired, the Navajo was flown from the holding pattern to the trajectory region of the storm and the pilot then began making measurement traverses along the line of the horizontal projection of the missile path. The traverses were each about 10 nautical miles in length and the pilot was directed along the path by radar vectoring from one of the NASA tracking radars. On completion of the first pass, at near the ceiling altitude of the aircraft, the pilot descended to a lower flight altitude and began a second measurement traverse, followed by a third, a fourth, and so forth. The traverse altitudes were specified on the bases of the particular storm characteristics, as supplemented by the pilot's radio descriptions of the hydrometeor conditions being encountered. About six to ten total traverses were usually made, separated in altitude by approximately 1000 to 5000 feet. The time required to accomplish the traverses following missile firing was some 50 to 90 minutes. Fewer traverses and less time were required if the AFGL C-130A aircraft was also present making storm measurements.

The MRI Navajo aircraft arrived at Wallops Station Airfield in mid-January. It flew a calibration sortie on 18 January 1973, in conjunction with the AFGL C-130A aircraft, for purposes of checking and cross-comparing the cloud-physics instrumentation aboard both aircraft. The first storm flight of the Navajo was on 2 February 1973, in support of the SAMS missile launches of this day. The second, and final, storm flight of the Navajo was in support of the SAMS launches of 27 February 1973. The Navajo flew additionally, later in the season, on 15 March and 7 April 1973, to obtain particular measurement information in upper-level, cirrus cloud situations.

The MRI work efforts and data results in support of the SAMSO/ABRES and DNA HEART programs have been summarized in the final report under Contract No. DNA 001-72-C-0130 (P00002) of 29 July 1974.¹⁸ Excerpts of the summary-tabular results of this report that specifically pertain to the SAMS missile launches of 2 February and 27 February 1973 are presented in Tables F1, F3, and F5 through F8. Additional analytical results based on the MRI data are shown in Figures F1 and F2 and in Tables F2 and F4.

18. Takeuchi, D. M., Knuth, W. R., and Green, W. D. (1974) Meteorological Support for the SAMSO/ABRES Program and the DNA HEART Program, Final Report under Contract DNA 001-72-C-0130 (P00002), Meteorology Research, Inc., Altadena, California.

Table F1. Quick-Look Summary of Cloud Particles in Storm of 2 February 1973, Wallops Island, Virginia

Alt. (x10 ³ ft)	Time (LST)	Temp. (°C)	Droplet Size Particles (dia. < 200 μm)			Precipitation Size (dia. > 200 μm)			Remarks
			Type	Conc (cm ⁻³)	Dia. Range (μm)	Type	Conc (lit ⁻¹)	Dia. Range (mm)	
15.0	918-920	-7.5	Droplets Drops	0.1 0.0005	10-30 50-100	Snow	2.0	>3	Cloud droplets are present in low concentrations varying between 0.01 to 0.5 cm ⁻³ . Drop splashing suggests that droplets in dia. range of 50 to 100 μm are present in low concentrations. Foil data reveal that the snow particles are as large as 5 to 6 mm. The snow particles appear to be spatial dendrites and appear to be fragile (low density (<0.1 g/cm ³)) with plate makeup.
12.0	925-930	-2.5	Droplets Drops	0.1-200 0.001	5-30 50-100	Snow	2.1	>>3	The wide spatial variations of cloud droplet concentrations is noted. Snow particle replicas look similar in makeup as at 15 k ft.
11.2	938-939	-0.5	Droplets	~200	5-30	Snow	2.2	>3	Snow melting starts at this level (Formvar Foil shows first rain at about 11.5 k ft.
11.0	940	-0.5	Droplets	10-100	5-30	Snow Rain	1.5 <1.0	>3 0.2-2.0	Melting is evident by decrease in snow concentration.
10.0	942-947	-0.5	Droplets	10-200	5-30	Snow Rain	0.1 0-0.5	5-7 0.2-3.0	Regions (~0.5 to 1 km) of only rain, only snow, and mixtures of rain and snow on foil records. In cloud regions between 11.2 and 10 k ft, rain regions associated with cloud regions containing higher concentrations of cloud droplets. All of the snow at 10 k appears wet.
9.3	952	1.0	Droplets	10-200	5-30	Snow Rain	0 0.2-0.5	>3 0.2-3.0	Last snow sampled.
6	1000-1010	6.0	Droplets	1-~200	5-30	Rain	~0.3	0.2-3.0	Sample volume of about 81 m ³ shows maximum raindrop diameters of 4.0, 4.25, and 5.0 mm in concentrations of 0.16, 0.0123, and 0.0123 m ⁻³ .
2	1021-1028	13.0	No Data			Rain	0.2-0.3	0.2-5.0	Sample volume of about 35 m ³ shows maximum raindrop diameter of 4 mm in concentration of about 0.2 m ⁻³ .
1	1030	15.0	No Data			Rain	~0.2	0.2-4.5	Run over JAFNA.

*Level runs.

Table F2. Foil Data for Flight of 2 February 1973
Wallops Island

Size Range (mm)	Time: 1448-1449Z Vol = 4.51 m ³ Conc (m ⁻³)	Time: 1450-1451Z Vol = 4.755 m ³ Conc (m ⁻³)	Time: 1526-1527Z Vol = 4.56 m ³ Conc (m ⁻³)
0.2 -1.0	149	143	144
1.0 -2.0	57.0	56.8	44.3
2.0 -3.0	17.5	18.9	11.6
3.0 -3.25	0.887	2.1	0.439
3.25-3.5	0.444	0.210	0.439
3.50-3.75	0	0.631	0
3.75-4.0	0.222	0.631	0.219
4.0 -4.25	0.222	0	0

Table F3. Raindrop Size Distribution for Storm of 2 February 1973

Diameter (mm)	Counts	Sample Vol. (m ³)	Remarks
0.2 to < 1.0	1006	5.48	Sample at 6 k ft
1.0 to < 2.0	569	5.48	
2.0 to < 3.0	93	5.48	
3.0 - 3.25	16	12.26	
3.25 - 3.50	6	12.26	
3.5 - 3.75	6	12.26	
3.75 - 4.0	13	81.0	
4.0 - 4.25	1	81.0	
4.25 - 4.50	0	81.0	
4.50 - 4.75	0	81.0	
4.75 - 5.0	1	81.0	
0.2 to < 1.0	992	6.0	Sample over JAFNA
1.0 to < 2.0	230	6.0	
2.0 to < 3.0	54	6.0	
3.0 - 3.25	8	6.0	
3.25 - 3.50	3	6.0	
3.50 - 3.75	2	6.0	
3.75 - 4.0	5	6.0	
4.0 - 4.25	1	6.0	

Table F4. Notes of Hydrometeor Conditions During Flight of 27 February

14 k ft	Lightly rimed particles of grauple type.
12 k ft	Mainly snow flakes up to 3 mm - some grauple.
descending	Heavy snow.
9 k ft	Heavy large snow - some rimed particles
descending	Heavy snow.
6 k ft	Large snow with a few particles of 5 mm. Some pockets of light concentration.
descending	Melting apparent - grauple type particles more dense - some water drops of 1 mm diameter or less - snow crystals mainly 2 to 3 mm and aggregates of up to 5 mm
5 k ft	About 85 percent rain with still some "core" to rain drops - maximum size of 1.5 mm. Some pockets of wet snow of 5 mm with little rain.
descending	About 95 percent rain - majority of maximum size drops are 1.5 mm, few up to 2.5 mm
3 k ft	Rain with drops up to 3 mm

Table F5. Summary of Continuous Cloud Particle Replicator Data Observations for Storm of 27 February 1973

Time (Z)	Alt. ($\times 10^3$ ft)	Temp. (C°)	Ice (conc)	J-W I.WG (g/m^3)	Remarks
1052-30	21.8	-31.5	1.47	0 - 0.3	Ice < 200 μ m, droplets present in regions of about 1.0 to 3 km. Ice particles are partly rimed. Ice particles composed of plate-like aggregates.
1054:00	21.0	-29.0	2.34	0 - 0.2	Ice < 400 μ m. Droplets present in localized regions. Some ice particles are heavily rimed.
1056:00	20.0	-27.0	14.1	0	No LWC evident. Particles larger than at higher levels. Breakup of ice makes it difficult to assess sizes. Ice conc. can be higher by 20 percent in regions.
1059:00	18.0	-22.5	12.1	0	No LWC evident. Description of ice similar to 20 k ft

Table F5. Summary of Continuous Cloud Particle Replicator Data Observations for Storm of 27 February 1973 (Cont)

Time (Z)	Alt. (x10 ³ ft)	Temp. (C°)	Ice (conc)	J-W LWC (g/m ³)	Remarks
1102:00	15.0	-15.0	4.83	0 - 0.2	No LWC evident. Ice particles composed of plate-like crystals with broad branches and aggregates within thin simple plates.
1107:45	13.0	-11.5	2.40	0.1 - 0.3	LWC present throughout. Droplets appearing regularly starting at about 13.5 k ft. Snow particles > 3 mm evident in sample run.
>1108	≤12.0				Formvar replicator malfunctioning. No Data.

Table F6. Foil Data Summary for Storm of 27 February 1973

Alt. (x10 ³ ft)	Remarks
23.0	Particles < 200 μm in dia if any.
21.0	Particles < 200 μm in dia if any.
20.0	Snow crystals up to 1 to 1.5 μm dia. Particle density too high to determine concentration.
18.0	Particle concentration too high to determine size and concentrations.
15 k	No data.
14.4 k	Definite indications of snow to 3 mm.
13 k	Mode size = 1.5 mm snow Maximum size = 3.5 mm snow Concentration = 100 m ⁻³
12 k	Mode = 1.5 mm Maximum size = 3.5 to 4.0 mm Concentration = 280 - 550 m ³
9 k	Snow too large and heavy to determine concentration.
5.4	First indications of complete melting.
5 k	Mixtures of rain (dia < 1 mm) and wet snow. See distribution data.
4.5	Last melting snow.
3 k	See rain distribution.
<3 k	No data.

Table F7. Foil Data Size-Distribution Summary for Storm on 27 February 1973, Wallops Island

Level Run at 3 k ft			
Length of Run (73.3 m/sec) (160 sec)			
Rain			
Dia. Range (mm)	Counts	Sample Vol. (m³)	Conc. (m⁻³)
0.18 to ≤1.0	975	4.435	220
>1.0 to ≤2.0	160	4.435	36.2
2.0 to ≤3.0	49	8.87	5.52
3.0 to 3.25	7	17.05	0.411
3.25 to 3.50	0	17.05	<0.06
Descent from 5 k to 3 k ft			
Length of Run (84.4 m/sec) (158 sec)			
Rain			
Dia. Range (mm)	Counts	Sample Vol. (m³)	Conc. (m⁻³)
0.18 to ≤1.0	4870	19.6	248
1.0 to ≤2.0	435	19.6	22.2
2.0 to 2.25	10	19.6	0.510
2.25 to 2.50	6	19.6	0.306
2.50 to 2.75	2	19.6	0.1275
2.75 to 3.0	1	19.6	0.05
>3.0	0	19.6	<0.05
Level Run at 5 k ft			
Length of Run (170 sec) 73.8 m/sec)			
Mixture Rain and Ice			
Rain - Maximum Diameter 1 mm			
	Dia. Range (mm)	Conc. (m⁻³)	Sample Vol. (m³)
Snow	0.5 to 1.0	10.4	18.2
	0.5 to 8.5	83.5	18.2

Table F8. Additional Foil Data for Storm on 27 February 1973

Time (Z)	Alt (k ft)	Conc (m^{-3}) in Diameter (mm) Range						Particle Type
		0-1	1-2	2-3	3-4	4-5	5-6	
1111	12	303	42	2	1			Snow Crystals
1113	12	579	24	6	10	2		Snow Crystals
1122:30	9	498	42	76	13	7	1	Aggregate Snow
1136:30	5.9	335	9	0.257				Rain
		--	19.5	3.08	0.257			Wet Snow
1137:30	5.5	252	45.9	4.58	0.834			Rain

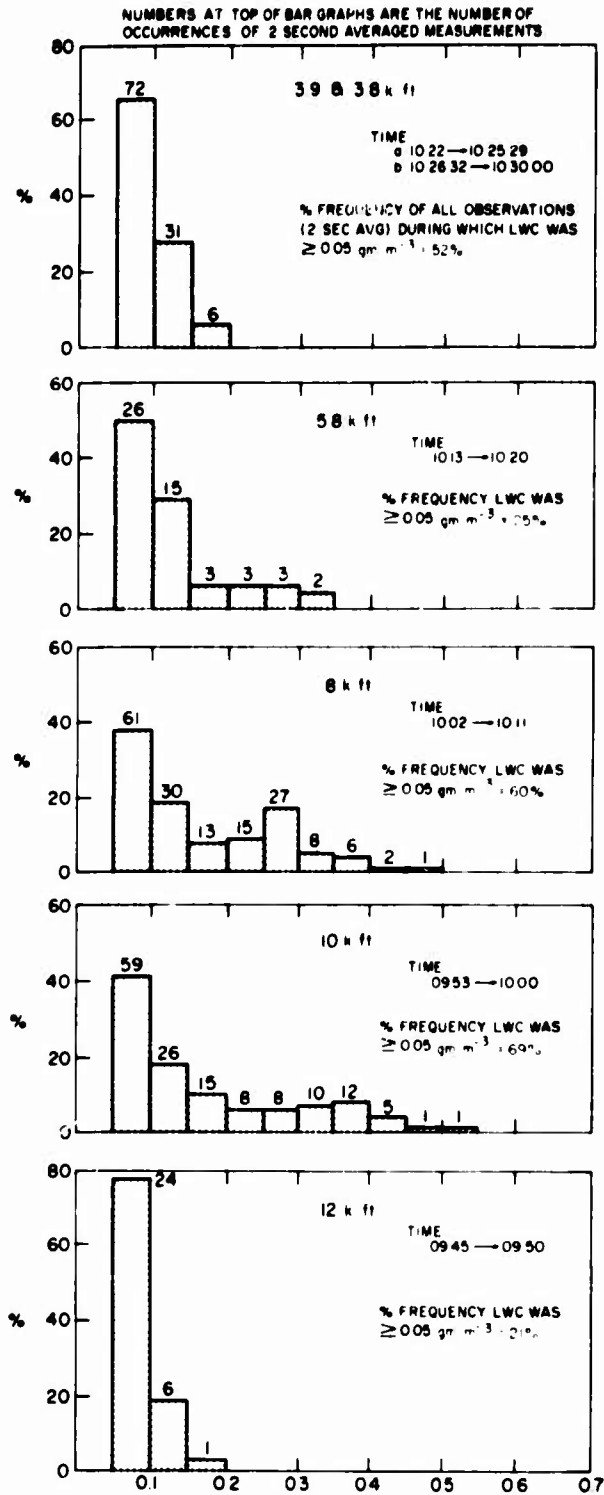


Figure F1. Frequency Distribution of Cloud Liquid-Water-Content for Five Different Flight Altitudes in Storm of 2 February 1973

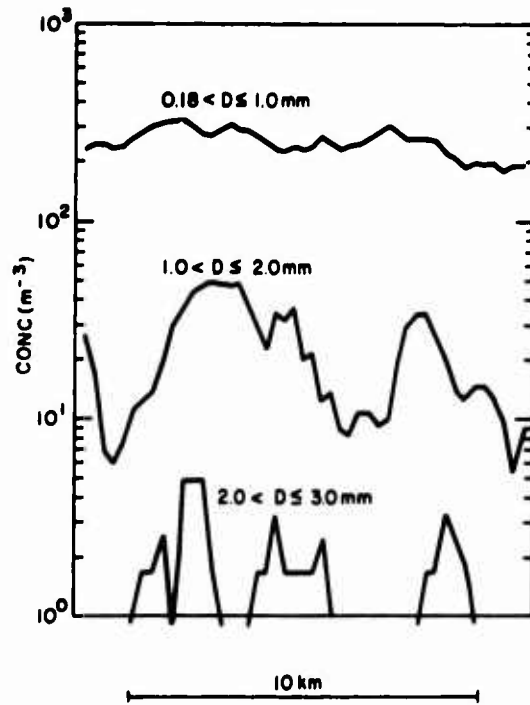


Figure F2. Spatial Variations of Raindrop Size-Distributions in Descent From 5 to 3 k ft During Storm on 27 February 1973

Appendix G

Summary and "Best Estimate" Information about the Spectral Distribution and Total Values of the Number Concentration and Liquid-Water-Content of the Hydrometeors along the Missile Trajectories

Approximate information about the spectral distribution and total values of the number concentration and liquid-water-content of the hydrometeors along the missile trajectories for the storms of the 1972-73 SAMS season is presented in Tables G2 through G5. The information is supplied for the particular diameter classes (equivalent-melted-diameter, in the case of ice hydrometeors) which are specified in Table G1.

The information in Tables G2 through G5 is based on theoretical models that were briefly described in R No. 3. Three models were used which were descriptive: (1) of the cloud size range of the hydrometeors, (2) of the precipitation size range of the hydrometeors, and (3) of the two types of hydrometeors, fully-melted-liquid-drops and water-coated-snow-particles, that occur within the melting zones of the storms. Since independent models were used for the cloud-size portion of the spectrum and for the precipitation-size portion, there are spectral discontinuities that occur across the separation boundary (at 79.4μ , or 0.0794 mm) between the two size ranges.

The reasons for the selection of the SAMS diameter classes indicated in Table G1 were explained in R No. 3 and the equations were presented that describe the geometric-mean-diameter of the classes (that is, the diameter values of the column headings of Tables G2 through G5).

The details of the mathematical development of the "precipitation model" used in the SAMS tables are described and illustrated in the last section of this Appendix. The details of the "cloud model" and the "model for the melting zone" will be presented in subsequent reports of the SAMS series.

G1. DESCRIPTION OF TABLES G2 THROUGH G5

The missile altitude is indicated in the first column of each of the Tables G2 through G5. The altitudes are listed for each 250 meters from the ground surface to the top altitude of the storm of the particular days (including the overlying cirrus layer above the top, for the storm of 27 February 1973). Size-distribution and liquid-water-content information is presented in the next sections of the table(s), first, for the cloud-size range of the spectrum, and second, for the precipitation-size range of the spectrum. Summary information about the cloud populations, and about the precipitation populations, is provided in the following two sections of the tables. The total liquid-water-content, of the liquid-drops and water-coated ice, of precipitation size, within the melting zone, is indicated in the next to the last column of the tables. The grand total of the liquid-water-content, for all types of hydrometeors, of both the cloud-size and precipitation size, is listed in the last columns of the tables.

The numbers above the diagonal lines, in the table sections concerned with the spectral distribution of the hydrometeors, give the number concentration of the drops or ice particles within the particular diameter classes identified in Table G1. For the cloud-size portion of the spectrum, the number concentrations (N_c) are listed in units of No. cm^{-3} ; for the precipitation-size portion, they are listed in units of No. m^{-3} . The reasons for the different units were explained in R No. 3.

The numbers below the diagonal lines, in the first two sections of the tables, indicate the class contributions of the contained hydrometeors to the total liquid-water-content of the cloud populations (first section tabulations) or to the total liquid-water-content of the precipitation (size) populations (second section tabulations). The class contributions are listed in units of gm m^{-3} . Any contribution smaller than 0.001 gm m^{-3} is listed as zero, in accord with the agreement of the SAMS-ABRES Conference at AFCRL on 7-8 March 1974.

Two types of precipitation-size hydrometeors exist within the melting zones of the Wallops storms. These are identified in Tables G2 through G5 as fully-melted liquid (symbolized by "W") and water-coated-ice (symbolized by "I"). Number concentration and class liquid-water-content information is supplied for both of these hydrometeor types. The information for the fully-melted-liquid, or raindrops, is listed in the first lines; information concerning the water-coated-ice is listed in the second lines.

Table G1. Diameter Classes Specified for SAMS

Class Number	Class Boundaries		Geometric Mean-Diameter (See Eqs. G3 & G4)	
	microns	mm	microns	mm
	0.7943	0.0007943		
First	1.259	0.001259	1.0	0.001
Second	1.995	0.001995	1.585	0.001585
Third	3.162	0.003162	2.512	0.002512
Fourth	5.012	0.005012	3.981	0.003981
Fifth	7.943	0.007943	6.309	0.006309
Sixth	12.59	0.01259	10.0	0.01
Seventh	19.95	0.01995	15.85	0.01585
Eighth	31.62	0.03162	25.12	0.02512
Ninth	50.12	0.05012	39.81	0.03981
Tenth	79.43	0.07943	63.09	0.06309
Eleventh	125.9	0.1259	100.0	0.1
Twelfth	199.5	0.1995	158.5	0.1585
Thirteenth	316.2	0.3162	251.2	0.2512
Fourteenth	501.2	0.5012	398.1	0.3981
Fifteenth	794.3	0.7943	630.9	0.6309
Sixteenth	1259	1.259	1000	1.0
Seventeenth	1995	1.995	1585	1.585
Eighteenth	3162	3.162	2512	2.512
Nineteenth	5012	5.012	3981	3.981
Twentieth	7943	7.943	6309	6.309
Twenty-first	12,590	12.59	10,000	10.0

Cloud Size-Range

Precipitation Size-Range

No.	Name	Address	1914				Total	Percentage
			Value	Area	Volume	Weight		
1	128	281	1.12	2.11	.241	
2	135	282	1.13	2.82	.272	
3	138	283	1.14	2.83	.283	
4	141	284	1.15	2.84	.284	
5	144	285	1.16	2.85	.285	
6	147	286	1.17	2.86	.286	
7	150	287	1.18	2.87	.287	
8	153	288	1.19	2.88	.288	
9	156	289	1.20	2.89	.289	
10	159	290	1.21	2.90	.290	
11	162	291	1.22	2.91	.291	
12	165	292	1.23	2.92	.292	
13	168	293	1.24	2.93	.293	
14	171	294	1.25	2.94	.294	
15	174	295	1.26	2.95	.295	
16	177	296	1.27	2.96	.296	
17	180	297	1.28	2.97	.297	
18	183	298	1.29	2.98	.298	
19	186	299	1.30	2.99	.299	
20	189	300	1.31	3.00	.300	
21	192	301	1.32	3.01	.301	
22	195	302	1.33	3.02	.302	
23	198	303	1.34	3.03	.303	
24	201	304	1.35	3.04	.304	
25	204	305	1.36	3.05	.305	
26	207	306	1.37	3.06	.306	
27	210	307	1.38	3.07	.307	
28	213	308	1.39	3.08	.308	
29	216	309	1.40	3.09	.309	
30	219	310	1.41	3.10	.310	
31	222	311	1.42	3.11	.311	
32	225	312	1.43	3.12	.312	
33	228	313	1.44	3.13	.313	
34	231	314	1.45	3.14	.314	
35	234	315	1.46	3.15	.315	
36	237	316	1.47	3.16	.316	
37	240	317	1.48	3.17	.317	
38	243	318	1.49	3.18	.318	
39	246	319	1.50	3.19	.319	
40	249	320	1.51	3.20	.320	
41	252	321	1.52	3.21	.321	
42	255	322	1.53	3.22	.322	
43	258	323	1.54	3.23	.323	
44	261	324	1.55	3.24	.324	
45	264	325	1.56	3.25	.325	
46	267	326	1.57	3.26	.326	
47	270	327	1.58	3.27	.327	
48	273	328	1.59	3.28	.328	
49	276	329	1.60	3.29	.329	
50	279	330	1.61	3.30	.330	
51	282	331	1.62	3.31	.331	
52	285	332	1.63	3.32	.332	
53	288	333	1.64	3.33	.333	
54	291	334	1.65	3.34	.334	
55	294	335	1.66	3.35	.335	
56	297	336	1.67	3.36	.336	
57	300	337	1.68	3.37	.337	
58	303	338	1.69	3.38	.338	
59	306	339	1.70	3.39	.339	
60	309	340	1.71	3.40	.340	
61	312	341	1.72	3.41	.341	
62	315	342	1.73	3.42	.342	
63	318	343	1.74	3.43	.343	
64	321	344	1.75	3.44	.344	
65	324	345	1.76	3.45	.345	
66	327	346	1.77	3.46	.346	
67	330	347	1.78	3.47	.347	
68	333	348	1.79	3.48	.348	
69	336	349	1.80	3.49	.349	
70	339	350	1.81	3.50	.350	
71	342	351	1.82	3.51	.351	
72	345	352	1.83	3.52	.352	
73	348	353	1.84	3.53	.353	
74	351	354	1.85	3.54	.354	
75	354	355	1.86	3.55	.355	
76	357	356	1.87	3.56	.356	
77	360	357	1.88	3.57	.357	
78	363	358	1.89	3.58	.358	
79	366	359	1.90	3.59	.359	
80	369	360	1.91	3.60	.360	
81	372	361	1.92	3.61	.361	
82	375	362	1.93	3.62	.362	
83	378	363	1.94	3.63	.363	
84	381	364	1.95	3.64	.364	
85	384	365	1.96	3.65	.365	
86	387	366	1.97	3.66	.366	
87	390	367	1.98	3.67	.367	
88	393	368	1.99	3.68	.368	
89	396	369	2.00	3.69	.369	
90	399	370	2.01	3.70	.370	
91	402	371	2.02	3.71	.371	
92	405	372	2.03	3.72	.372	
93	408	373	2.04	3.73	.373	
94	411	374	2.05	3.74	.374	
95	414	375	2.06	3.75	.375	
96	417	376	2.07	3.76	.376	
97	420	377	2.08	3.77	.377	
98	423	378	2.09	3.78	.378	
99	426	379	2.10	3.79	.379	
100	429	380	2.11	3.80	.380	

Table G3. Summary and "Best Estimate" Information About the Spectral Distribution and Total Values of Hydrometeor Number Concentration and Liquid-Water-Content Along the Missile Trajectory of Flight No. Q2-8361 (Unit No. R487102) of 2 February 1973, Launched at 1408:30 GMT (See text for description of table)

Time (GMT)	Altitude (km)	Number Concentration (No./cc)		Liquid Water Content (g/cc)	
		Best Estimate	Upper Limit	Best Estimate	Upper Limit
1408:30	0.0	0.0	0.0	0.0	0.0
1408:35	0.5	0.0	0.0	0.0	0.0
1408:40	1.0	0.0	0.0	0.0	0.0
1408:45	1.5	0.0	0.0	0.0	0.0
1408:50	2.0	0.0	0.0	0.0	0.0
1408:55	2.5	0.0	0.0	0.0	0.0
1409:00	3.0	0.0	0.0	0.0	0.0
1409:05	3.5	0.0	0.0	0.0	0.0
1409:10	4.0	0.0	0.0	0.0	0.0
1409:15	4.5	0.0	0.0	0.0	0.0
1409:20	5.0	0.0	0.0	0.0	0.0
1409:25	5.5	0.0	0.0	0.0	0.0
1409:30	6.0	0.0	0.0	0.0	0.0
1409:35	6.5	0.0	0.0	0.0	0.0
1409:40	7.0	0.0	0.0	0.0	0.0
1409:45	7.5	0.0	0.0	0.0	0.0
1409:50	8.0	0.0	0.0	0.0	0.0
1409:55	8.5	0.0	0.0	0.0	0.0
1410:00	9.0	0.0	0.0	0.0	0.0
1410:05	9.5	0.0	0.0	0.0	0.0
1410:10	10.0	0.0	0.0	0.0	0.0
1410:15	10.5	0.0	0.0	0.0	0.0
1410:20	11.0	0.0	0.0	0.0	0.0
1410:25	11.5	0.0	0.0	0.0	0.0
1410:30	12.0	0.0	0.0	0.0	0.0
1410:35	12.5	0.0	0.0	0.0	0.0
1410:40	13.0	0.0	0.0	0.0	0.0
1410:45	13.5	0.0	0.0	0.0	0.0
1410:50	14.0	0.0	0.0	0.0	0.0
1410:55	14.5	0.0	0.0	0.0	0.0
1411:00	15.0	0.0	0.0	0.0	0.0
1411:05	15.5	0.0	0.0	0.0	0.0
1411:10	16.0	0.0	0.0	0.0	0.0
1411:15	16.5	0.0	0.0	0.0	0.0
1411:20	17.0	0.0	0.0	0.0	0.0
1411:25	17.5	0.0	0.0	0.0	0.0
1411:30	18.0	0.0	0.0	0.0	0.0
1411:35	18.5	0.0	0.0	0.0	0.0
1411:40	19.0	0.0	0.0	0.0	0.0
1411:45	19.5	0.0	0.0	0.0	0.0
1411:50	20.0	0.0	0.0	0.0	0.0
1411:55	20.5	0.0	0.0	0.0	0.0
1412:00	21.0	0.0	0.0	0.0	0.0
1412:05	21.5	0.0	0.0	0.0	0.0
1412:10	22.0	0.0	0.0	0.0	0.0
1412:15	22.5	0.0	0.0	0.0	0.0
1412:20	23.0	0.0	0.0	0.0	0.0
1412:25	23.5	0.0	0.0	0.0	0.0
1412:30	24.0	0.0	0.0	0.0	0.0
1412:35	24.5	0.0	0.0	0.0	0.0
1412:40	25.0	0.0	0.0	0.0	0.0
1412:45	25.5	0.0	0.0	0.0	0.0
1412:50	26.0	0.0	0.0	0.0	0.0
1412:55	26.5	0.0	0.0	0.0	0.0
1413:00	27.0	0.0	0.0	0.0	0.0
1413:05	27.5	0.0	0.0	0.0	0.0
1413:10	28.0	0.0	0.0	0.0	0.0
1413:15	28.5	0.0	0.0	0.0	0.0
1413:20	29.0	0.0	0.0	0.0	0.0
1413:25	29.5	0.0	0.0	0.0	0.0
1413:30	30.0	0.0	0.0	0.0	0.0
1413:35	30.5	0.0	0.0	0.0	0.0
1413:40	31.0	0.0	0.0	0.0	0.0
1413:45	31.5	0.0	0.0	0.0	0.0
1413:50	32.0	0.0	0.0	0.0	0.0
1413:55	32.5	0.0	0.0	0.0	0.0
1414:00	33.0	0.0	0.0	0.0	0.0
1414:05	33.5	0.0	0.0	0.0	0.0
1414:10	34.0	0.0	0.0	0.0	0.0
1414:15	34.5	0.0	0.0	0.0	0.0
1414:20	35.0	0.0	0.0	0.0	0.0
1414:25	35.5	0.0	0.0	0.0	0.0
1414:30	36.0	0.0	0.0	0.0	0.0
1414:35	36.5	0.0	0.0	0.0	0.0
1414:40	37.0	0.0	0.0	0.0	0.0
1414:45	37.5	0.0	0.0	0.0	0.0
1414:50	38.0	0.0	0.0	0.0	0.0
1414:55	38.5	0.0	0.0	0.0	0.0
1415:00	39.0	0.0	0.0	0.0	0.0
1415:05	39.5	0.0	0.0	0.0	0.0
1415:10	40.0	0.0	0.0	0.0	0.0
1415:15	40.5	0.0	0.0	0.0	0.0
1415:20	41.0	0.0	0.0	0.0	0.0
1415:25	41.5	0.0	0.0	0.0	0.0
1415:30	42.0	0.0	0.0	0.0	0.0
1415:35	42.5	0.0	0.0	0.0	0.0
1415:40	43.0	0.0	0.0	0.0	0.0
1415:45	43.5	0.0	0.0	0.0	0.0
1415:50	44.0	0.0	0.0	0.0	0.0
1415:55	44.5	0.0	0.0	0.0	0.0
1416:00	45.0	0.0	0.0	0.0	0.0
1416:05	45.5	0.0	0.0	0.0	0.0
1416:10	46.0	0.0	0.0	0.0	0.0
1416:15	46.5	0.0	0.0	0.0	0.0
1416:20	47.0	0.0	0.0	0.0	0.0
1416:25	47.5	0.0	0.0	0.0	0.0
1416:30	48.0	0.0	0.0	0.0	0.0
1416:35	48.5	0.0	0.0	0.0	0.0
1416:40	49.0	0.0	0.0	0.0	0.0
1416:45	49.5	0.0	0.0	0.0	0.0
1416:50	50.0	0.0	0.0	0.0	0.0
1416:55	50.5	0.0	0.0	0.0	0.0
1417:00	51.0	0.0	0.0	0.0	0.0
1417:05	51.5	0.0	0.0	0.0	0.0
1417:10	52.0	0.0	0.0	0.0	0.0
1417:15	52.5	0.0	0.0	0.0	0.0
1417:20	53.0	0.0	0.0	0.0	0.0
1417:25	53.5	0.0	0.0	0.0	0.0
1417:30	54.0	0.0	0.0	0.0	0.0
1417:35	54.5	0.0	0.0	0.0	0.0
1417:40	55.0	0.0	0.0	0.0	0.0
1417:45	55.5	0.0	0.0	0.0	0.0
1417:50	56.0	0.0	0.0	0.0	0.0
1417:55	56.5	0.0	0.0	0.0	0.0
1418:00	57.0	0.0	0.0	0.0	0.0
1418:05	57.5	0.0	0.0	0.0	0.0
1418:10	58.0	0.0	0.0	0.0	0.0
1418:15	58.5	0.0	0.0	0.0	0.0
1418:20	59.0	0.0	0.0	0.0	0.0
1418:25	59.5	0.0	0.0	0.0	0.0
1418:30	60.0	0.0	0.0	0.0	0.0
1418:35	60.5	0.0	0.0	0.0	0.0
1418:40	61.0	0.0	0.0	0.0	0.0
1418:45	61.5	0.0	0.0	0.0	0.0
1418:50	62.0	0.0	0.0	0.0	0.0
1418:55	62.5	0.0	0.0	0.0	0.0
1419:00	63.0	0.0	0.0	0.0	0.0
1419:05	63.5	0.0	0.0	0.0	0.0
1419:10	64.0	0.0	0.0	0.0	0.0
1419:15	64.5	0.0	0.0	0.0	0.0
1419:20	65.0	0.0	0.0	0.0	0.0
1419:25	65.5	0.0	0.0	0.0	0.0
1419:30	66.0	0.0	0.0	0.0	0.0
1419:35	66.5	0.0	0.0	0.0	0.0
1419:40	67.0	0.0	0.0	0.0	0.0
1419:45	67.5	0.0	0.0	0.0	0.0
1419:50	68.0	0.0	0.0	0.0	0.0
1419:55	68.5	0.0	0.0	0.0	0.0
1420:00	69.0	0.0	0.0	0.0	0.0
1420:05	69.5	0.0	0.0	0.0	0.0
1420:10	70.0	0.0	0.0	0.0	0.0
1420:15	70.5	0.0	0.0	0.0	0.0
1420:20	71.0	0.0	0.0	0.0	0.0
1420:25	71.5	0.0	0.0	0.0	0.0
1420:30	72.0	0.0	0.0	0.0	0.0
1420:35	72.5	0.0	0.0	0.0	0.0
1420:40	73.0	0.0	0.0	0.0	0.0
1420:45	73.5	0.0	0.0	0.0	0.0
1420:50	74.0	0.0	0.0	0.0	0.0
1420:55	74.5	0.0	0.0	0.0	0.0
1421:00	75.0	0.0	0.0	0.0	0.0
1421:05	75.5	0.0	0.0	0.0	0.0
1421:10	76.0	0.0	0.0	0.0	0.0
1421:15	76.5	0.0	0.0	0.0	0.0
1421:20	77.0	0.0	0.0	0.0	0.0
1421:25	77.5	0.0	0.0	0.0	0.0
1421:30	78.0	0.0	0.0	0.0	0.0
1421:35	78.5	0.0	0.0	0.0	0.0
1421:40	79.0	0.0	0.0	0.0	0.0
1421:45	79.5	0.0	0.0	0.0	0.0
1421:50	80.0	0.0	0.0	0.0	0.0
1421:55	80.5	0.0	0.0	0.0	0.0
1422:00	81.0	0.0	0.0	0.0	0.0
1422:05	81.5	0.0	0.0	0.0	0.0
1422:10	82.0	0.0	0.0	0.0	0.0
1422:15	82.5	0.0	0.0	0.0	0.0
1422:20	83.0	0.0	0.0	0.0	0.0
1422:25	83.5	0.0	0.0	0.0	0.0
1422:30	84.0	0.0	0.0	0.0	0.0
1422:35	84.5	0.0	0.0	0.0	0.0
1422:40	85.0	0.0	0.0	0.0	0.0
1422:45	85.5	0.0	0.0	0.0	0.0
1422:50	86.0	0.0	0.0	0.0	0.0
1422:55	86.5	0.0	0.0	0.0	0.0
1423:00	87.0	0.0	0.0	0.0	0.0
1423:05	87.5	0.0	0.0	0.0	0.0
1423:10	88.0	0.0	0.0	0.0	0.0
1423:15	88.5	0.0	0.0	0.0	0.0
1423:20	89.0	0.0	0.0	0.0	0.0
1423:25	89.5	0.0	0.0	0.0	0.0
1423:30	90.0	0.0	0.0	0.0	0.0
1423:35	90.5	0.0	0.0	0.0	0.0
1423:40	91.0	0.0	0.0	0.0	0.0
1423:45	91.5	0.0	0.0	0	

Table G5. Summary and "Best Estimate" Information About the Spectral Distribution and Total Values of Hydrometeor Number Concentration and Liquid-Water-Content Along the Missile Trajectory of Flight No. Q2-6363 (Unit No. R487104) of 27 February 1973, Launched at 1040:30 GMT (See text for description of table)

Missile Altitude (km)	Time (GMT)										Time (GMT)									
	00	01	02	03	04	05	06	07	08	09	10	11	12	13	14	15	16	17	18	19
0																				
10																				
20																				
30																				
40																				
50																				
60																				
70																				
80																				
90																				
100																				
110																				
120																				
130																				
140																				
150																				
160																				
170																				
180																				
190																				
200																				
210																				
220																				
230																				
240																				
250																				
260																				
270																				
280																				
290																				
300																				
310																				
320																				
330																				
340																				
350																				
360																				
370																				
380																				
390																				
400																				
410																				
420																				
430																				
440																				
450																				
460																				
470																				
480																				
490																				
500																				
510																				
520																				
530																				
540																				
550																				
560																				
570																				
580																				
590																				
600																				
610																				
620																				
630																				
640																				
650																				
660																				
670																				
680																				
690																				
700																				
710																				
720																				
730																				
740																				
750																				
760																				
770																				
780																				
790																				
800																				
810																				
820																				
830																				
840																				
850																				
860																				
870																				
880																				
890																				
900																				
910																				
920																				
930																				
940																				
950																				
960																				
970																				
980																				
990																				
1000																				

Summary information is presented in the tables for the "cloud populations" and for the "precipitation populations". The type of population is identified in the first columns of these sections. The total number of drops or particles, of all sizes within the populations, is listed second. The total liquid-water-content content is listed third. It should be emphasized that this total, in the case of clouds, corresponds to the aircraft-measured value for the particular altitude, and, in the case of precipitation, the total corresponds to the radar-measured value for the particular altitude point along the SAMS missile trajectory.

Two additional parameters are also listed in the summary sections of Tables G2 through G5. These are the median volume diameter (D_o) and the maximum diameter (D_m). The maximum diameter, in the case of clouds, is always 79.4 μ , which is the upper truncation boundary of the cloud-size portion (or "cloud population portion") of the spectrum. The maximum diameter, in the case of precipitation, is based on several assumptions (data supported, in part, see Sections G2.2 and G2.4) that were made for the different categories of precipitation, that is, rain, snow, and ice-crystals.

As mentioned in R No. 3, the diameter classes (those of the second sections of Tables G2 through G5) that contain the precipitation-size drops or particles of the D_m size must be interpreted differently than the other table classes containing the smaller drops or particles. The particular diameter classes containing the drops or particles of the D_m size are only "partially filled" with hydrometeors (D_m is smaller than the upper-diameter boundary of the class) and the geometric mean diameters listed in the column headings of Tables G2 through G5 do not provide a measure of the "average size" of the hydrometeors within these classes. An equation specifying the geometric mean diameter for these classes was presented in R No. 3.

It was assumed for the storms of the 1972-73 season, as for those of the 1971-72 season, that the cloud type "nimbostratus" (N_g) was the one that best applied to the aircraft measurements.

The precipitation types in Tables G2 through G4 are identified by symbols. These conform to the category-type specifications of Table 2, R No. 2. Rain is "R"; large-snow is "LS"; small-snow is "SS"; ice-crystals are "C". The subscripts on these symbols identify the hydrometeor type.

*The cloud liquid-water-content values for the storm of 2 February 1973 correspond to the 50th percentile values of the JW liquid-water-contents measured by the AFGL C-130A aircraft, as shown in Figure 5 of the main text. The cloud liquid-water content values for the storm of 27 February 1973 correspond to our "best trajectory estimates" based on the MRI, Navajo measurements indicated in Tables F5, F7, and F8, of Appendix F. The precipitation liquid-water-content values correspond to the profile values for the missile trajectories, which are shown in Figures 1 through 4 of the main text.

"Totals Information" is presented in the last two columns of Tables G2 through G5. The total values of liquid-water-content, in the precipitation size-range, in the melting zone, are listed in the first of these columns. The values are the sum of the liquid-water-content (contribution) of the "fully-melted-drops" (W) plus that of the "water-coated-ice" (I). The grand-total values of the last columns of the tables are the sum of the liquid-water-content (contribution) of the cloud-size hydrometeors plus that of the precipitation-size hydrometeors.

The equations, for the case of ice hydrometeors, specifying the relations between the equivalent-melted-diameter and the approximate, average physical dimensions of the particles were stated in R No. 3. These same relationships pertain to the tabulation herein.

G2. THE SAMS PRECIPITATION MODEL

G2.1 Theory

The development of the distribution model for single-phase (pure water or pure ice) hydrometeors of precipitation size parallels the development described in Section 7 of R No. 2. However, whereas the equations of this cited report were non-truncated, with integration being accomplished between the diameter limits zero to infinity, the equations to be described herein are "double truncated" and the integration is performed between the specific diameters $D = d$, where d is a "minimum diameter size" of the hydrometeors, and $D = D_m$, where D_m is a "maximum diameter size" of the hydrometeors. For ice hydrometeors, that is, snow and ice-crystals, it is presumed that the diameters of discussion are the "equivalent-melted-diameters".

As mentioned in R No. 2, it has been demonstrated by Marshall and Palmer, Marshall and Gunn, Imai et al, and numerous others, ^{15, 19, 20, 21} that the size distribution properties of raindrops, snowflakes, and ice-crystals of precipitable size can be reasonably described by a distribution function of exponential type. This distribution function specifies that the number concentration of the hydrometeor particles will decrease with increasing diameter (or equivalent-melted-diameter) in the manner

$$N = N_0 e^{-\Lambda D}, \text{ No. m}^{-3} \text{ mm}^{-1}, (d \leq D \leq D_m), \quad (G1)$$

19. Marshall, J.S., and Palmer, W. McK. (1948) The distribution of raindrops with size, J. Meteorol. 5:165-166
20. Marshall, J.S., and Gunn, K.I.S. (1952) Measurement of snow parameters by radar, J. Meteorol. 9:322.
21. Imai, I., Fujiwara, M., Ichimura, I., and Toyama, Y. (1955) Radar reflectivity of falling snow, Pap. in Meteorol. and Geophys. (Japan)6:130-139.

where N_0 and Λ have particular values dependent on the category and type of the hydrometeors being considered. The equation, as applied herein, is presumed to be descriptive only between the truncation limits $D = d$ (a minimum diameter) and $D = D_m$ (a maximum diameter).

The total number of hydrometeors in such population is

$$N_T = \int_d^{D_m} N \, dD \text{ No. m}^{-3}, \quad (\text{G2})$$

or

$$N_T = \frac{N_0 r_n}{\Lambda} \text{ No. m}^{-3}, \quad (\text{G3})$$

where r_n is a "truncation ratio", specified by

$$r_n = \frac{\int_d^{D_m} N \, dD}{\int_0^{\infty} N \, dD}, \quad (\text{G4})$$

which, from Eq. (G1) becomes

$$r_n = e^{-d\Lambda} - e^{-D_m\Lambda}. \quad (\text{G5})$$

Values of r_n computed from this equation are shown plotted in Figure G1, for $d\Lambda$ values between 0 and 3 and $D_m\Lambda$ values between 0 and 30. Two sets of scales are shown in the figure. The $d\Lambda$ and $D_m\Lambda$ scales are the inner ones; the others will be discussed later.

The liquid-water-content of the hydrometeor populations described by Eq. (G1) is distributed with diameter as a function of the third moment of Eq. (G1), or as

$$M_D = \frac{\pi}{6} \times 10^{-3} \rho_w N_0 D^3 e^{-\Lambda D}, \text{ gm m}^{-3} \text{ mm}^{-1}, (d \leq D \leq D_m), \quad (\text{G6})$$

where ρ_w is the density of liquid-water, in gm cm^{-3} .

The total liquid-water-content of the population is

$$M = \int_d^{D_m} M_D \, dD, \quad (\text{G7})$$

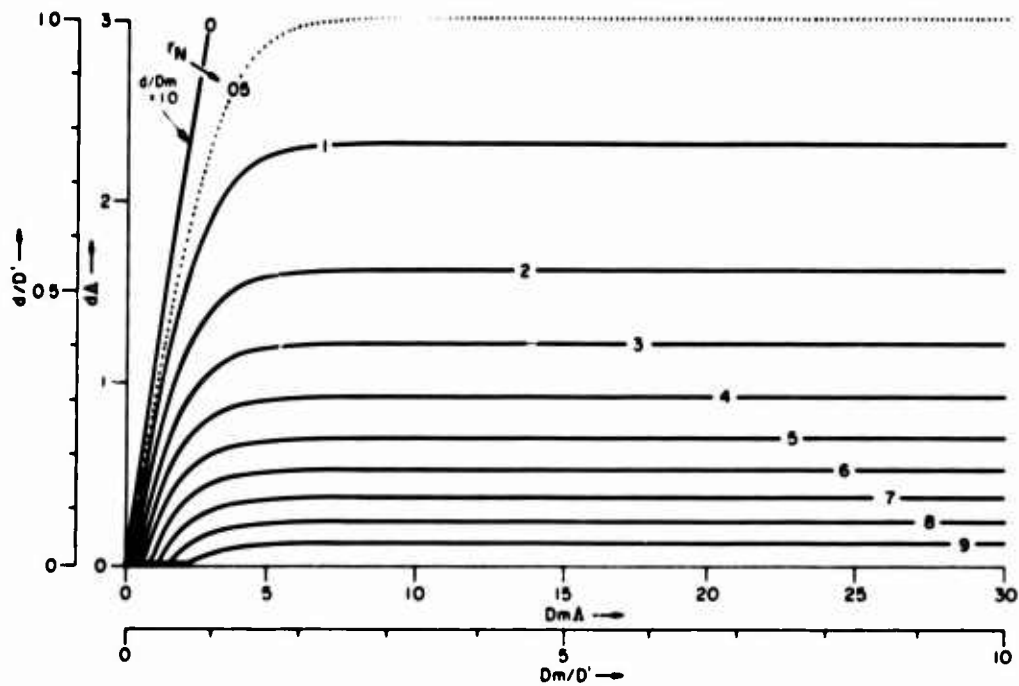


Figure G1. Values of the Truncation Ratio for Particle Number Concentration as a Function of d^Λ and D_m^Λ

which, from Eq. (G6) on performance of the integration, yields

$$M = \frac{\pi \times 10^{-3} \rho_w N_0 \Gamma(4) r_M}{6 \Lambda^4} \text{ gm m}^{-3}, \quad (\text{G8})$$

where $\Gamma(4)$ is the gamma function of 4 and r_M is a truncation ratio for liquid-water-content given by

$$r_M = \frac{\int_0^{D_m} M_D dD}{\int_0^{\infty} M_D dD}. \quad (\text{G9})$$

or, from Eq. (6),

$$r_M = \frac{1}{6} \left\{ e^{-d^\Lambda} \left[(d^\Lambda)^3 + 3(d^\Lambda)^2 + 6d^\Lambda + 6 \right] - e^{-D_m^\Lambda} \left[(D_m^\Lambda)^3 + 3(D_m^\Lambda)^2 + 6D_m^\Lambda + 6 \right] \right\}. \quad (\text{G10})$$

Values of r_M computed from this equation are shown in Figure G2, for the same ranges of d^\wedge and D_m^\wedge previously cited for Figure G1.

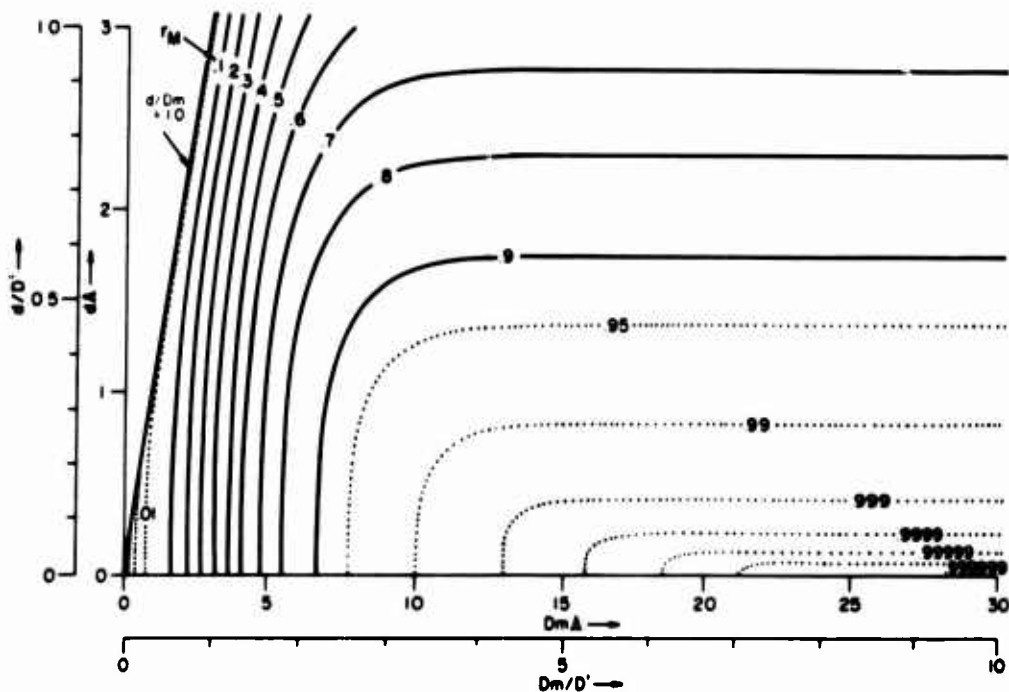


Figure G2. Values of the Truncation Ratio for Distributed Liquid-Water-Content as a Function of d^\wedge and D_m^\wedge

The distributed values of the radar reflectivity factor for the hydrometeor populations described by Eq. (G1) are specified by

$$Z_D = N_0 D^6 e^{-\wedge D}, \text{ mm}^6 \text{ m}^{-3} \text{ mm}^{-\wedge} (d \leq D \leq D_m), \quad (\text{G11})$$

The total value of the radar reflectivity factor, for the entire population of hydrometeors, is

$$Z = \int_d^{D_m} Z_D dD, \quad (\text{G12})$$

*The radar reflectivity factor was discussed in R No. 1 and equations of definition [Eqs. (56) and (63)] were presented for water and ice hydrometeors. The different methods of evaluating the radar reflectivity factor were explained in R No. 2, in Section 3.1.

or, from Eq. (G11) on integration,

$$Z = \frac{N_o \Gamma(7) r_Z}{\Lambda^7} \text{ mm}^6 \text{ m}^{-3}, \quad (\text{G13})$$

where $\Gamma(7)$ is the gamma function of 7 and r_Z is the truncation ratio for the radar reflectivity factor as defined by

$$r_Z = \frac{\int_{d_m}^D Z_D dD}{\int_0^D Z_D dD}, \quad (\text{G14})$$

which, from Eq. (11) becomes

$$r_Z = \frac{1}{720} \left\{ e^{-d\Lambda} \left[(d\Lambda)^6 + 6(d\Lambda)^5 + 30(d\Lambda)^4 + 120(d\Lambda)^3 + 360(d\Lambda)^2 + 720 d\Lambda + 720 \right] - e^{-D\Lambda} \left[(D_m\Lambda)^6 + 6(D_m\Lambda)^5 + 30(D_m\Lambda)^4 + 120(D_m\Lambda)^3 + 360(D_m\Lambda)^2 + 720(D_m\Lambda) + 720 \right] \right\}. \quad (\text{G15})$$

Values of r_Z computed from this equation are shown in Figure G3.

The slope parameter Λ may be eliminated between Eqs. (G8) and (G13) to obtain

$$N_o = \frac{6 \times 10^3 M}{\pi \Gamma(4) \rho_w r_M} \left[\frac{6 \times 10^3 \Gamma(7) r_Z M}{\pi \Gamma(4) \rho_w r_M Z} \right]^{4/3}, \quad (\text{G16})$$

which, from knowledge that $\rho_w = 1.0 \text{ gm cm}^{-3}$, $\Gamma(4) = 6$ and $\Gamma(7) = 720$, simplifies to

$$N_o = 4.46 \times 10^9 \frac{M}{r_M} \left(\frac{M r_Z}{Z r_M} \right)^{4/3} \text{ m}^{-3} \text{ mm}^{-1}. \quad (\text{G17})$$

Alternately, the parameter N_o may be eliminated between Eqs. (G8) and (G13) with the result, after the evaluation of ρ_w , $\Gamma(4)$ and $\Gamma(7)$,

$$\Lambda = 61.2 \left(\frac{M r_Z}{Z r_M} \right)^{1/3} \text{ mm}^{-1}. \quad (\text{G18})$$

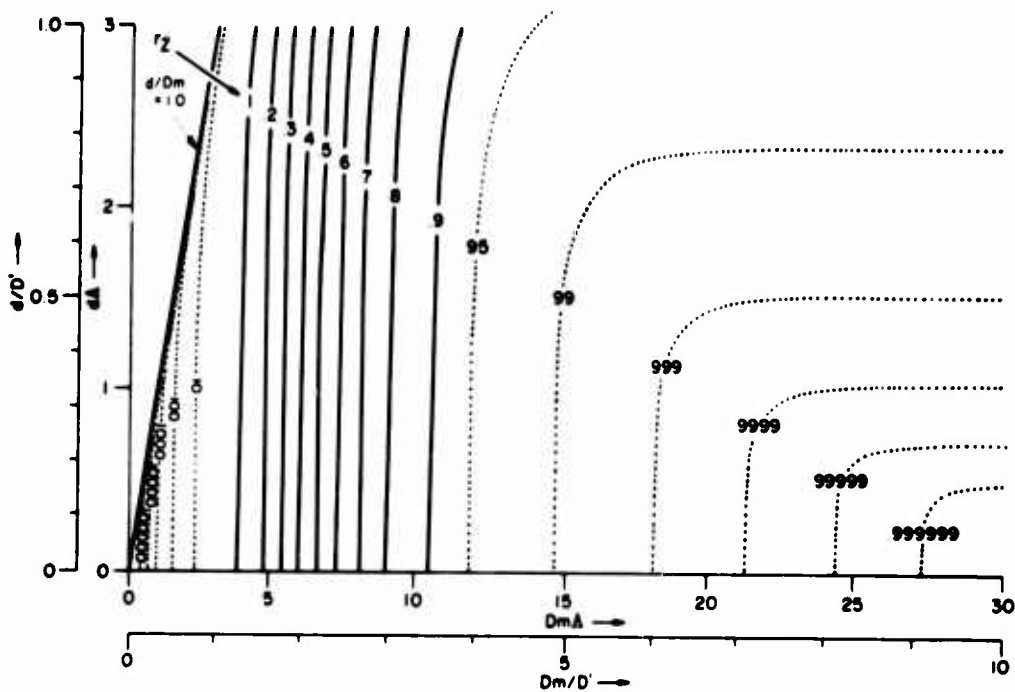


Figure G3. Values of the Truncation Ratio for Distributed Radar-Reflectivity-Factor as a Function of d/Δ and D_m/Δ

The empirical equations of relationship between the hydrometeor liquid-water-content, M , and the radar reflectivity factor, Z , were discussed in R No. 2, Section 4.2. It was explained therein that the equations have the power-function form

$$M = K_M Z^{E_M} \quad (G19)$$

where K_M and E_M have particular values depending on the category and type of hydrometeors under consideration. The K_M and E_M values used in the SAMS program were listed in Table 2 of the cited report.

If Eq. (G19) is substituted into Eq. (G17) first, and into Eq. (G18) second, we obtain

$$N_o = 4.46 \times 10^9 \psi K_M \frac{4}{3E_M} M^{\frac{7E_M-4}{3E_M}} \quad (G20)$$

where

$$\psi = \left(\frac{rZ}{r_M} \right)^{1/3} \quad (G21)$$

and

$$\Lambda = 61.2 \phi K_M \frac{1}{3E_M} M^{\frac{E_M-1}{3E_M}} \quad (G22)$$

where

$$\phi = \left(\frac{r_Z}{r_M} \right)^{1/3} \quad (G23)$$

The reader will note that the Eqs. (G20) and (G22) for double truncated spectra, differ from the equations for non-truncated spectra (Eqs. (76) and (77) of R No. 2) only in that the truncation parameters, ψ and ϕ , appear in the former equations, whereas, in the latter, they do not (they have the value unity for no truncation).

Values of the truncation parameter, ψ , computed from Eqs. (G10), (G15), and (G21) are shown plotted in Figure G4. Values of the parameter, ϕ , computed from Eqs. (G10), (G15), and (G23) are shown in Figure G5. The coordinate scales and ranges are as described previously for the other figures.

Equations (G10), (G15), and (G20) through (G23) permit the evaluation of N_0 and Λ for any category and type of hydrometeor distribution for which the values of K_M and E_M have been empirically established and for which the lower and upper truncation diameters, d and D_m , can be specified. The SAMS assumptions regarding these truncation diameters and the methods of evaluating N_0 and Λ will be explained presently, following the discussion of the model and median diameters.

As noted in R No. 2, the "modal diameters" of the M_D and Z_D distributions are "characteristic parameters" of the hydrometeor populations. These diameters, which specify the peak value points of liquid-water-content and radar reflectivity factor, are given respectively by

$$D' = 3/\Lambda \quad (G24)$$

and

$$D'_Z = 6/\Lambda \quad (G25)$$

These truncation diameters may be instrumentally dictated [because a particular instrument can only obtain measurements over a restricted range of particle diameters (equivalent-melted-diameters)] or they may be "physical diameters" which reflect the actual atmospheric composition of the given hydrometeor spectra.

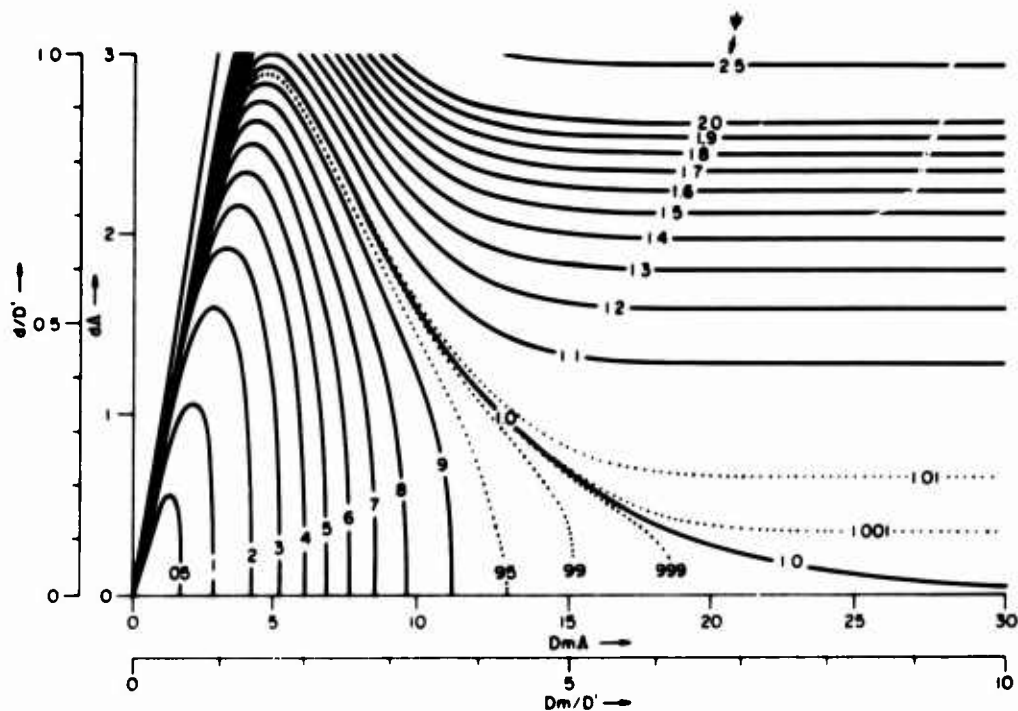


Figure G4. Values of the Truncation Parameter, ψ , as a Function of d^Δ and D_m^Δ

These equations are obtained from the differentiation of Eqs. (G6) and (G11), solving for the diameter values of maximum M_D and Z_D . The equations are identical to those for a non-truncated distribution (see Eqs. (82) and (83) of R No. 2).

It was also noted in this cited report that the "median volume diameter", $D_{0.5}$, of the hydrometeor population is a parameter of common, conventional, cloud-physics interest. The median volume diameter is the particular diameter (value) that separates the liquid-water-content, of the M_D distribution, into two equal parts, half of which is contained in drops or particles having diameters (equivalent-melted-diameters) smaller than $D_{0.5}$, the other half being contained in drops or particles having diameters larger than $D_{0.5}$.

The equations are identical but the values of the modal diameters for truncated vs non-truncated distributions will differ, since the values of Δ will differ.

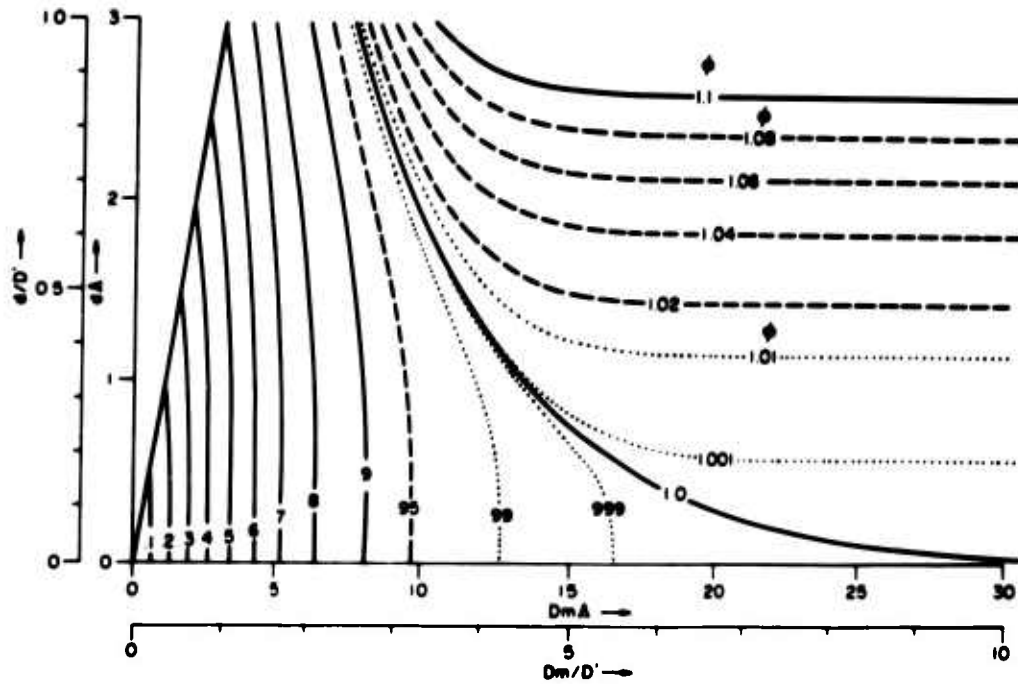


Figure G5. Values of the Truncation Parameter, ϕ , as a Function of d^Λ and D_m^Λ

Thus, for a double-truncated hydrometeor-spectrum of exponential type, the median volume diameter satisfies the integral relationship

$$\int_d^{D_o} M_D dD = \int_{D_o}^{D_m} M_D dD, \quad (G26)$$

which, if the integration is performed, using Eq. (G6), and if all Λ terms are included on the right, yields

$$D_o = \frac{1}{\Lambda} \ln \left\{ \frac{2 \left[(D_o^\Lambda)^3 + 3(D_o^\Lambda)^2 + 6D_o^\Lambda + 6 \right]}{e^{-d^\Lambda} \left[(d^\Lambda)^3 + 3(d^\Lambda)^2 + 6d^\Lambda + 6 \right] + e^{-D_m^\Lambda} \left[(D_m^\Lambda)^3 + 3(D_m^\Lambda)^2 + 6D_m^\Lambda + 6 \right]} \right\}. \quad (G27)$$

It can be seen that D_o in the above equation is a "non-separable variable", since it appears on the left side of the equation and also appears in the D_o^Λ terms in the numerator on the right. The equation cannot be solved analytically for D_o , however, it can be solved by trial and error methods (once truncation assumptions about d and D_m have been made, see Sections G2.2 and G2.4). Particular non-dimensionalized

plots of the parameter $D_0 \lambda$ are shown in Figure G6, plotted vs the coordinates of $d \lambda$ and $D_m \lambda$. The isolines of this figure are also specified in values of D_0/D' , which demonstrates the non-dimensional relationships between the median and modal diameters of the liquid-water-content distributions. The slope parameter, λ , is related to D' as stated in Eq. (G24).

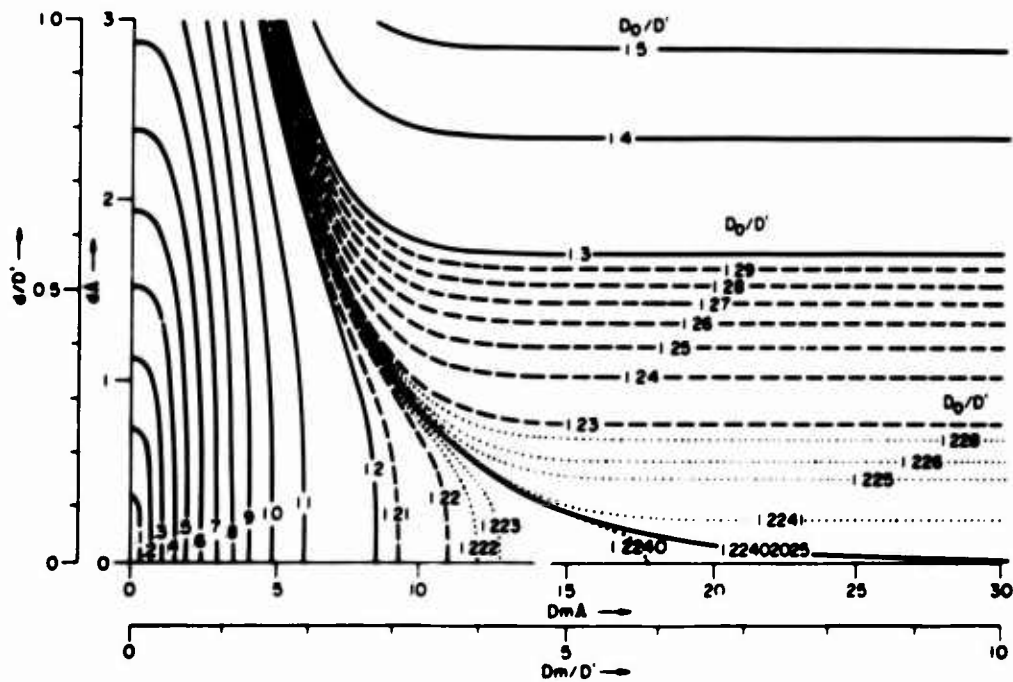


Figure G6. Values of D_0/D' as a Function of $d \lambda$ and $D_m \lambda$

With regard to the $d \lambda$ and $D_m \lambda$ coordinates of Figures G1 through G6, these coordinates are readily converted into equivalent coordinates of d/D' and D_m/D' . Such conversion, as shown accomplished on the outer scales of the figure diagrams, better illustrates the true nature of the truncation situation (in terms of diameter ratios, rather than coordinates involving the slope parameter, λ). Thus, the outer ordinate scale of each of the figures is scaled in units of d/D' , which is the ratio of the lower truncation diameter to the modal diameter, and the outer abscissa scale of each of the figures is scaled in units of D_m/D' , which is the ratio of the upper truncation diameter to the modal diameter.

These figures demonstrate that the mathematics of truncation for the distribution Eqs. (G1), (G6), and (G11) is relatively simple and straightforward when formulated in terms of the non-dimensional ratios of d/D' and D_m/D' , that is,

when formulated in terms of ratios involving the modal diameter, D' . This is because the modal diameter does not depend on the truncation parameters but is a simple function of λ only, see Eq. (G24). The method of formulation also permits truncation in terms of the absolute values of d and D_m , although this is not specifically demonstrated herein.

It might be noted that the mathematics of truncation is considerably complicated if problem formulation is attempted in terms of the median volume diameter, D_o , rather than the mode. Such formulation has been reported by Sekhon and Srivastava²² (also University of Chicago manuscript report). The added complexity stems basically from having to consider Eq. (G27), in specifying the truncation limits, rather than the much simpler Eq. (G24). (In this regard, the reader is forewarned that the nomogram of Figure G6 pertains strictly to truncation in terms of λD , or D/D' . The nomogram cannot be used in any reverse manner to "reason about", or infer, situations of D_o truncation. The analogous nomogram for D_o truncation is presented in Figure G7; it is presented for information only and will not be discussed. A comparison of the nomograms reveals important differences in the two methods of truncation.)

G2.2 Truncation Assumptions of the Model

The particular truncation assumptions used in the SAMS precipitation model were the following:

For the lower truncation diameter, it was commonly assumed for all hydrometeor categories and types that

$$d = 0.07943 \text{ mm} . \quad (\text{G28})$$

This is the lower boundary of the eleventh SAMS class specified in Table G1 which is the approximate separation diameter that is commonly and conventionally assumed to distinguish the cloud-size portion of hydrometeor spectra from the precipitation-size portion. The distinction is physically real for water clouds in contrast to precipitation, since water clouds can exist without the also

There is one difficulty that can conceivably arise with problem formulation in terms of the mode. With very severe truncation, of either the lower or upper diameter limits, it is possible to have a "fictitious mode" which lies outside the diameter range of the truncation. This is mathematically possible under circumstances in which $d > 3/\lambda$, [that is, $d > D'$, see Eq. (G24)] or in which $D_m < 3/\lambda$ (that is, $D_m < D'$). Such circumstances are not physically common but can occur, as, for example, in the case of heavy rain with the maximum drop size limited to the breakup size for raindrops, see the fourth example of Table G6, for truncated solutions.

22. Sekhon, R.S., and Srivastava, R.C. (1970) Snow size spectra and radar reflectivity, J. Atmos. Sci. 27:299-307.

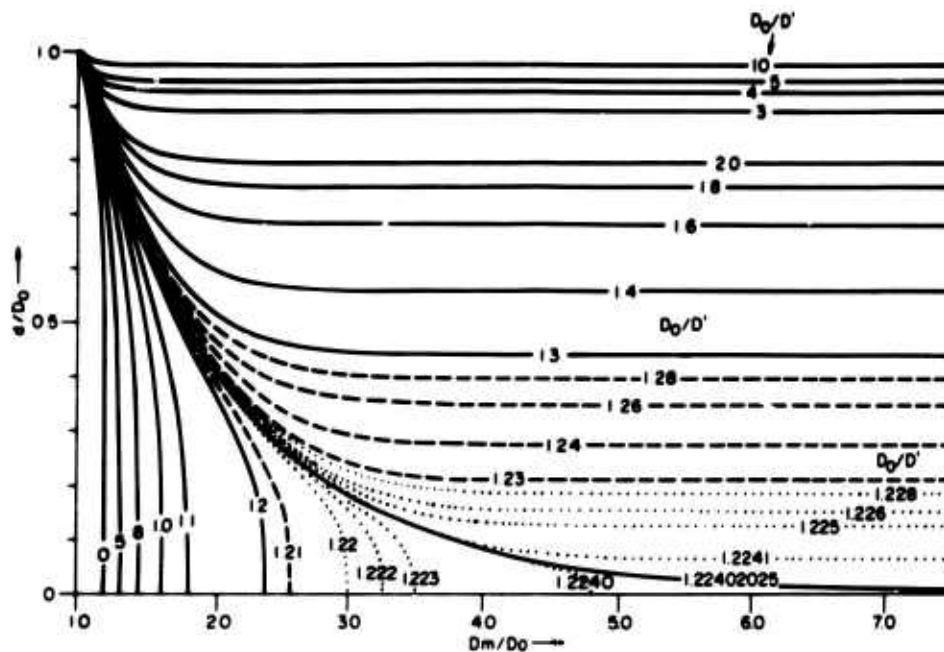


Figure G7. Values of D_0/D' as a Function of d/D_0 and D_m/D_0 (based on the equations and assumptions of Sekhon and Srivastava). The nomogram illustrates the situation of double truncation in terms of the median volume diameter, D_0 , which differs appreciably from truncation in terms of the modal diameter, D' (as used for the SAMS precipitation model and as illustrated in Figure G6)

presence of water drops (or ice or snow particles) of precipitation size, and vice versa. The distinction is less clear, however, regarding the spectrum separability of cloud size ice crystals from the larger-size ice or snow particles of precipitable size. The two size ranges might be clearly demarked in observed distributions (by bi-modal characteristics) but it is also possible that the spectra might be more or less continuous across both size ranges. We do not know, at the moment. Continued acquisition of aircraft data under the SAMS program should shed considerable light on this matter.

With regard to the upper truncation diameter, it was assumed, for large-snow, small-snow and ice-crystals, that this would be specified, in the model, by the relationship

$$D_m^{\wedge} = 15.0 . \quad (G29)$$

where D_m is the maximum equivalent-melted-diameter of the hydrometeor particles

of the populations and Λ is the "slope parameter" of the basic distribution function of Eq. (G1). This same relationship, specified in terms of the modal diameter, through use of Eq. (G24) is

$$D_m/D' = 5.0 . \quad (G30)$$

At the time of the first formulation of the model, this upper truncation assumption for snow and ice crystals was not supported by direct data results. Rather, the assumption was made on the basis that, for the d value of Eq. (G28) and for most distributions of average liquid-water-content, it would provide a truncation ratio for liquid-water-content in the range

$$0.70 \leq r_M \leq 0.999 , \quad (G31)$$

see Eq. (G10) and Figure G2, and a truncation ratio for radar reflectivity factor in the range

$$0.95 \leq r_Z \leq 0.990 , \quad (G32)$$

see Eq. (G15) and Figure G3. These ranges were regarded as reasonable first approximations for snow and ice hydrometeors. (Subsequently, from the SAM-3 data, we have had an opportunity to check the assumption, see later comments.)

The upper truncation assumption for rain was based on disdrometer data which revealed that, for rain having drop sizes smaller than the "breakup size" (~ 5 mm), the maximum drop sizes generally adhered to the relationship

$$D_m/D' = 2.5 , \quad (G33)$$

or

$$D_m^\Lambda = 7.5 , \quad (G34)$$

from Eq. (G24), where the D_m and D' values were measured from the disdrometer samples.

The D_m values of the model were never permitted to exceed the raindrop breakup size. In other words, a stipulation was placed on the assumption of Eq. (G33) that, in no event (under no combination of Λ and liquid-water-content values), would D_m be permitted to exceed

$$D_m = 5.0 \text{ mm} . \quad (G35)$$

G2.3 Equation-Set Solutions and Examples

It will be informative, at this point, to tell how the equations of the precipitation model were solved for SAMS purposes, also to provide several examples of particular solutions that will demonstrate how the truncated equations differ from the non-truncated equations.

The first step in the solution of the equation set for any given hydrometeor type and liquid-water-content is the determination of the values of r_M , r_Z , and Λ , from a trial and error solution of the equation subset (G10), (G15), (G22), and (G23) using the truncation assumptions just discussed. With this knowledge, the values of r_N , N_O , N_T , and Z can be computed from Eqs. (G5), (G21), (G10), (G3), and (G13) in sequence. The modal diameters, D' and D'_Z , can then be established from Eqs. (G24) and (G25) and the maximum diameter, D_m , can be assessed from Eqs. (G29), (G34), or (G35) whichever is appropriate for the given hydrometeor type. Additionally, the median volume diameter, D_o , can be computed from a trial and error solution of Eq. (G27).

Actually, in our evaluations for the SAMS missile trajectories, the Z values (at the various altitude points), from Eq. (G13), are held identical to the radar-measured values (except for computational "round off" errors). The trajectory M values are given, of course, by the particular M vs Z relationships that pertain to the different hydrometeor types.

The constants and exponents of the distribution equations, Eqs. (G1), (G6), and (G11) (for number-concentration, liquid-water-content, and radar reflectivity factor) are also known and these can be integrated over the SAMS class intervals which, in Table G1, are indicated as pertaining to the precipitation size-range of the hydrometeors. The details of this "class interval integration" will not be discussed herein.

Specific solution-examples of the double truncated equations are presented in the upper portion of Table G6. For comparison, the solutions of the non-truncated equations are shown in the lower portion of the table. The example of the first lines of the table shows the solutions for ice-crystals of the C_1 type (bullets and rosettes), for which $K_M = 0.038$, $E_M = 0.529$, and for which it was assumed that the liquid-water-content, M , was 0.05 gm m^{-3} . The example of the second lines reveals the solutions for large snow of the LS_3 type (aggregates of plates), for which $K_M = 0.00495$, $E_M = 0.596$, and for which it was assumed that $M = 0.3 \text{ gm m}^{-3}$. The example of the third lines indicates the solutions for rain of the R_{JW} type (Joss Widespread), for which $K_M = 0.00314$, $E_M = 0.576$, and for which it was assumed that $M = 0.3 \text{ gm m}^{-3}$. For this rain type and M value, the maximum drop size (under the truncation assumption of $D_m^\Lambda = 7.5$, see Eq. (G34)) is smaller than the 5 mm "breakup diameter" for raindrops. The example of the fourth lines of the table illustrates contrast solutions for rain of the R_{JT} type (Joss Thunderstorm),

for which $K_m = 0.00162$, $E_M = 0.576$, and for which it was assumed that $M = 2.0 \text{ gm m}^{-3}$. For this rain type and M value, the maximum drop size would exceed the 5 mm breakup size (under the $D_m^\Lambda = 7.5$ assumption); hence, the limiting stipulation, of Eq. (G35) that $D_m = 5.0 \text{ mm}$, pertains and is employed with the truncated equations of this example. It should be noted that the upper diameter truncation imposed by this stipulation, at this M value, is "very severe".

If the truncated and non-truncated solutions of Table G6 are compared, it is seen that appreciable differences exist for all of the hydrometeor examples, excepting large snow. The differences for C_1 ice-crystals stem primarily from the lower-diameter truncation (since $d = 0.07943 \text{ mm}$ is an appreciable fraction of $D_m = 0.774 \text{ mm}$). The small differences for large-snow are explained by the large diameter range of the spectrum; the truncated portions at either end do not materially affect the values of the distribution parameters, relative to the non-truncated values. The differences for Joss Widespread rain are substantial and these are chiefly the result of upper diameter truncation. The differences for Joss Thunderstorm rain are very large and are due, almost entirely, to the severe upper diameter truncation associated with heavy rain in which the drop sizes cannot exceed the breakup size.

The truncated distribution equations for the hydrometeor types and M values identified in Table G6 are [(see Eqs. (G1) and (G6), also the Λ , N_0 , and D_M values at Table G6)]

$$N = 2.41 \times 10^6 e^{-19.4 D} \quad (0.07943 \leq D \leq 0.774), \quad (\text{G36})$$

$$M = 1260 D^3 e^{-19.4 D} \quad (0.07943 \leq D \leq 0.774), \quad (\text{G37})$$

for C_1 ice crystals (bullets and rosettes),

$$N = 27,400 e^{-4.12 D} \quad (0.07943 \leq D \leq 3.64), \quad (\text{G38})$$

$$M = 14.3 D^3 e^{-4.12 D} \quad (0.07943 \leq D \leq 3.64), \quad (\text{G39})$$

for large snow (LS_3 , aggregates of plates),

$$N = 4290 e^{-2.56 D} \quad (0.07943 \leq D \leq 2.94), \quad (\text{G40})$$

$$M = 2.25 D^3 e^{-2.56 D} \quad (0.07943 \leq D \leq 2.94), \quad (\text{G41})$$

for Joss Widespread rain, where $D_m < 5 \text{ mm}$, and

$$N = 96 e^{-0.355 D} \quad (0.07943 \leq D \leq 5.0), \quad (\text{G42})$$

$$M = 0.050 D^3 e^{-0.355 D} \quad (0.07943 \leq D \leq 5.0), \quad (\text{G43})$$

for Joss Thunderstorm rain, where $D_m = 5.0 \text{ mm}$.

Table G6. Values and Comparisons of Certain of the Distribution Parameters for Four Examples of Hydrometeor Populations Which are Diameter-Truncated (upper section of table, see Eqs. (G29), (G34), (G35)) or Non-Truncated (lower section of table)

Type of Solution	Hydrometeor Type	Assumed Value $gm\ m^{-3}$	Values of Distribution Parameters												
			r_N	r_M	r_Z	ϕ	ψ	λ	N_0 No. m^{-3} mm^{-1}	N_T No. m^{-3}	D' mm	D_Z mm	D_p mm	D_0 mm	Z mm
Truncated	Ice Crystals - C_1	.05	.215	.929	.661	1.02	1.17	10.4	2.41×10^6	2.67×10^4	.155	.309	.774	.200	1.68
Truncated	Large Snow - L_{S_3}	.3	.721	.999	.992	.998	.991	4.12	27,400	4790	.728	1.46	3.64	.895	.78
Truncated	Rain - R_{JT} , $D_m < 5\ mm$.3	.816	.941	.622	.871	.612	2.56	4290	1370	1.17	2.34	2.94	1.39	27.40
Truncated	Rain - R_{JT} , $D_m = 5\ mm$	2.0	.803	.105	.00238	.283	.0615	.355	.96	218	8.45*	16.9*	5.0	3.91	233,000
Non-Truncated	Ice Crystals - C_1	.05	1.0	1.0	1.0	1.0	1.0	16.0	2.06×10^6	1.08×10^5	.158	.316	.774	.200	1.68
Non-Truncated	Large Snow - L_{S_3}	.3	1.0	1.0	1.0	1.0	1.0	4.13	27,500	6700	.727	1.45	3.64	.889	.78
Non-Truncated	Rain - R_{JT} , $D_m < 5\ mm$.3	1.0	1.0	1.0	1.0	1.0	2.93	7000	2390	1.02	2.05	2.94	1.25	27.40
Non-Truncated	Rain - R_{JT} , $D_m = 5\ mm$	2.0	1.0	1.0	1.0	1.0	1.0	1.25	1570	1250	2.39*	4.79*	5.0	3.91	233,000

* See footnote on page 205.

For purposes of comparison, the non-truncated distribution equations for these same hydrometeor types and M values are, respectively,

$$N = 2.06 \times 10^6 e^{-19.0 D}, \quad (G44)$$

$$M = 1080 D^3 e^{-19.0 D}, \quad (G45)$$

for C_1 ice-crystals,

$$N = 27,600 e^{-4.13 D}, \quad (G46)$$

$$M = 14.5 D^3 e^{-4.13 D}, \quad (G47)$$

for large snow, LS_3 ,

$$N = 7000 e^{-2.93 D}, \quad (G48)$$

$$M = 3.67 D^3 e^{-2.93 D}, \quad (G49)$$

for rain, R_{JW} , and

$$N = 1570 e^{-1.25 D}, \quad (G50)$$

$$M = 0.822 D^3 e^{-1.25 D}, \quad (G51)$$

for rain, R_{JT} . In all of these non-truncated equations, the distribution extends continuously from $d = 0$ to $D_m = \infty$.

Comparisons of the truncated and non-truncated distribution equations of these examples reveal that substantial differences exist, again with the exception of large snow.

It should be apparent that the truncated equations are prerequisite for SAMS, to provide spectral information that is reasonably descriptive of actual atmospheric hydrometeors. The non-truncated equations simply cannot be used for such application.

G2.4 Model Prediction vs Data Results

The SAMS precipitation model described herein was used to provide information about the drop or particle distributions of number concentration and liquid-water-content for the hydrometeors that were present along the path trajectories of all of the missile flights of the SAMS-1 through SAMS-4 seasons at Wallops Island, Virginia. It should be noted that, to serve immediate operational needs,

this particular, spectral information was submitted to SAMSO well in advance of the detailed analyses and formal report descriptions of the storm and hydrometeor conditions of the individual seasons.

Certain surface and aircraft data acquired during the SAMS-3 season provided comparison-verification checks on the assumptions and predictions of the model. These comparisons will be described in the following paragraphs.

Observed spectra of raindrop number-concentration, liquid-water-content and radar reflectivity factor were presented in Table D2, of Appendix D, which were obtained from disdrometer data and filter paper samples. Comparison spectra determined from the precipitation model, for common values of total liquid-water-content and common class intervals, are shown in Tables G7 and G8. The truncation limits used for the Table G7 results were the normal SAMS limits of $d = 0.07943$ mm and $D_m = 7.5/\Lambda$, see Eq. (G34). The lower truncation limits of the Table G8 results was specified to be equal to the diameter of minimum sensitivity (detectability) of the disdrometer and filter paper samples, with $D_m = 7.5/\Lambda$, as in Table G7.

The precipitation rates of the model computations are listed in the last columns of Tables G7 and G8. These precipitation rates may be compared with those for the tipping-bucket instruments, the disdrometers and the filter-paper samples that are listed in Table D1, of Appendix D. The rates are in general agreement, within the difference spread of the observational values.

Comparison of Tables D2, G7, and G8 reveals that the upper truncation diameters of the model, prescribed by Eq. (G33), correspond well with the observed maximum diameters of the disdrometer samples but that they are smaller than the maximum diameters recorded on the filter papers. It is also seen that the class number concentration values and liquid-water-content contributions predicted by the model are in good agreement with the filter-paper samples over the comparable diameter ranges. For the disdrometer samples, the model predicts larger drop concentrations and liquid-water-contents in the smaller size classes than were detected instrumentally. However, as noted in Appendix D, the disdrometers, for drop sizes smaller than about 0.75 mm generally lacked the sensitivity to detect and record the numbers of the drops that were actually present (as revealed by the filter papers). Thus, at least for the rainstorm and sample period of 26 February 1973, we can state that the model provided a better description of the spectral characteristics of the rain, for drop sizes < 0.75 mm, than did the disdrometer instruments, with their sensitivity problems.

Table G7. Distributions of Number Concentration, Liquid-Water-Content and Radar Reflectivity Factor Computed From the Precipitation Model for Conditions of Matching Correspondence With the Disdrometer and Filter-Paper Samples of Rain, of Table D2, Appendix D. The truncation assumptions were $d = 0.07943$ mm, with $D_{max} = 7.5$, which are the standard assumptions, discussed in the text, that were used throughout the SAMS-1 through SAMS-4 seasons. The total liquid-water-content values for the model and samples were assumed to be identical. The rain type assumed for the model computations was "loss Widespread"

Sample Identification of Model Correspondence	Distribute Parameter	Class Diameter (mm)															$\sqrt{N_T}$	F	k	P				
		.15	.25	.35	.45	.55	.65	.75	.8	1.1	1.3	1.5	1.7	1.95	2.25	2.55								
26 Feb 73 Dis. No. 1 Filter Paper 1249:00 to 1249:30	Number Concentration	258	186	134	97	70	50	36	24	16	11	7	5	3	2	.5	2.2%	.222	.108	30.4	.308	.00490	1.51	
	Liquid-Water-Content	0	.002	.003	.005	.006	.007	.008	.017	.016	.014	.011	.008	.008	.003	.003			140					
	Radar Reflectivity Factor	.003	.045	.246	.095	1.4	3.77	6.41	23.4	40.7	57.3	64.3	72.4	110	55.5									
26 Feb 73 Dis. No. 3 Filter Paper 1249:00 to 1249:30	Number Concentration	249	177	125	88	63	44	31	21	15	10	7	5	3	2	1.5	.1	2.17	.452	.086	29.2	.303	.00483	1.16
	Liquid-Water-Content	0	.001	.003	.004	.005	.006	.007	.014	.013	.011	.008	.006	.006	.002	.002								
	Radar Reflectivity Factor	.003	.043	.230	.734	1.73	3.33	5.57	19.8	33.0	44.9	51.5	55.5	82.5	11.4									
26 Feb 73 Filter Paper 1249:00 to 1249:30	Number Concentration	274	205	153	114	85	64	48	34	24	17	11	6	4	2	.4	2.57	1081	.172	32.9	.302	.00519	2.58	
	Liquid-Water-Content	0	.002	.003	.005	.007	.009	.011	.023	.024	.022	.014	.015	.016	.012	.003								
	Radar Reflectivity Factor	.001	.050	.281	.947	2.35	4.83	8.54	32.4	60.2	91.7	125	145	220	259	.942								
26 Feb 73 Dis. No. 4 South Site 1341:00 to 1341:30	Number Concentration	252	180	128	91	65	46	33	20	10	5	3	2	2	.2	2.21	875	.095	29.6	.302	.00467	1.30		
	Liquid-Water-Content	0	.001	.003	.004	.006	.007	.007	.015	.014	.012	.009	.008	.008	.001									
	Radar Reflectivity Factor	.003	.044	.235	.756	1.80	3.47	5.87	21.2	35.4	48.3	57.0	72.4	110	20.0									
26 Feb 73 Filter Paper South Site 1341:00 to 1341:30	Number Concentration	276	207	155	117	87	66	49	36	20	11	6	5	2	.6	2.61	1102	.181	33.2	.302	.00526	2.74		
	Liquid-Water-Content	0	.002	.003	.006	.008	.009	.011	.024	.025	.023	.019	.015	.019	.012	.005								
	Radar Reflectivity Factor	.003	.051	.285	.972	2.41	4.98	8.72	34.0	63.8	96.5	125	145	275	259	135								

Comparison of the total Z values of the filter-paper samples and the "model corresponding values" reveal that the observed values are appreciably larger than those of the model. This suggests that the upper-truncation assumption of the model, that is, $D_m = 7.5/\Lambda$, might be too small and that a better Z value approximation might be achieved by use of an assumption that would give somewhat larger D_m values, perhaps an assumption of $D_m = 9.0/\Lambda$, or thereabouts.

The upper truncation assumption of the model for ice hydrometeors was checked by comparison with the foil-impactor data described in Section E2, of Appendix E. These data consisted of analytical measurements of the maximum-size particles that were recorded on the foil impactor instrument of the C-130A aircraft during the storm flight of 2 February 1973. The maximum sizes were determined by two different analysts for sampling volumes ranging from 20 to 60 m³. The analytical results were listed in Table E3 and are shown plotted in Figure G8. The solid vertical bars of the figure indicate the maximum-size particles (maximum physical size) that were determined by the first analyst (Analyst A₁ of Table E3); the dotted bars show the sizes determined by the second analyst (A₂). No foil data were available for storm altitudes below 11,000 ft (3.35 km).

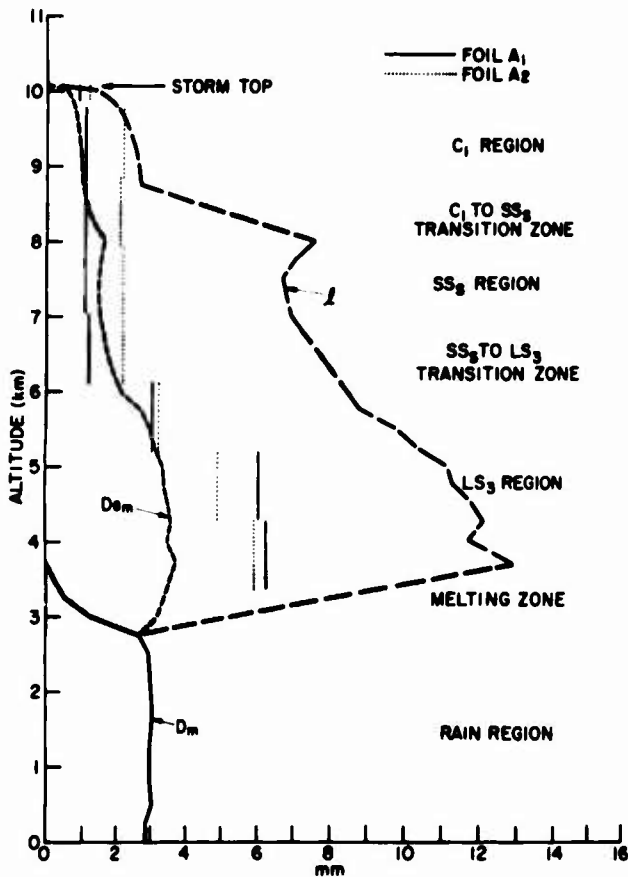


Figure G8. Comparisons of Model Predicted Maximum Particle Sizes With the Maximum Sizes Determined From Aircraft, Foil-Impactor Data for Large Sampling Volumes

The left hand profile of the figure, above the base of the melting zone, shows the maximum equivalent-melted-diameters of the hydrometeors as predicted by the precipitation model for the path trajectories of the two SAMS missiles that were fired through the storm. Specifically, they are the average \overline{D}_m values of the ones listed in Tables G2 and G3.

The right hand profile in Figure G8, above the base of the melting zone, indicates the maximum physical sizes of the particles, corresponding to the \overline{D}_m values of the model and presuming that the D_m to l_m conversions for large-snow, small-snow, and ice-crystals were those specified by Eqs. (G6) through (G8) of R No. 3. There is appreciable uncertainty in these relationships, as has been mentioned elsewhere herein.

The figure reveals that the physical sizes of the particles predicted by the model (plus the D_m to l_m assumptions) are considerably larger, in the large-snow and small-snow regions, than those determined from the foil record by the two analysts. The difference in the large-snow region is about a factor of two; in the small-snow region it is about a factor of three. The model values in the ice-crystal region are in fair agreement with the ones measured by the second analyst but are appreciably larger than those measured by the first.

Other comparisons of this type were also made for certain of the Wallops storms of the SAMS-4 season. The model again tended to overpredict, but not as badly as in the cases of the large-snow and small-snow regions of Figure G9. The comparisons, overall, suggest that the upper truncation assumption of the model for ice hydrometeors should perhaps be modified to a value of about

$$D_m \cong 12/\Lambda, \quad (G52)$$

rather than $D_m = 15/\Lambda$, as at present.

There are various questions concerning these comparisons for which answers are not presently available. There are questions of the correctness of the D_m to l_m assumptions. Also, there are questions of the representativeness of the foil data cited previously. Are these data, which were obtained from sampling volumes of 20 to 60 m³, representative of the "largest-particle-size-situations" in radar volumes of 10⁶ to 10⁷ m³, that we are attempting to describe with the model?

Additional checks on the descriptivity of the precipitation model can be made by comparing the model-prescribed values of the "form factor", F , and total number concentration, N_T (and their variations across the Z range of expectation) with the values and variations that are present in actual data. The "form factor" and the other physical factors that cause the constants and exponents of the M vs Z regression equations to have particular values for the different hydrometeor types were discussed in Appendix E. Data were presented in this appendix (and Appendix H) to show the typical, normal values of the form factor, also to demonstrate,

for sets of data pertaining to rain, large-snow, and ice crystals, the regression trends of the gradient parameters $\Delta \log F / \Delta \log Z$, $\Delta \log N_T / \Delta \log Z$, and $\Delta \log k / \Delta \log Z$.

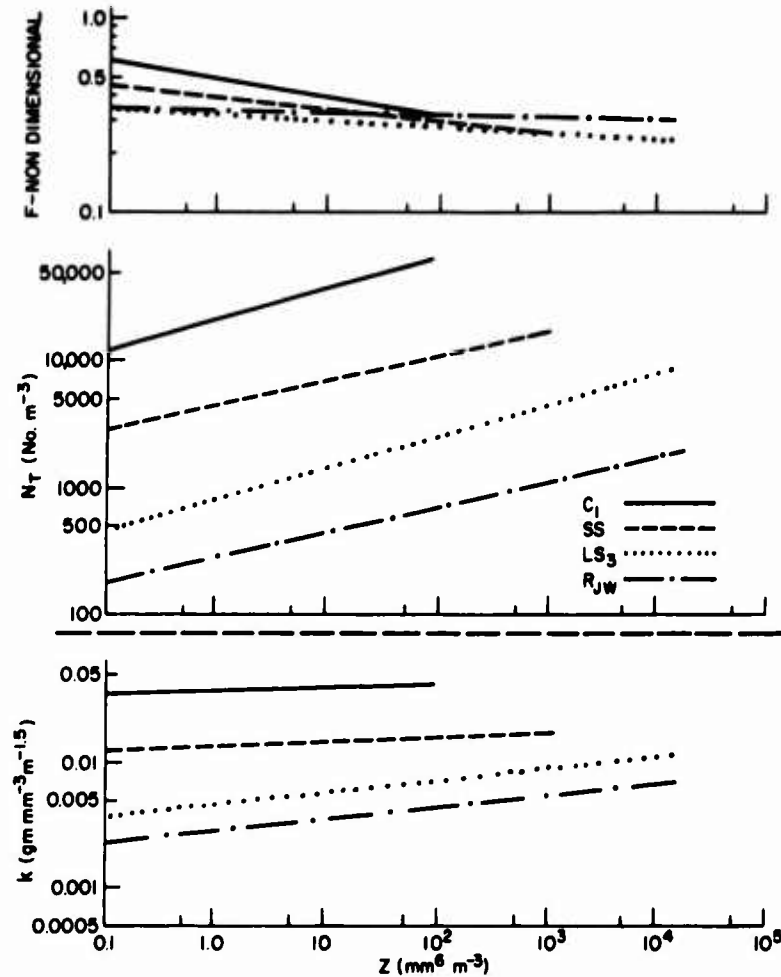


Figure G9. Value Trends With Z of the Form Factor, F, Upper Diagram, of the Total Number Concentration of the Drops or Particles, N_T, Middle Diagram, and of the Spectral Parameter, k, Lower Diagram, as Prescribed by the SAMS Precipitation Model for the Hydrometeor Types Cited in the Text

The upper diagram of Figure G9 shows the variation of log F vs log Z that is predicted by the precipitation model for C₁ ice crystals (solid line), for small-snow,

SS_2 (dashed line), for large-snow, LS_3 (dotted line) and for rain, R_{JW} (dashed-dotted line). The middle and lower diagrams of the figure show the variation of $\log N_T$ vs $\log Z$ and $\log k$ vs $\log Z$ for these same hydrometeor types and coding scheme.

The variation lines of these diagrams are comparable, on a one for one basis, with the regression lines of the diagrams of Figure E12, for the ice crystal data of PFM-5, of Figure E11, for the large-snow data of Ohtake and Henmi¹⁵, and of Figures E9 and E10, for the disdrometer data for rain. The comparison values of $\Delta \log F / \Delta \log Z$, $\Delta \log N_T / \Delta \log Z$, $\Delta \log k / \Delta \log Z$, E_M , $\overline{\log k}$, $\overline{\log Z}$, and K_M for the data and model are listed in Table G9.

These figures and table reveal that the values and trends of $\Delta \log F / \Delta \log Z$, $\Delta \log N_T / \Delta \log Z$ and $\Delta \log k / \Delta \log Z$ prescribed by the precipitation model are quite similar to those that are present in the data. It will be noted, however, that the absolute values of the model parameters (that is, of F , N_T , and k , for any common Z value) are larger than the ones of the data. This is explained by the fact that the lower truncation diameter of the model is smaller than the minimum diameters that were measurable by the instruments or techniques used to acquire the data. Previous comments herein, specifically regarding rain, have noted the problems involved in measurement attempts to determine the numbers and sizes of the smallest hydrometeors of the populations.

To summarize the descriptivity of the precipitation model presented herein, the model provides a good description of rain, large-snow and small-snow. The upper truncation assumption of $D_m^\wedge = 7.5$, for rain, should, perhaps, be increased somewhat, to about 9.0, for better conformity with data we have acquired thus far. For ice hydrometeors, the upper truncation assumption of $D_m^\wedge = 15$ seems overly large, relative to data for large sampling volumes, and a value of about 12 would appear to be more realistic. With regard to the lower truncation assumption, of $d = 0.07943$ mm, this seems quite reasonable for rain and large-snow. However, data presently available suggests that the exponential trend of the model could probably be extended downward to smaller minimums for small-snow and ice-crystals, perhaps to $d = 0.05012$ mm, for small-snow, and $d = 0.03162$ mm, for ice-crystals (see the SAMS class-boundary values of Table G1).

Table G9. Comparison Parameters of Hydrometeor Data and Precipitation Model.
See Eqs. (E60), (E83), and (E84), Also Table E11

Data Source	Hydrometeor Type	$\frac{\Delta \log F}{\Delta \log Z}$	$\frac{\Delta \log N_T}{\Delta \log Z}$	$\frac{\Delta \log k}{\Delta \log Z}$	E_M	$\log k$	$\log Z$	K_M
Disdrometer A 22 March 1972	Rain	-0.041	0.521	0.219	0.719	-2.565	2.087	0.000930
Disdrometer B 22 March 1972	Rain	-0.045	0.365	0.137	0.637	-2.507	2.268	0.00150
Ohtake-Henmi (1970)	Large-Snow LS ₅	-0.116	0.290	0.0290	0.529	-2.316	2.495	0.00411
PVM-5	Ice Crystals	-0.0736	0.607	0.230	0.730	-1.579	1.267	0.0109

Precipitation Model	Rain R _{JW}	-0.021	0.195	0.076	0.576	-	-	0.038
Precipitation Model	Large-Snow LS ₃	-0.026	0.244	0.096	0.596	-	-	0.0145
Precipitation Model	Small-Snow SS _s	-0.057	0.186	0.036	0.538	-	-	0.00495
Precipitation Model	Ice Crystals C ₁	-0.075	0.207	0.029	0.529	-	-	0.00314

Appendix H

Special Background Studies

Two special studies are described in this appendix that provide background information that is used and discussed in Appendix E. The first study concerns the development and presentation of the form-factor equations and graphs for exponentially-distributed, linearly-classified spectral data for hydrometeors. The second describes how the uncertainty effects of converting basic measurement data for ice hydrometeors into terms of equivalent-melted-diameter will cause resultant uncertainties in the values of liquid-water-content (M), radar reflectivity factor (Z), and the spectral parameter (k). The relative and absolute uncertainties are discussed and methods are suggested whereby the values of k can be computed with acceptable accuracy without the necessity for detailed hydrometeor categorization or typing.

The studies are presented with a minimum of commentary, since the primary study results and conclusions are discussed in Appendix E.

H1. FORM FACTOR EQUATIONS AND GRAPHS FOR EXPONENTIALLY-DISTRIBUTED, LINEARLY-CLASSIFIED, SPECTRAL DATA FOR HYDROMETEORS

The distribution function describing the exponential distribution of the number concentration of hydrometeor drops or ice particles with the drop or particle diameter (equivalent-melted-diameter) is from Eq. (G1) of Appendix G.

$$N = N_0 e^{-\Lambda D} \text{ No. m}^{-3} \text{ mm}^{-1}, \quad (\text{H1})$$

where N is the number concentration of the drops or particles of diameter, D , N_0 is the "zero intercept" of the equation and Λ is the "ln slope" of the distribution (when $\ln N$ is plotted vs D).

For this distribution function, the diameter bandwidth is infinitesimally small. However, the function, as written, has in effect, been normalized to pertain to a diameter bandwidth of 1 mm. If we wish to assume some bandwidth other than 1 mm, such as a diameter width equal to ΔD , then we may rewrite Eq. (H1) as

$$N = N_0 \Delta D e^{-\Lambda D} \text{ No. m}^{-3} \Delta D^{-1}. \quad (\text{H2})$$

The bandwidth, ΔD , may be considered to be equivalent to the "class width", for classified data which are exponentially distributed. For such data, if we assume that the classification is linear, which means that ΔD is commonly the same for all diameter classes of the distribution, the "zero intercept" of Eq. (H2) will be

$$N_0^* = N_0 \Delta D, \quad (\text{H3})$$

rather than N_0 , as in the case of Eq. (H1). This permits us to rewrite Eq. (H2) as

$$N_i = N_0^* e^{-\Lambda D_i} \text{ No. m}^{-3} D^{-1} \quad (\text{H4})$$

where N_i is the class number concentration of the drops or particles having the mid-diameter size, D_i , which exist in classes of width, ΔD , and N_0^* is the "zero intercept value" of N_i .

If the data are linearly classified, then, from Eq. (E14), of Appendix E,

$$D_i = \frac{(2i - 1)}{(2n - 1)} D_n, \quad (\text{H5})$$

where n is the number of diameter classes in the distribution, D_i is the mid-diameter of any given, or i 'th, and D_n is the mid-diameter of the n 'th, or last, class, which contains the drops or particles of the largest size. For linear classification, the classwidth is

$$\Delta D = D_{i+1} - D_i, \quad (\text{H6})$$

or, from Eq. (H5),

$$\Delta D = \frac{D_n}{n - 1/2}. \quad (\text{H7})$$

The total number concentration, of the drops or particles of all sizes in the classified distribution, is

$$N_T = \sum_{i=1}^{i=n} N_i \quad (H8)$$

which, from Eq. (H4), becomes

$$N_T = N_0^* \sum_{i=1}^{i=n} e^{-\Lambda D_i} \quad (H9)$$

In Appendix E, the equation specifying the form factor for linearly classified data was written as [see Eq. (E23)]

$$F = \frac{\sum_{i=1}^{i=n} (2i - 1)^3 \alpha_i}{\left[\sum_{i=1}^{i=n} (2i - 1)^6 \alpha_i \right]^{0.5}} \quad (H10)$$

where the coefficients, α_i , were defined as

$$\alpha_i = N_i / N_T \quad (H11)$$

From Eqs. (H4) and (H9), it follows that α_i , for an exponential distribution, is

$$\alpha_i = \frac{e^{-\Lambda D_i}}{\sum_{i=1}^{i=n} e^{-\Lambda D_i}} \quad (H12)$$

which, for linear classification, becomes, from Eq. (H5),

$$\alpha_i = \frac{\Omega^i}{\sum_{i=1}^{i=n} \Omega^i} \quad (H13)$$

where

$$\Omega = e^{\frac{-\Lambda D_n}{(n - 0.5)}} \quad (H14)$$

and where Ω^i , in Eq. (H13), in case there should be any question, is Ω raised to the i 'th power.

When α_1 , from Eq. (H13), is substituted into Eq. (H10), we obtain

$$F = \sqrt{\frac{1}{\sum_{i=1}^{i=n} \Omega^i} \frac{\sum_{i=1}^{i=n} (2i-1)^3 \Omega^i}{\left[\sum_{i=1}^{i=n} (2i-1)^6 \Omega^i \right]^{0.5}}} \quad (H15)$$

which is the form factor equation for exponentially-distributed, linearly classified data which are truncated at the upper diameter limit of the n'th class, or at

$$D_{UL} = D_n + \Delta D/2. \quad (H16)$$

Equations (H14) and (H15), which pertain to the situation of no lower diameter truncation (such truncation will be considered presently), were evaluated for ΔD_n values between -20 and 140 and for n values between 2 and 100. The results are shown in Figure H1. It is seen that the form factor has a maximum value of unity and that the values are never smaller than 0.222 (the approximate mathematical minimum). It might also be noted, with reference to Eqs. (H14) and (H15), that the parameter ΔD_n is a non-dimensional measure of the upper truncation limit of the exponential spectra.

The diagram of Figure H1 is actually a "gross overplot" of the actual atmospheric range of the ΔD_n values. In Appendix G, it is pointed out that available data concerning the maximum equivalent-melted-diameters of ice-hydrometeors reveal that ΔD_n (the SAMS model equivalent) has a value of about 12, possibly as large as 15, in certain cases. Under the assumption that the atmospheric range of ΔD_n would certainly be bracketed by values from -5 to 20, the isolines of Figure H1 were plotted at expanded scale, as shown in Figure H2. Our comments will be made relative to this figure, rather than Figure H1.

There are two special cases of exponential distributions that should be noted. A monodispersed distribution is one such case, although it is a rather trivial one. The form factor value for a monodispersed distribution is 1.0; the point of its occurrence on the Figure H2 diagram is indicated by the point labeled "M". The other special case is that of a "uniform distribution" (in which all classes contain equal numbers of the drops or particles). For such distribution, $\lambda = 0$, $\Omega = 1.0$, see Eq. (H14), and the form factor is specified by

$$F = \sqrt{\frac{1}{n} \frac{\sum_{i=1}^{i=n} (2i-1)^3}{\left[\sum_{i=1}^{i=n} (2i-1)^6 \right]^{0.5}}} \quad (H17)$$

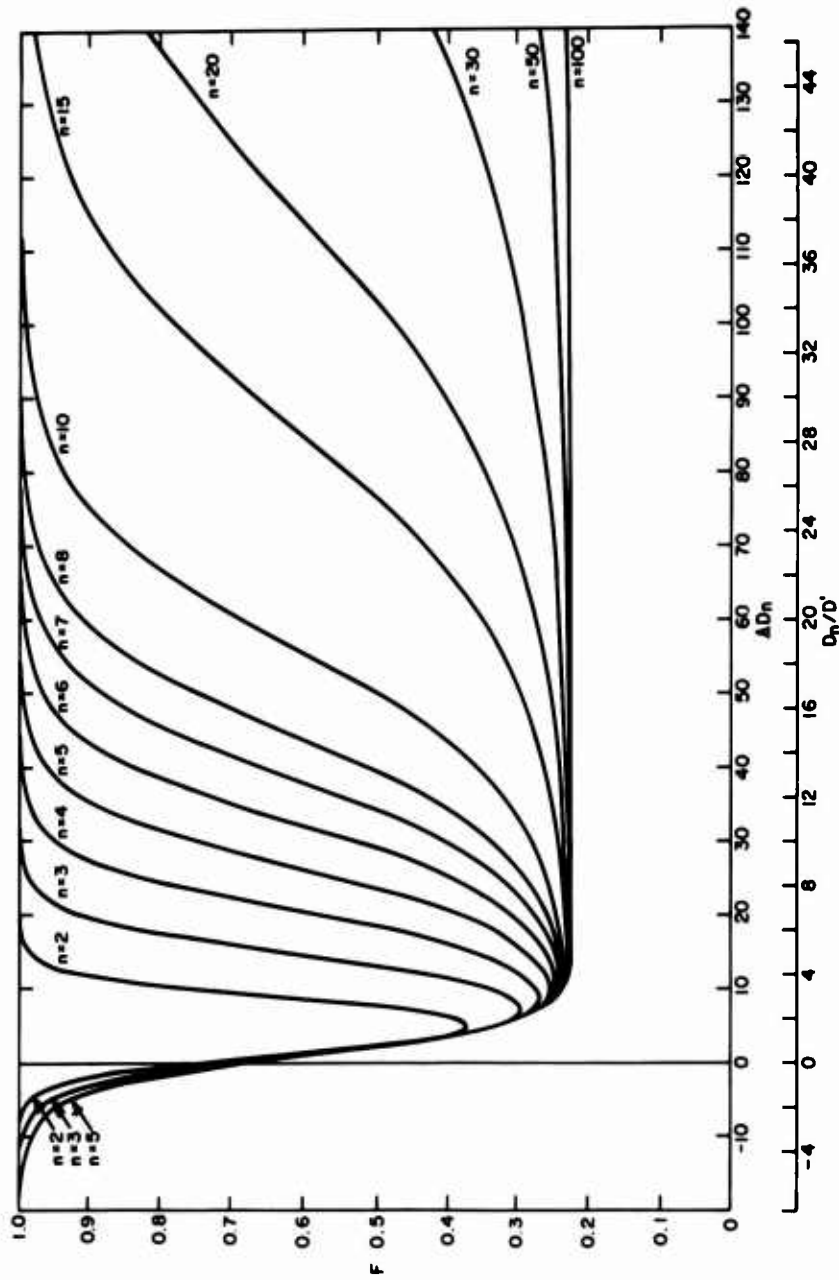


Figure H1. Values of the Form Factor as a Function of AD_n and n , for AD_n Values Ranging From -20 to 140, No Lower Diameter Truncation

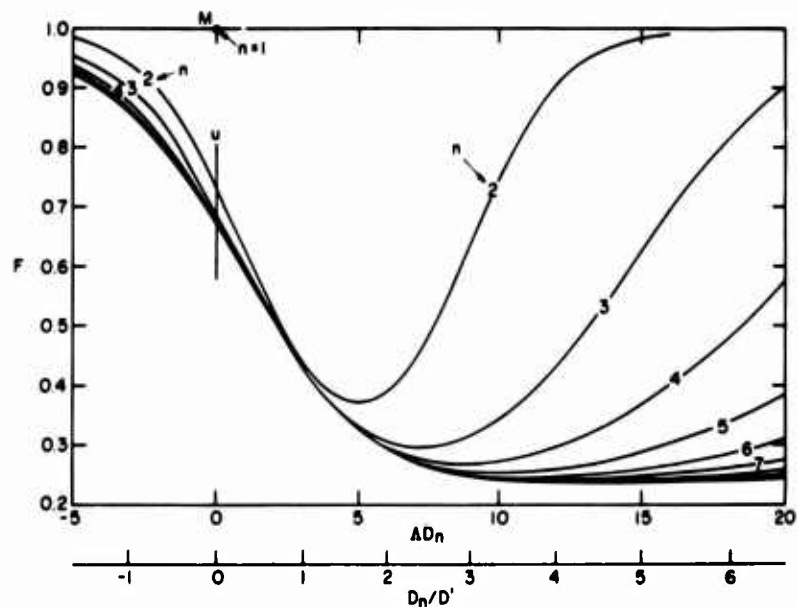


Figure H2. Values of the Form Factor as a Function of AD_n and n , for AD_n Values in the Typical Atmospheric Range of -5 to 20, No Lower Diameter Truncation

This case is also indicated on the Figure H2 diagram. It is the vertical line at $AD_n = 0$, which is labeled "U".

The diagram shows that the F values vary considerably with n between $n = 2$ and $n \approx 10$. As explained in Appendix E (footnote page 151), this occurs because, except for monodispersed distributions, at least 10 classes ($n = 10$) are required with classified data to provide an adequate description of a theoretical distribution function, such as one of exponential type. The same holds in general regarding the number of classes needed to provide adequate description of any continuous spectra, either atmospherically-observed or theoretical. Thus, with reference to the Figure H2 diagram, the form factor values for $n < 10$ really represent a special category of classified data in which the number of classes is insufficient to describe adequately the true nature of the continuous distribution.

With regard to the matter of the lower diameter truncation of the exponential distributions, this was investigated by assuming in Eq. (H15), (1) that the first size class of the distribution had zero number concentration, (2) that the first two classes had zero number concentration, and (3) that the first three classes had zero

number concentration. This is equivalent to lower diameter truncation, moving upward from a lower diameter boundary of $d = 0$ (to which Figures H1 and H2 pertain) to $d = \Delta D$ (see the results of Figure H3), to $d = 2\Delta D$ (see Figure H4), to $d = 3\Delta D$ (see Figure H5). These figures compared to Figure H2, clearly demonstrate that the form factor values for any given ΔD_n and n increase with increasing lower diameter truncation. The figures also show that, with lower diameter truncation, the form factor values vary appreciably with n , even for $n \geq 10$. This implies that the number of classes needed to provide an adequate description of an exponential distribution which is truncated at the small diameter end of the spectra exceeds the number required to describe a non-truncated distribution.

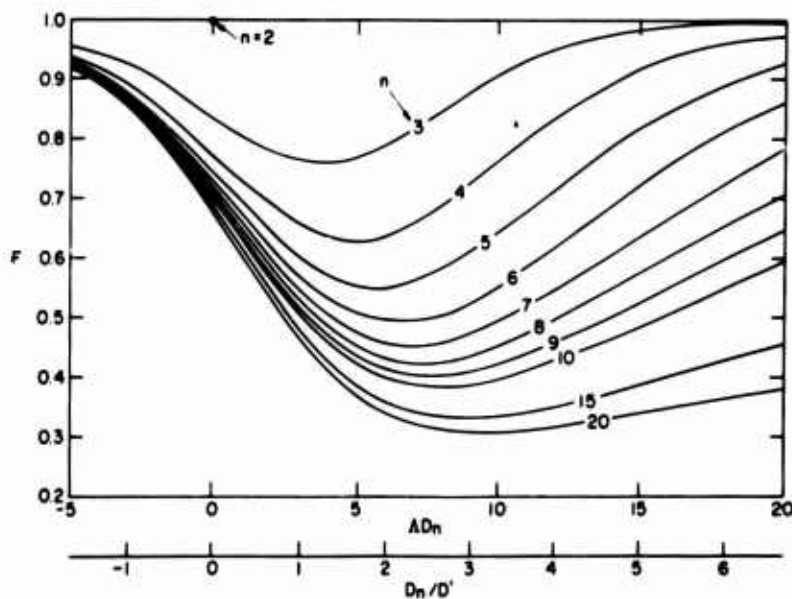


Figure H3. Values of the Form Factor as a Function of ΔD_n and n , Atmospheric Range, With Lower Diameter Truncation of $d = \Delta D$

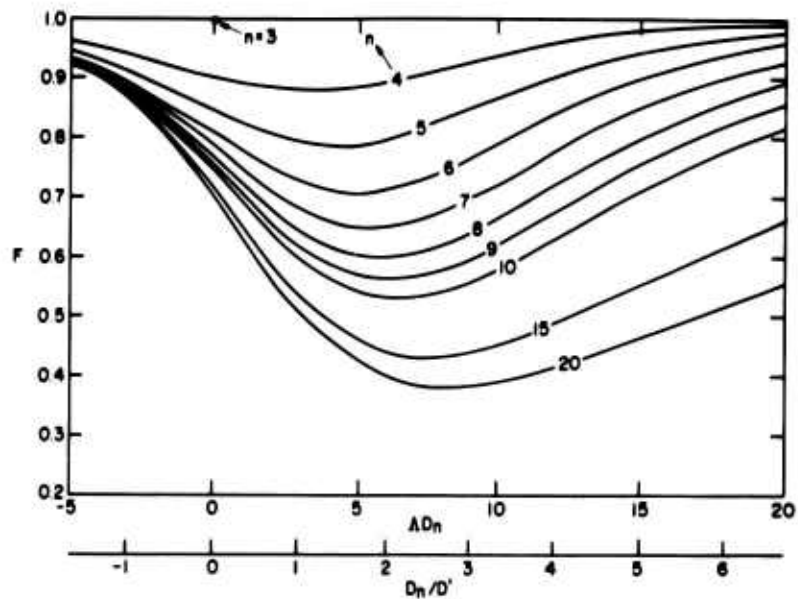


Figure H4. Values of the Form Factor as a Function of ΔD_n and n , Atmospheric Range, With Lower Diameter Truncation of $d = 2\Delta D$

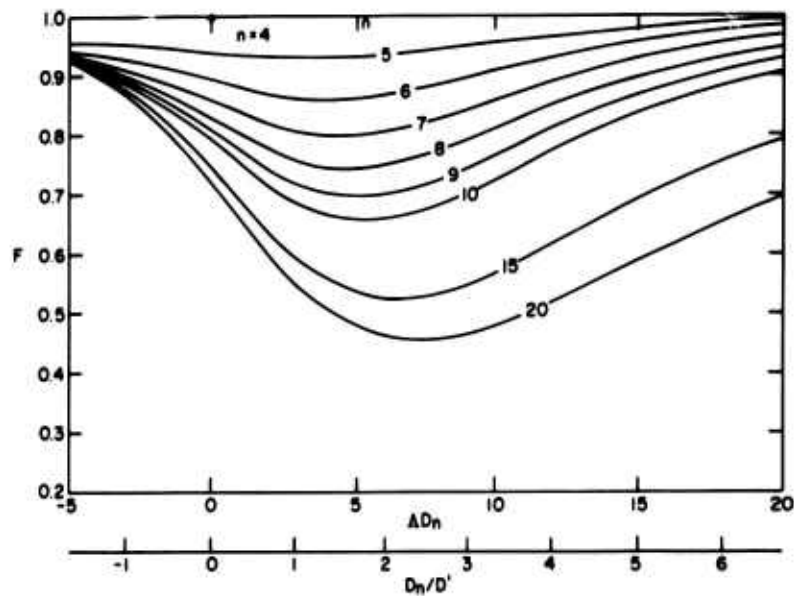


Figure H5. Values of the Form Factor as a Function of ΔD_n and n , Atmospheric Range, With Lower Diameter Truncation of $d = 3\Delta D$

H2. UNCERTAINTY EFFECTS OF l TO D CONVERSION ON THE VALUES M_s , Z_s , AND k

H2.1 The Uncertainty Equations, Evaluations, and Tabular Results

Consider the single-sample equations for M_s and Z_s which are given, respectively, by Eqs. (E11) and (E13). By the use of Eq. (E21), we may write the expressions for M_s and Z_s as

$$M_s = C N_T \sum_{i=1}^{i=n} D_i^3 \alpha_i \quad (H18)$$

and

$$Z_s = N_T \sum_{i=1}^{i=n} D_i^6 \alpha_i \quad (H19)$$

where

$$C = \pi/6 \times 10^{-3} \quad (H20)$$

We may also write the expression for k , which, from Eq. (E17), is

$$k = C \sqrt{N_T} F \quad (E17)$$

where the form factor, F , for irregularly-classified data, as given by Eq. (E23a) of the footnote on page 119, is

$$F = \frac{\sum_{i=1}^{i=n} D_i^3 \alpha_i}{\left[\sum_{i=1}^{i=n} D_i^6 \alpha_i \right]^{0.5}} \quad (E23a)$$

In these equations, which are written for hydrometeor spectra that are classified in terms of equivalent-melted-diameter, the parameter D_i is the mid-diameter of any given, or i 'th, class and D_n is the mid-diameter of the n 'th, or last, class, which contains the ice or snow particles of the largest size. N_T is the total number concentration of the ice or snow particles of all sizes in the distribution: C is a numerical constant specified by Eq. (H20) and α_i is the ratio of the class number concentration of the particles, N_i , to the total number concentration, N_T , see Eq. (E21) and associated discussion.

We wish, now, to investigate the uncertainty effects of l to D conversion on the M_s , Z_s , and k values that are determined from the size-distribution data for any given sample of ice hydrometeors. We will develop the uncertainty equations for M_s and Z_s first and then follow with the development of the equation for k .

The l (physical length measure) to D (equivalent-melted-diameter) conversion equations of conventional SAMS usage are of the power-function form

$$D = \gamma l^\phi, \quad (\text{H21})$$

where γ and ϕ have particular values that depend on the category and type of the ice hydrometeors (snow or ice crystals, of different types) contained in the samples and that also depend on whose values, from among those of diverse investigators, are considered to be the "most accurate". (In fact, even the accuracy and authenticity of the power-function form of the conversion equation is subject to question in the present state of our knowledge.)

From Eq. (H21), assuming that this was the equation form used in conversion, it follows that the "physical sizes" of the ice hydrometeors which corresponded to the D_i values of Eqs. (H18), (H19), and (E23a) mentioned herein, were related to the l_i values as

$$D_i = \gamma l_i^\phi. \quad (\text{H22})$$

If we substitute Eq. (H22) into Eqs. (H18) and (H19), we obtain

$$M_s = C N_T \gamma^3 \sum_{i=1}^{i=n} l_i^{3\phi} \alpha_i \quad (\text{H23})$$

and

$$Z_s = N_T \gamma^6 \sum_{i=1}^{i=n} l_i^{6\phi} \alpha_i, \quad (\text{H24})$$

which are the equations for M_s and Z_s written in terms of the length measure of physical size of the basic data of original measurement.

In the process of l to D conversion, if it is performed correctly, each lower and upper boundary of the size classes of the original " l data" will be converted, through Eq. (H22), into new, corresponding lower and upper boundaries for the size classes of the equivalent-melted-diameter, or " D data". There will be no change in the number of the classes, in the class number concentrations of the particles, in the total number concentration of all of the particles of the given sample, or in

the values of the α coefficients for the different classes. Moreover, since we presume that the original data was measured accurately, there are no uncertainties in our knowledge of any of the class boundary, or mid-values, of the " δ data". (We are not concerned with instrumental or measurement uncertainties in this investigation.)

The only parameters of the above equations that are subject to conversion-type uncertainty are the coefficient, γ and the exponent, ϕ , of the l to D conversion equation, Eq. (H22). Thus, we may write the total derivative (or uncertainty derivative) of M_s as

$$dM_s = \frac{\partial M_s}{\partial \gamma} d\gamma + \frac{\partial M_s}{\partial \phi} d\phi \quad (H25)$$

and that for Z_s as

$$dZ_s = \frac{\partial Z_s}{\partial \gamma} d\gamma + \frac{\partial Z_s}{\partial \phi} d\phi. \quad (H26)$$

When the partial derivatives of these equations are determined, from Eqs. (H23) and (H24),

$$dM_s = 3 C N_T \gamma^2 \left[d\gamma \sum_{i=1}^{i=n} l_i^{3\phi} \alpha_i + \gamma d\phi \sum_{i=1}^{i=n} l_i^{3\phi} (1n l_i) \alpha_i \right], \quad (H27)$$

and

$$dZ_s = 6 N_T \gamma^5 \left[d\gamma \sum_{i=1}^{i=n} l_i^{6\phi} \alpha_i + \gamma d\phi \sum_{i=1}^{i=n} l_i^{6\phi} (1n l_i) \alpha_i \right], \quad (H28)$$

or, in finite difference form,

$$\Delta M_s = 3 C N_T \gamma^2 \left[\Delta\gamma \sum_{i=1}^{i=n} l_i^{3\phi} \alpha_i + \gamma \Delta\phi \sum_{i=1}^{i=n} l_i^{3\phi} (1n l_i) \alpha_i \right], \quad (H29)$$

and

$$\Delta Z_s = 6 N_T \gamma^5 \left[\Delta\gamma \sum_{i=1}^{i=n} l_i^{6\phi} \alpha_i + \gamma \Delta\phi \sum_{i=1}^{i=n} l_i^{6\phi} (1n l_i) \alpha_i \right], \quad (H30)$$

If we write the above equations in the form most convenient for the subsequent discussion, we obtain

$$\Delta M_s = \Delta M_{s\gamma} + \Delta M_{s\phi} \quad (H31)$$

where

$$\Delta M_{s\gamma} = 3 C N_T \gamma^2 \Delta\gamma \sum_{i=1}^{i=n} l_i^{3\phi} \alpha_i \quad (H32)$$

and

$$\Delta M_{s\phi} = 3 C N_T \gamma^3 \Delta\phi \sum_{i=1}^{i=n} \gamma_i^{3\phi} \ln(l_i) \alpha_i \quad (H33)$$

likewise

$$\Delta Z_s = \Delta Z_{s\gamma} + \Delta Z_{s\phi} \quad (H34)$$

where

$$\Delta Z_{s\gamma} = 6 N_T \gamma^5 \Delta\gamma \sum_{i=1}^{i=n} l_i^{6\phi} \alpha_i \quad (H35)$$

and

$$\Delta Z_{s\phi} = 6 N_T \gamma^6 \Delta\phi \sum_{i=1}^{i=n} l_i^{6\phi} \ln(l_i) \alpha_i \quad (H36)$$

Equations (H31) through (H36) specify the uncertainties in M_s and Z_s that will result from uncertainties in our knowledge of the coefficient, γ , and exponent, ϕ , of the l to D conversion equation. We will consider the evaluation of these equations after we discuss the uncertainty equation for k .

If we substitute Eq. (H22) into Eq. (E23a), thence into Eq. (E22) (the latter equations are presented on pages 229 and 119), the expression for k , written in terms of the length measures of the basic data, becomes

$$k = \frac{C \sqrt{N_T} \sum_{i=1}^{i=n} l_i^{3\phi} \alpha_i}{\left[\sum_{i=1}^{i=n} l_i^{6\phi} \alpha_i \right]^{0.5}} \quad (H37)$$

It is seen that k , in this equation, does not depend on the coefficient, γ , of the l to D conversion equation, but only on the exponent, ϕ .

The derivative of k with respect to ϕ , written in finite difference form, is

$$\Delta k = \frac{3 C \sqrt{N_T}}{\left(\sum_{i=1}^{i=n} l_i^{6\phi} \alpha_i \right)^{0.5}} \left[\sum_{i=1}^{i=n} l_i^{3\phi} \alpha_i \ln l_i - \frac{\left(\sum_{i=1}^{i=n} l_i^{3\phi} \alpha_i \right) \left(\sum_{i=1}^{i=n} l_i^{6\phi} \alpha_i \ln l_i \right)}{\sum_{i=1}^{i=n} l_i^{6\phi} \alpha_i} \right] \Delta \phi . \quad (H38)$$

This specifies the uncertainties in k that result from uncertainties in ϕ .

Equations (H34), (H37), and the preceding equation were evaluated for three different categories of ice hydrometeors. They were evaluated for large-snow, of type LS_3 , for small-snow, of type SS_g and for C_1 type ice-crystals. The initial " l data" were assumed to be exponentially distributed and three different values of liquid-water-content were considered, per category, which typify atmospheric values of large, medium, and small.

The distribution and conversion parameters of reference are listed in Table H1. Reference is the assumed conversion condition of zero uncertainty. The particular truncation assumptions, distribution equations and N_T values for the " l data" are listed in the first section of the table. The assumed γ and ϕ values of conversion, see Eq. (H22), are noted in the second section of the table. These are the same values specified in R No. 2 (page 65). The resultant parameters of the "distributions", after conversion, are shown in the third section of the table. It should be mentioned that the initial distributions were deliberately chosen such that the liquid-water-content, that is, M_g , values of the converted distributions would be close to 1.0, 0.1, and 0.01, for large snow, and close to 0.5, 0.1, and 0.01, for small snow and ice crystals. Also listed in the table, for information, are the values of the form factor, F , as given by the series terms of Eq. (H37), that is, the terms excluding C and $\sqrt{N_T}$, see Eq. (E23A).

The uncertainty effects of l to D conversion on the M_g , Z_g , and k values were determined for these reference conditions. Two assumptions of uncertainty were made regarding the coefficient, γ , of the conversion equation: first, that $\Delta\gamma = 0.1$; second, that $\Delta\gamma = 0.2$. Similar assumptions were made about the exponent of the conversion equation; first, that $\Delta\phi = 0.1$; second, that $\Delta\phi = 0.2$. The 0.1 assumptions on $\Delta\gamma$ and $\Delta\phi$ were considered to be the normal, typical uncertainties; the 0.2 assumptions were considered to be the maximum expected. Equations (H29), (H30), and (H38) were evaluated for each of the four combinations of the $\Delta\gamma$ and $\Delta\phi$

* Assistance in this differentiation was given by Mr. Lawrence E. Belsky, of Digital Programming Services, Inc., Waltham, Massachusetts.

values. The results are shown in Table H2 and summarized in Figures E15, E16, and E17, of Appendix E. Briefly, the results reveal that the decimal uncertainties of the radar reflectivity factor, $\Delta Z_s / Z_s$ (the subscript "s" is not retained in the table), range from 1.4 to 5.2; that the decimal uncertainties in the liquid-water-content, $\Delta M_s / M_s$, range from 0.71 to 2.0, whereas the decimal uncertainties in the spectral parameter, k , that is, the $\Delta k/k$ values, only range from 0.1 to 0.34. As emphasized in Appendix E, this demonstrates that the k values can be computed from spectral data with considerably better accuracy than either the M_s or Z_s values.

The normal, typical uncertainties of k , which are presumed to be associated with the $\Delta\phi = 0.1$ assumption, are seen to range from 0.1 to 0.17 (10 to 17 percent); the probable maximum uncertainties, associated with $\Delta\phi = 0.2$, vary from 0.20 to 0.34.

H2.2 Errors Involved in the Determination of k Under the Assumption That l to D Conversion Effects are Neglected

It is of interest to consider the magnitude of the k uncertainties (errors) that would be associated with a complete neglect of l to D conversion, that is, with the situation in which the k values were computed directly from the " l data", of basic instrumental measurement, rather than from the " D data", of assumptive conversion.

* For computing the individual terms of Eqs. (H29) and (H30) [also see (H31) and (H34)], the $\Delta\gamma$ and $\Delta\phi$ changes were considered positive and the sign of the resultant $\Delta M\gamma$, $\Delta M\phi$, $\Delta Z\gamma$, and $\Delta Z\phi$ changes were retained and identified in the Table H2 listings. Likewise, the sign of the Δk and $\Delta k/k$ changes (always negative) were identified in the table. It should be noted, however, that the $\Delta\gamma$ and $\Delta\phi$ uncertainties in l to D conversion could be either + or -, and non-correlated. Hence, the $\Delta M\gamma$ and $\Delta M\phi$ values of the table were added in rms fashion to obtain the ΔM values. Similarly, the $\Delta Z\gamma$ and $\Delta Z\phi$ values were rms summed to obtain the ΔZ values. In the text discussion of the M , Z , and k uncertainties, it is assumed that these might be either + or -, thus no mention is made of sign.

Table H1. Parameters and Equations of the "λ" Distributions Parameters of λ to D Conversion and the Resultant Parameters of the "D" Distributions

Hydrometeor Category and Type	Parameters and Equations of the "λ" Distribution				Parameters of the "λ" to "D" Conversion	Resultant Parameters of the "D" Distribution										
	Δλ mm	λ min mm	n	λ max mm		λ n mm	Distribution Equation	N _{T-3} No. m ⁻³	γ	σ	d	D _{max}	D _n	M	Z	F
Large Snow LS ₃	0.5	0.5	20	10.0	9.75	$N_1 = 1.175 e^{-0.707 \lambda}$	2319	0.400	0.875	0.218	3.90	2.93	1.00	10.454	0.388	0.00978
	0.5	0.5	12	6.0	5.75	$N_1 = 484 e^{-1.030 \lambda}$	553	0.400	0.875	0.218	1.92	1.85	0.100	330	0.447	0.00550
	0.5	0.5	7	3.5	3.25	$N_1 = 235 e^{-1.5500 \lambda}$	134	0.400	0.875	0.218	1.20	1.12	0.0100	9.59	0.541	0.00323
Small Snow	0.3	0.3	23	6.9	6.75	$N_1 = 6.375 e^{-1.269 \lambda}$	11,372	0.324	0.805	0.123	1.53	1.51	0.500	487	0.406	0.0227
	0.3	0.3	15	4.5	4.35	$N_1 = 5,028 e^{-1.894 \lambda}$	4945	0.324	0.805	0.123	1.09	1.06	0.10	36.6	0.449	0.0165
	0.3	0.3	7	2.1	1.95	$N_1 = 9,231 e^{-4.348 \lambda}$	1790	0.324	0.805	0.123	0.589	0.555	0.0100	0.551	0.608	0.0135
Ice Crystals C ₁	0.1	0.1	26	2.6	2.55	$N_1 = 5.028 \times 10^4 e^{-4.163 \lambda}$	79,076	0.440	0.840	0.0636	0.982	0.966	0.500	81.4	0.376	0.0554
	0.1	0.1	16	1.6	1.55	$N_1 = 5.885 \times 10^4 e^{-6.859 \lambda}$	42,375	0.440	0.840	0.0636	0.653	0.636	0.100	4.67	0.429	0.0463
	0.1	0.1	8	0.8	0.75	$N_1 = 8.064 \times 10^4 e^{-14.13 \lambda}$	12,799	0.440	0.840	0.0636	0.365	0.346	0.0100	0.0825	0.587	0.0348

Table H2. Term, Total, and Ratio Uncertainties in M, Z, and k Resulting From the Uncertainties of γ and ϕ , in λ to D Conversion [see Eqs. (H29), (H30), and (H38)]

Hydrometeor Category and Type	M gm m ⁻³	Assumed		Term, Total, and Ratio Uncertainties of Liquid-Water-Content from Eq. (H34)				Term, Total, and Ratio Uncertainties of Radar Reflectivity Factor from Eq. (H37)				Total and Ratio Uncertainties of k, From Eq. (H41)	
		$\Delta\gamma$	$\Delta\phi$	$\Delta M_{\gamma-3}$ gm m ⁻³	ΔM_{ϕ} gm m ⁻³	rms	$\Delta M/M$	$\Delta Z\gamma$ mm ⁶ m ⁻³	$\Delta Z\phi$ mm ⁶ m ⁻³	rms	$\Delta Z/Z$	Δk gm m ^{1.5} mm ⁻³	$\Delta k/k$
Large-Snow LS ₃ LS ₃ LS ₃	1.00	0.100	0.100	0.754	0.435	0.0870	0.870	16511	12504	20711	1.98	-0.00131	-0.134
	1.00	0.200	0.200	1.53	0.898	1.77	1.77	38041	29462	48116	4.60	-0.00262	-0.268
	1.00	0.100	0.200	0.754	0.898	1.17	1.17	16511	29462	33773	3.23	-0.00262	-0.268
	1.00	0.200	0.100	1.53	0.435	1.59	1.59	38041	12504	40043	3.83	-0.00131	-0.134
Large-Snow LS ₃ LS ₃ LS ₃	0.100	0.100	0.100	0.0754	0.0304	0.0813	0.813	521	291	597	1.81	-0.000653	-0.119
	0.100	0.200	0.200	0.153	0.0630	0.165	1.65	1200	642	1361	4.12	-0.00130	-0.237
	0.100	0.100	0.200	0.0754	0.0630	0.0983	0.983	521	642	827	2.51	-0.00130	-0.237
	0.100	0.200	0.100	0.153	0.0304	0.156	1.56	1200	291	1235	3.74	-0.000653	-0.119
Large-Snow LS ₃ LS ₃ LS ₃	0.0100	0.100	0.100	0.0075	0.0017	0.00769	0.769	14.8	5.23	15.7	1.64	-0.000330	-0.201
	0.0100	0.200	0.200	0.0153	0.0035	0.0157	1.57	34.0	10.9	35.7	3.72	-0.00066	-0.201
	0.0100	0.100	0.200	0.0075	0.0035	0.00828	0.828	14.8	10.9	18.4	1.92	-0.00066	-0.201
	0.0100	0.200	0.100	0.0153	0.0017	0.0154	1.54	34.0	5.23	34.4	3.59	-0.00033	-0.100
Small-Snow SS _g SS _g SS _g	0.500	0.100	0.100	0.467	0.125	0.483	0.967	971	407	1053	2.16	-0.00356	-0.157
	0.500	0.200	0.200	0.956	0.253	0.989	1.98	2387	896	2550	5.24	-0.00712	-0.314
	0.500	0.100	0.200	0.467	0.253	0.531	1.06	971	896	1321	2.71	-0.00712	-0.314
	0.500	0.200	0.100	0.956	0.125	0.964	1.93	2387	407	2421	4.97	-0.00356	-0.157
Small-Snow SS _g SS _g SS _g	0.100	0.100	0.100	0.0933	0.0131	0.0942	0.942	73.1	20.9	76.0	2.08	-0.00250	-0.151
	0.100	0.200	0.200	0.191	0.0263	0.192	1.93	180	44.3	185	5.06	-0.00501	-0.303
	0.100	0.100	0.200	0.0933	0.0263	0.0969	0.969	73.1	44.3	85.5	2.34	-0.00501	-0.303
	0.100	0.200	0.100	0.191	0.0131	0.191	1.91	180	20.9	181	4.95	-0.00250	-0.151
Small-Snow SS _g SS _g SS _g	0.0100	0.100	0.100	0.00933	-0.00087	0.00937	0.937	1.10	0.045	1.10	2.00	-0.00171	-0.127
	0.0100	0.200	0.200	0.0191	-0.00175	0.0192	1.92	2.71	0.090	2.71	4.92	-0.00343	-0.254
	0.0100	0.100	0.200	0.00933	-0.00175	0.00949	0.949	1.10	0.090	1.10	2.00	-0.00343	-0.254
	0.0100	0.200	0.100	0.0191	-0.00087	0.0191	1.91	2.71	0.045	2.71	4.92	-0.00171	-0.127
Ice Crystals C ₁ C ₁ C ₁	0.500	0.100	0.100	0.343	-0.0480	0.346	0.693	116	12.3	117	1.43	-0.00944	-0.170
	0.500	0.200	0.200	0.697	-0.0970	0.704	1.41	261	25.1	262	3.22	-0.0189	-0.340
	0.500	0.100	0.200	0.343	-0.0970	0.356	0.713	116	25.1	119	1.46	-0.0189	-0.340
	0.500	0.200	0.100	0.697	-0.0480	0.699	1.40	261	12.3	261	3.21	-0.00944	-0.170
Ice Crystals C ₁ C ₁ C ₁	0.100	0.100	0.100	0.0685	-0.0242	0.0726	0.726	6.64	-0.696	6.68	1.43	-0.00769	-0.166
	0.100	0.200	0.200	0.139	-0.0491	0.147	1.47	15.0	-1.44	15.1	3.23	-0.0154	-0.332
	0.100	0.100	0.200	0.0685	-0.0491	0.0843	0.843	6.64	-1.44	6.79	1.45	-0.0154	-0.332
	0.100	0.200	0.100	0.139	-0.0242	0.141	1.41	15.0	-0.696	15.0	3.22	-0.00769	-0.166
Ice Crystals C ₁ C ₁ C ₁	0.0100	0.100	0.100	0.00685	-0.00430	0.00809	0.809	0.117	-0.0485	0.127	1.54	-0.00478	-0.137
	0.0100	0.200	0.200	0.0139	-0.00880	0.0165	1.65	0.264	-0.103	0.283	3.43	-0.00959	-0.275
	0.0100	0.100	0.200	0.00685	-0.00880	0.0112	1.12	0.117	-0.103	0.156	1.89	-0.00959	-0.275
	0.0100	0.200	0.100	0.0139	-0.00430	0.0145	1.45	0.264	-0.0485	0.268	3.25	-0.00478	-0.137

If the k values were approximated from the " ℓ data", we would be assuming, in essence, that ϕ , in Eq. (H37), had the value unity, such that

$$k_\ell = \frac{C\sqrt{N_T} \sum_{i=1}^{i=n} \ell_i^3 \alpha_i}{\left[\sum_{i=1}^{i=n} \ell_i^6 \alpha_i \right]^{0.5}} \quad (\text{H39})$$

The errors of approximation would be given by the difference between this equation and the correct equation, (H37), or by

$$\Delta k_E = C\sqrt{N_T} \left\{ \frac{\sum_{i=1}^{i=n} \ell_i^3 \alpha_i}{\left[\sum_{i=1}^{i=n} \ell_i^6 \alpha_i \right]^{0.5}} - \frac{\sum_{i=1}^{i=n} \ell_i^{3\phi} \alpha_i}{\left[\sum_{i=1}^{i=n} \ell_i^{6\phi} \alpha_i \right]^{0.5}} \right\} \quad (\text{H40})$$

The values of Δk_E were computed from this equation for the hydrometeor categories, reference parameters, and assumptions listed in Tables H1 and H2. The results are shown in Table H3. It is seen that the errors in k resulting from direct use of the " ℓ data", without any attempted ℓ to D conversion, are of the order of 0.12 to 0.30, which is about the same as that of the probable maximum uncertainties of the $\Delta\phi = 0.2$ assumption of Table H2, as discussed previously.

Table H3. Values of k_ℓ , k , Δk_E , and $\Delta k_E/\bar{k}$, Where $\bar{k} = (k_\ell + k)/2$, as Computed From Eqs. (H37), (H39), and (H40) for the Hydrometeor Categories (see parameters and assumptions listed in Tables H1 and H2)

Hydrometeor Category and Type					
	M	k_ℓ	k	Δk_E	$\Delta k_E/\bar{k}$
Large Snow LS ₃	1.0	0.00831	0.00978	-0.00147	-0.162
	0.1	0.00477	0.00551	-0.00736	-0.143
	0.01	0.00290	0.00323	-0.000378	-0.122
Small Snow SS _s	0.5	0.0168	0.0227	-0.00578	-0.297
	0.1	0.0124	0.0165	-0.00416	-0.288
	0.01	0.0104	0.0135	-0.00309	-0.258
Ice Crystals C ₁	0.5	0.0423	0.0554	-0.0132	-0.270
	0.1	0.0355	0.0463	-0.0109	-0.266
	0.01	0.0276	0.0348	-0.00722	-0.231

H2.3 Category-type Differences in k

As aircraft-radar information is accumulated in the SAMS program, concerning the k values and the l to D conversions that are applicable to the different categories and types of ice hydrometeors, we will progressively build a stock of knowledge about the normal, average value of ϕ that pertains generally to all ice hydrometeors, and about the usual category-type departures from this average. It is suspected that these departures, as they affect the k values, may be of negligible, second order importance, relative to other uncertainties of the overall SAMS program (such as the uncertainties of radar measurement, see R No. 1, Tables B1 through B4).

For example, we presently contend, in our SAMS analyses, that we can distinguish the category-type differences between large-snow, LS_3 , small-snow SS_3 , and type C_1 ice-crystals. The average value of ϕ for these three category-types is 0.84, see Table H1. The k value corresponding to this average is, from Eq. (H37).

$$k_{\phi} = C \sqrt{N_T} \frac{\sum_{i=1}^{i=n} l_i^{2.52} \alpha_i}{\left[\sum_{i=1}^{i=n} l_i^{5.04} \alpha_i \right]^{0.5}} \quad (H41)$$

The departures of the actual k values from the Eq. (41) value are given by the difference between this equation and Eq. (H37). Thus,

$$\Delta k_D = C \sqrt{N_T} \left\{ \frac{\sum_{i=1}^{i=n} l_i^{2.52} \alpha_i}{\left[\sum_{i=1}^{i=n} l_i^{5.04} \alpha_i \right]^{0.5}} - \frac{\sum_{i=1}^{i=n} l_i^{3\phi} \alpha_i}{\left[\sum_{i=1}^{i=n} l_i^{6\phi} \alpha_i \right]^{0.5}} \right\} \quad (H42)$$

The values of Δk_D and $\Delta k_D/\bar{k}$ are shown in Table H4 which correspond to the three category-types, reference parameters, and assumptions stated in Tables H1 and H2. The departures are seen to range from 0.001 to 0.05 (0.1 to 5 percent). The values are small, compared to the uncertainty and error values cited heretofore.

These results suggest that our contended ability to differentiate category-type differences among ice hydrometeors, in terms of k values (or M or Z values, by implication), may be illusory, because the uncertainties within any single category-type may exceed the contended differentiability.

Table H4. Values of $k_{\bar{\phi}}$, k , Δk_D , and $\Delta k_D/\bar{k}$, Where $\bar{k} = (k_{\bar{\phi}} + k)/2$, as Computed From Eqs. (H37), (H41), and (H42) for the Hydrometeor Categories, (see parameters and assumptions listed in Tables H1 and H2)

Hydrometeor Category and Type	M	$k_{\bar{\phi}}$	k	Δk_D	$\Delta k_D/\bar{k}$
Large Snow LS ₃	1.0	0.0103	0.00978	0.00052	0.0532
	0.1	0.00574	0.00551	0.00023	0.0417
	0.01	0.00340	0.00323	0.00017	0.0526
Small Snow SS _s	0.5	0.0215	0.0227	-0.0012	-0.0529
	0.1	0.0157	0.0165	-0.0008	-0.0485
	0.01	0.0129	0.0135	-0.0006	-0.0444
Ice Crystals C ₁	0.5	0.0555	0.0554	0.0001	0.00180
	0.1	0.0463	0.0463	0.0001	0.00149
	0.01	0.0348	0.0348	-0.00001	-0.000302

Therefore, at the present stage of the SAMS program, we may very well be able to neglect all details of the category-type differences of k to D conversion, which only affect the k values in minor degree through the ϕ differences. * We can assume, instead, a single average value of ϕ , which pertains to ice hydrometeors in general. The resultant uncertainties in the assessment of liquid-water-content along the SAMS missile trajectories for storm altitudes above the 0° isotherm should be negligible, relative to other uncertainties of the program.

* These details may still be important, of course, in the explanation of various erosion effects.